Convention on Long-range Transboundary Air Pollution

emep

Co-operative programme for monitoring and evaluation of the long-range transmission of air pollutants in Europe

STATUS REPORT 1/2017

Transboundary particulate matter, photo-oxidants, acidifying and eutrophying components

Status Report 1/2017

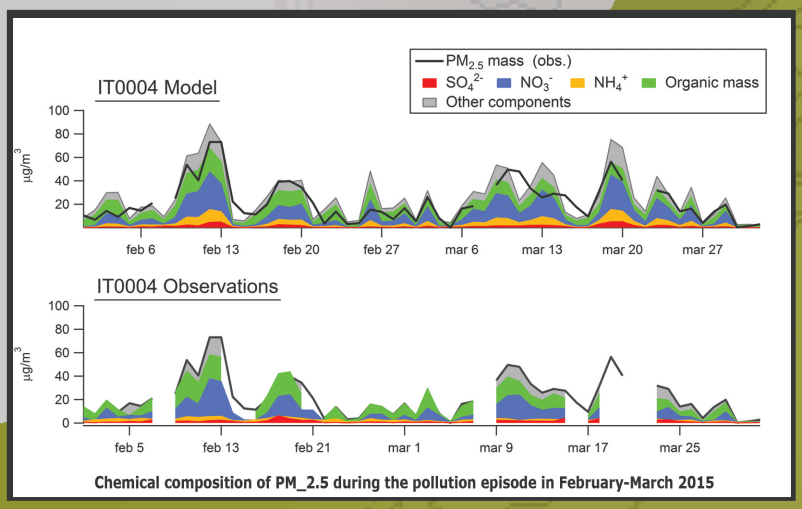

Chemical composition of PM_2.5 during the pollution episode in February-March 2015

msc-w & ccc & ceip

EMEP Report 1/2017
Date: August 23, 2017

METEOROLOGISK INSTITUTT
Norwegian Meteorological Institute

Transboundary particulate matter, photo-oxidants, acidifying and eutrophying components

EMEP/MSC-W:	Hilde Fagerli, Svetlana Tsyro, Bruce Rolstad Denby, Ágnes Nyíri, Michael Gauss, David Simpson, Peter Wind, Anna Benedictow, Jan Eiof Jonson, Heiko Klein, Michael Schulz, Jan Griesfeller
EMEP/CCC:	Wenche Aas, Anne-Gunn Hjellbrekke, Sverre Solberg, Stephen Matthew Platt, Markus Fiebig, Karl Espen Yttri, Richard Olav Rud, Kjetil Tørseth
EMEP/CEIP:	Katarina Mareckova, Marion Pinterits, Melanie Tista, Bernhard Ullrich, Robert Wankmüller
CCE/RIVM:	Maximilian Posch
Chalmers Univ. Tech.	Robert Bergström[1], Hannah Imhof ([1] SMHI, Gothenburg Univ., prior to Aug 2017)
IDAEA-CSIC:	Maria Cruz Minguillón
JRC Ispra:	Jean-Philippe Putaud, Fabrizia Cavalli
TROPOS:	Laurent Poulain
JÜLICH:	Patrick Schlag
Univ. of Helsinki:	Liine M. Heikkinen
Lund Univ.:	Erik Swietlicki, Johan Martinsson
CHMI:	Milan Vana
CzechGlobe:	Adeala Holubova Smejkalova
Univ. of Crete:	Giorgos Kouvarakis, Nikos Mihalopoulos

EMEP Status Report 2017; August 23, 2017

ISSN 1504-6109 (print)
ISSN 1504-6192 (on-line)

Executive Summary

This report presents the EMEP activities in 2016 and 2017 in relation to transboundary fluxes of particulate matter, photo-oxidants, acidifying and eutrophying components, with focus on results for 2015. It presents major results of the activities related to emission inventories, observations and modelling. The report also introduces specific relevant research activities addressing EMEP key challenges, as well as technical developments of the observation and modelling capacities.

An important topic this year is the transition to the new EMEP grid and resolution. For the first time, officially reported fine scale emissions ($0.1^\circ \times 0.1^\circ$resolution) have been used in the EMEP MSC-W model runs for air pollution assessment. The impacts of this change on model results and its comparisons to observations are analyzed in this report.

Measurements and model results for 2015

In the first chapter, the status of air pollution in 2015 is presented, combining meteorological information with numerical simulations using the EMEP MSC-W model together with observed air concentration and deposition data.

Altogether 31 Parties reported measurement data for 2015, from 158 sites in total. Of these, 125 sites reported measurements of inorganic ions in precipitation and/or main components in air; 72 of these sites had co-located measurements in both air and precipitation. The ozone network consisted of 133 sites, particulate matter was measured at 73 sites, of which 44 performed measurements of both PM_{10} and $PM_{2.5}$. In addition, 56 sites reported at least one of the components required in the advanced EMEP measurement program (level 2); however, only 9 of these sites had a complete aerosol program and even fewer sites provided the required oxidant precursor measurements.

The EMEP MSC-W model was run with meteorology and emission data for 2015, this year for the first time with fine scale reported emissions ($0.1^\circ \times 0.1^\circ$resolution). The modelled mean daily max O_3, SOMO35[1] and AOT40[2] for 2015 all show a distinct gradient with levels increasing from north to south, a well established feature for ozone, in general reflecting the

[1]The Sum of Ozone Means Over 35 ppb is the indicator for health impact assessment recommended by WHO. It is defined as the yearly sum of the daily maximum of 8-hour running average over 35 ppb.

[2]The accumulated amount of ozone over the threshold value of 40 ppb.

dependency of ozone on the photo-chemical conditions. The highest levels of these ozone metrics are modelled over the Mediterranean Sea and in the southeast corner of the model grid (e.g. Iran, Afghanistan, Tajikistan, Kyrgyzstan). The measurement network is limited to the continental western part of the model domain with no valid data in Belarus, Ukraine, Romania, Turkey and the area further east. For the region covered by the monitoring sites, the pattern with increased levels to the south with maximum levels near the Mediterranean is seen in the measurement data as well as in the model. The geographical pattern in the measured values is fairly well reflected in the model results for all these three metrics. The modelled POD_1[3] pattern is more homogenous over Europe than the other metrics - reflecting the influence of additional parameters such as plant physiology, soil moisture etc., and is a metric more indicative of the direct impact of ozone on vegetation than e.g. AOT40.

The dominant weather conditions in 2015, with a hot and dry summer in central/southern Europe and cool and wet conditions in Northern Europe, is clearly reflected in the summer ozone levels. Numerous heat waves accompanied by episodes of elevated ozone occurred on the European continent this year, most pronounced in the period June-August. Thus, the situation in 2015 was the direct opposite to the previous year, 2014, when central Europe experienced a cool and wet summer with very few ozone episodes and the Nordic countries had hot and dry conditions. In 2015 the summer ozone levels in the UK and North Europe were generally low with few peaks and episodes.

The modelled particulate matter (PM) concentrations in 2015 show large regional gradients across the EMEP domain, with low levels in Northern Europe and the highest ones in the very south of Europe and Central Asia (due to windblown dust), a pattern confirmed by the observations. There is a pronounced hot-spot of PM pollution in the Po Valley, and elevated PM levels are seen in the Benelux countries and parts of Hungary, Serbia, Germany and Poland. The overall agreement between the modelled and observed PM distributions is relatively good, although the high PM in the south/south-east cannot be verified due to the lack of measurements.

Both modelled and observed annual mean concentrations of PM_{10} and $PM_{2.5}$ were below the EU limit values (40 μg m^{-3} and 25 μg m^{-3}, respectively), with the exception of $PM_{2.5}$ modelled in the Po Valley. For daily concentrations, no violations of the PM_{10} EU limit value were observed at EMEP background sites, but the WHO air quality guidelines were not satisfied at 22 sites (of 55 EMEP sites). For daily $PM_{2.5}$, the observations reveal that the WHO air quality guidelines were not fully respected at 27 sites (of 42 EMEP sites). The model results for PM exceedances are in a quite good correspondence with the observations (better for PM_{10} than for $PM_{2.5}$), although there is some tendency to overestimate the frequency of exceedances in Mediterranean regions, while underestimating it in Northern Europe and the Baltic countries.

Among the most prominent features of PM pollution in 2015 was a series of episodes in Western, Central and South-Eastern Europe in February, March and November, caused by both local (traffic and residential heating) and long-range pollution and exacerbated by stagnant and dry weather conditions.

In terms of acidification, hot-spots of exceedances can be found in the Netherlands and its border areas to Germany and Belgium as well as in southern Germany, whereas in most of Europe critical loads are not exceeded. In Europe as a whole, acidity exceedances occur in about 5.3% of the ecosystem area, and the European average exceedance is about 17 eq

[3]Phyto-toxic ozone dose, here the accumulated stomatal ozone flux over a threshold 1 nmol m^{-2} s^{-1}.

$ha^{-1}yr^{-1}$. In contrast, critical loads for eutrophication are exceeded in virtually all countries (in about 60% of the ecosystem area) and the European average exceedance is around 200 eq $ha^{-1}yr^{-1}$. The highest exceedances are found in the Po Valley in Italy, the Dutch-German-Danish border areas and in north-western Spain.

Status of emissions
The completeness and consistency of submitted emission data have improved significantly since EMEP started collecting information on emissions, and between 41 and 48 Parties have reported data regularly since 2010. In 2017, 45 out of 51 Parties (88%) submitted emission inventories. There has been an improvement of reporting by EECCA countries in the last four years. However, the quality of submitted data differs significantly across countries, and the uncertainty in the data is considered relatively high.

2017 is the first year with reporting obligation of gridded emissions in the new grid resolution of $0.1^\circ \times 0.1^\circ$longitude-latitude. Only 22 of the 48 countries which are considered to be part of the new EMEP domain, reported sectoral gridded emissions in the new grid in 2017. Reported gridded sectoral data covers less than 20% of the grid cells within the geographical EMEP domain.

The development in emissions in the eastern and western parts of the EMEP area seems to follow different patterns. Emissions in the western part of the EMEP area are slowly decreasing, while emissions in the east seem to fluctuate around the same level or even increase. The emissions in western parts of the EMEP area are almost entirely based on reported data, while the emissions in eastern parts often are based on expert estimates (with larger uncertainty). From 2000 to 2015, the total change in emissions for the EMEP area was: NO_x (-22%), NMVOCs (-27%), SO_2 (-24%), NH_3 (+21%), $PM_{2.5}$ (-1%), PM_{coarse} (+38%) and CO (-22%).

Ship traffic emissions
For the first time this year, MSC-W has used data for international ship traffic emissions from the Finnish Meteorological Institute (FMI) in the model calculations for EMEP. Until last year, the MACC-TNO-III data set for 2011 was used for EMEP reporting, but this data set was not updated with information about the years after 2011. The new IMO (International Maritime Organization) regulation on sulfur emissions from international shipping, which came into effect in January 2015, has led to a significant reduction in sulfur emissions within the so-called Sulfur Emission Control Areas (SECAs) in Europe, i.e. the Baltic Sea and the North Sea, and thus the 2011 MACC-TNO-III data set was clearly not valid anymore.

The FMI data set, on the other hand, has been made available to us for 2015. It is based on accurate ship position data from AIS (Automated Identification System) and also takes into account the new IMO regulations. As part of the Copernicus Atmospheric Monitoring Service (CAMS), ship emissions will be calculated by FMI also for years after 2015, and it is assumed that data for 2016 will arrive in time for next year's EMEP reporting.

Model results in $0.1^\circ \times 0.1^\circ$and 50×50km^2 resolution and comparison to observations
In order to investigate whether the increased resolution of the new EMEP emissions (and model) have led to better model results, 2 different sets of model runs have been compared to EMEP and Airbase observation;

$EMEP_{50km}$: 'old gridding' of emissions, 50×50km^2 model resolution, 20 vertical layers (thickness of surface level ca. 90 m)

$EMEP_{0.1}$: new emissions, $0.1^{\circ} \times 0.1^{\circ}$ model resolution, 34 vertical layers (thickness of surface level ca. 50 m)

In addition, a $0.1^{\circ} \times 0.1^{\circ}$ model run with the same vertical structure as the $EMEP_{50km}$ run has been performed ($EMEP_{0.1_L20}$).

For NO_2, the model results on fine resolution are clearly better than $EMEP_{50km}$ compared to measurements. The spatial correlations between the fine resolution runs and Airbase data improve for almost all countries, providing confidence in the new gridded emissions of NO_x. For SO_2, the results are more mixed. For some countries the spatial correlation between model results and measurements improves significantly, while for other countries the correlation decreases considerably.

As expected, the results for secondary components show less changes than the primary components when going down in scale. An interesting exception is the wet deposition of sulfate and nitrate, where the spatial correlation between the model results and the EMEP observations improves notably. Some improvements in spatial correlation can be seen for PM_{10}, both when comparing model results to EMEP and Airbase data, while for $PM_{2.5}$ this is less clear. For both PM_{10} and $PM_{2.5}$, the bias between model results and measurements becomes somewhat smaller in the fine scale calculations (around zero).

The spatial correlation between modelled and measured annual mean of ozone is better for the fine scale model runs than for $EMEP_{50km}$, even on a country level. The general improvement in modelling the annual mean O_3 likely reflects the direct (titration) effect of the finer spatial resolution of the new emission data. It furthermore gives confidence that the fine resolution EMEP MSC-W model can be used to predict quantities related to long-term exposure (or deposition) on a better resolution than the $EMEP_{50km}$ model.

For the ozone metric d8hMAX (the daily maximum running 8h mean concentration) the results are more mixed, but show that $EMEP_{0.1_L20}$ overall is the model that performs the best of these three model versions. The latter result indicates that it would be worthwhile looking further into the vertical resolution definitions and the boundary layer assumptions in the fine resolution model. Overall the increased resolution of the new EMEP emissions (and model) have led to model results that improve compared to EMEP and Airbase observations.

Local Fractions in the EMEP MSC-W model

A new and computationally efficient methodology has been developed to track pollutants within the model (so far only primary pollutants). This development, called 'Local fraction', allows the calculation of source and pollutant specific contributions to and from any grid cell within a predefined area surrounding each grid cell, up to around 30 grid cells.

The 'Local fraction' methodology can be applied for three specific purposes. Firstly, information concerning the local contribution resulting from the emissions in each EMEP grid cell is required for the downscaling application uEMEP (urban EMEP) in order to redistribute the locally emitted concentrations. Secondly, knowledge of the local and non-local contributions can be used for improving the vertical profile parametrisation used for calculating near surface concentrations. Thirdly, the methodology generates local source receptor maps, allowing 'grid to grid' source contributions to be determined in the predefined area surrounding each grid cell. This provides very relevant information concerning contributions from one city to another or from cities to the nearby regional background. A visualization tool has been developed for displaying these source receptor maps, making the results easily accessible.

Observed and modelled concentrations of aerosols at high time resolution

In the last decade, high time resolution instruments less affected by artifacts have become available for the wider monitoring community, e.g. the Aerosol Chemical Speciation Monitor (ACSM). In this report, we give a brief illustration of the possibilities associated with ACSM measurements for characterization of the ambient aerosol at high time resolution and for model evaluation with respect to its ability to reproduce observed aerosol diurnal variations. We look at the chemical composition of non-refractory PM_1 and its temporal variability at four sites representative of different parts of Europe (in Finland, Netherlands, Germany and Spain).

One of the findings is that there are pronounced geographical and seasonal differences in aerosol diurnal profiles. The observations show that in Northern Europe (FI1778), the diurnal variations of all aerosol components are small, while in Central Europe (NL0044 and DE0044) the diurnal profiles show a characteristic minimum in the early afternoon and increased night-time levels for NO_3^- and organic mass. For these sites, the model calculates variation patterns quite close to the observed, though there are also some discrepancies. The site in Spain differs distinctly from the other sites with its daytime peaks, particularly pronounced for organic mass and especially in summer, as the site receives polluted air from the Barcelona region brought with the afternoon breeze from the Mediterranean. This meteorological phenomena is not captured in the model results.

Organic aerosol is underestimated by the model through all hours of a day. Furthermore, the study reveals that the model tend to overestimate the night-time levels of NO_3^-, which points to an over-production of NO_3^- aerosol during late evening/night hours and/or to too weak pollutants dispersion at night/early morning. The most pronounced diurnal variations are typically observed in summer and spring, whereas variability in winter in general is minor. Future studies should include more sites and years, and use the source apportioned fractions of the organic mass, obtained by positive matrix factorization (PMF), to compare with source profiles in the model.

Equivalent Black Carbon (EBC) from fossil fuel and biomass burning sources

A joint EMEP/ACTRIS intensive measurement period on source apportionment of EBC is planned for winter 2018, using multi-wavelength aethalometers. In this report, we carried out a first feasibility study for selected sites to illustrate some possible outcomes and challenges.

Equivalent black carbon from fossil fuel (EBC_{ff}) and biomass burning (EBC_{bb}) was calculated for four EMEP sites along a north to south transect for 2015, using a modification of the multi-wavelength aethalometer approach that involves positive matrix factorization (PMF). PMF derived levels of EBC_{bb} and EBC_{ff} at an hourly time resolution were compared to EMEP MSC-W model output.

The spatial resolution of the annual mean EBC level closely resembled that previously seen for EC, with elevated levels in Eastern and continental Europe compared to e.g. Scandinavia. EBC_{ff} dominated at all sites (54-82%) annually, and by a noticeable margin at the two southernmost sites, whereas EBC_{bb} nearly equaled that of EBC_{ff} at the Eastern European and Scandinavian site. The seasonal and diurnal variation seen for EBC_{bb}, clearly showed that residential heating was the main source. The diurnal variability of EBC_{ff} was particularly pronounced at the central European site and revealed the influence of the morning and afternoon vehicular rush hours.

Slightly higher daily correlations were found when comparing PMF derived levels of EBC_{bb} and EBC_{ff} with model output for the Eastern and the continental European site, than

for the Mediterranean and Scandinavian sites, but the model tended to underpredict in some cases. The results are in line with those obtained in previous studies, highlighting problems with underestimates of the biomass burning emissions in most countries. The most likely explanation for the observed underestimation is the underlying inventory.

It is expected that the joint EMEP/ACTRIS intensive measurement period in winter 2018 will be a valuable source of new information about BC sources, covering larger parts of Europe and additional analysis.

Model improvements

The main new features of the EMEP MSC-W model this year are (i) implementation of the local fraction capabilities as described above, and (ii) a new land-cover scheme with associated biogenic VOC emission rates, aimed at improved global-scale calculations. In addition, we have started the process of updating the chemical scheme, to better match the latest 'Master Chemical Mechanism'. Simple monoterpene chemistry was added for the first time also. Work continues to make the model more flexible in terms of the emissions sectors in use (SNAP, GNFR etc), emission factors, and to simplify application of the EMEP model with for example the WRF meteorological model.

Development in the monitoring network and database infrastructure

The last chapter of the report presents the implementation of the EMEP monitoring strategy and general development in the monitoring programme including data submission. There are large differences between Parties in the level of implementation, as well as significant changes in the national activities during the period 2000-2015. With respect to the requirement for level 1 monitoring, 42% of the Parties have had an improvement since 2010, while 28% have reduced the level of monitoring. For level 2 monitoring there has been a general positive development in recent years. However, in large parts of Europe the implementation of the EMEP monitoring strategy is still unsatisfactory.

The complexity of data reporting has increased in recent years. To improve the quality and timeliness of data reporting a new online data submission and validation tool has been developed, which was launched in spring 2016. There are many users that check their files using the submission tool, more than 700 users in the last year, and this has improved the correctness of the data files significantly.

Acknowledgments

This work has been funded by the EMEP Trust Fund.

The development of the EMEP MSC-W model has also been supported by Copernicus Atmosphere Modelling Service (CAMS) projects and the EU-project PANDA, the Nordic Council of Ministers, the Norwegian Space Centre and the Norwegian Ministry of the Environment. Development work has also been supported in Sweden, at Chalmers University of Technology and Gothenburg University (c/o Mattias Hallquist), both using funds from the Swedish Strategic Research project MERGE.

The work on the local fraction of the EMEP MSC-W model has been supported by the Norwegian Research Council project AIRQUIP.

The work presented here has benefited largely from the work carried out under the four EMEP Task Forces and in particular under TFMM.

A large number of co-workers in participating countries have contributed in submitting quality assured data. The EMEP centers would like to express their gratitude for continued good co-operation and effort. The institutes and persons providing data are listed in the EMEP/CCCs data report and identified together with the data-sets in the EBAS database.

For developing standardized methods and harmonization of measurements, the close co-operation with participants in the European Research Infrastructure for the observation of Aerosol, Clouds, and Trace gases (ACTRIS) as well as with the Scientific Advisory Groups (SAGs) in WMO/GAW are especially appreciated. ACTRIS has also been supporting the work on Equivalent Black Carbon presented in Chapter 7

Melissa Anne Pfeffer from the volcanic hazard team at the Icelandic Met Office is acknowledged for kindly providing us with the time series of plume height observations and the SO_2 emission rate measurements from the Holuhraun fissure eruption.

Dr. Jukka-Pekka Jalkanen (FMI, Finland) is acknowledged for valuable comments on the chapter on Emissions from International Shipping. The European Regional Development Fund has supported the work on ship emissions through the Interreg BSR project EnviSum.

The Working Group on Effects and its ICPs and Task Forces are acknowledged for their assistance in determining the risk of damage from air pollution. The Coordination Center for Effects (CCE) and Jean Paul Hettelingh have provided the latest data on critical loads.

This work has received support from the Research Council of Norway (Programme for Supercomputing) through CPU time granted at the super computers at NTNU in Trondheim, the University of Tromsø, and the University of Bergen through the EMEP project (grant NN2890K) for CPU, and the NorStore project European Monitoring and Evaluation Programme (grant NS9005K) for storage. IT infrastructure in general was available through the Norwegian Meteorological Institute. The CPU time made available by the ECMWF to generate meteorology has been of crucial importance for this year's status calculations.

Contents

1 Introduction **1**
1.1 Purpose and structure of this report . . . 1
1.2 Definitions, statistics used . . . 2
1.3 The new EMEP grid . . . 4
1.4 Country codes . . . 5
1.5 Other publications . . . 5
References . . . 12

I Status of air pollution **13**

2 Status of transboundary air pollution in 2015 **15**
2.1 Meteorological conditions in 2015 . . . 15
2.1.1 Temperature . . . 15
2.1.2 Precipitation . . . 17
2.1.3 2015 compared to the 2005-2014 average . . . 19
2.2 Measurement network 2015 . . . 19
2.3 Model setup for 2015 model runs . . . 20
2.4 Air pollution in 2015 . . . 20
2.4.1 Ozone . . . 20
2.4.2 Particulate matter . . . 24
2.4.3 Deposition of sulphur and nitrogen . . . 31
References . . . 35

3 Emissions for 2015 **37**
3.1 Emissions for 2015 . . . 37
3.1.1 Reporting of emission inventories in 2017 . . . 38
3.1.2 Reporting of gridded data . . . 38
3.1.3 Gap filling in 2017 . . . 38
3.1.4 Contribution of individual sectors to total EMEP emissions . . . 39
3.2 Emission trends in the EMEP area . . . 41
3.3 Comparison of emission levels . . . 42

3.3.1 Trend analysis . . . 43
3.3.2 NO_x emissions . . . 43
3.3.3 NMVOC emissions . . . 43
3.3.4 SO_x emissions . . . 44
3.3.5 NH_3 emissions . . . 45
3.3.6 CO emissions . . . 46
3.3.7 $PM_{2.5}$ emissions . . . 46
3.3.8 PM_{coarse} emissions . . . 47
3.4 Comparison of 2014 and 2015 . . . 47
3.4.1 Changes due to the gap-filling . . . 47
3.4.2 Changes in reported data . . . 50
3.5 Spatial distribution of emissions . . . 51
3.6 Volcanic emissions in 2015 . . . 52
3.6.1 Holuhraun fissure . . . 52
3.6.2 Passive degassing of SO_2 from Italian volcanoes . . . 52
3.7 International shipping . . . 53
References . . . 54

II Research Activities 57

4 EMEP MSC-W model runs using the EMEP emissions in fine resolution - comparison to observations 59
4.1 Model setup . . . 59
4.2 Short overview: comparison to EMEP background observations . . . 60
4.3 Comparison to Airbase data; primary components . . . 61
4.4 Comparison to Airbase and EMEP data; secondary components . . . 64
4.5 Summary and conclusions . . . 74
References . . . 76

5 Local Fractions in the EMEP MSC-W model 77
5.1 Introduction . . . 77
5.2 Calculation of Local Fractions . . . 78
5.2.1 Emissions . . . 78
5.2.2 Advection . . . 78
5.2.3 General expression . . . 79
5.2.4 Diffusion . . . 79
5.2.5 Deposition . . . 80
5.2.6 Chemistry . . . 80
5.2.7 Computational aspects . . . 80
5.3 Examples and validation . . . 82
5.4 Conclusions and future development . . . 83
References . . . 86

6 Comparison of model calculations with ACSM data 87
6.1 Introduction . . . 87
6.2 Results . . . 88

6.2.1 Mean chemical composition . . . 88
6.2.2 Mean diurnal profiles . . . 89
6.2.3 Seasonal diurnal profiles . . . 91
6.3 Recommendations and future work . . . 92
References . . . 94

7 Equivalent Black Carbon from fossil fuel and biomass burning sources at European rural background sites assessed by high time resolution measurements and modelling 97
7.1 Introduction . . . 97
7.2 Methodology . . . 98
7.2.1 Observations and the multi-wavelength PMF approach . . . 98
7.2.2 Modelling EC . . . 100
7.3 Seasonal and annual observations . . . 100
7.4 Observed diurnal variability . . . 102
7.5 Validation of the multi-wavelength PMF approach . . . 103
7.6 Comparison of EMEP model with observational derived results . . . 105
References . . . 109

III Technical EMEP Developments 113

8 Updates to the EMEP MSC-W model, 2016-2017 115
8.1 Chemical mechanism . . . 115
8.2 Deposition . . . 116
8.3 Land-cover and biogenic VOC . . . 116
8.4 Local fractions . . . 118
8.5 Other improvements . . . 118
References . . . 120

9 Development in the monitoring network, data quality and database infrastructure 123
9.1 Compliance with the EMEP monitoring strategy . . . 123
9.2 Updates in reporting templates and guidelines . . . 125
9.3 Data Quality . . . 126
References . . . 128

10 Emissions from international shipping 129
10.1 Background . . . 129
10.2 The FMI data on ship emissions . . . 130
10.3 The way ahead . . . 131
References . . . 133

IV Appendices 135

A National emissions for 2015 in the EMEP domain A:1
References . . . A:2

B Model Evaluation **B:1**
References B:1

CHAPTER 1

Introduction

1.1 Purpose and structure of this report

The mandate of the European Monitoring and Evaluation Programme (EMEP) is to provide sound scientific support to the Convention on Long-range Transboundary Air Pollution (LRTAP), particularly in the areas of atmospheric monitoring and modelling, emission inventories, emission projections and integrated assessment. Each year EMEP provides information on transboundary pollution fluxes inside the EMEP area, relying on information on emission sources and monitoring results provided by the Parties to the LRTAP Convention.

The purpose of the annual EMEP status reports is to provide an overview of the status of transboundary air pollution in Europe, tracing progress towards existing emission control Protocols and supporting the design of new protocols, when necessary. An additional purpose of these reports is to identify problem areas, new aspects and findings that are relevant to the Convention.

The present report is divided into four parts. Part I presents the status of transboundary air pollution with respect to acidification, eutrophication, ground level ozone and particulate matter in Europe in 2015. Part II summarizes research activities of relevance to the EMEP programme, while Part III deals with technical developments going on within the centres.

Appendix A in Part IV contains information on the national total emissions of main pollutants and primary particles for 2015.

Appendix B introduces the model evaluation report for 2015 (Gauss et al. 2017c) which is available online and contains time-series plots of acidifying and eutrophying components (Gauss et al. 2017b), ozone (Gauss et al. 2017a) and particulate matter (Tsyro et al. 2017). These plots are provided for all stations reporting to EMEP (with just a few exclusions due to data-capture or technical problems). This online information is complemented by numerical fields and other information on the EMEP website. The reader is encouraged to visit the website, `http://www.emep.int`, to access this additional information.

1.2 Definitions, statistics used

For sulphur and nitrogen compounds, the basic units used throughout this report are μg (S or N)/m^3 for air concentrations and mg (S or N)/m^2 for depositions. Emission data, in particular in some of the Appendices, is given in Gg (SO_2) and Gg (NO_2) in order to keep consistency with reported values.

For ozone, the basic units used throughout this report are ppb (1 ppb = 1 part per billion by volume) or ppm (1 ppm = 1000 ppb). At 20°C and 1013 mb pressure, 1 ppb ozone is equivalent to 2.00 μg m^{-3} .

A number of statistics have been used to describe the distribution of ozone within each grid square:

Mean of Daily Max. Ozone - First we evaluate the maximum modelled concentration for each day, then we take either 6-monthly (1 April - 30 September) or annual averages of these values.

SOMO35 - The Sum of Ozone Means Over 35 ppb is the indicator for health impact assessment recommended by WHO. It is defined as the yearly sum of the daily maximum of 8-hour running average over 35 ppb. For each day the maximum of the running 8-hours average for O_3 is selected and the values over 35 ppb are summed over the whole year.

If we let A_8^d denote the maximum 8-hourly average ozone on day d, during a year with N_y days (N_y = 365 or 366), then SOMO35 can be defined as:

$SOMO35 = \sum_{d=1}^{d=N_y} \max\big(A_8^d - 35 \text{ ppb}, 0.0\big)$

where the max function evaluates $\max(A-B,0)$ to $A-B$ for $A > B$, or zero if $A \leq B$, ensuring that only A_8^d values exceeding 35 ppb are included. The corresponding unit is ppb.days.

POD$_Y$ - Phyto-toxic ozone dose, is the accumulated stomatal ozone flux over a threshold Y, i.e.:

$$\text{POD}_Y = \int \max(F_{st} - Y, 0)\, dt \tag{1.1}$$

where stomatal flux F_{st}, and threshold, Y, are in nmol m^{-2} s^{-1}. This integral is evaluated over time, from the start of the growing season (SGS), to the end (EGS).

For the generic crop and forest species, the suffix gen can be applied, e.g. POD$_{Y,gen}$ (or $AF_{st}1.6_{gen}$) is used for forests. POD was introduced in 2009 as an easier and more descriptive term for the accumulated ozone flux. The definitions of AFst and POD are identical however, and are discussed further in Mills and Simpson (2010). See also Mills et al. (2011a) and Mills et al. (2011b).

AOT40 - is the accumulated amount of ozone over the threshold value of 40 ppb, i.e..

$AOT40 = \int \max(O_3 - 40 \text{ ppb}, 0.0)\, dt$

where the max function ensures that only ozone values exceeding 40 ppb are included. The integral is taken over time, namely the relevant growing season for the vegetation

concerned. The corresponding unit are ppb.hours (abbreviated to ppb.h). The usage and definitions of AOT40 have changed over the years though, and also differ between UNECE and the EU. LRTAP (2009) give the latest definitions for UNECE work, and describes carefully how AOT40 values are best estimated for local conditions (using information on real growing seasons for example), and specific types of vegetation. Further, since O_3 concentrations can have strong vertical gradients, it is important to specify the height of the O_3 concentrations used. In previous EMEP work we have made use of modelled O_3 from 1 m or 3 m height, the former being assumed close to the top of the vegetation, and the latter being closer to the height of O_3 observations. In the Mapping Manual (LRTAP 2009) there is an increased emphasis on estimating AOT40 using ozone levels at the top of the vegetation canopy.

Although the EMEP MSC-W model now generates a number of AOT-related outputs, in accordance with the recommendations of LRTAP (2009) we will concentrate in this report on two definitions:

AOT40$^{\mathbf{uc}}_{f}$ - AOT40 calculated for forests using estimates of O_3 at forest-top (uc: upper-canopy). This AOT40 is that defined for forests by LRTAP (2009), but using a default growing season of April-September.

AOT40$^{\mathbf{uc}}_{c}$ - AOT40 calculated for agricultural crops using estimates of O_3 at the top of the crop. This AOT40 is close to that defined for agricultural crops by LRTAP (2009), but using a default growing season of May-July, and a default crop-height of 1 m.

In all cases only daylight hours are included, and for practical reasons we define daylight for the model outputs as the time when the solar zenith angle is equal to or less than 89°. (The proper UNECE definition uses clear-sky global radiation exceeding 50 W m^{-2} to define daylight, whereas the EU AOT definitions use day hours from 08:00-20:00.). In the comparison of modelled and observed AOT40$^{\mathrm{uc}}_{f}$ in chapter 2, we have used the EU AOT definitions of day hours from 08:00-20:00.

The AOT40 levels reflect interest in long-term ozone exposure which is considered important for vegetation - critical levels of 3 000 ppb.h have been suggested for agricultural crops and natural vegetation, and 5 000 ppb.h for forests (LRTAP 2009). Note that recent UNECE workshops have recommended that AOT40 concepts are replaced by ozone flux estimates for crops and forests. (See also (Mills and Simpson 2010)).

This report includes also concentrations of particulate matter (PM). The basic units throughout this report are μg m^{-3} for PM concentrations and the following acronyms are used for different components to PM:

PBAP - primary biological aerosol particles describes airborne solid particles (dead or alive) that are or were derived from living organisms, including microorganisms and fragments of all varieties of living things (Matthias-Maser (1998)).

SOA - secondary organic aerosol, defined as the aerosol mass arising from the oxidation products of gas-phase organic species.

SIA - secondary inorganic aerosols, defined as the sum of sulphate (SO_4^{2-}), nitrate (NO_3^-) and ammonium (NH_4^+). In the EMEP MSC-W model SIA is calculated as the sum: SIA= SO_4^{2-} + NO_3^-(fine) + NO_3^-(coarse) + NH_4^+.

SS - sea salt.

PPM denotes primary particulate matter, originating directly from anthropogenic emissions. One usually distinguishes between fine primary particulate matter, $PPM_{2.5}$, with dry aerosol diameters below 2.5 μm and coarse primary particulate matter, PPM_{coarse} with dry aerosol diameters between 2.5 μm and 10 μm.

$PM_{2.5}$ denotes fine particulate matter, defined as the integrated mass of aerosol with dry diameters up to 2.5 μm. In the EMEP MSC-W model $PM_{2.5}$ is calculated as $PM_{2.5}$ = SO_4^{2-} + NO_3^-(fine) + NH_4^+ + SS(fine) + $PPM_{2.5}$ + 0.27 NO_3^-(coarse).

PM_{coarse} denotes coarse particulate matter, defined as the integrated mass of aerosol with dry diameters between 2.5μm and 10μm. In the EMEP MSC-W model PM_{coarse} is calculated as PM_{coarse} = 0.33 NO_3^-(coarse)+ SS(coarse) + PPM_{coarse}.

PM_{10} denotes particulate matter, defined as the integrated mass of aerosol with dry diameters up to 10 μm. In the EMEP MSC-W model PM_{10} is calculated as PM_{10} = $PM_{2.5}$+PM_{coarse}.

In addition to bias, correlation and root mean square the statistical parameter, index of agreement, are used to judge the model's agreement with measurements:

IOA - The index of agreement (IOA) is defined as follows (Willmott 1981, 1982):

$$IOA = 1 - \frac{\sum_{i=1}^{N}(m_i - o_i)^2}{\sum_{i=1}^{N}(|m_i - \bar{o}| + |o_i - \bar{o}|)^2} \tag{1.2}$$

where $\bar{o}$ is the average observed value. Similarly to correlation, IOA can be used to assess agreement either spatially or temporally. When IOA is used in a spatial sense, N denotes the number of stations with measurements at one specific point in time, and m_i and o_i are the modelled and observed values at station i. For temporal IOA, N denotes the number of time steps with measurements, while m_i and o_i are the modelled and observed value at time step i. IOA varies between 0 and 1. A value of 1 corresponds to perfect agreement between model and observations, and 0 is the theoretical minimum.

1.3 The new EMEP grid

At the 36^{th} session of the EMEP Steering Body the EMEP Centres suggested to increase spatial resolution and projection of reported emissions from 50×50 km polar stereographic EMEP grid to 0.1°×0.1°longitude-latitude grid in a geographic coordinate system (WGS84). The new EMEP domain shown in Figure 1.1 will cover the geographic area between 30°N-82°N latitude and 30°W-90°E longitude. This domain represents a balance between political needs, scientific needs and technical feasibility. Parties are obliged to report gridded emissions in the new grid resolution from year 2017.

The higher resolution means an increase of grid cells from approximately 21500 cells in the 50×50 km^2 grid to 624000 cells in the new longitude-latitude grid.

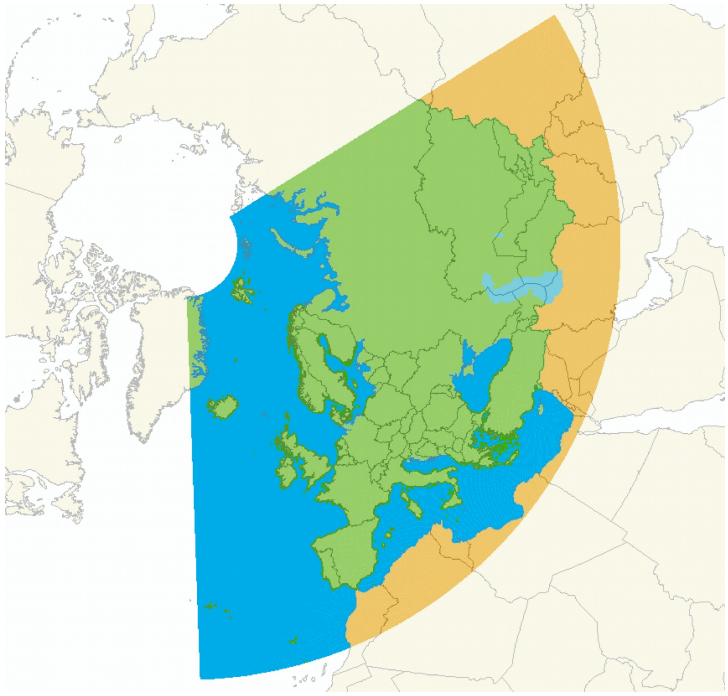

Figure 1.1: The new EMEP domain covering the geographic area between 30°N-82°N latitude and 30°W-90°E longitude.

1.4 Country codes

Several tables and graphs in this report make use of codes to denote countries and regions in the EMEP area. Table 1.1 provides an overview of these codes and lists the countries and regions included.

All 51 Parties to the LRTAP Convention, except two, are included in the analysis presented in this report. The Parties that are excluded of the analysis are Canada and the United States of America, because they lie outside the EMEP domain.

1.5 Other publications

This report is complemented by a report on EMEP MSC-W model performance for acidifying and eutrophying components, photo-oxidants and particulate matter in 2015 (Gauss et al. 2017c), made available online, at `www.emep.int`.

A list of all associated technical reports and notes by the EMEP centres in 2017 (relevant for transboundary acidification, eutrophication, ozone and particulate matter) follows at the end of this section.

Peer-reviewed publications

The following scientific papers of relevance to transboundary acidification, eutrophication, ground level ozone and particulate matter, involving EMEP/MSC-W and EMEP/CCC staff, have become available in 2016:

Acosta Navarro, J.-C., Ekman, A., Pausata, F. S. R., Lewinschal, A., Varma, V., Seland, Ø., Gauss, M., Iversen, T., Kirkevåg, A., Riipinen, I., Hansson, H. C.: Future response of temperature and pre-

Code	Country/Region
AL	Albania
AM	Armenia
AST	Remaining Asian areas
AT	Austria
ATL	Remaining N.-E. Atlantic Ocean
AZ	Azerbaijan
BA	Bosnia and Herzegovina
BAS	Baltic Sea
BLS	Black Sea
BE	Belgium
BG	Bulgaria
BIC	Boundary and Initial Conditions
BY	Belarus
CH	Switzerland
CY	Cyprus
CZ	Czech Republic
DE	Germany
DK	Denmark
EE	Estonia
EXC	EMEP land areas
ES	Spain
EU	European Union (EU28)
FI	Finland
FR	France
GB	United Kingdom
GE	Georgia
GL	Greenland
GR	Greece
HR	Croatia
HU	Hungary
IE	Ireland

Code	Country/Region
IS	Iceland
IT	Italy
KG	Kyrgyzstan
KZ	Kazakhstan
LI	Liechtenstein
LT	Lithuania
LU	Luxembourg
LV	Latvia
MC	Monaco
MD	Republic of Moldova
ME	Montenegro
MED	Mediterranean Sea
MK	The FYR of Macedonia
MT	Malta
NL	Netherlands
NO	Norway
NOA	North Africa
NOS	North Sea
PL	Poland
PT	Portugal
RO	Romania
RS	Serbia
RU	Russian Federation
SE	Sweden
SI	Slovenia
SK	Slovakia
TJ	Tajikistan
TM	Turkmenistan
TR	Turkey
UA	Ukraine
UZ	Uzbekistan

Table 1.1: Country/region codes used throughout this report.

cipitation to reduced aerosol emissions as compared with increased greenhouse gas concentrations. Journal of Climate,p. 1-45, 2016 DOI: 10.1175/JCLI-D-16-0466.1

Acosta Navarro, J.-C., Varma, V., Riipinen, I., Seland, Ø., Kirkevåg, A., Struthers, H., Iversen, T., Hansson, H.-C., Ekman, A.: Amplification of Arctic warming by past air pollution reductions in Europe. Nature Geoscience, 9 (4) , p. 277-281, 2016 DOI: 10.1038/ngeo2673

Alastuey, A., Querol, X., Aas, W., Lucarelli, F., Pèrez, N., Moreno, T., Cavalli, F., Areskoug, H., Balan, V., Catrambone, M., Ceburnis, D., Cerro, J. C., Conil, S., Gevorgyan, L., Hueglin, C., Imre, K., Jaffrezo, J.-L., Leeson, S. R., Mihalopoulos, N., Mitosinkova, M., O'Dowd, C. D., Pey, J., Putaud, J.-P., Riffault, V., Ripoll, A., Sciare, J., Sellegri, K., Spindler, G., Yttri, K. E. Geochemistry of PM10 over Europe during the EMEP intensive measurement periods in summer 2012 and winter 2013. Atmospheric Chemistry and Physics, 16, 6107-6129, 2016 DOI:10.5194/acp-16-6107-2016

Arnold, S. R., Law, K. S., Brock, C. A., Thomas, J. L., Starkweather, S. M., Salzen, K. von, Stohl, A., Sharma, S., Lund, M. T., Flanner, M. G., Petäjä, T., Tanimoto, H., Gamble, J., Dibb, J. E., Melamaed, M., Johnson, N., Fidel, M., Tynkkynen, V.-P., Baklanov, A., Eckhardt, S., Monks, S. A., Browse, J., Bozem, H. Arctic air pollution: Challenges and opportunities. Elementa, 4, 104, 2016 DOI.10.12952/journal.elementa.000104

Baklanov, A., Molina, L. T., Gauss, M.: Megacities, air quality and climate. Atmospheric Environment, 126 , p. 235-249, 2016 DOI: 10.1016/j.atmosenv.2015.11.059

Bellouin, N., Baker, L., Hodnebrog, Ø., Oliviè, D. J. L., Cherian, R., Macintosh, C., Samset, B. H., Esteve, A., Aamaas, B., Quaas, J., Myhre, G.: Regional and seasonal radiative forcing by perturbations to aerosol and ozone precursor emissions. Atmospheric Chemistry and Physics, 16 (21) , p. 13885-13910, 2016 DOI: 10.5194/acp-16-13885-2016

Bessagnet, B., Pirovano, G., Mircea, M., Cuvelier, C., Aulinger, A., Calori, G., Ciarelli, G., Manders, A., Stern, R., Tsyro, S. G., García Vivanco, M., Thunis, P., Pay, M.-T., Colette, A., Couvidat, F., Meleux, F., Rouïl, L., Ung, A., Aksoyoglu, S., Baldasano, J. M., Bieser, J., Briganti, G., Cappelletti, A., D'Isidoro, M., Finardi, S., Kranenburg, R., Silibello, C., Carnevale, C., Aas, W., Dupont, J.-C., Fagerli, H., Gonzalez, L., Menut, L., Prévôt, A. S. H., Roberts, P., White, L.: Presentation of the EURODELTA III intercomparison exercise-evaluation of the chemistry transport models' performance on criteria pollutants and joint analysis with meteorology. Atmospheric Chemistry and Physics, 16 (19) , p. 12667-12701, 2016 DOI: 10.5194/acp-16-12667-2016

Boichu, M., Chiapello, I., Brogniez, C., Péré, J.-C., Thieuleux, F., Torres, B., Blarel, L., Mortier, A., Podvin, T., Goloub, P., Söhne, N., Clarisse, L., Bauduin, S., Hendrick, F., Theys, N., Van Roozendael, M., Tanré, D.: Current challenges in modelling far-range air pollution induced by the 2014-2015 Bárdarbunga fissure eruption (Iceland). Atmospheric Chemistry and Physics, 16 (17) , p. 10831-10845, 2016 DOI: 10.5194/acp-16-10831-2016

Bovchaliuk, V., Goloub, P., Podvin, T., Veselovskii, I., Tanré, D., Chaikovsky, A., Dubovik, O., Mortier, A., Lopatin, A., Korenskiy, M., Victori, S.: Comparison of aerosol properties retrieved using GARRLiC, LIRIC, and Raman algorithms applied to multi-wavelength lidar and sun/skyphotometer data. Atmospheric Measurement Techniques, 9 (7) , p. 3391-3405, 2016 DOI: 10.5194/amt-9-3391-2016

Brown, J. E., Amundsen, I., Bartnicki, J., Dowdall, M., Dyve, J. E., Hosseini, A., Klein, H., Standring, W.: Impacts on the terrestrial environment in case of a hypothetical accident involving the recovery of the dumped Russian submarine K-27. Journal of Environmental Radioactivity, 165 , p. 1-12, 2016 DOI: 10.1016/j.jenvrad.2016.08.015

Cassiani, M., Stohl, A., Oliviè, D. J. L., Seland, Ø, Bethke, I., Pisso, I., Iversen, T.: The offline Lagrangian particle model FLEXPART-NorESM/CAM (v1): Model description and comparisons with the online NorESM transport scheme and with the reference FLEXPART model. Geoscientific Model Development, 9 (11) , p. 4029-4048, 2016 DOI: 10.5194/gmd-9-4029-2016

Cavalli, F., Alastuey, A., Areskoug, H., Ceburnis, D., Cech, J., Genberg, J., Harrison, R.M., Jaffrezo, J.L., Kiss, G., Laj, P., Mihalopoulos, N., Perez, N., Quincey, P., Schwarz, J., Sellegri, K., Spindler, G., Swietlicki, E., Theodosi, C., Yttri, K.E., Aas, W., Putaud, J.P. (2016): A European aerosol phenomenology-4: Harmonized concentrations of carbonaceous aerosol at 10 regional background sites across Europe. Atmospheric Environment, 144, 133-145, 2016 DOI:10.1016/j.atmosenv.2016.07.050

Clappier, A., Fagerli, H., Thunis, P.: Screening of the EMEP source receptor relationships: application to five European countries. Air quality, atmosphere and health, p. 1-11, 2016 DOI: 10.1007/s11869-016-0443-y

Denby, B., Ketzel, M., Ellermann, T., Stojiljkovic, A., Kupiainen, K., Niemi, J.V., Norman, M., Johansson, C., Gustafsson, M., Blomqvist, G., Janhäll, S., Sundvor, I.: Road salt emissions: A comparison of measurements and modelling using the NORTRIP road dust emission model. Atmospheric Environment, 141 , p. 508-522, 2016 DOI: 10.1016/j.atmosenv.2016.07.027

Forster, P. M., Richardson, T., Maycock, A. C., Smith, C. J., Samset, B. H., Myhre, G., Andrews, T., Pincus, R., Schulz, M.: Recommendations for diagnosing effective radiative forcing from climate models for CMIP6. Journal of Geophysical Research - Atmospheres, 121 (20) , p. 12460-12475, 2016 DOI: 10.1002/2016jd025320

Ghan, S., Wang, M., Zhang, S., Ferrachat, S., Gettelman, A., Griesfeller, J., Kipling, Z., Lohmann, U., Morrison, H., Neubauer, D., Partridge, D. G., Stier, P., Takemura, T., Wang, H., Zhang, K.: Challenges in constraining anthropogenic aerosol effects on cloud radiative forcing using present-day spatiotemporal variability. Proceedings of the National Academy of Sciences of the United States of America, 113 (21) s.5804-5811, 2016 DOI: 10.1073/pnas.1514036113

Giamarelou, M., Eleftheriadis, K., Nyeki, S., Tunved, P., Tørseth, K., Biskostic, G. Indirect evidence of the composition of nucleation mode atmospheric particles in the high Arctic. Journal of Geophysical Research - Atmospheres, 121, 965-975, 2016 DOI:10.1002/2015JD023646

Hallquist, M., Munthe, J., Hu, M., Wang, T., Chan, C. K., Gao, J., Boman, J., Guo, S., Hallquist, Å. M., Mellqvist, J., Moldanova, J., Pathak, R. K., Pettersson, J. B. C., Pleijel, H., Simpson, D., Thynell, M.: Photochemical smog in China: scientific challenges and implications for air-quality policies. ; National Science Review , 3 (4), p. 401-403, 2016 DOI: 10.1093/nsr/nww080

Huneeus, N., Basart, S., Fiedler, S., Morcrette, J.-J., Benedetti, A., Mulcahy, J., Terradellas, E., Garcia-Pando, C. P., Pejanovic, G., Nickovic, S., Arsenovic, P., Schulz, M., Cuevas, E., Baldasano, J. M., Pey, J., Remy, S., Cvetkovic, B.: Forecasting the northern African dust outbreak towards Europe in April 2011: A model intercomparison. Atmospheric Chemistry and Physics, 16 (8) , p. 4967-4986, 2016 DOI: 10.5194/acp-16-4967-2016

Kipling, Z., Stier, P., Johnson, C. E., Mann, G. W., Bellouin, N., Bauer, S. E., Bergman, T., Chin, M., Diehl, T., Ghan, S. J., Iversen, T., Kirkevåg, A., Kokkola, H., Liu, X., Luo, G., van Noije, T. P.C., Pringle, K. J., von Salzen, K., Schulz, M., Seland, Ø., Skeie, R. B., Takemura, T., Tsigaridis, K., Zhang, K.: What controls the vertical distribution of aerosol? Relationships between process sensitivity in HadGEM3-UKCA and inter-model variation from AeroCom Phase II. Atmospheric Chemistry and Physics, 16 (4) s.2221-2241, 2016 DOI: 10.5194/acp-16-2221-2016

Klein, H., Bartnicki, J., Dyve, J. E.: Improved source term description in Eulerian models in ARGOS. Radioprotection - Revue de la Societé Francaise de Radioprotection, 51 (2) Suppl. HS2. , p. S125-S127, 2016 DOI: 10.1051/radiopro/2016047

Koffi, B., Schulz, M., Bréon, F.-M., Dentener, F., Steensen, B. M., Griesfeller, J., Winker, D., Balkanski, Y., Bauer, S. E., Bellouin, N., Berntsen, T. K., Bian, H., Chin, M., Diehl, T., Easter, R., Ghan, S., Hauglustaine, D. A., Iversen, T., Kirkevåg, A., Liu, X., Lohmann, U., Myhre, G., Rasch, P., Seland, Ø., Skeie, R. B., Steenrod, S. D., Stier, P., Tackett, J., Takemura, T., Tsigaridis, K., Vuolo, M. R., Yoon, J., Zhang, K.: Evaluation of the aerosol vertical distribution in global aerosol models through comparison against CALIOP measurements: AeroCom phase II results. Journal of Geophysical Research - Atmospheres, 121 (12) , p. 7254-7283, 2016 DOI: 10.1002/2015JD024639

Kristiansen, N. I., Stohl, A., Oliviè, D. J. L., Croft, B., Søvde, O. A., Klein, H., Christoudias, T., Kunkel, D., Leadbetter, S. J., Lee, Y., Zhang, K., Tsigaridis, K., Bergman, T., Evangeliou, N., Wang, H., Ma, P.-L., Easter, R. C., Rasch, P. J., Liu, X., Pitari, G., Di Genova, G., Zhao, S., Balkanski, Y., Bauer, S. E., Faluvegi, G. S., Kokkola, H., Martin, R. V., Pierce, J. R., Schulz, M., Shindell, D. T., Tost, H., Zhang, H.: Evaluation of observed and modelled aerosol lifetimes using radioactive tracers of opportunity and an ensemble of 19 global models. Atmospheric Chemistry and Physics, 16 (5) , p. 3525-3561, 2016 DOI: 10.5194/acp-16-3525-2016

Kukkonen, J., Karl, M., Keuken, M. P., Denier van der Gon, H. A.C., Denby, B., Singh, V., Douros, I., Manders, A. A., Samaras, Z., Moussiopoulos, N., Jonkers, S., Aarnio, M. A., Karppinen, A., Kangas, L., Lützenkirchen, S., Petäjä, T., Vouitsis, I., Sokhi, R. S.: Modelling the dispersion of particle numbers in five European cities. Geoscientific Model Development, 9 (2) , p. 451-478, 2016 DOI: 10.5194/gmd-9-451-2016

Lacressonnière, G., Forêt, G., Beekmann, M., Siour, G., Engardt, M., Gauss, M., Watson, L., Andersson, C., Colette, A., Josse, B., Marécal, V., Nyiri, A., Vautard, R.: Impacts of regional climate change on air quality projections and associated uncertainties. Climatic Change, 136 (2) , p. 309-324, 2016 DOI: 10.1007/s10584-016-1619-z

Norman, M., Sundvor, I., Denby, B., Johansson, C., Gustafsson, M., Blomqvist, G., Janhäll, S.: Modelling road dust emission abatement measures using the NORTRIP model: Vehicle speed and studded tyre reduction. Atmospheric Environment, 134 , p. 96-108, 2016 DOI: 10.1016/j.atmosenv.2016.03.035

Popp, T., de Leeuw, G., Bingen, C., Brühl, C., Capelle, V., Chedin, A., Clarisse, L., Dubovik, O., Grainger, R. G., Griesfeller, J., Heckel, A., Kinne, S., Klüser, L., Kosmale, M., Kolmonen, P., Lelli, L., Litvinov, P., Mei, L., North, P., Pinnock, S., Povey, A., Robert, C., Schulz, M., Sogacheva, L., Stebel, K., Zweers, D. S., Thomas, G., Tilstra, L. G., Vandenbussche, S., Veefkind, P., Vountas, M., Xue, Y.: Development, production and evaluation of aerosol climate data records from European satellite observations (Aerosol_cci). Remote Sensing, 8 (5) , 2016 DOI: 10.3390/rs8050421

Prank, M., Sofiev, M., Tsyro, S. G., Hendriks, C., Valiyaveetil, S., Francis, X. V., Butler, T., van der Gon, H. D., Friedrich, R., Hendricks, J., Kong, X., Lawrence, M., Righi, M., Samaras, Z., Sausen, R., Kukkonen, J., Sokhi, R.: Evaluation of the performance of four chemical transport models in predicting the aerosol chemical composition in Europe in 2005. Atmospheric Chemistry and Physics, 16 (10) , p. 6041-6070, 2016 DOI: 10.5194/acp-16-6041-2016

Quennehen, B., Raut, J.-C., Law, K. S., Daskalakis, N., Ancellet, G. M., Clerbaux, C., Kim, S., Lund, M. T., Myhre, G., Oliviè, D. J. L., Safieddine, S., Skeie, R. B., Thomas, J. L., Tsyro, S. G., Bazureau, A., Bellouin, N., Hu, M., Kanakidou, M., Klimont, Z., Kupiainen, K., Myriokefalitakis, S., Quaas, J. R., Rumbold, S. T., Schulz, M., Cherian, R., Shimizu, A., Wang, J., Yoon, S., Zhu, T.: Multi-model evaluation of short-lived pollutant distributions over east Asia during summer 2008. Atmospheric Chemistry and Physics, 16 (17) , p. 10765-10792, 2016 DOI: 10.5194/acp-16-10765-2016

Samset, B. H., Myhre, G., Forster, P. M., Hodnebrog, Ø., Andrews, T., Faluvegi, G. S., Fläschner, D., Kasoar, M., Kharin, V. V., Kirkevåg, A., Lamarque, J.-F., Oliviè, D. J. L., Richardson, T. B., Shindell, D. T., Shine, K. P., Takemura, T., Voulgarakis, A.: Fast and slow precipitation responses to individual climate forcers: A PDRMIP multimodel study. Geophysical Research Letters, 43 (6), p. 2782-2791, 2016 DOI: 10.1002/2016GL068064

Schutgens, N. A. J., Gryspeerdt, E., Weigum, N., Tsyro, S. G., Goto, D., Schulz, M., Stier, P.: Will a perfect model agree with perfect observations? The impact of spatial sampling. Atmospheric Chemistry and Physics, 16 , p..6335-6353, 2016 DOI: 10.5194/acp-16-6335-2016

Soares, J., Sofiev, M., Geels, C., Christensen, J. H., Andersson, C., Tsyro, S. G., Langner, J.: Impact of climate change on the production and transport of sea salt aerosol on European seas. Atmospheric Chemistry and Physics, 16 (20) , p.13081-13104, DOI: 10.5194/acp-16-13081-2016

Sofen, E.D., Bowdalo, D., Evans, M.J., Apadula, F., Bonasoni, P., Cupeiro, M., Ellul, R., Galbally, I. E., Girgzdiene, R., Luppo, S., Mimouni, M., Nahas, A.C., Saliba, M., Tørseth, K. Gridded global surface ozone metrics for atmospheric chemistry model evaluation. Earth System Science Data, 8, 41-59. DOI:10.5194/essd-8-41-2016

Steensen, B. M., Schulz, M., Theys, N., Fagerli, H.: A model study of the pollution effects of the first 3 months of the Holuhraun volcanic fissure: Comparison with observations and air pollution effects. Atmospheric Chemistry and Physics, 16 (15) , p. 9745-9760, 2016 DOI: 10.5194/acp-16-9745-2016

Stjern, C. W., Samset, B. H., Myhre, G., Bian, H., Chin, M., Davila, Y., Dentener, F., Emmons, L., Flemming, J., Haslerud, A. S., Henze, D., Jonson, J. E., Kucsera, T., Lund, M. T., Schulz, M., Sudo, K., Takemura, T., Tilmes, S.: Global and regional radiative forcing from 20% reductions in BC, OC and SO4 - An HTAP2 multi-model study. Atmospheric Chemistry and Physics, 16 (21) , p. 13579-13599, 2016 DOI: 10.5194/acp-16-13579-2016

Theobald, M., R., Simpson, D., Vieno, M.: Improving the spatial resolution of air-quality modelling at a European scale - development and evaluation of the Air Quality Re-gridder Model (AQR v1.1). Geoscientific Model Development, 9 , p..4475-4489, 2016 DOI: 10.5194/gmd-9-4475-2016

Watson, L., Lacressonnière, G., Gauss, M., Engardt, M., Andersson, C., Josse, B., Marécal, V., Nyiri, A., Sobolowski, S. P., Siour, G., Szopa, S. Vautard, R.: Impact of emissions and +2 °C climate change upon future ozone and nitrogen dioxide over Europe. Atmospheric Environment, 142 , p. 271-285, 2016 DOI: 10.1016/j.atmosenv.2016.07.051

Winiger, P., Andersson, A., Eckhardt, S., Stohl, A., Gustafsson, O. The sources of atmospheric black carbon at a European gateway to the Arctic. Nature Communications, 12776, 2016 DOI:10.1038/ncomms12776

Zanatta, M., Gysel, M., Bukowiecki, N., Muller, T., Weingartner, E., Areskoug, H., Fiebig, M., Yttri, K.E., Mihalopoulos, N., Kouvarakis, G., Beddows, D., Harrison, R.M., Cavalli, F., Putaud, J.P., Spindler, G., Wiedensohler, A., Alastuey, A., Pandolfi, M., Sellegri, K., Swietlicki, E., Jaffrezo, J.L., Baltensperger, U., Laj, P. A. European aerosol phenomenology-5: Climatology of black carbon optical properties at 9 regional background sites across Europe. Atmospheric Environment, 145, 346-364, 2016

Zwaaftink, C.D.G., Grythe, H., Skov, H., Stohl, A. Substantial contribution of northern high-latitude sources to mineral dust in the Arctic. Journal of Geophysical Research: Atmospheres, 121, 13678-13697. 2016 DOI:10.1002/2016JD025482

Associated EMEP reports and notes in 2017

Joint reports

Transboundary particulate matter, photo-oxidants, acidification and eutrophication components. Joint MSC-W & CCC & CEIP Report. EMEP Status Report 1/2017

EMEP MSC-W model performance for acidifying and eutrophying components, photo-oxidants and particulate matter in 2015. Supplementary material to EMEP Status Report 1/2017

CCC Technical and Data reports

Anne-Gunn Hjellbrekke. Data Report 2015 Particulate matter, carbonaceous and inorganic compounds. EMEP/CCC-Report 1/2017

Anne-Gunn Hjellbrekke and Sverre Solberg. Ozone measurements 2015. EMEP/CCC-Report 2/2017

Wenche Aas and Pernilla Bohlin Nizzetto. Heavy metals and POP measurements 2015. EMEP/CCC-Report 3/2017

Sverre Solberg et al. VOC measurements 2014 and 2015. EMEP/CCC-Report 4/2017

Fabrizia Cavalli, Jean-Philippe Putaud and Karl Espen Yttri. Availability and quality of the EC and OC measurements, including results of the interlaboratory comparison of analytical methods for carbonaceous particulate matter within EMEP in 2015. EMEP/CCC-Report 5/2017

CEIP Technical and Data reports

Mareckova, K., Pinterits, M., Tista, M., Ullrich, B., Wankmüller, R. Inventory review 2017. Review of emission data reported under the LRTAP Convention and NEC Directive. Stage 1 and 2 review. Status of gridded and LPS data. EEA/CEIP Vienna. EMEP/CEIP Technical Report 1/2017

References

Gauss, M., Hjellbrekke, A.-G., Aas, W., and Solberg, S.: Ozone, Supplementary material to EMEP Status Report 1/2017, available online at www.emep.int, The Norwegian Meteorological Institute, Oslo, Norway, 2017a.

Gauss, M., Tsyro, S., Fagerli, H., Hjellbrekke, A.-G., and Aas, W.: Acidifying and eutrophying components, Supplementary material to EMEP Status Report 1/2017, available online at www.emep.int, The Norwegian Meteorological Institute, Oslo, Norway, 2017b.

Gauss, M., Tsyro, S., Fagerli, H., Hjellbrekke, A.-G., Aas, W., and Solberg, S.: EMEP MSC-W model performance for acidifying and eutrophying components, photo-oxidants and particulate matter in 2015., Supplementary material to EMEP Status Report 1/2017, available online at www.emep.int, The Norwegian Meteorological Institute, Oslo, Norway, 2017c.

LRTAP: Mapping critical levels for vegetation, in: Manual on Methodologies and Criteria for Mapping Critical Loads and Levels and Air Pollution Effects, Risks and Trends. Revision of 2009, edited by Mills, G., UNECE Convention on Long-range Transboundary Air Pollution. International Cooperative Programme on Effects of Air Pollution on Natural Vegetation and Crops, updated version available at www.icpmapping.com/, 2009.

Matthias-Maser, S.: Primary biological aerosol particles: Their significance, sources, sampling methods and size distribution in the atmosphere, in: Atmospheric particles, edited by Harrison, R. M. and van Grieken, R., pp. 349–368, John Wiley & Sons, Chichester, 1998.

Mills, G. and Simpson, D.: The Mediterranean region, in: Transboundary acidification, eutrophication and ground level ozone in Europe. EMEP Status Report 1/2010, pp. 37–48, The Norwegian Meteorological Institute, Oslo, Norway, 2010.

Mills, G., Hayes, F., Simpson, D., Emberson, L., Norris, D., Harmens, H., and Büker, P.: Evidence of widespread effects of ozone on crops and (semi-)natural vegetation in Europe (1990-2006) in relation to AOT40- and flux-based risk maps, Global Change Biology, 17, 592–613, doi:10.1111/j.1365-2486.2010.02217.x, 2011a.

Mills, G., Pleijel, H., Braun, S., Büker, P., Bermejo, V., Calvo, E., Danielsson, H., Emberson, L., Grünhage, L., Fernández, I. G., Harmens, H., Hayes, F., Karlsson, P.-E., and Simpson, D.: New stomatal flux-based critical levels for ozone effects on vegetation, Atmos. Environ., 45, 5064 – 5068, doi:10.1016/j.atmosenv.2011.06.009, 2011b.

Tsyro, S., Gauss, M., Hjellbrekke, A.-G., and Aas, W.: PM10, PM2.5 and individual aerosol components, Supplementary material to EMEP Status Report 1/2017, available online at www.emep.int, The Norwegian Meteorological Institute, Oslo, Norway, 2017.

Willmott, C. J.: On the validation of models, Physical Geography, 2, 184–194, 1981.

Willmott, C. J.: Some Comments on the Evaluation of Model Performance, Bulletin American Meteorological Society, 63, 1309–1313, doi:10.1175/1520-0477(1982)063<1309:SCOTEO>2.0.CO;2, 1982.

Part I

Status of air pollution

CHAPTER 2

Status of transboundary air pollution in 2015

Svetlana Tsyro, Wenche Aas, Sverre Solberg, Anna Benedictow, Hilde Fagerli and Maximilian Posch

This chapter describes the status of transboundary air pollution in 2015. A short summary of the meteorological conditions for 2015 is presented and the EMEP network of measurements in 2014 is briefly described. Thereafter, the status of air pollution and exceedances in 2015 is discussed.

2.1 Meteorological conditions in 2015

The meteorological data to drive the EMEP MSC-W air quality model have been generated by the Integrated Forecast System model (IFS) of the European Centre for Medium-Range Weather forecasts (ECMWF), hereafter referred to as the ECMWF-IFS model. In the meteorological community the ECMWF-IFS model is considered as state-of-the-art, and MSC-W has been using this model in hindcast mode to generate meteorological reanalyses for the year to be studied (Cycle 40r1 is the modelversion used for the year 2015 model run).

2.1.1 Temperature

The year 2015 was among the warmest in Europe and Russia, and global temperatures were again reported as the highest on record by the World Meteorological Organisation (WMO 2016). In winter and spring 2015, NOAA reported anomalously high temperatures due to advection of warm air from the south explained by the Arctic and Mid-latitudes Connections (Overland et al. 2015). The most characteristic features in year 2015 were temperatures above normal reported throughout Europe and the European part of Russia in winter and the extremely high summer temperatures in Southern Europe with unusual long heatwaves.

A persistent southwesterly flow with a well established Icelandic low and Azores high brought warm subtropical air into northern, eastern and southeastern Europe in the beginning

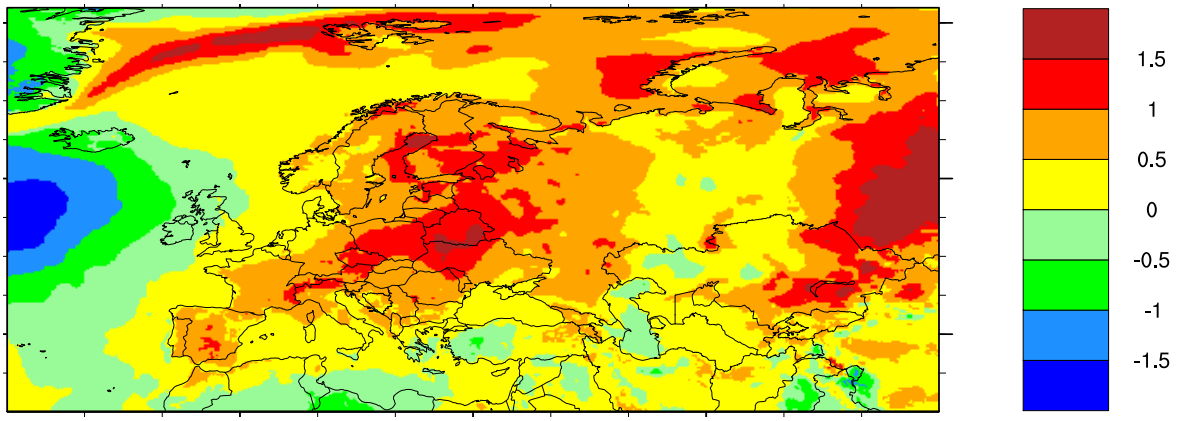

(a) Δtemperature at 2m (2015-climavg)

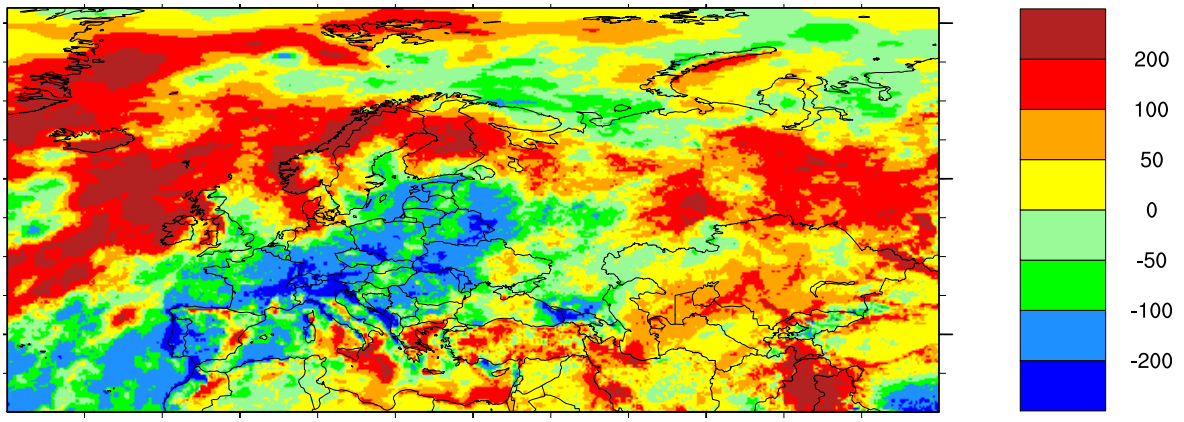

(b) Δprecipitation (2015-climavg)

Figure 2.1: Meteorological conditions in 2015 compared to the 2005-2014 average (climavg) for: (a) Annual mean temperature at 2m [K] and (b) Annual precipitation [mm]

of 2015. Sweden, Belarus, the European part Russia, Turkey and Serbia reported temperatures above normal. While the Iberian Peninsula experienced below normal temperatures and United Kingdom had near average temperatures. In February the flow of warm air reached Siberia, and in addition Norway and Finland experienced unusually high temperatures as well.

In spring a prolonged high pressure was established over the Iberian Peninsula and Siberia leading to above average temperatures in Portugal, Spain and the European part of Russia. Temperatures were more variable in northern, central and eastern Europe. March was warmer than usual in Norway, Finland and Germany. Turkey was colder than normal in April. Iceland and Ireland experiences the lowest temperatures in decades in May, while Spain and Portugal were affected by the first heat wave this year.

In summer a persistent high pressure system was established over central Europe bringing hot air from Africa to Europe and the heat gradually spread north and eastward. July was the warmest on record in Spain, Italy, Switzerland and Austria. Iceland, United Kingdom, Scandinavia and the European part of Russia July was very cool. An extraordinary and long-lasting heatwave affected Spain in July, while south-central and east-central Europe were affected by heat waves later in the season.

The hot summer temperatures prevailed into Autumn at least for eastern part of Europe. September was record warm in the Republic of Moldova, Serbia and Cyprus, and the warmest

month of the year in Iceland. In November temperatures were above normal in Norway and Finland, Germany and United Kingdom experienced record breaking high temperatures.

In December United Kingdom, France, Germany, the Netherlands, Sweden, Finland and Moldova set new records in maximum temperatures and in the European part of Russia temperatures were the second highest on record. The warm conditions in December were caused by a very high frequency of westerly or south-westerly winds across the regions.

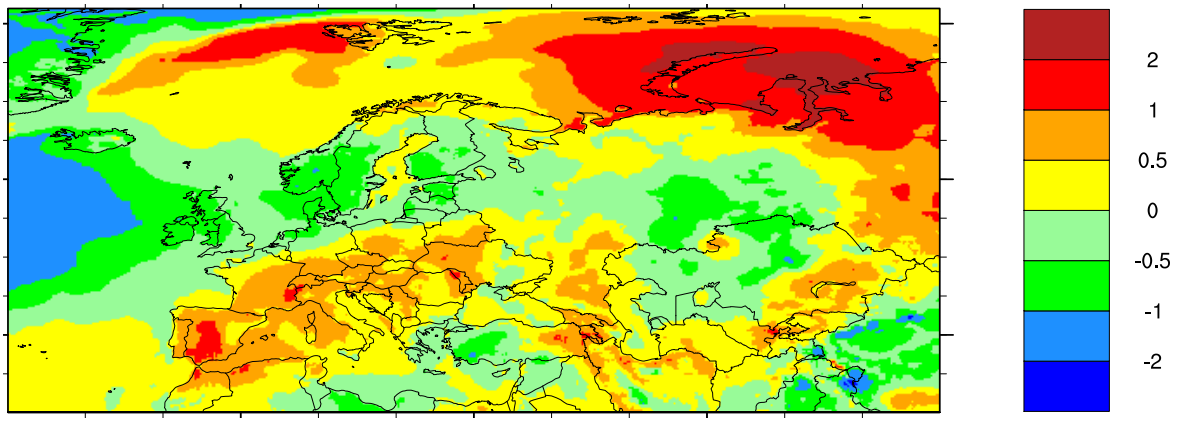

(a) Δtemperature at 2m (AprSep 2015-climavg)

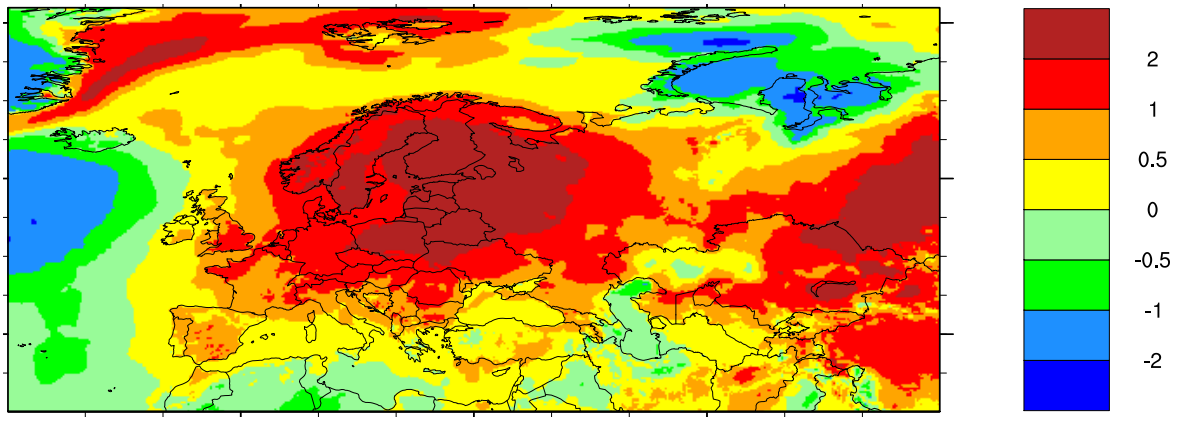

(b) Δtemperature at 2m (OctMar 2015-climavg)

Figure 2.2: Meteorological conditions in 2015 compared to the 2005-2014 average (climavg) for: (a) Summer (April-September) temperature [K], (b) Winter (January-March and October-December) temperature [K]

2.1.2 Precipitation

WMO reported global precipitation close to normal in 2015, but highly variable at regional and local scales (WMO 2016). There were areas of unusually high rainfall in northern and southeastern Europe and extremely dry areas in parts of central and southern Europe. The wetter than normal conditions in northeastern Europe in winter and the drought in central and southern Europe during summer were the most characteristic features in Europe in 2015.

An exceptional high frequency of westerly winds across Europe in the beginning of 2015 resulted in wetter than normal conditions in northern Europe. High precipitation records were

broken many places in Finland, Norway and Sweden. Germany was very wet in January, but very dry in February. Above normal rainfall was reported in Iceland in February.

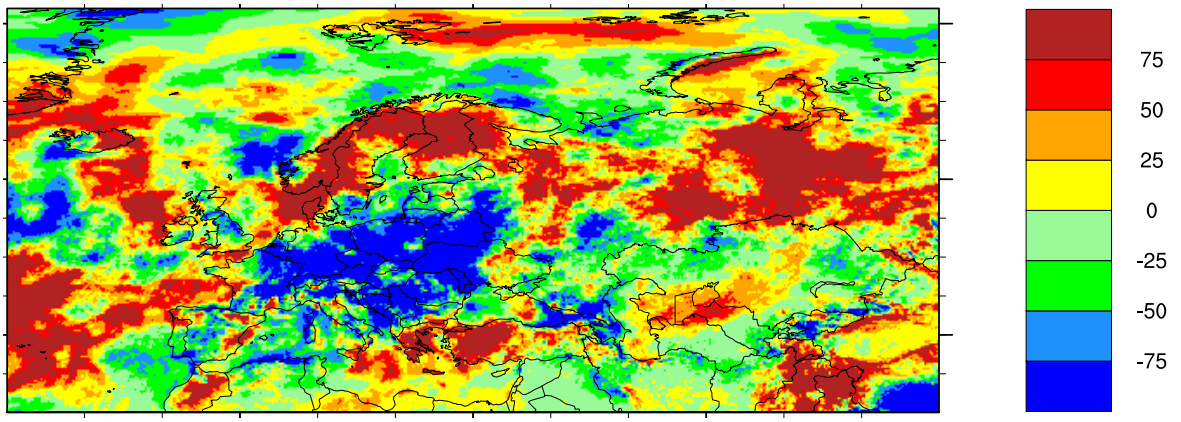

(a) Δprecipitation (AprSep 2015-climavg)

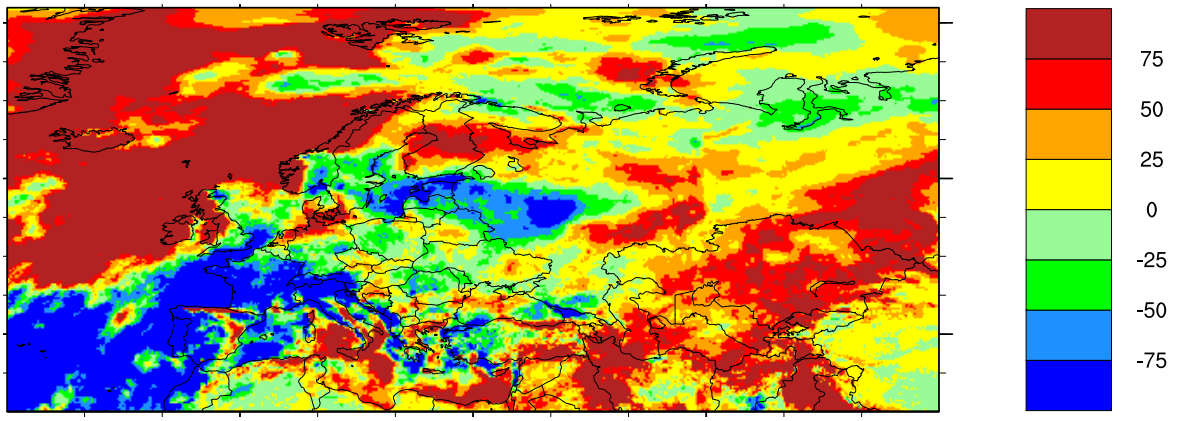

(b) Δprecipitation (OctMar 2015-climavg)

Figure 2.3: Meteorological conditions in 2015 compared to the 2005-2014 average (climavg) for: (a) Summer (April-September) precipitation [mm], (b) Winter (January-March and October-December) precipitation [mm]

In April some parts of Austria experienced its second driest conditions since 1813, which led to forest fires. In May Spain was driest on record whereas i Finland, Norway and Denmark had their second wettest April on record.

April, May and June was very dry in Germany and led to severely low levels soil moisture and water levels in rivers. Western Slovakia recorded its lowest rainfall since 1872 between May and August. Turkey was very wet in June, but exceptionally dry in July. Hungary reported its sixth driest June since 1901. Belarus experienced its driest August on record since 1945.

Northern Portugal and many parts of France received record high rainfall in September. At the same time northwestern United Kingdom was very dry. High pressure over northern Europe in October caused dry conditions in the United Kingdom, southern Norway and Sweden, but very wet conditions in Turkey . Ireland reported its sixth wettest November since records began in 1866, and in parts of Sweden maximum rainfall records were broken. November was much drier than normal in Turkey.

December was much drier than normal in Turkey and Germany, second driest in Austria,

and third driest in Hungary. The flooding experienced over northern England in December was caused by a high frequency of low-pressure systems crossing the North Atlantic and northern Europe. Some parts of Ireland reported more than double normal December rainfall.

2.1.3 2015 compared to the 2005-2014 average

Calculations of meteorological data have been made with the ECMWF-IFS model with virtually the same model setup for the years 2005-2014, including also 2015. Here the 2005-2014 model calculated climatology is compared to 2015. Compared to the 2005-2014 average, higher temperatures are clearly seen in 2015 in Figure 2.2 (a) over northern, central and southern Europe. The 2015 summer months (April-September) compared to the 2005-2014 average in Figure 2.2 (a) show higher temperatures in southern and central Europe and lower temperatures in northeast Europe and the European part of Russia. Figure 2.2 (b) highlights that the 2015 winter months (January-March and October-December) differs from the 2005-2014 average were strongly influenced by the exceptionally warm weather over Europe in December, but also the relatively warm start of the year and the warm March had large effects on the annual temperature. In Figure 2.3 (b) shows that northwestern Europe received larger amounts of precipitation, whereas central and southern Europe received far less precipitation than the 2005-2014 average. Compared to the 2005-2014 average, the 2015 summer months (April-September) (Figure 2.3 (a)) northern Europe was wet, while southern and central Europe was very dry. Figure 2.3 (b) show that for the 2015 winter months (January-March and October-December) precipitation was higher in northwestern Europe and lower in southwestern Europe and northern Baltic than for the 2005-2014 average.

2.2 Measurement network 2015

In 2015, a total of 31 Parties reported measurement data of inorganic components, particulate matter and/or ozone to EMEP from altogether 158 sites, which is the relevant components for level 1 sites (UNECE 2009). All the data are available from the EBAS database (`http://ebas.nilu.no/`) and are also reported separately in technical reports by EMEP/CCC (Hjellbrekke 2017, Hjellbrekke and Solberg 2017). Figure 2.4 shows an overview of the spatial distribution of the sites reporting data for inorganic ions in air and precipitation, particulate matter and ozone in 2015.

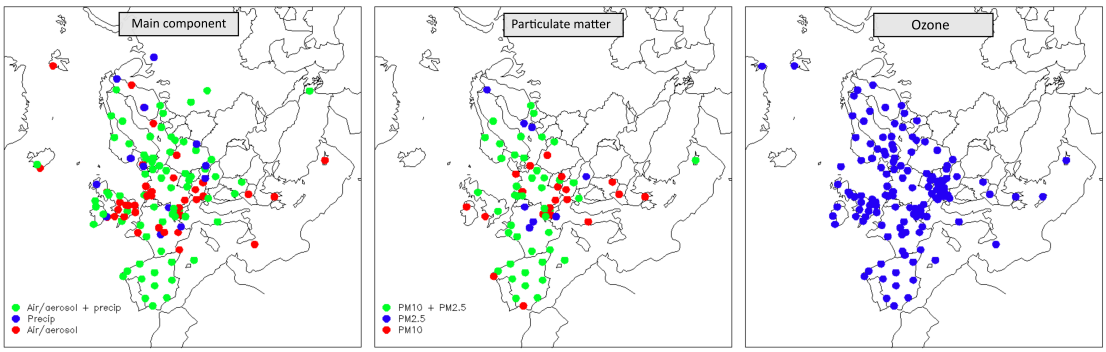

Figure 2.4: EMEP measurement network for main components (left), particulate mass (middle) and ozone (right) in 2015

125 sites reported measurements of inorganic ions in precipitation and/or main components in air; however not all of these sites were co-located as illustrated in Figure 2.4. There were 72 sites with measurements in both air and precipitation. The network of ozone measurements in EMEP included 133 sites.

There were 73 sites measuring either PM_{10} or $PM_{2.5}$ mass. 44 of these sites measured both size fractions, as recommended in the EMEP Monitoring strategy (UNECE 2009). The stations measuring EMEP level 2 variables are shown in Figure 9.2. Compliance with the monitoring obligations, and the development of the programme the last decade is discussed in Chapter 9.1.

2.3 Model setup for 2015 model runs

The EMEP MSC-W model version rv4.15 has been used for the 2015 model runs. Emissions are for the first time reported in $0.1^\circ \times 0.1^\circ$ resolution, and model runs have been performed on the same resolution. The vertical resolution has also been improved, namely the model has used 34 vertical layers, with the thickness of the lowest model layer being reduced from 92 to 50 m. The emission vertical profiles have been kept close to those used until now, with emissions corresponding to SNAP sectors 7 (Road traffic), 8 (Off-road traffic/machinery) and 10 (Agriculture) distributed within the lowest 50 m layer.

In addition, model runs on 50 km $\times$ 50 km resolution have been performed, using a set of emissions with the same national totals, but the base grid in 50 km $\times$ 50 km from last year (see section 3.5).

Meteorology, emissions, boundary conditions and forest fires for 2015 have been used as input (for a description of these input data see Simpson et al. 2012). In addition, the SO_2 emissions from the Holuhraun eruption in 2015 are included (see section 3.6). DMS emissions are created 'on-the-fly', e.g. they are meteorology dependent (see chapter 9 in EMEP Status Report 1/2016). For ship emissions, data from FMI (based on AIS data) for 2015 have been applied (see chapter 10 for a discussion on ship emissions).

2.4 Air pollution in 2015

2.4.1 Ozone

The ozone observed at a surface station is the net result of various physio-chemical processes; surface dry deposition and uptake in vegetation, titration by nearby NO_x emissions, regional photochemical ozone formation and atmospheric transport of baseline ozone levels, each of which may have seasonal and diurnal systematic variations. Episodes with elevated levels of ozone are observed during the summer half year when certain meteorological situations (dry, sunny, cyclonic stable weather) promotes the formation of ozone over the European continent.

Figure 2.5 shows various modelled ozone metrics for 2015 with the corresponding metrics based on the EMEP measurement sites plotted on top of the maps. Only stations located below 1000 m asl were used in this comparison to avoid uncertainties related to the extraction of model data in regions with complex topography. The maps show a) the mean of the daily max concentration for the period April-September, b) SOMO35, c) 6-months AOT40 for forests (April-September) using the hours between 08 and 20 and d) POD_1. POD_1 could not be calculated from the ozone monitoring data directly and are thus not given in plot d).

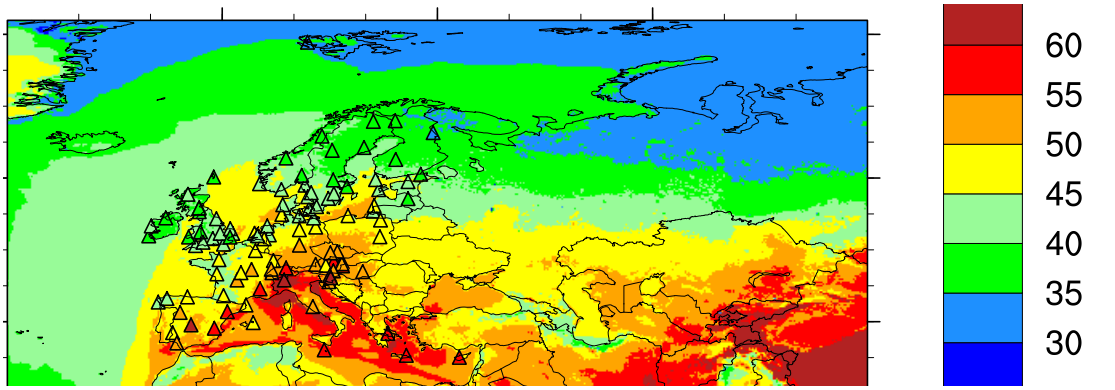

(a) Max. O_3

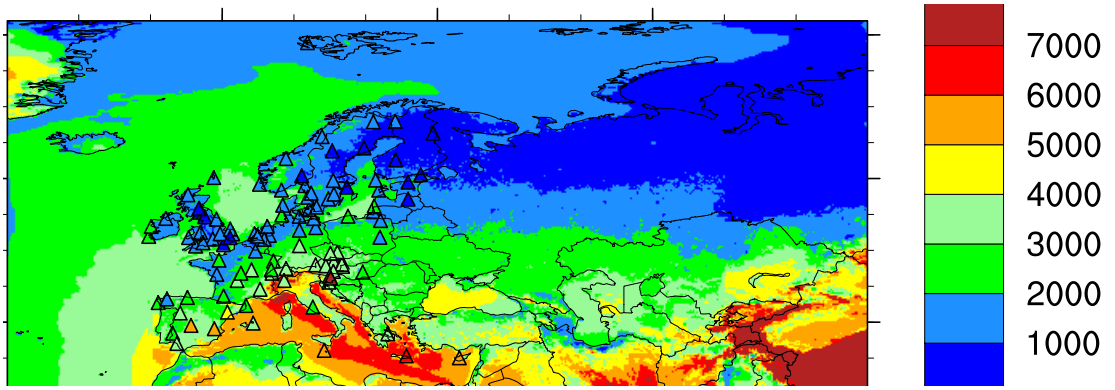

(b) SOMO35

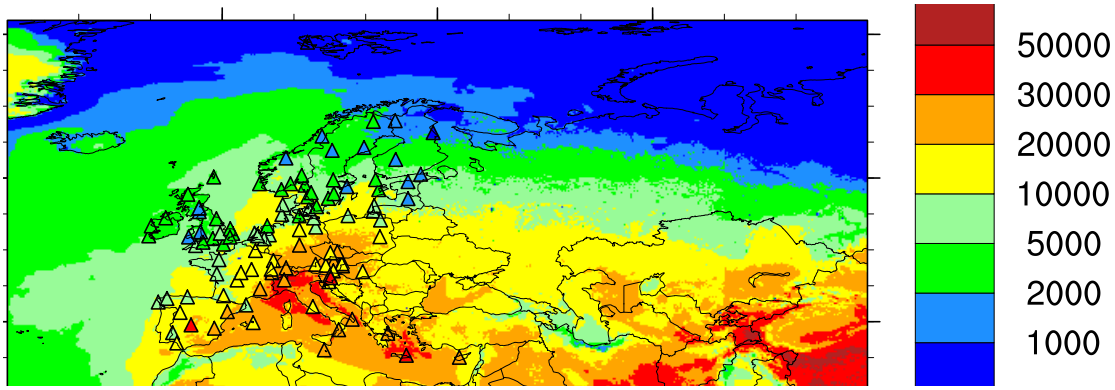

(c) AOT40

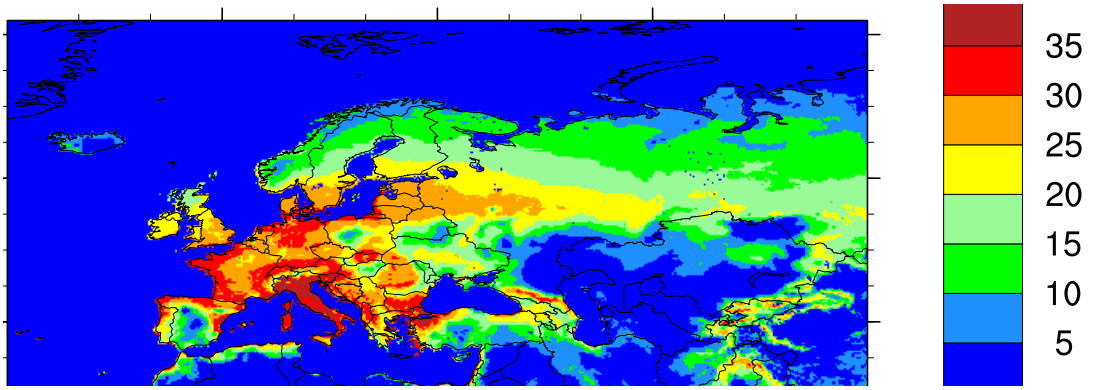

(d) POD1

Figure 2.5: Model results and observations (triangles) for mean of daily maximum ozone concentrations (ppb, April-September), SOMO35 [ppd.days], AOT40 [ppb.hours] for forests and POD_1 for forests [mmol m^{-2}] in 2015. Only data from measurement sites below 1000 meter above sea level are shown.

The mean daily max O_3, SOMO35 and AOT40 all show a distinct gradient with levels increasing from north to south, a well established feature for ozone in general reflecting the dependency of ozone on the photochemical conditions. Ozone formation is promoted by solar radiation and high temperatures. The highest levels of these ozone metrics are predicted over the Mediterranean Ocean and in the southeast corner of the model grid. The measurement network are limited to the continental western part of the model domain with no valid data in Belarus, Ukraine, Romania, Turkey or the area further east.

For the region covered by the monitoring sites, the pattern with increased levels to the south with maximum levels near the Mediterranean is seen in the measurement data as well as the model. The geographical pattern in the measured values are fairly well reflected by the model results for all these three metrics. Higher observed daily max levels than modelled are seen at a few sites (Spain, France, Austria) whereas for AOT40 an underestimation by the model is seen for sites in some areas (UK and the Nordic countries). The modelled POD_1 pattern differs from the other metrics reflecting the influence of additional parameters such as plant physiology, soil moisture etc and is a metric more indicative of the direct impact of ozone on vegetation than e.g. AOT40. The POD_1 field could however not be validated by the EMEP ozone measurement data alone.

It should be noted that the O_3 metrics such as AOT40 and SOMO35 are very sensitive to the calculation of vertical O_3 gradients between the middle of the surface layer and the 3m height used for comparison with measurements (Tuovinen et al. 2007). Indeed, the formulation we use (Simpson et al. 2012) is probably better suited to the 20-layer model's 90m height (since we equate the centre of this, ca. 45m, with a 'blending-height') than to the 34-layer model's 50m height, and probably needs reformulating for the new resolution. For this reason, it seems premature to compare the model AOT40 values with critical levels; this work will continue once the characteristics of the new resolution have been studied and accounted for in more detail.

The dominant weather conditions in 2015 with a hot and dry summer in central/southern Europe and cool and wet conditions in North Europe is clearly reflected in the summer ozone levels. Numerous heat waves accompanied by episodes of elevated ozone occurred at the European continent this year, most pronounced in the period June-August. Thus, the situation in 2015 was the direct opposite of the year before, 2014, when central Europe experienced a cool and wet summer with very few ozone episodes whereas the Nordic countries had hot and dry conditions. In 2015 the summer ozone levels in the UK and North Europe was generally low with few peaks and episodes.

A more detailed comparison between model and measurements for ozone for the year 2015 can be found in Gauss et al. (2017a).

Ozone episodes in 2015

As mentioned, there were several marked ozone episodes in 2015, most pronounced in July and August associated with heat waves over the European continent. Below we show maps for two of these: 30 June - 6 July and 6-14 August.

30 June - 6 July

On average July was a very hot month in various regions of Europe with monthly mean daily max temperatures 2-4 degrees above the normal. Peak temperatures of 35 to almost 40°

were experienced over large areas, like in Paris, Madrid, Bucharest etc. The weather situation during this first ozone episode was characterised by a high pressure area over the Baltic region setting up hot winds from the south over continental Europe. The ozone map for 4 July shown in Figure 2.6 show high ozone levels over a large region from southeastern France to Poland and the model captured the situation this day fairly well although with some tendency for an underestimation.

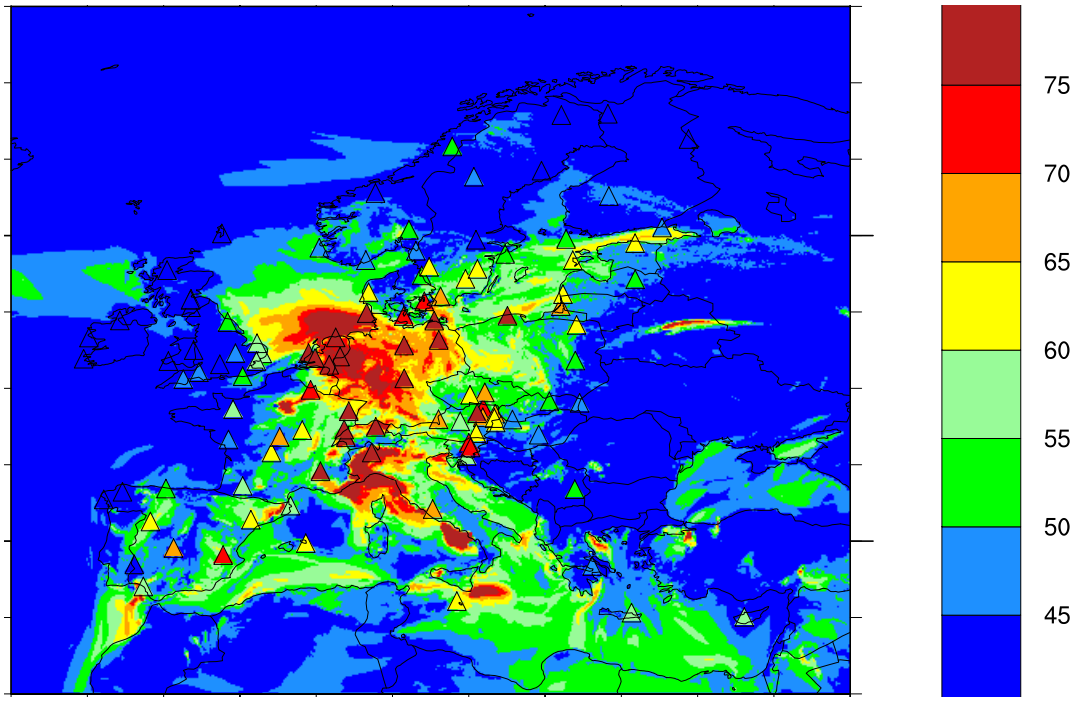

Figure 2.6: Modelled and measured daily max ozone 4 July 2015

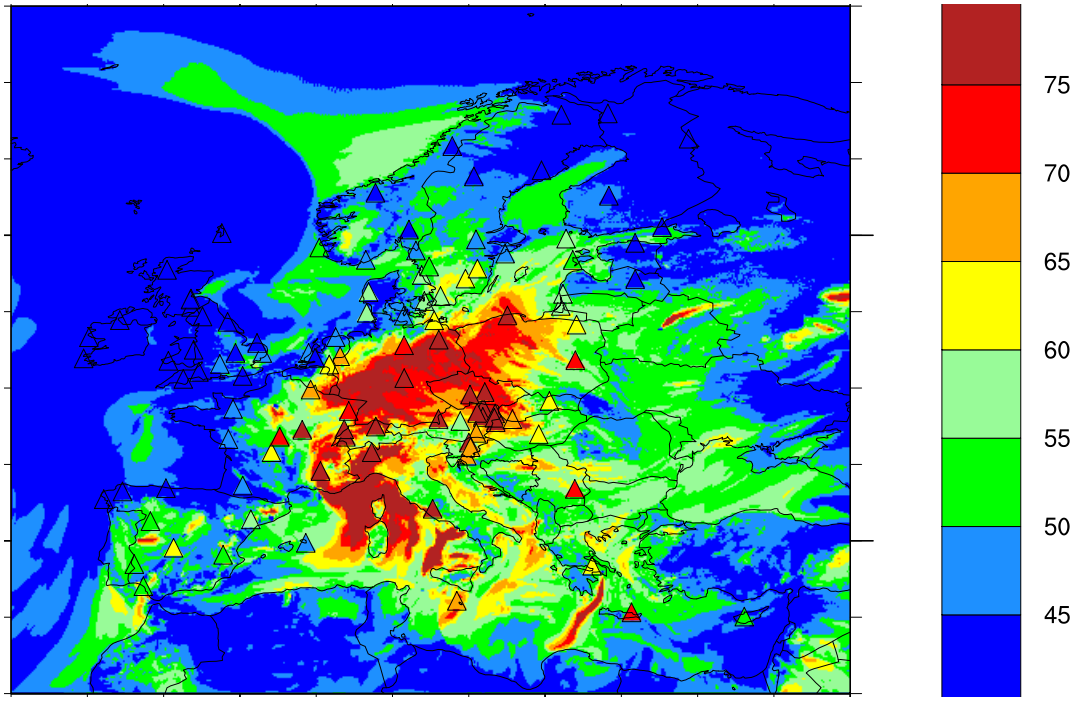

Figure 2.7: Modelled and measured daily max ozone 7 August 2015

6-14 August

This period was also characterised by a high pressure over the continent with warm air masses advected gently from the south. An anomaly in the mean daily max temperature of August exceeding 5° was seen in parts of Europe with several hot spells during the month. Peak temperatures above 35° were experienced in many regions this month. The ozone map for 7 August shown in Figure 2.7 show a region from the Mediterranean to Poland with very high ozone levels both modelled and observed.

2.4.2 Particulate matter

Maps of annual mean concentrations of PM_{10} and $PM_{2.5}$ in 2015, calculated by the EMEP MSC-W model are presented in Figure 2.8. The figures also show annual mean PM_{10} and $PM_{2.5}$ concentrations observed at EMEP monitoring network, represented by colour triangles overlaying the modelled concentration fields.

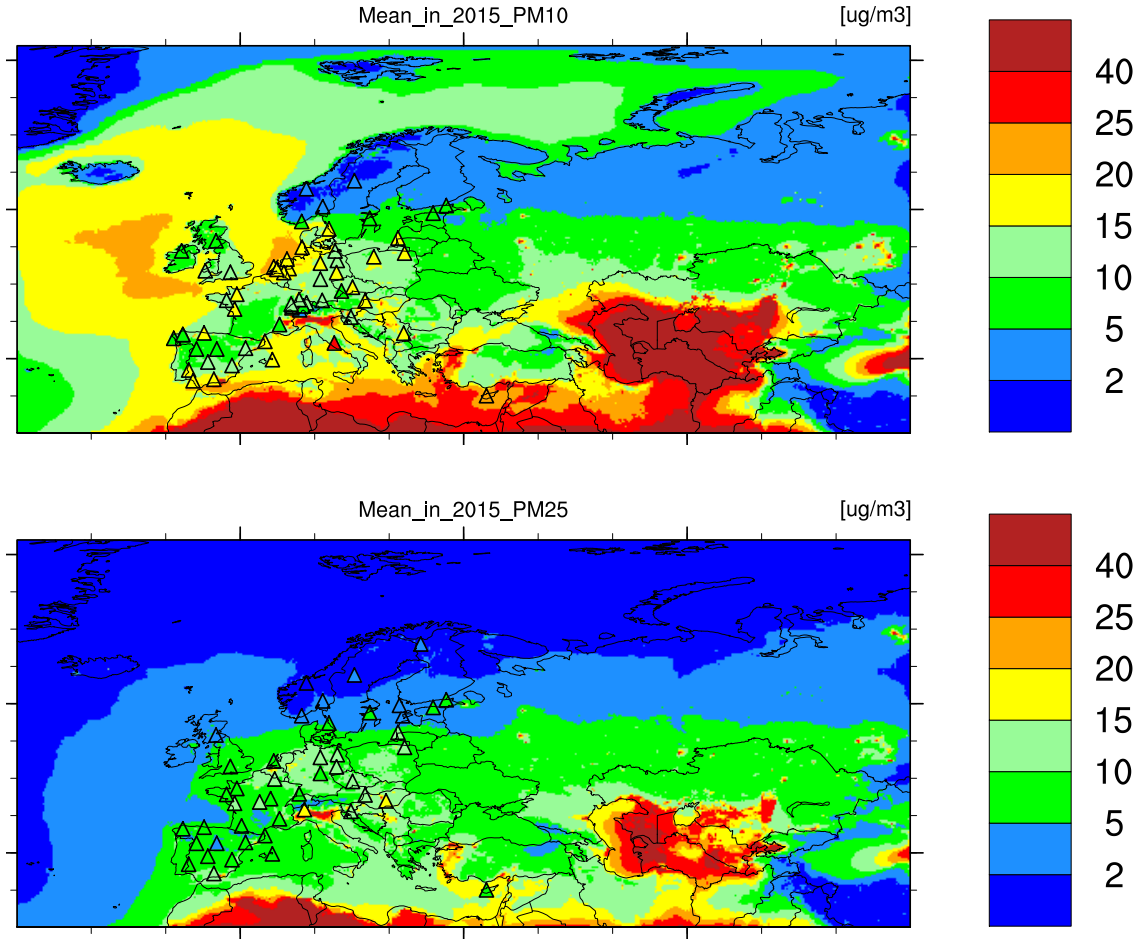

Figure 2.8: Annual mean concentrations of PM_{10} and $PM_{2.5}$ in 2015: calculated with the EMEP MSC-W model (colour contours) and observed EMEP monitoring network (colour triangles). *Note: Observations include hourly, daily and weekly data.*

There is a distinct north-south gradient in the annual mean levels of PM_{10} and $PM_{2.5}$ calculated with the model, which is also seen in the observational data. The concentration levels

are below 2-5 μg m^{-3} in Northern Europe, increasing to 10-15 μg m^{-3} in the mid-latitude and farther south. Also seen are areas experiencing elevated PM_{10} and $PM_{2.5}$ levels (15-20 μg m^{-3}), such as the Benelux countries and parts of Hungary, Serbia, Germany and Poland; and a hot-spot with calculated PM_{10} and $PM_{2.5}$ exceeding 30 μg m^{-3} is seen in the Po Valley. In the regions east from the Caspian Sea (parts of Kazakhstan, Uzbekistan, Turkmenistan) and in southern Mediterranean, the model calculates annual mean PM levels far in excess of 50 μg m^{-3} . These high PM concentrations are due to windblown dust from the arid soils, though the accurateness of the calculated values cannot be verified due to the lack of observations in these regions.

There is quite a good agreement between the modelled and observed distribution of mean PM_{10} and $PM_{2.5}$, with annual mean correlation coefficients of 0.74 and 0.84 respectively, as documented in Gauss et al. 2017b). Overall, the model underestimates the observed annual mean PM_{10} levels by 10%, while the calculated $PM_{2.5}$ is on average practically unbiased (-1% bias). Comprehensive model evaluation is provided in Gauss et al. 2017b).

Exceedances of EU limit values and WHO Air Quality Guidelines in 2015

This section compares the exceedances by PM_{10} and $PM_{2.5}$ concentrations of EU critical limits and WHO recommended Air Quality Guidelines WHO (2005) calculated with the EMEP MSC-W model and measured at EMEP sites. The EU limit values for PM_{10} (Council Directive 1999/30/EC) are 40 μg m^{-3} for the annual mean and 50 μg m^{-3} for the daily mean concentrations, with the daily limit not to be exceeded more than 35 times per calendar year (EU 2008). For $PM_{2.5}$, the annual mean limit value of 25 μg m^{-3} entered into force 01.01.2015.

The Air Quality Guidelines (AQG) recommended by WHO (WHO 2005) are:

- for PM_{10}: 20 μg m^{-3} annual mean, 50 μg m^{-3} 24-hourly (99th perc. or 3 days per year)
- for $PM_{2.5}$: 10 μg m^{-3} annual mean, 25 μg m^{-3} 24-hourly (99th perc. or 3 days per year)

The EU limit values for protection of human health from particulate matter pollution and the WHO AQG for PM should apply to concentrations for so-called zones, or agglomerations, in rural and urban areas, which are representative for exposure of the general population. Prior to this report, operational EMEP MSC-W model calculations were performed on 50×50km^2 grid and provided regional background PM concentrations. PM_{10} and $PM_{2.5}$ concentrations calculated on $0.1^\circ\times 0.1^\circ$ grid are expected to offer a better representation of PM levels occurring in rural and to some extend in urban areas.

Model results and EMEP observational data show that the annual mean PM_{10} concentrations were below the EU limit value of 40 μg m^{-3} for all of Europe in 2015 (Figure 2.8 (a)). The observational data reveal that the WHO recommended AQG of 20 μg m^{-3} was exceeded by annual mean PM_{10} at two sites, in Italy (IT0001) and Cyprus (CY0002) marked as red and orange triangles respectively in Figure 2.8 (a). The model calculates annual mean PM_{10} above 20 μg m^{-3} in the Po Valley, the western parts of Turkey and in Caucasus. There are not any PM_{10} EMEP observations in these regions.

Further, the observations and model calculations show that in 2015, $PM_{2.5}$ pollution did not exceed the EU limit value of 25μg m^{-3} for annual mean level (except in the Po Valley according to the model). However, the WHO AQG value of 10 μg m^{-3} was exceeded by observed annual mean $PM_{2.5}$ at fourteen sites, with the highest values in the Po Valley (IT0004), in Hungary (HU0002), and also at some French, German, Austrian, Polish and Czech sites. This pattern is quite well reproduced by the model.

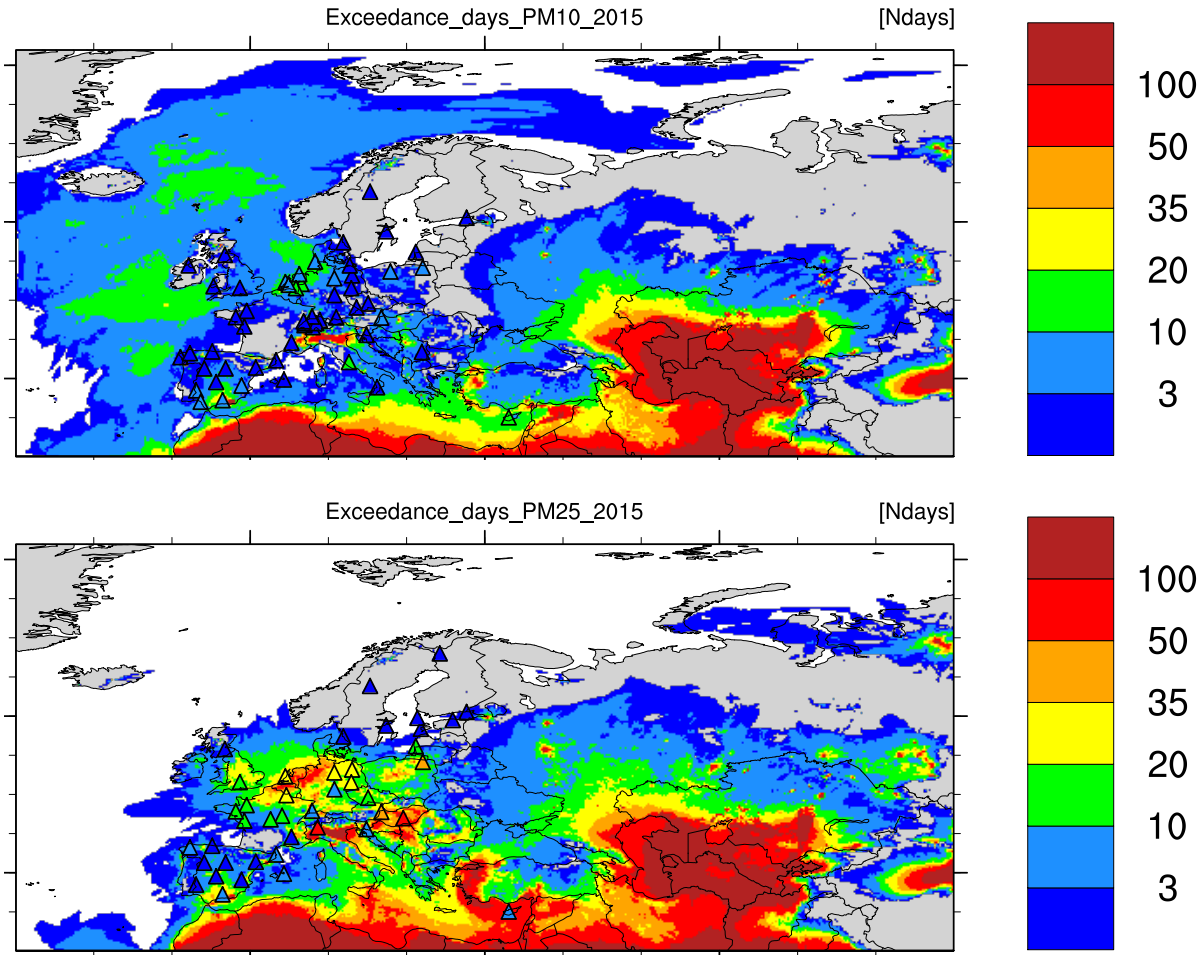

Figure 2.9: Calculated (with 0.1 °resolution) and observed (triangles) number of days with exceedances in 2015: PM_{10} exceeding 50 μg m^{-3} (upper) and $PM_{2.5}$ exceeding 25 μg m^{-3} (lower). *Note: EU Directive requires no more than 35 days with exceedances for PM_{10}, whereas WHO recommends no more than 3 days with exceedances PM_{10} and $PM_{2.5}$ per a calendar year*

The maps in Figure 2.9 show the number of days with exceedances of 50 μg m^{-3} for PM_{10} and 25 μg m^{-3} for $PM_{2.5}$ in 2015: model calculated as colour contours and observed as triangles.

The sites with the highest number of days (19 and, 16 respectively) with observed exceedences of PM_{10} are the ones where the highest annual mean concentration were measured, namely IT0001 and CY0002. Further, two Dutch sites have more than 10 exceedence days for PM_{10} in 2015. For $PM_{2.5}$, the highest number of exceedence days are observed at IT0004 and HU0002, with 79 and 63 days receptively. One site in Austria and one in Poland have around 40 exceedence days of $PM_{2.5}$ in 2015.

In summary, daily PM_{10} exceedances were observed at 34 (out of totally 55) sites. Although no violations of the PM_{10} EU limit value (more than 35 exceedance days) were observed, WHO air quality guidelines were disrespected at 22 sites. For daily $PM_{2.5}$, exceedances were observed at 35 (out of totally 42) sites; whereas at 27 sites the number of exceedance days was more that 3 (as recommended by WHO air quality guidelines).

The model calculated exceedance days in 2015 are in a quite good agreement with the observations (somewhat better for PM_{10} than for $PM_{2.5}$), though it tends to somewhat over-

estimate the frequency of exceedances in Mediterranean regions, while underestimating in Northern Europe and the Baltic countries. At the sites severely affected by Saharan dust (CY0002 and ES0007), $PM_{2.5}$ exceedances are over-predicted by the model, though calculated PM_{10} exceedances are in much better agreement with observations. The model show some overestimation of the number of exceedance days at a few other Spanish sites and at the Dutch site (especially for $PM_{2.5}$). For Italy, compared to the observations the model calculates fewer PM_{10} exceedance days at Montelibretti (IT0001), which is effected by Rome's emissions, but more days with exceedances for $PM_{2.5}$ at Ispra (IT0004).

PM pollution episodes in 2015

In 2015, the most notable large-scale PM pollution episodes occurred in February, March and also in November.

Winter episodes of particulate pollution in Central, Western and Northern Europe were already discussed in a number of earlier EMEP Status Reports (e.g. 4/2013, 1/2014, and 1/2016). The meteorological situations favouring them are typically characterized by low temperatures and stagnant air conditions, and in addition the enhanced use of wood burning for residential heating in the cold weather leads to considerable increase of local PM emissions. In the CAMS Interim Annual Assessment Report for 2015 (Tarrason et al. 2016), three PM_{10} episodes are identified: 12-20 February; 17-20 March and 29 October to 7 November.

These episodes are confirmed both by the EMEP model and observations, though the March episode is observed during a longer period than indicated by the calculations. In this chapter, details on PM chemistry are included to better describe the possible origins of the air pollution. Due to the observational data availability we look at $PM_{2.5}$ only, since few sites have measurements of chemical composition of the coarse fraction.

In Figures 2.10 and 2.11, the time series of observed and model chemical composition of $PM_{2.5}$ are shown for sites in Germany (4 sites), France (3 sites), Slovenia (SI0008) and the Po Valley (IT0004).

In February 2015, an episode of elevated PM pollution occurred over central and east/south-eastern parts of Europe was observed at several sites. The highest $PM_{2.5}$ concentrations are registered at DE0002, where observed levels reached 72-76 μg m^{-3} on 15 and 16 February, and at IT0004, where 73 μg m^{-3} $PM_{2.5}$ was measured 12 and 13 February. The model show lower concentrations at the German and French sites, but matches the peak concentrations at IT0004 well.

The model calculations suggest that the episode was caused by local emissions, most likely from residential heating during the relatively cold and dry weather conditions that inhibited dispersion. The enhanced concentrations of organic aerosol measured in the period of 12-20 February strongly suggest that the emissions from wood burning played an important role in this PM episode. Such elevated levels of organic aerosol are not well captured by the model. As reported before, the main reason for that is related to problems with the current emission inventories for primary organic aerosol. As concluded in Denier van der Gon et al. (2015), the current emission inventories have major issues, especially with regard to the inclusion or exclusion of condensible organics (see also Simpson and Denier van der Gon 2015). The enhanced NO_3^- levels, seen in Figures 2.10 and 2.11 are probably due to local traffic emissions contributing to the PM pollution.

In March 2015, several PM pollution episodes occurred over Western, Central and South-Eastern Europe. While mainly central and east/south-eastern parts of Europe experienced the

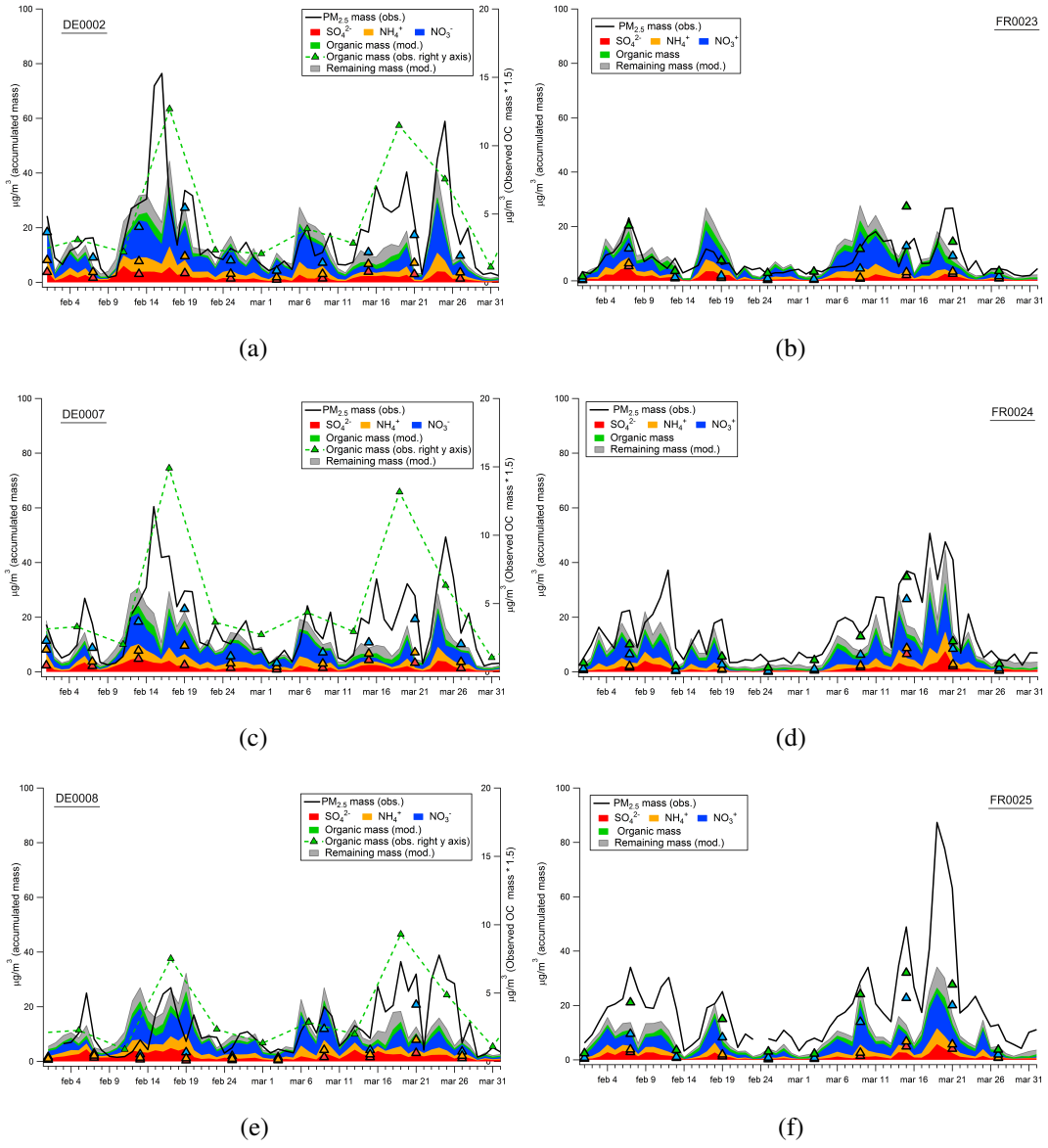

Figure 2.10: Chemical composition of PM_{25} during the pollution episode in February-March, observed and modelled at German and French sites. Note that organic mass at the German sites are measure at a different day than the SIA components

February episode, Western Europe and especially France were also affected by the pollution events in March. Figures 2.10 and 2.11 show that the pollution episodes started around 6 March, peaking on 19 March in France with the highest level of 83 μg m^{-3} observed at FR0025. On 16 March, $PM_{2.5}$ reached 36 μg m^{-3} at SI0008; then on 19 March, the highest $PM_{2.5}$ concentration of 56 μg m^{-3} was observed at IT0004. In Germany, the episode peaked around 25 March, with the highest $PM_{2.5}$ levels of almost 50 μg m^{-3} observed at DE0007.

As discussed in Petit et al. (2017), in France high levels of PM in March coincided with a period with very little precipitation, which inhibited wet scavenging of pollutants from the air. The PM episode is clearly seen at French sites FR0024 (north-west) and FR0025 (mid-east), but less pronounced at FR0023 (south-east) (Figure 2.10). Increased levels of ammonium nitrate in $PM_{2.5}$ were observed and also calculated by the model at those French sites during

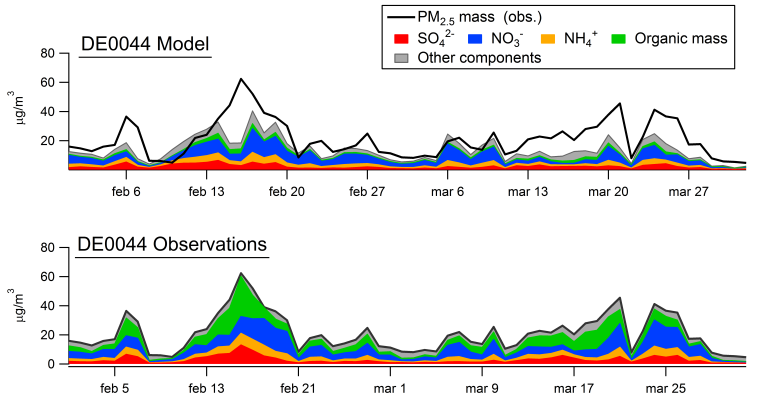

(a)

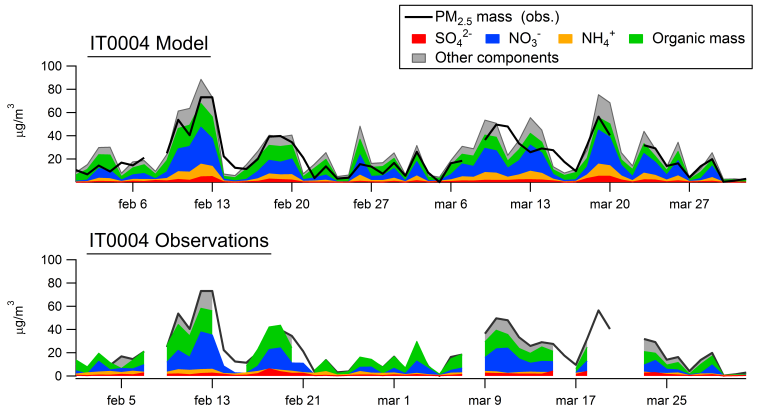

(b)

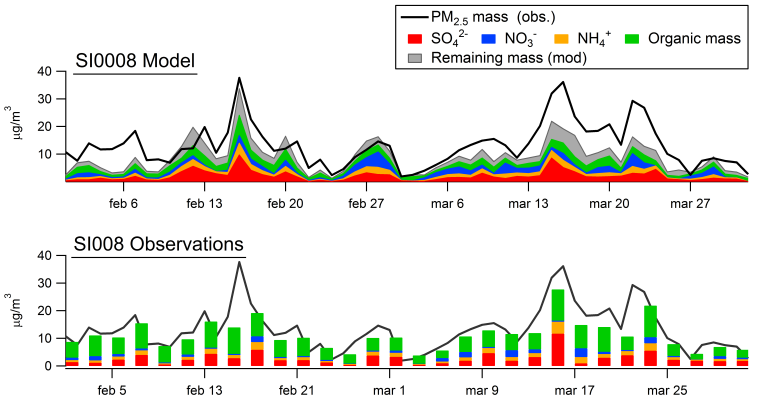

(c)

Figure 2.11: Chemical composition of PM_{25} during the pollution episode in February-March, observed and modelled at DE0044, IT0004 and SI0008

the PM episode. In addition, the model results show enhanced transboundary transport of PM from the Benelux countries to France, thus suggesting that NH_3 emissions from application of agricultural fertilisers, both domestic and abroad, and the NO_x from local traffic were the

main sources of the ammonium nitrate (similar episode took place in France in 2014 and was discussed in EMEP Status Report 1/2016 (2016)).

The episodes in Germany also appear to be caused by enhanced ammonium nitrate formation from agricultural NH_3 (probably both domestic and transboundary) and NO_x emissions from traffic and other local sources. The observed organic mass is also high during this period, i.e. 10-15 μg m^{-3}. It is however difficult to quantify the relative contribution of organic mass compared to SIA since these measurements were taken on different days. The model reproduces $PM_{2.5}$ levels and its composition in the beginning of the period (5-10 March) quite well, and it also captures the observed PM evolution over the period of 22-26 March, while in the period of 16-20 March the PM levels are under-predicted compared to the observations.

The episodes in the Po Valley, as indicated by the model and observations at IT0004, are also accompanied by increased ammonium nitrate contributions. Organic mass is also significant, though due to the lack of observations in the last part of the period, an accurate quantification of its relative importance is difficult.

The Slovenian site SI0008 differs from the other sites by the absence of enhanced ammonium nitrate concentrations, whereas the elevated $PM_{2.5}$ appears to be due to increased sulfate and organic mass concentrations. The ECMWF calculated surface temperatures show that it was relatively cool in Slovenia in March, which suggests that the residential heating could have been one of the major causes for the PM episode (this is further supported by the increased levels of organic aerosol). The model reproduces the observed $PM_{2.5}$ episode and the role of sulfate, but underestimates the organic and total $PM_{2.5}$ mass.

As we can see from ECMWF meteorology, March 2015 was rather dry. This appears to create very favourable conditions for the occurrence of PM episodes over large parts of Europe.

In the period October–November (not shown), high concentrations are mainly seen in central Europe, i.e. in Germany, the Netherlands and Poland. In Poland, the highest concentration of $PM_{2.5}$ in 2015 was observed 17 October, when it reached 72 μg m^{-3}. According to the CAMS report (Tarrason et al. 2016), the highest concentration in the considered period from 29 October to 7 November was seen on 31 October at DE0007, with daily mean $PM_{2.5}$ of 54 μg m^{-3}.

2.4.3 Deposition of sulphur and nitrogen

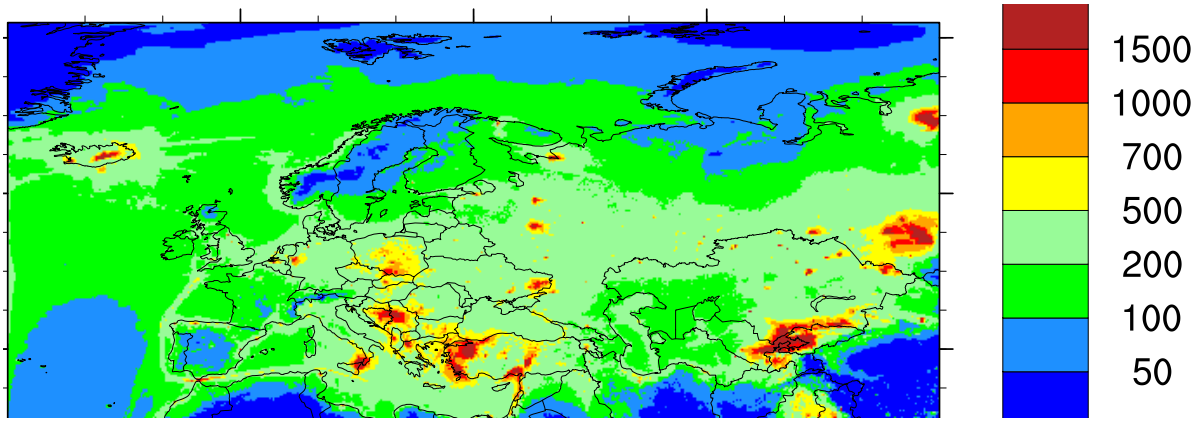

(a) oxidized S

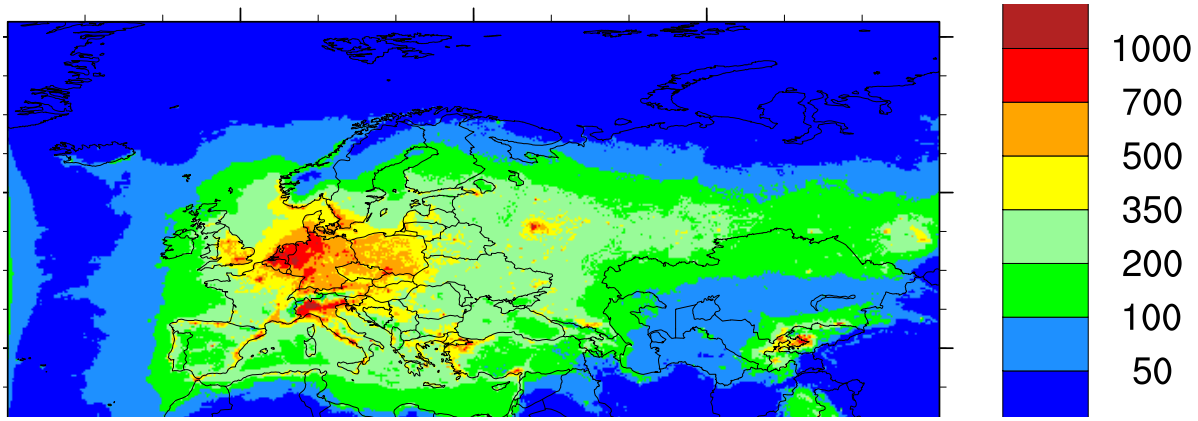

(b) oxidized N

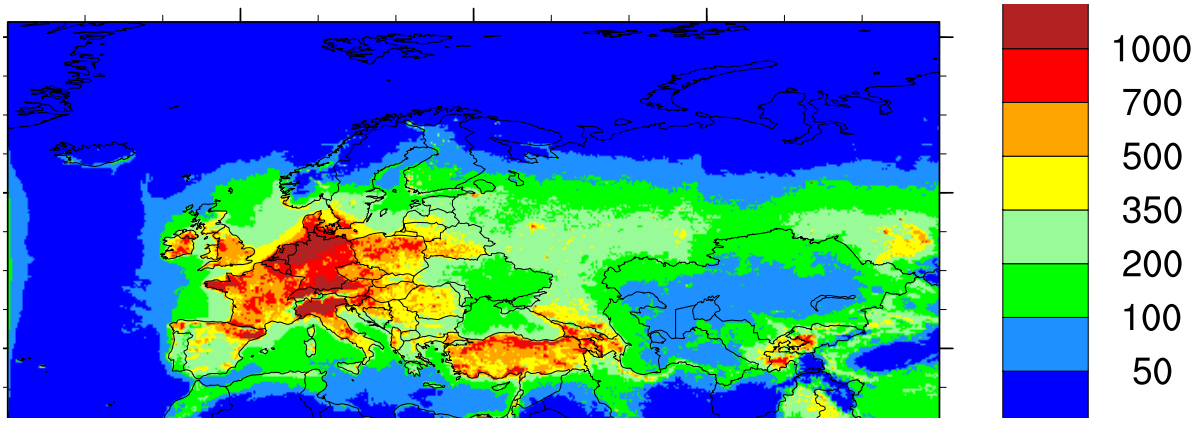

(c) Reduced N

Figure 2.12: Deposition of sulphur and nitrogen [mgS(N)m^{-2}] in 2015.

Modelled total depositions of sulphur and oxidized and reduced nitrogen are presented in Figure 2.12. For sulphur, many hot spot areas are found in the eastern part of the domain. In addition, volcanic emissions of SO_2 leads to high depositions over Iceland and areas around Sicily. Oxidized nitrogen depositions are highest in northern Germany, the Netherlands, Denmark and northern Italy. These countries also have high depositions of reduced nitrogen, as

does parts of the United Kingdom, France, Belgium in western Europe, and Turkey, Georgia and Armenia, Kyrgyzstan and Tajikistan in the east.

In Figure 2.13 wet depositions of nitrogen and sulphur compounds are compared to measurements at EMEP sites for 2015. Overall, the bias between model and measurements are around -2 to -10%, but higher for individual sites. A more detailed comparison between model and measurements for the year 2015 can be found in Gauss et al. (2017b).

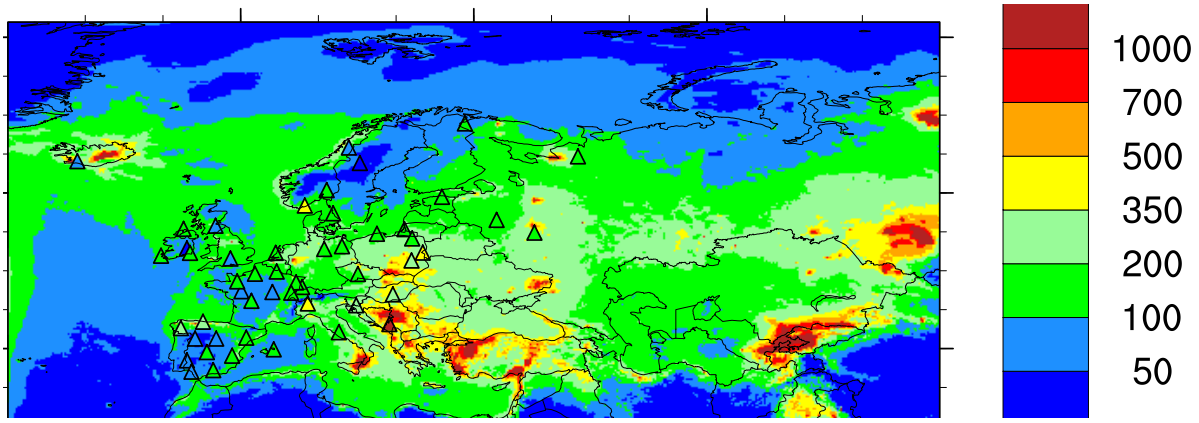

(a) oxidized S

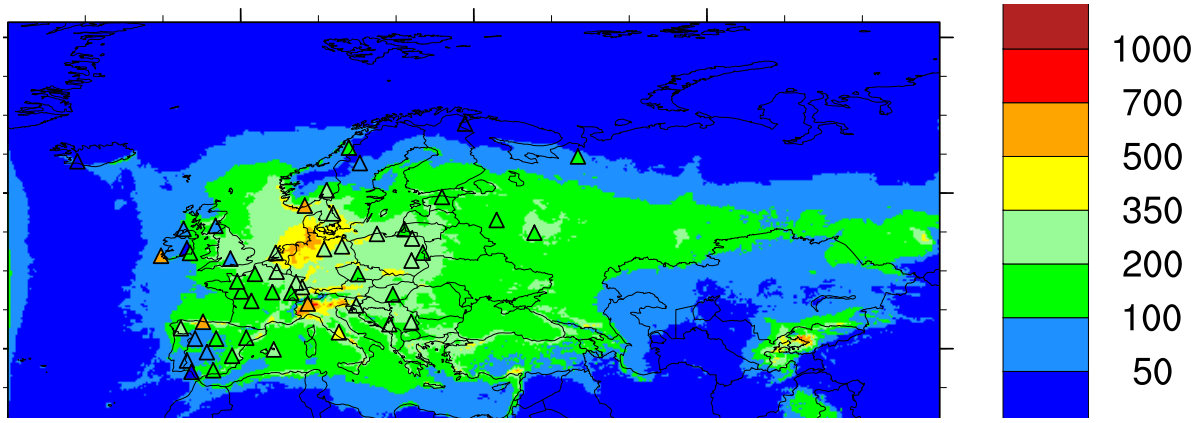

(b) oxidized N

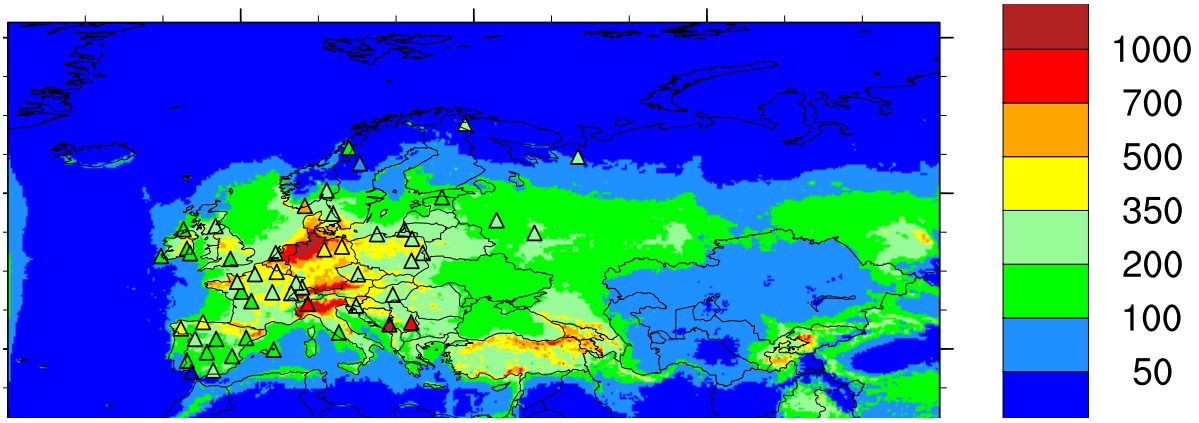

(c) Reduced N

Figure 2.13: Wet deposition of sulphur and nitrogen [mgS(N)m^{-2}] in 2015. EMEP observations on top (triangles).

Region	Acidity exceedance: Area (AAE)		Eutrophication exceedance: Area (AAE)	
	50×50km^2	$0.1\times0.1^\circ$	50×50km^2	$0.1\times0.1^\circ$
EU28	5.90 % (22.6)	5.94 % (23.7)	73.6 % (287.6)	72.3 % (272.1)
Europe	5.28 % (16.6)	5.26 % (17.3)	62.5 % (209.2)	61.2 % (197.5)

Table 2.1: Area exceeded (in % of total ecosystem area) and, between parentheses, average exceedance (AAE; in eq/ha/yr) for acidity and eutrophication CLs under the 2015 deposition given on the 50×50km^2 and the $0.1\times0.1^\circ$grid, resp., for the European Union and the whole of Europe (west of 45°E).

Exceedances of critical loads of acidification and eutrophication

The exceedances of European critical loads (CLs) are computed for two different sets of 2015 total N and S depositions. In the first set the depositions are given on the traditional 50×50km^2 EMEP grid and in the second set the depositions are modelled on the finer $0.1\times0.1^\circ$ longitude-latitude grid (approx. 11×5.5 km^2 at 60°N).

Exceedances are calculated for the critical load data described in Slootweg et al. (2015), which are also used by TFIAM in integrated assessment modelling. The exceedance in a grid cell is the so-called 'average accumulated exceedance' (AAE), computed as the area-weighted mean of the exceedances of the critical loads of all ecosystems in that grid cell.

The critical loads (for about 2.2 million ecosystems in Europe covering an area of about 3.3 million km^2) are mapped on a $0.5\times0.25^\circ$ longitude-latitude grid. In Figure 2.14, the exceedances are displayed for acidity critical loads, caused by both N and S deposition, and the exceedances of eutrophication critical loads, caused by excess N deposition.

In terms of acidification, hot-spots of exceedances can be found in the Netherlands and its border areas to Germany and Belgium as well as in southern Germany, whereas most of Europe is not exceeded. The high exceedance areas, especially those in the Netherlands, are slightly more extended when calculated with the finer resolution compared to calculations with the traditional 50×50km^2 resolution, and small hot-spots are also more distinguished (e.g. around Moscow). Also overall exceedance is slightly higher with the high-resolution depositions (see Table 2.1). In Europe as a whole, acidity exceedances occur in about 5.3% of the ecosystem area, and the European average AAE is about 17 eq ha^{-1}yr^{-1}.

In contrast, critical loads for eutrophication are exceeded in virtually all countries (in about 60% of the ecosystem area) and the European average exceedance is around 200 eq ha^{-1}yr^{-1}. The highest exceedances are found in the Po valley in Italy, the Dutch-German-Danish border areas and in north-western Spain. Again, the high exceedance area in and around the Netherlands is slightly more extended with the $0.1\times0.1^\circ$deposition, whereas the exceedances in northern Italy are smaller. The overall pattern, however, is very similar for both deposition sets.

The overall exceedances of eutrophication CLs are slightly smaller under the $0.1\times0.1^\circ$ depositions (see Table 2.1). A reason for this could be that the high-resolution deposition resolves the population centres much better. These areas generally have higher depositions but less (semi-)natural ecosystems. This may be an additional argument for the use of high resolution depositions for exceedance calculations.

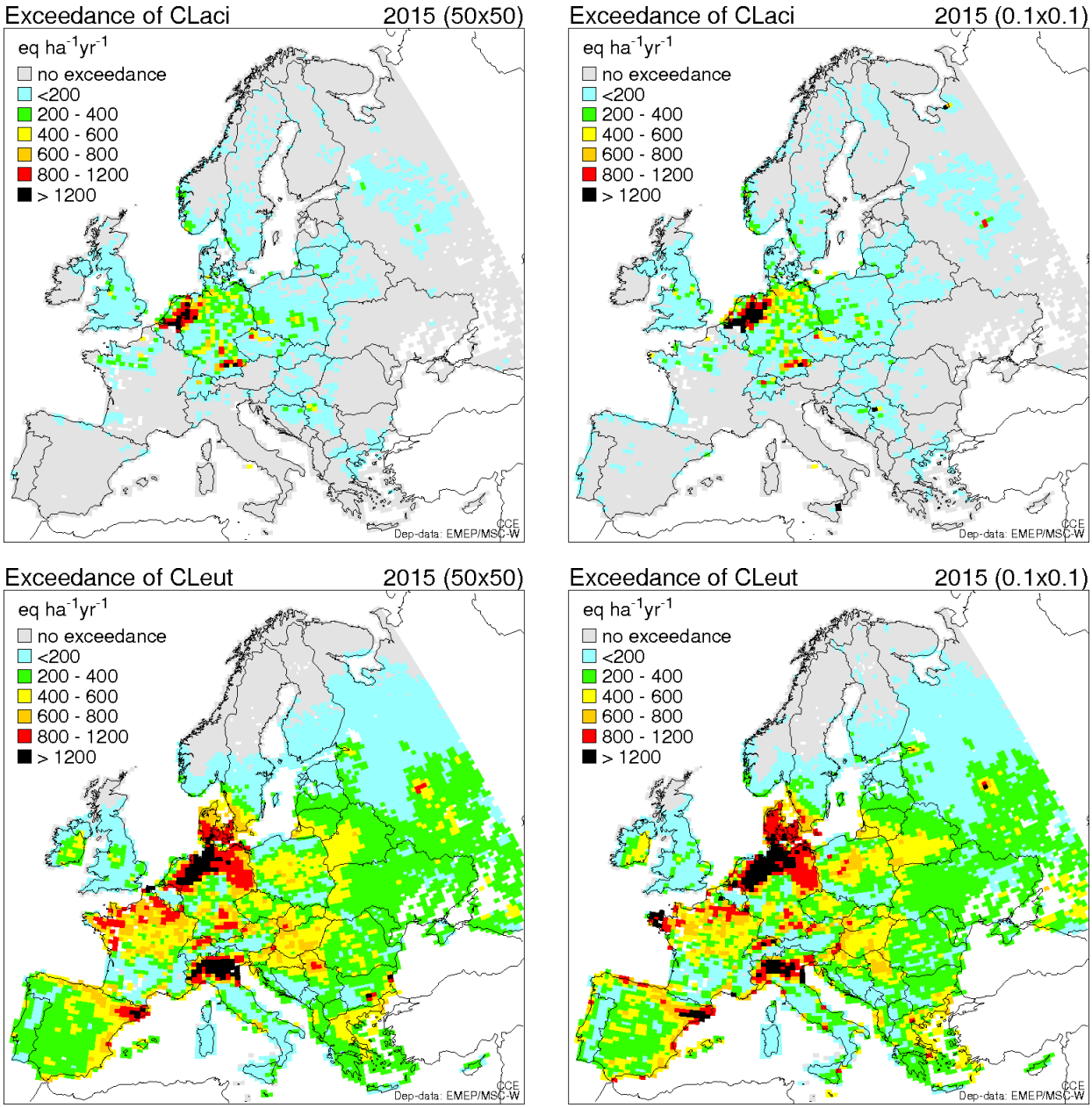

Figure 2.14: Exceedances of critical loads for eutrophication, mapped on a $0.5\times0.25°$longitude-latitude grid, computed with the 2015 EMEP N and S depositions simulated on the 50×50km^2 (left) and on the $0.1\times0.1°$longitude-latitude grid (right).

References

Denier van der Gon, H. A. C., Bergström, R., Fountoukis, C., Johansson, C., Pandis, S. N., Simpson, D., and Visschedijk, A. J. H.: Particulate emissions from residential wood combustion in Europe - revised estimates and an evaluation, Atmos. Chem. Physics, pp. 6503–6519, doi:doi:10.5194/acp-15-6503-2015, URL http://www.atmos-chem-phys.net/15/6503/2015/, 2015.

EMEP Status Report 1/2016: Transboundary particulate matter, photo-oxidants, acidifying and eutrophying components, EMEP MSC-W & CCC & CEIP, Norwegian Meteorological Institute (EMEP/MSC-W), Oslo, Norway, 2016.

EU: Directive 2008/50/EC of the European Parliament and of the Council on ambient air quality and cleaner air for Europe., Official Journal of the European Union L 152, 11 June 2008, pp. 1-44., L 152, 1–44, URL http://faolex.fao.org/docs/pdf/eur80016.pdf, 2008.

Gauss, M., Hjellbrekke, A.-G., Aas, W., and Solberg, S.: Ozone, Supplementary material to EMEP Status Report 1/2017, available online at www.emep.int, The Norwegian Meteorological Institute, Oslo, Norway, 2017a.

Gauss, M., Tsyro, S., Fagerli, H., Hjellbrekke, A.-G., Aas, W., and Solberg, S.: EMEP MSC-W model performance for acidifying and eutrophying components, photo-oxidants and particulate matter in 2015., Supplementary material to EMEP Status Report 1/2017, available online at www.emep.int, The Norwegian Meteorological Institute, Oslo, Norway, 2017b.

Hjellbrekke, A.-G.: Data Report 2015 Acidifying and eutrophying compounds and particulate matter, Tech. Rep. EMEP/CCC Report 1/2017, Norwegian Institute for Air Research, Kjeller, Norway, 2017.

Hjellbrekke, A.-G. and Solberg, S.: Ozone measurements 2016, Tech. Rep. EMEP/CCC Report 2/2017, Norwegian Institute for Air Research, Kjeller, Norway, 2017.

Overland, J., Hanna, E., Hanssen-Bauer, I., Kim, S.-J., Walsh, J., Walsh, J. E., Wang, M., Bhatt, U. S., and Thoman, R. L.: Air Temperature, in Arctic Report Card 2015, NOAA, http://www.arctic.noaa.gov/Report-Card/Report-Card-Archive, 2015.

Petit, J.-E., Amodeo, T., Meleux, F., Bessagnet, B., Menut, L., Grenier, D., Pellan, Y., Ockler, A., Rocq, B., Gros, V., et al.: Characterising an intense PM pollution episode in March 2015 in France from multi-site approach and near real time data: Climatology, variabilities, geographical origins and model evaluation, Atmospheric Environment, 155, 68–84, 2017.

Simpson, D. and Denier van der Gon, H.: Problematic emissions - particles or gases?, in: Transboundary particulate matter, photo-oxidants, acidifying and eutrophying components. EMEP Status Report 1/2015, pp. 87–96, The Norwegian Meteorological Institute, Oslo, Norway, 2015.

Simpson, D., Benedictow, A., Berge, H., Bergström, R., Emberson, L. D., Fagerli, H., Hayman, G. D., Gauss, M., Jonson, J. E., Jenkin, M. E., Nyíri, A., Richter, C., Semeena, V. S., Tsyro, S., Tuovinen, J.-P., Valdebenito, A., and Wind, P.: The EMEP MSC-W chemical transport model – technical description, Atmos. Chem. Physics, 12, 7825–7865, doi:10.5194/acp-12-7825-2012, 2012.

Slootweg, J., Posch, M., , and Hettelingh, J.-P.: Modelling and mapping the impacts of atmospheric deposition of nitrogen and sulphur, in: CCE Status report 2015, RIVM Report 2015-0193, p. 141 pp, Coordination Centre for Effects, RIVM, Bilthoven, The Netherlands, URL http://www.wge-cce.org, 2015.

Tarrason, L., Hamer, P., Guerreiro, C., Meleux, F., and Rouil, L.: Interim Annual Assessment Report for 2015. European air quality in 2015, Tech. Rep. CAMS71_2016SC1_D71.1.1.2_201609, URL http://policy.atmosphere.copernicus.eu/reports/CAMS71_2016SC1_D71.1.1.2_201609_final.pdf/, 2016.

Tuovinen, J.-P., Simpson, D., Ashmore, M., Emberson, L., and Gerosa, G.: Robustness of modelled ozone exposures and doses, Environ. Poll., 146, 578–586, 2007.

UNECE: Progress in activities in 2009 and future work. Measurements and modelling (acidification, eutrophication, photooxidants, heavy metals, particulate matter and persistent organic pollutants). Draft revised monitoring strategy., Tech. Rep. ECE/EB.AIR/GE.1/2009/15, UNECE, URL http://www.unece.org/env/documents/2009/EB/ge1/ece.eb.air.ge.1.2009.15.e.pdf, 2009.

WHO: Air quality guidelines. Global update 2005. Particulate matter, ozone, nitrogen dioxide and sulfur dioxide, URL http://www.who.int/phe/health_topics/outdoorair/outdoorair_aqg/en/, World Health Organisation, European Centre for Environment and Health Bonn Office, ISBN 92 890 2192, 2005.

WMO: WMO statement on the status of the global climate in 2015, WMO-No. 1167, http://library.wmo.int/opac/, ISBN 978-92-63-11167-8, 2016.

CHAPTER 3

Emissions for 2015

Katarina Mareckova, Marion Pinterits, Melanie Tista, Bernhard Ullrich and Robert Wankmüller
with contribution to the volcano and shipping emissions by
Ágnes Nyíri

In addition to meteorological variability, changes in the emissions affect the inter-annual variability and trends of air pollution, deposition and transboundary transport. The main changes in emissions in 2015 with respect to previous years are documented in the following sections.

3.1 Emissions for 2015

The EMEP Reporting guidelines (UNECE 2014) requests all Parties to the LRTAP Convention to report annually emissions of air pollutants (SO_x[1], NO_2[2], NMVOCs [3], NH_3, CO, HMs, POPs, PM [4] and voluntary BC), activity data, projections, gridded data and information on large point sources (LPS) to the EMEP Centre on Emission Inventories and Projections (CEIP).

[1]"Sulphur oxides (SO_x)" means all sulphur compounds, expressed as sulphur dioxide (SO_2), including sulphur trioxide (SO_3), sulphuric acid (H_2SO_4), and reduced sulphur compounds, such as hydrogen sulphide (H_2S), mercaptans and dimethyl sulphides, etc.

[2]"Nitrogen oxides (NO_x)" means nitric oxide and nitrogen dioxide, expressed as nitrogen dioxide (NO_2).

[3]"Non-methane volatile organic compounds" (NMVOCs) means all organic compounds of an anthropogenic nature, other than methane, that are capable of producing photochemical oxidants by reaction with nitrogen oxides in the presence of sunlight.

[4]"Particulate matter" (PM) is an air pollutant consisting of a mixture of particles suspended in the air. These particles differ in their physical properties (such as size and shape) and chemical composition. Particulate matter refers to:
(i) "$PM_{2.5}$", or particles with an aerodynamic diameter equal to or less than 2.5 micrometers (μm);
(ii) "PM_{10}", or particles with an aerodynamic diameter equal to or less than 10 (μm).

3.1.1 Reporting of emission inventories in 2017

Completeness and consistency of submitted data have improved significantly since EMEP started collecting information on emissions. About 41 to 48 Parties report data regularly since 2010. Slight improvement of reporting by EECCA countries has been observed in the last four years. 45 Parties (88%) submitted inventories[5] in 2017; six Parties[6] did not submit any data; and 33 countries reported black carbon (BC) emissions. 27 countries reported information on large point sources (LPS) (Mareckova et al. 2017).

The quality of submitted data across countries differs quite significantly. By compiling the inventories, countries have to use the newest available version of the EMEP/EEA air pollutant emission inventory guidebook, which is version of 2016 (EMEP/EEA 2013b). However, many countries still use the Guidebook 2013 (EMEP/EEA 2013a) or older versions. Uncertainty of reported data (national totals, sectoral data) is considered relatively high, the completeness of reported data has not turned out satisfactory for all pollutants and sectors either.

Detailed information on recalculations, completeness and key categories, plus additional review findings can be found in the annual EEA & CEIP technical inventory review reports (Mareckova et al. 2017) and its Annexes[7].

3.1.2 Reporting of gridded data

2017 is the first year with reporting obligation of gridded emissions in the new grid resolution of $0.1^\circ \times 0.1^\circ$longitude-latitude. Only 22 of the 48 countries which are considered to be part of the new EMEP domain reported sectoral gridded emissions in the new grid in 2017. One country reported gridded national total values (instead of sectoral data) and one country reported its gridded sectoral emissions in the old 50×50 km grid resolution.

For the year 2015, gridded sectoral emissions in $0.1^\circ \times 0.1^\circ$longitude-latitude resolution have been reported by 21 countries. Only 6 countries reported gridded emissions additionally for previous years (3 countries for the years 1990, 1995, 2000, 2005 and 2010; one country for the whole time series from 1980 to 2015; one country for the whole time series from 1990 to 2015 and one country for the year 2014). One country reported gridded emissions only for the year 2005.

Reported gridded sectoral data in $0.1^\circ \times 0.1^\circ$longitude-latitude resolution covers less than 20% of the grid cells within the geographic EMEP area. For remaining areas missing emissions are gap-filled and spatially distributed by expert estimates.

Reported gridded data can be downloaded from the CEIP website[8].

3.1.3 Gap filling in 2017

In order to create emission data sets which can be used for the spatial distribution in $0.1^\circ \times 0.1^\circ$longitude-latitude resolution, reported sectoral (NFR14) emissions were aggregated to 13 GNFR (Gridding Nomenclature For Reporting) sectors and gap filled afterwards as needed.

[5]The original submissions from the Parties can be accessed via the CEIP homepage on `http://www.ceip.at/status_reporting/2017_submissions`.

[6]Armenia, Belarus, Bosnia and Herzegovina, Greece, Montenegro and the Russian Federation

[7]`http://www.ceip.at/review_proces_intro/review_reports`

[8]`http://www.ceip.at/status_reporting/2017_submissions`

In cases where no data have been submitted by countries, or the reporting is not complete, missing information has to be filled in. To gap-fill those missing data, CEIP applied different gap-filling methods:

- The first step was to collect official submissions by the Parties to the LRTAP Convention. All submissions received before 20th March 2017 have been used as a base for the gap-filled data set. Parties reported their emission inventories as sectoral emissions (NFR14) and National Total emissions according to the UNECE guidelines for reporting emissions and projections data under the LRTAP Convention.

- The second step was to aggregate the NFR data to 13 GNFR sectors and to check reported data for plausibility by comparing it with reported data of other countries, expert data and their ratio to population data, GDP (Gross Domestic Product) and area in comparison with other countries. If regarded as implausible, reported data were replaced.

- The third step was to gap-fill the inventory. Gap-filling was applied if (1) no data were submitted by the Parties, (2) the reporting was not complete, (3) if there was a notable discrepancy for several sectors and the National Totals between the reported data and expert data or (4) if there was no reporting obligation for a certain area.

The gap-filling in 2017 is documented in detail in a technical report (Technical report CEIP 03/2017), which can be downloaded from the CEIP website[9].

3.1.4 Contribution of individual sectors to total EMEP emissions

Figure 3.1 shows the contribution of each GNFR sector to the total emissions of individual air pollutants (SO_x, NO_x, CO, NMVOC, NH_3, $PM_{2.5}$ and PM_{coarse}). The share of individual sectors typically does not change significantly over years, the changes between 2014 and 2015 were minor.

The values above the graphs in Figure 3.1 are emission totals shown in thousand tons (kt). Only percentages above 10% are shown (percentages below are not included in the graphs).

It is evident that the combustion of fossil fuels is responsible for a significant part of all emissions. 57% of NO_x emissions are produced by transport (F, G, H, I) but 18% of NO_x also comes from large power plants (A).

NMVOC sources are distributed more evenly among the different sectors, such as 'Solvent use' (33%), 'Other stationary combustion' (14%), 'Road transport' (12%), 'Fugitive Emissions' (12%), 'Agriculture' (12%) as well as 'Industry combustion' (9%).

The main source of SO_x emissions are large point sources from combustion in energy and transformation industries (70%).

Ammonia arises mainly from agricultural activities, about 94% , while CO emissions originate primarily from 'Road transport' (29%) and 'Other stationary combustion' (32%).

The main sources of primary PM emissions (up to 60%) are industry and other stationary combustion processes and agriculture with a share of 15% to 30%.

Figure 3.2 illustrate the sector contribution for the sum of total emissions in the EMEP West region and the EMEP East region. The split between EMEP West and EMEP East

[9] http://www.ceip.at/fileadmin/inhalte/emep/pdf/2017/MAIN_PM_gap-filling_documentation_2017.pdf

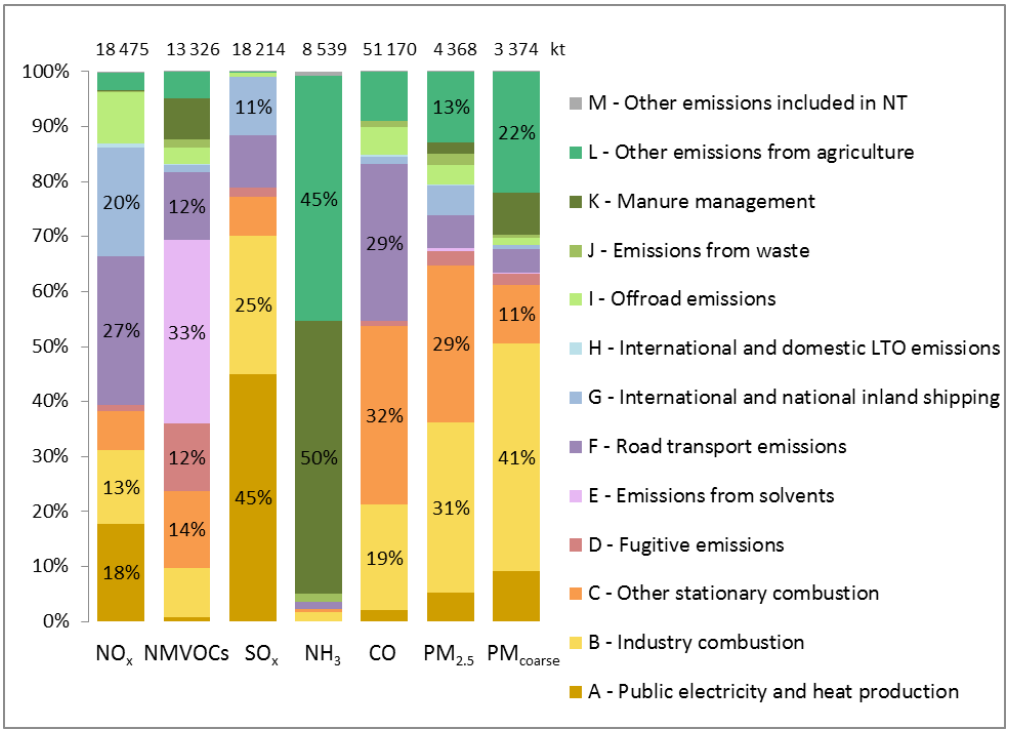

Figure 3.1: GNFR sector contribution to national total emissions in 2015 for the new EMEP area (only percentages above 10% are visible).

regions is according to `http://www.ceip.at/emep_countries`. Asian areas are included in the EMEP East region. The comparison of both graphs highlights some significant differences between west and east.

Whilst 'International and national inland shipping' (G) have a quite high share (up to 33%) for the pollutants NO_x, SO_x and $PM_{2.5}$ in the EMEP West area, the same sector is not really relevant for the EMEP East area, for example it is only 3% of the NO_x emissions.

For NMVOC in the EMEP West region the most relevant sector is 'Emissions from solvents' (E) with a share of 41%. In the EMEP East region the same sector has a considerable lower share (25%).

The main source of SO_x is 'Public electricity and heat production' (A) with 55% in the EMEP West area, but in the EMEP East region this sector contributes even 76% of the SO_x emissions. The sector 'Road transport emissions' (F) contribute to 13% of the SO_x emissions in the EMEP East region, but has almost no source for the EMEP West region (0.1%).

The main source of NH_3 emissions for both EMEP West and EMEP East are the agricultural sectors (K and L) with 93% and 95% respectively.

CO emissions arise mainly from 'Road transport' (34%) in EMEP East. In the EMEP West region the main sector is 'Other stationary combustion' (40%).

For $PM_{2.5}$ 'Other stationary combustion' (C) holds a quite significant share (47%) of the total in the EMEP West area. For the EMEP East area the sector 'Industry combustion' (B) has the highest share, 42% of total emissions. Whilst for PM_{coarse} emissions 'Industry combustion' (B) is a major source for both the EMEP East (44%) and the EMEP West (32%) region.

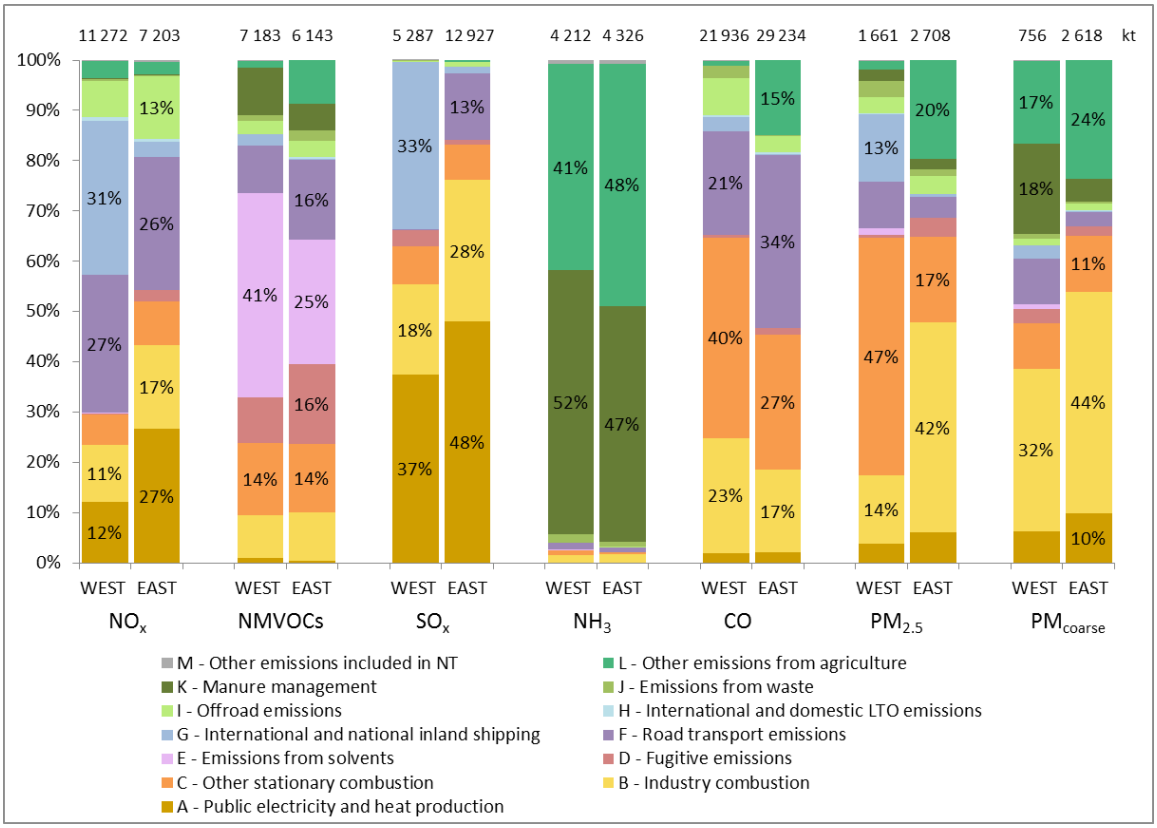

Figure 3.2: GNFR sector contribution to national total emissions in 2015 for the EMEP West and East regions (only percentages above 10% are visible). Asian areas are included in the EMEP East region.

3.2 Emission trends in the EMEP area

The emission trend in Figure 3.3 indicates that in the EMEP area total emissions (excluding shipping, natural and volcanic emissions and the North African area) of reported pollutants have decreased overall since 1990 or 2000. The emission trends presented are partly based on reported data and partly on expert estimates, therefore there is a certain uncertainty in the magnitude of this development. The observed decrease is rather significant for SO_x, NO_x, CO and NMVOC. NH_3 emissions show only a slight increase, and $PM_{2.5}$ emissions in year 2015 are at almost the same level as in the year 2000. PM_{coarse} emissions increased since the year 2000 by 38%.

A more detailed assessment shows that emission developments in the eastern and western part of EMEP area seem to follow different patterns (see Figure 3.4)[10]. While emissions of most of the pollutants in the western part of EMEP area are slowly decreasing, emissions in the east seem to fluctuate around the same level or even increase. The emissions in the western parts of EMEP area are nearly 100% based on reported data, while the emissions in the eastern parts are often expert estimates so the uncertainty is rather high. Decreases in Turkey and the Ukraine are the main reason for the change in $PM_{2.5}$ emission between 2013 and 2015.

A major reason for divergences in the trends is the implementation of various energy- and pollution-related EU directives into national law, which led to substantial increases in energy

[10]The split between EMEP West and EMEP East regions is according to `http://www.ceip.at/emep_countries`. 'North Africa' is not included and 'Asian areas' are included in the EMEP East region.

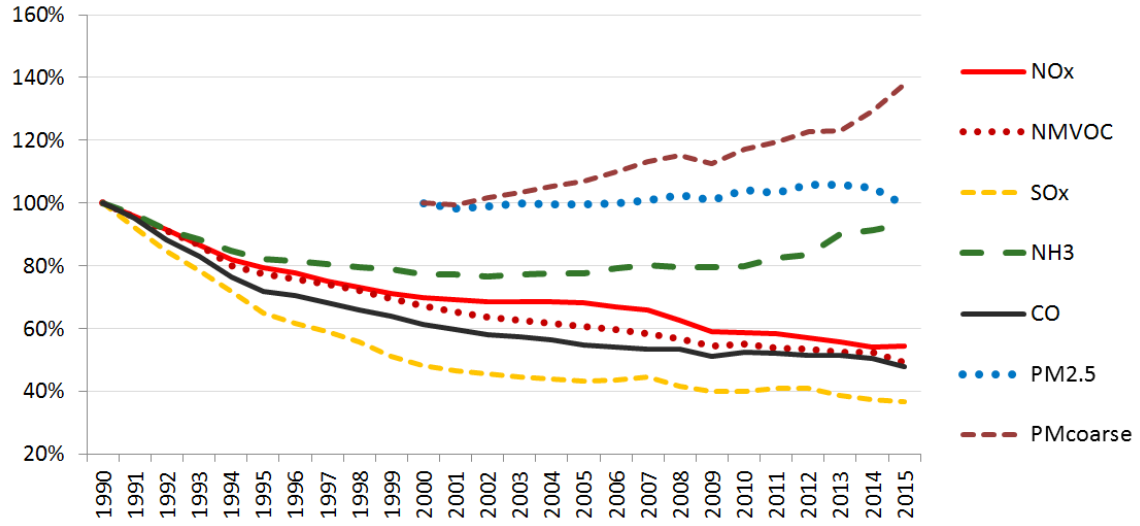

Figure 3.3: Emission trends for 1990-2015 in the EMEP area based on data reported by countries and gap-filled with expert estimates. (Shipping emissions are not included.)

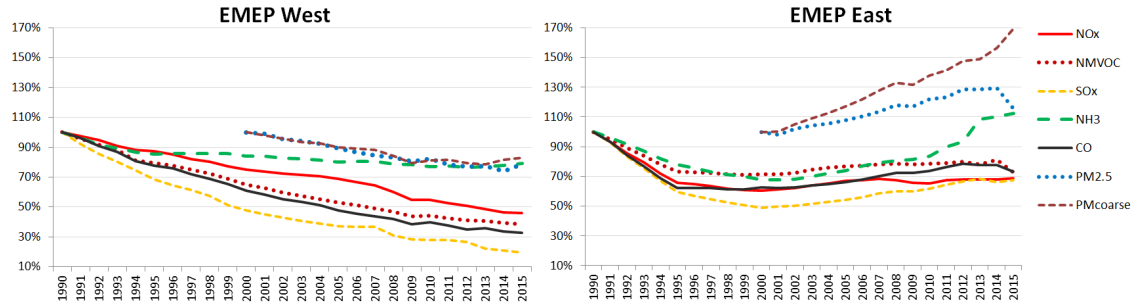

Figure 3.4: Emission trends for 1990-2015 in the EMEP area based on data reported by countries (gap-filled with expert estimates) divided in 2 areas "EMEP West" (left), "EMEP East" (right).

efficiency especially in the former communist new EU member states. A further reason is the economic recovery in the East region following the collapse of the Soviet Union. As a result, emissions in EMEP East began to stabilise or even increase slightly between 1995 and 2000. In the early 2000s, strong economic growth took place in this region. More information on socioeconomic drivers can be found in Colette et al. (2016).

3.3 Comparison of emission levels from the current year, the year 2000 and emission commitments

Emission levels for 2015 of individual countries[11] are compared to 2000 emission levels for SO_x, NO_x, NMVOC, CO, NH_3 and PMs (see Figures 3.5 - 3.7). Overview tables with re-

[11]Emissions from Tajikistan, Turkmenistan, Uzbekistan and Asian areas are not included in this assessment because data are 100% expert estimates. Also shipping, natural and volcanic emissions and the North African area are excluded.

ported emission trends for individual countries have been published on the CEIP website[12] and detailed information on the sectoral level can be accessed in WebDab[13].

The 1999 Gothenburg Protocol (GP) lists emission reduction commitments for SO_x, NO_x, NMVOC and NH_3 for thirty-three Parties[14] to the LRTAP Convention for the year 2010. These commitments should not be exceeded in subsequent years either. However, Figure 3.5 and Figure 3.6 indicate that a number of countries could not reduce their emissions[15] regarding the GP requirements.

3.3.1 Trend analysis

The assessment of emission levels in individual countries show an increase of emissions compared to 2000 emission levels in several countries. In the case of NH_3 even 23 countries have emissions in 2015 which are higher than in the year 2000. In the case of PM_{coarse} there are 21 countries, for $PM_{2.5}$ 14 countries, for NO_x 11 countries, for NMVOC 7 countries and for SO_x and CO 9 countries with emission levels higher than in year 2000. Furthermore, a comparison with last year's submissions showed, that for NO_x (+1 country), SO_x (+1 country), CO (+1 country), NH_3 (+3 countries), PM_{coarse} (+4 countries) and for $PM_{2.5}$ (+2 countries) the number of countries with emissions above the year 2000 level increases. This indicates that after the year 2000 the emission reductions slowed down and trends did reverse in a certain number of countries. Detailed explanatory information on emission trends should be provided in the informative inventory reports (IIRs).

3.3.2 NO_x emissions

On the basis of reported data, the total reduction of NO_x emissions in the EMEP area for the period 2000–2015 was estimated at -22%. Emissions decreased in 36 countries and increased in 11 countries (see Figure 3.5). The strongest increase occurred in Kyrgyzstan (+176%). Five countries still exceed their NO_x ceilings stipulated in the GP, e.g. Luxembourg (by 97%) and Austria (by 39%).

3.3.3 NMVOC emissions

Emissions in the EMEP area have decreased by -27% compared with 2000 levels. Compared with 2000, NMVOC emissions have decreased in 40 countries and increased in 7 countries (see Figure 3.5). The strongest NMVOC increase can be observed in Armenia (+107%) and the Republic of Moldova (+91%). Emissions of Ireland, Denmark, Luxembourg, Belarus, Germany and Hungary are above the GP ceilings (+84%, +29%, +8%, +7%, +3% and +1%,

[12] http://www.ceip.at/status_reporting/2017_submissions

[13] http://www.ceip.at/webdab_emepdatabase/reported_emissiondata and/or http://www.ceip.at/webdab_emepdatabase/emissions_emepmodels

[14] 34 Parties with 2010 targets listed in 1999 GP: Armenia, Austria, Belgium, Bulgaria, Belarus, Croatia, Cyprus, Czech Republic, Denmark, EU15, Finland, France, Germany, Greece, Hungary, Ireland, Italy, Liechtenstein, Lithuania, Luxembourg, Latvia, the Republic of Moldova, the Netherlands, Norway, Poland, Portugal, Romania, Slovakia, Slovenia, Spain, Sweden, Switzerland, the United Kingdom and Ukraine. Of these 10 (Armenia, Austria, Belarus, Greece, Ireland, Italy, Liechtenstein, the Republic of Moldova, Poland and Ukraine) have not signed/ratified the 1999 GP yet.

[15] Based on 'fuel sold' data.

respectively). Last year, Hungary and Belarus have reached the GP emission target (-15% and -42%, respectively, as reported in 2016).

3.3.4 SO_x emissions

Of all reported pollutants, SO_x emissions decreased by -24% between 2000 and 2015. Compared with 2000, SO_x emissions have decreased in 38 countries and increased in 9 countries -

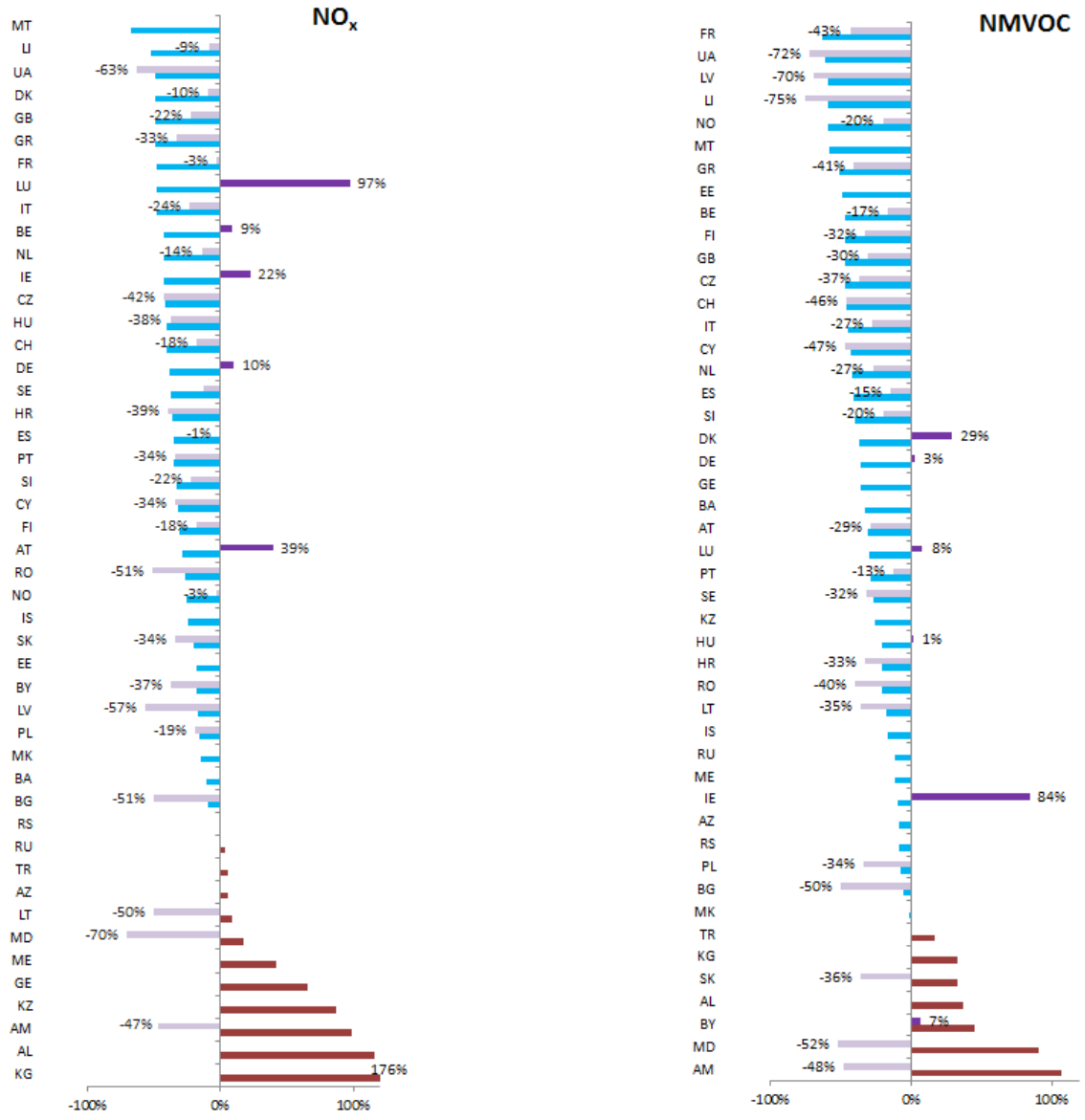

Figure 3.5: NO_x and NMVOC emissions - differences 2000-2015 and distance of 2015 emissions to the Gothenburg Protocol targets. *Blue and red bars: Differences between emissions reported for 2000 and 2015. Blue means that 2015 emissions were lower than 2000 emissions. Red means that 2015 emissions were higher than 2000 emissions. Purple bars: Distance of 2015 emissions to the GP targets. Light purple means that the reported 2015 emission value was below the GP target. Dark purple means that the 2015 emission value was above the GP target.*

among them Armenia (+2951%) and Montenegro (+195%). No country exceeded its SO_x GP target, neither in 2010, nor in the years after (see Figure 3.6).

3.3.5 NH_3 emissions

Emissions in the EMEP area have increased by +21% compared with 2000 levels. NH_3 emissions have decreased in 24 countries and increased in 23 countries (see Figure 3.6). The

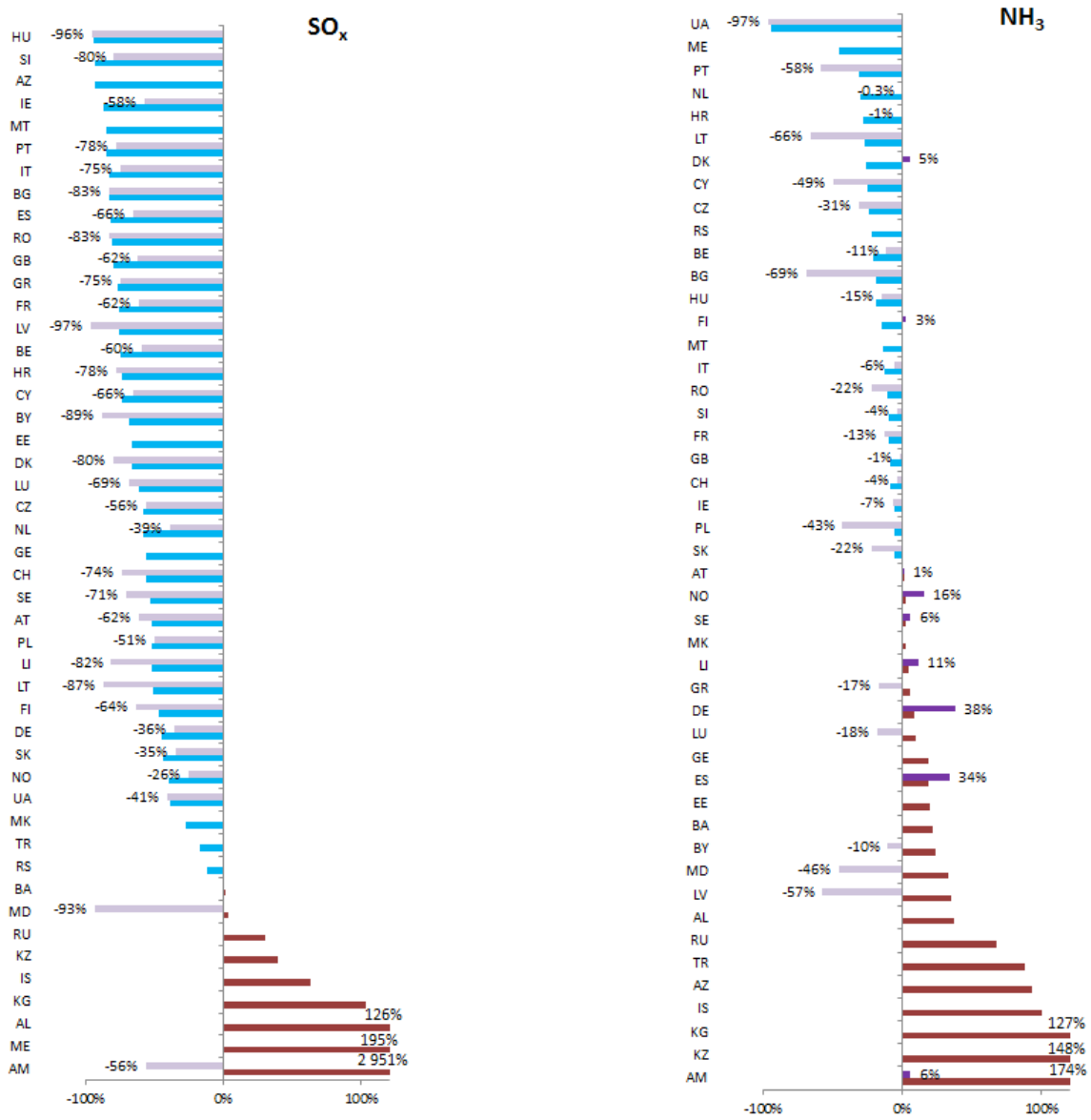

Figure 3.6: SO_x and NH_3 emissions - differences 2000-2015 and distance of 2015 emissions to the Gothenburg Protocol targets. *Blue and red bars: Differences between emissions reported for 2000 and 2015. Blue means that 2015 emissions were lower than 2000 emissions. Red means that 2015 emissions were higher than 2000 emissions. Purple bars: Distance of 2015 emissions to the GP targets. Light purple means that the reported 2015 emission value was below the GP target. Dark purple means that the 2015 emission value was above the GP target.*

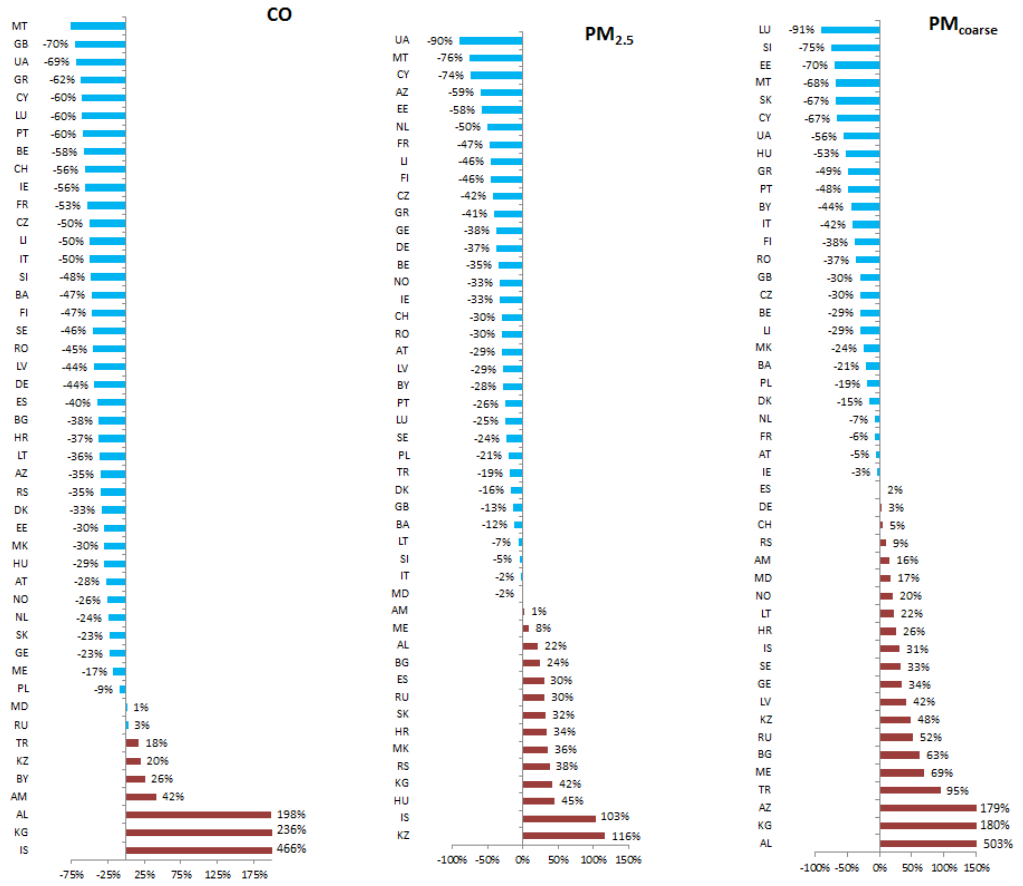

Figure 3.7: CO, $PM_{2.5}$ and PM_{coarse} emissions - differences 2000-2015. *Blue and red bars: Differences between emissions reported for 2000 and 2015. Blue means that 2015 emissions were lower than 2000 emissions. Red means that 2015 emissions were higher than 2000 emissions.*

strongest increases were observed in Kazakhstan (+148%) and Armenia (+174%). 9 countries exceeded their GP targets also in 2015. In comparison with last year, the emissions of the Netherlands are now below the GP ceilings, while emissions from Sweden and Armenia exceeded the GP target.

3.3.6 CO emissions

The total decrease in CO emissions from 2000 to 2015 amounted to -22%. Compared with 2000 CO emissions have decreased in 38 countries and increased in nine countries (see Figure 3.7), particularly in Iceland (+466%), Kyrgyzstan (+236%) and and Albania (+198%).

3.3.7 $PM_{2.5}$ emissions

$PM_{2.5}$ emissions in the EMEP area have decreased by -1% compared with 2000 levels. Compared with the year 2000, $PM_{2.5}$ emissions have decreased in 33 countries and increased in 14 countries (see Figure 3.7). The largest increases occurred in Kazakhstan (+116%), Iceland (+103%), Hungary (+45%) and Kyrgyzstan (+42%).

3.3.8 PM_{coarse} emissions

The total increase in PM_{coarse} emissions from 2000 to 2015 amounted to +38%. Compared with 2000, PM_{coarse} emissions have decreased in 26 countries and increased in 21 countries (see Figure 3.7). The strongest increases can be observed in Albania (+503%), Kyrgyzstan (+180%) and Azerbaijan (+179%).

3.4 Comparison of 2014 data (reported in 2016) and 2015 data (reported in 2017)

The comparison of 2014 emissions (reported in 2016) and 2015 emissions (reported in 2017) showed, that for 40 countries data changed by more than 15% for one or several pollutants (see Figure 3.8). These changes can be caused either by the gap-filling procedure or due to emission reductions or increases and recalculations made by the respective country.

In ten countries, NO_x emissions changed more than 15%, these are Albania, Luxembourg, Macedonia, Malta, Republic of Moldova, Serbia, Turkey, Turkmenistan, Ukraine and Uzbekistan (see Figure 3.8).

For NMVOC, emissions changed more than 15% in Albania, Azerbaijan, Belarus, Finland, Georgia, Hungary, Iceland, Ireland, Kazakhstan, Kyrgyzstan, Latvia, Macedonia, Malta, Moldova, Slovakia, Turkey, Turkmenistan, Ukraine and Uzbekistan.

SO_x emissions changed more than 15% for 22 countries: Albania, Armenia, Azerbaijan, Belarus, Bulgaria, Cyprus, Estonia, Georgia, Iceland, Luxembourg, Macedonia, Malta, Republic of Moldova, Serbia, Slovakia, Slovenia, Sweden, Switzerland, Turkmenistan, Ukraine, the United Kingdom and Uzbekistan. Also, the largest relative changes occurred for this pollutant (see Figure 3.9).

For NH_3, emissions changed more than 15% in 17 countries Albania, Armenia, Azerbaijan, Croatia, Greece, Kyrgyzstan, Lithuania, Macedonia, Republic of Moldova, Russian Federation, Serbia, Slovakia, Spain, Turkey, Turkmenistan, Ukraine and Uzbekistan.

CO emissions changed more than 15% for 19 countries: Albania, Azerbaijan, Belarus, Bosnia and Herzegovina, Georgia, Hungary, Iceland, Kazakhstan, Luxembourg, Macedonia, Malta, Norway, Serbia, Spain, Tajikistan, Turkmenistan, Ukraine, the United Kingdom and Uzbekistan.

In 16 countries, $PM_{2.5}$ emissions changed more than 15%: Azerbaijan, Belarus, Bulgaria, Estonia, Hungary, Iceland, Kazakhstan, Macedonia, Malta, Serbia, Spain, Tajikistan, Turkey, Turkmenistan, Ukraine and Uzbekistan.

For PM_{coarse}, emissions more than 15% changed in 24 countries: Albania, Azerbaijan, Belarus, Bulgaria, Cyprus, Denmark, Georgia, Italy, Kazakhstan, Kyrgyzstan, Lithuania, Luxembourg, Malta, Portugal, Republic of Moldova, Serbia, Slovenia, Spain, Sweden, Tajikistan, Turkey, Turkmenistan, Ukraine and Uzbekistan.

3.4.1 Changes due to the gap-filling

For some countries (Albania, Azerbaijan, Georgia, Iceland, Kazakhstan, Kyrgyzstan, the Republic of Moldova, FYR of Macedonia and Ukraine) the difference between 2014 and 2015 emission data occurred due to different data sources. In 2016, data for the year 2014 were gap-filled, but in 2017 data for the year 2015 were reported by the respective country. The

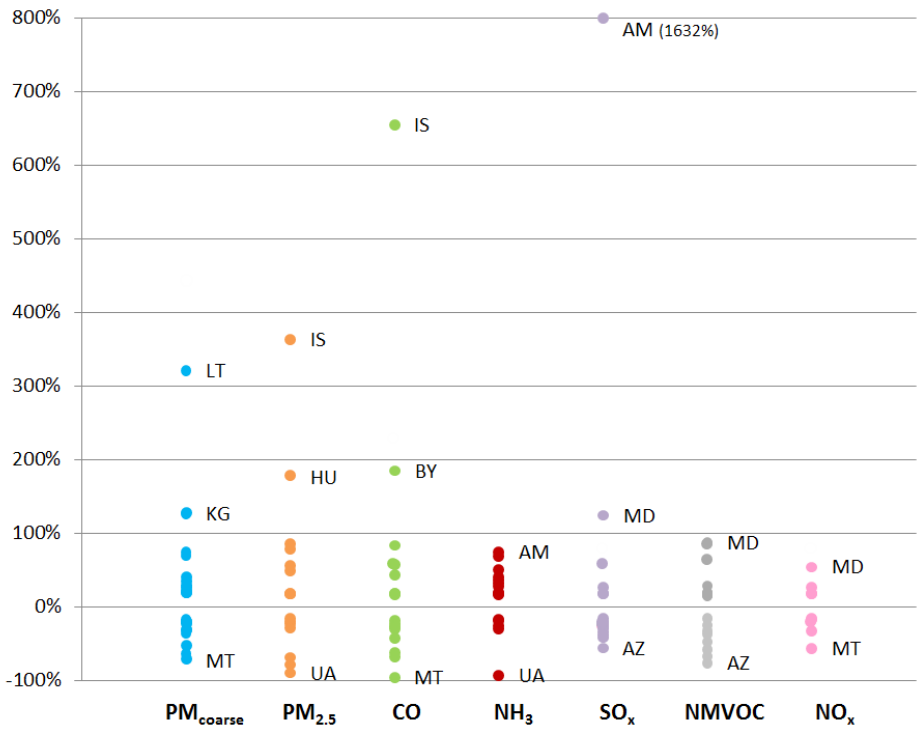

Figure 3.8: Changes between 2014 and 2015 (only changes larger than 15% are shown).

largest changes occurred for Iceland (CO, +651%), Albania (CO, +200%) and the Republic of Moldova (SO_x, +102%).

The emission changes for NH_3 (+75%) in Armenia can be explained by the gap-filling procedure for 2017 where TNO data (Kuenen et al. (2014)) was used to calculate 2015 emissions. On the contrary extrapolated GAINS data (IIASA (2014)) were used to calculate 2014 data in 2016. For SO_x (+1632%) the same method was used for 2014 data, but in 2017, interpolation of reported data using population data was done to calculate 2015 emissions.

In Belarus, changes in CO (+109%), NMVOC (+84%), $PM_{2.5}$ (-20%) and SO_x (-41%) emissions between 2014 and 2015 occurred. In 2016, interpolated GAINS data (IIASA (2014)) were used to calculate 2014 data. In 2017, interpolation of reported data using population data was done to calculate 2015 emissions.

Emission data of Bosnia and Herzegovina for CO showed large changes (+44%) between 2014 and 2015. For the gap-filling in 2016 interpolated GAINS data (IIASA (2014)) were used. In 2017 extrapolation of TNO data (Kuenen et al. (2014)) was done to calculate 2015 emissions.

NH_3 emissions in Greece changed by +20% compared to last year. Greece has provided National Totals and sectoral data up to 2012. In 2016, interpolated GAINS data (IIASA (2014)) were used to calculate 2014 data. In 2017, extrapolation of reported data was done to calculate 2015 emissions.

NH_3 emission data of the Russian Federation showed large changes (+39%) between 2014 and 2015. In 2016, interpolated GAINS data (IIASA (2014)) were used to calculate 2014 data. In 2017, extrapolation of reported data was done to calculate 2015 emissions.

In Tajikistan, changes of 23% occurred in CO and $PM_{2.5}$ emissions, respectively, between

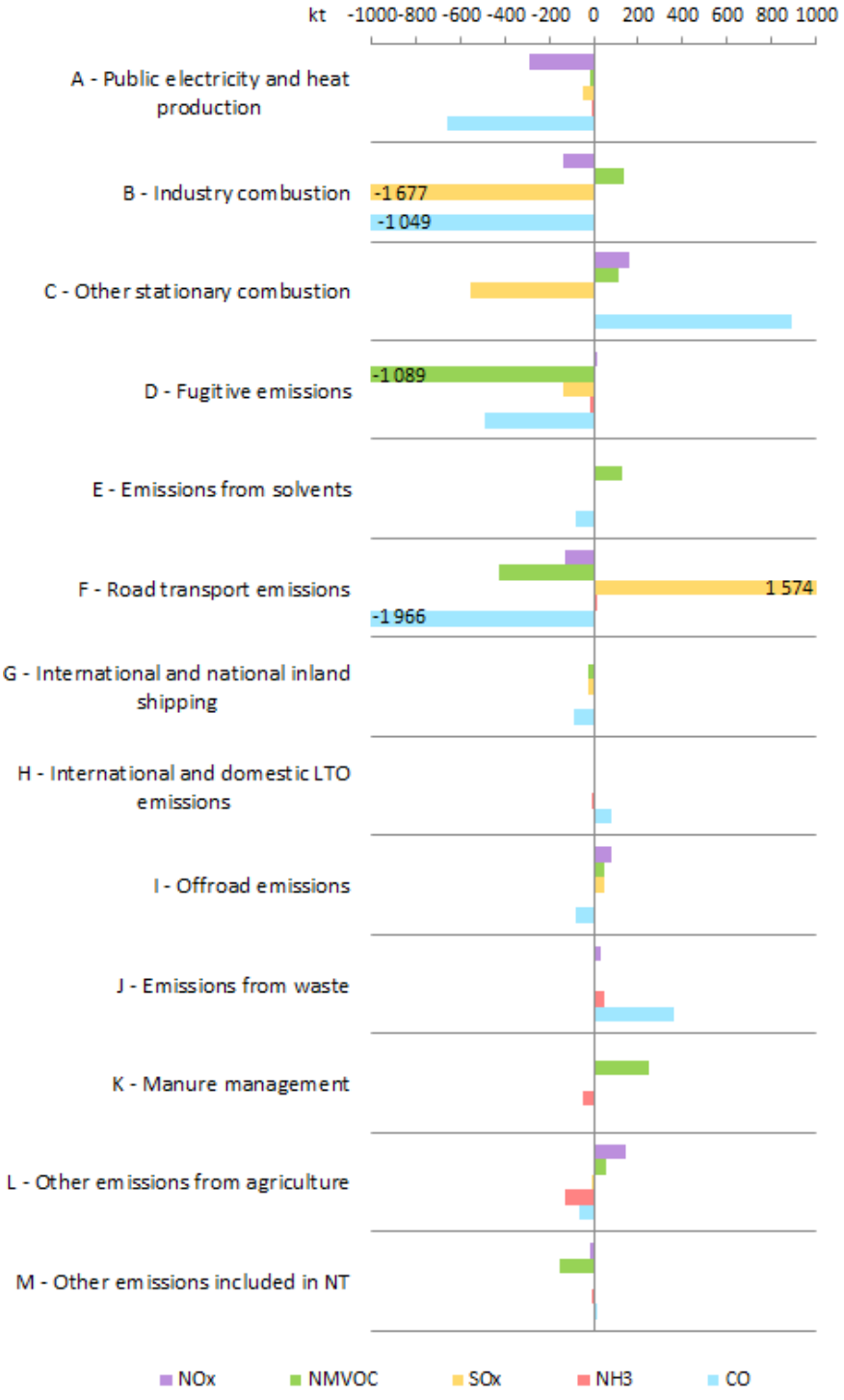

Figure 3.9: Total emission changes between 2014 and 2015 in the EMEP area, located in the individual GNFR sectors.

2014 and 2015. In 2016, the GDP trend of Tajikistan was used to extrapolate 2014 emissions using expert data. In 2017, extrapolation of expert data using population data was done to calculate 2015 emissions.

Turkey's $PM_{2.5}$ emissions decreased by 29% between 2014 and 2015. In 2016, extrapo-

lation of expert estimates using the PM $_{10}$ trend was done to calculate 2014 data. In 2017, extrapolation of TNO data (Kuenen et al. (2014)) was done to calculate 2015 emissions.

Emissions for all pollutants were calculated with the same gap-filling method for 2014 and 2015 emissions in Turkmenistan and Uzbekistan. The difference is 18% for all of them. Expert data and the GPD trend of the countries were used to extrapolate the emissions.

3.4.2 Changes in reported data

Large changes in country emissions between 2014 and 2015 are due to emission reductions or increases, and - more often - due to recalculations of the time series, mostly because of changes in emission factors or activity data, methodology updates or additional reporting. Some explanations were given in the Informative Inventory Reports (IIRs) of the countries:

In Cyprus, changes of NO_x emissions (-22%) occurred. Cyprus stated in its IIR[16] that the decrease in SO_x emissions observed in 2015 was due to the fact that the Flue-Gas Desulphurization Unit (FGD) installed in Steam Turbine Unit 3 of the 'Vassilikos PS' was again in full operation.

Between 2014 and 2015, a $PM_{2.5}$ emission increase (+18%) was detected in Estonia. Estonia explained in its IIR[17], that particulate emissions increased mainly due to the increase of emissions in combustion in manufacturing industries, where the amount of the burned wood and wood waste has increased, and the construction/demolition sectors. On the other hand emissions of SO_x saw a decrease (-22%) between 2014 and 2015. The country stated in its IIR that the main reason was the decrease of electricity production by 16.3%. Another reason is that alongside oil shale, biomass is now used in the newer units of the 'Narva power stations' to produce electricity.

In Hungary, changes of CO (+58%), NMVOC (+20%) and $PM_{2.5}$ (+108%) emissions were given between 2014 and 2015. Hungary stated in its IIR[18] , that the reason for these changes was switching from T1 to T2 methodology.

There is a quite large change in the $PM_{2.5}$ emissions in Iceland between 2014 and 2015. Iceland stated in its IIR[19], that some recalculations were performed to adjust the ratios between TSP, PM_{10} and $PM_{2.5}$ and to match them to the ratios suggested in the EMEP/EEA Inventory Guidebook 2016 (EMEP/EEA 2013b).

Ireland stated in its IIR[20], that the increase (+16%) of NMVOC emissions is due to the inclusion of NMVOC emissions from the food and beverages industry in 2017.

In Latvia, changes of SO_x emissions (+24%) occurred. Latvia stated in its IIR[21], that since the submission in 2016 recalculations have been carried out due to changes in the methodology in the 'Industrial Processes and Product Use' (IPPU) sector.

Malta pointed out in its IIR[22], that the changes in NMVOC (-32%) and NO_x (-56%) emissions between 2014 and 2015 can be explained by the update from a customized T2 method to the T3 method provided within the EMEP/EEA Emission Inventory Guidebook 2016 (EMEP/EEA 2013b) and subsequent recalculations.

[16] http://cdr.eionet.europa.eu/cy/eu/nec_revised/iir/envwmkrrq
[17] http://cdr.eionet.europa.eu/ee/un/clrtap/iir/envwmllmg
[18] http://cdr.eionet.europa.eu/hu/un/clrtap/iir/envwonj3q
[19] http://cdr.eionet.europa.eu/is/un/clrtap/iir/envwmkiqg
[20] http://cdr.eionet.europa.eu/ie/un/clrtap/iir/envwmlohg
[21] http://cdr.eionet.europa.eu/lv/un/clrtap/iir/envwmlmda
[22] http://cdr.eionet.europa.eu/mt/un/clrtap/iir/envwsw90a

Between 2014 and 2015, a CO emission increase (+59%) was detected in Norway. Norway explained in its IIR[23], that emissions of CO from production of aluminum have been included for all years, which led to a strong increase in total CO emissions.

In Slovakia, large changes of SO_x emissions (+67%) were given between 2014 and 2015. Slovakia explained in its IIR[24], that all this emissions originated from the source 'Slovenské elektrá rne'. According to the records this facility burnt twice the amount of brown coal in 2015 as in the previous year. On the other hand emissions of NH_3 (-15%) and NMVOC (-18%) decreased between 2014 and 2015. In the case of NH_3 the country stated in its IIR, that this is due to a sharp decrease in synthetic fertilizers and the continual decrease in the use of animal manure. According to Slovakia's IIR, recent NMVOC emissions declined due to technological improvements in the industry.

Between 2014 and 2015, a CO emission decrease (-21%) was detected in the United Kingdom. The United Kingdom explained in its IIR[25], that the main change between the 2016 submission and the 2017 is mainly due to a revised approach for industrial and agricultural use of biomass fuels. Emission factors are now taken from the EMEP/EEA Emission Inventory Guidebook (EMEP/EEA 2013b), and these are much lower than the values used previously. In addition, emissions from cars and LDVs are lower in the 2017 submission due to changes in methodology to account for emission degradation (switching from TRL method to COPERT method). There was also a decrease in the United Kingdom's SO_x emissions (-22%), which was due to some updates to industrial coal consumption data in DUKES.

3.5 Spatial distribution of emissions

For this year it was agreed with the modellers to perform gap-filling and gridding for the year 2015 in $0.1°\times0.1°$longitude/latitude resolution on GNFR sector level and in addition to 50×50 km^2 (PS) resolution on SNAP 10 sector level.

For the distribution of the 50×50 km^2 SNAP grid of NO_x, SO_x, NMVOC, NH_3, CO, $PM_{2.5}$, PM_{10} and PM_{coarse} for 2015, the same base grid data as last year was used. CEIP used national total emissions from the gap-filling on GNFR sector level and adjusted the SNAP sector emissions for the 50×50 km^2 SNAP grid accordingly.

The $0.1°\times0.1°$GNFR grid of NO_x, SO_x, NMVOC, NH_3, CO, $PM_{2.5}$, PM_{10} and PM_{coarse} for 2015 were gridded based on the gridding system developed by CEIP.

Reported gridded data in $0.1°\times0.1°$resolution was used for Austria, Belgium, Bulgaria, Croatia, Czech Republic, Denmark, Finland, Germany, Ireland, Latvia, Luxembourg, Poland, Portugal, Slovakia, Slovenia, Spain, United Kingdom, Monaco, Norway and Switzerland. For all other areas a combination of reported LPS data and EDGAR data[26], upgraded with point source information available under E-PRTR, was used. An example for visualizing the gap-filled gridded NO_x emissions in $0.1°\times0.1°$longitude-latitude resolution is shown in Figure 3.10.

Comparisons between gridded emissions in 50×50 km^2 and $0.1°\times0.1°$resolutions are available on the CEIP website[27].

[23] http://cdr.eionet.europa.eu/no/un/clrtap/inventories/envwklkhq
[24] http://cdr.eionet.europa.eu/sk/un/clrtap/iir/envwmma7w
[25] https://cdr.eionet.europa.eu/gb/un/clrtap/iir/envwmfebw
[26] http://edgar.jrc.ec.europa.eu/methodology.php
[27] http://www.ceip.at/new_emep-grid/grid_comparisons

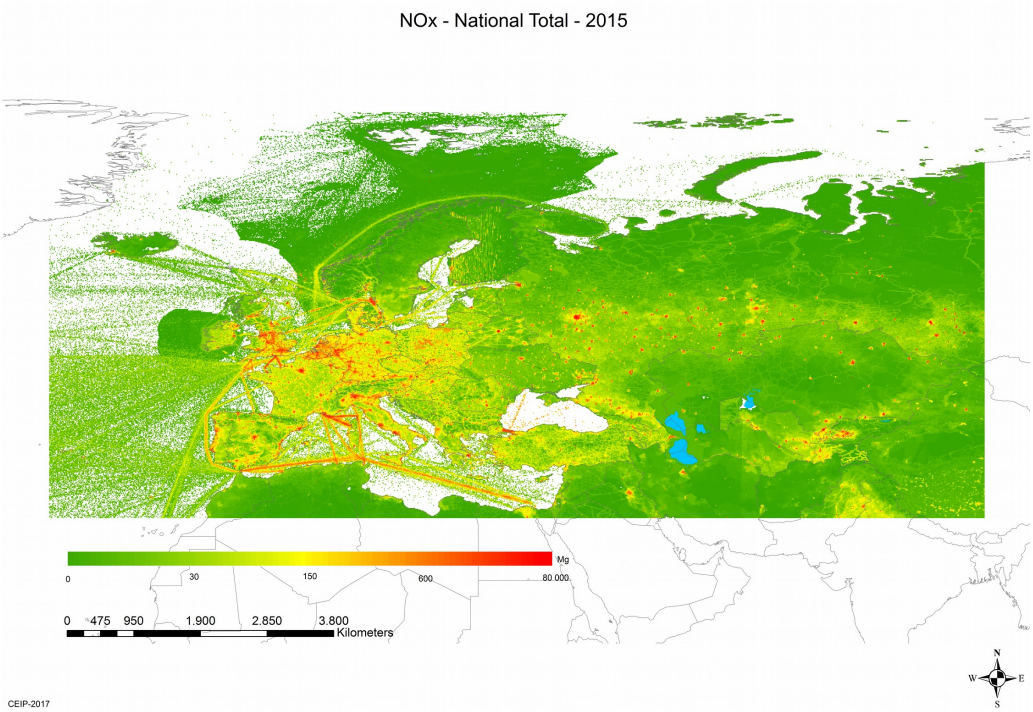

Figure 3.10: Total emission changes between 2014 and 2015 in the EMEP area, located in the individual GNFR sectors.

3.6 Volcanic emissions in 2015

3.6.1 Holuhraun fissure

The long lasting fissure eruption which started at the Barðarbunga volcanic system in Iceland (Sigmundsson et al. 2015) in August 2014 ended only on 27 February 2015. There was little ash released in the eruption, but large amounts of SO_2 were emitted into the atmosphere and the transport of SO_2 influenced air quality in Iceland, Scandinavia and central Europe.

In both 2016 and 2017 Iceland included SO_2 emissions from this eruption in the emission data reported under the LRTAP Convention. According to the IIRs of Iceland[28] the total SO_2 emission from the Holuhraun eruption was estimated to be 12,006 kt. Divided on calender years 10,880 kt of SO_2 was emitted in the year 2014 and 1,126 kt of SO_2 in the year 2015.

For transport modelling, however, more detailed information about the source term of the eruption, that is, the source strength as a function of altitude and time is needed.

Time series of plume height observations/measurements and the time series of the SO_2 emission rate measurements have been kindly provided by Melissa Anne Pfeffer from the volcanic hazard team at the Icelandic Met Office with permission to use the information for input data in the EMEP MSC-W model simulation.

3.6.2 Passive degassing of SO_2 from Italian volcanoes

SO_x emissions from passive degassing of Italian volcanoes (Etna, Stromboli and Volcano) are

[28] http://cdr.eionet.europa.eu/is/un/UNECE_CLRTAP_IS/envvuhkya/Infomative_Inventory_Report_Iceland_2016.pdf

included in the emission data reported by Italy. According to the reported data, SO_x emissions from the Italian volcanoes shows a generally down-going trend for the last two decades and decreased from 8326 Gg/year in 1990 to 943 Gg/year in 2010, then remained on the same level between 2010 and 2015.

3.7 Emissions from international shipping

For the last two years EMEP/MSC-W have been using ship emissions based on the MACC-III (MACC-III 2015) inventory developed by TNO extending up to year 2011 (see discussion in Gauss and Jonson (2016)). Due to the lack of reliable data, no further trend in ship emissions was assumed for the years 2012, 2013 and 2014. Following the implementation of the stricter SECA regulations in 2015 this assumption is no longer accurate.

By courtesy of the Finnish Meteorological Institute (FMI) we have been granted access to a newly developed ship emission data set for year 2015 . The data are based on real ship movements obtained from data collected through the Automatic Identification System (AIS), mandatory worldwide for all ships with a gross tonnage of 300 tonnes or more, and all passenger ships regardless of size. The ship movements are combined with vessel specific technical data (ship size, engines installed, speed, etc.) for each individual ship. Emissions are then calculated using the STEAM model as described in Jalkanen et al. (2016).

The 2015 global ship emissions from FMI are provided daily on a $0.1^\circ \times 0.1^\circ$longitude-latitude grid for NO_x, SO_x, CO, and particulate matters. For NMVOC (Non Methane Volatile Organic Compounds) emissions from TNO-MACC-III are used, as these are not included in the global FMI emission inventory.

A more detailed description of the FMI shipping emissions can be found in Chapter 10.2.

References

Colette, A., Aas, W., Banin, L., Braban, C., Ferm, M., González Ortiz, A., Ilyin, I., Mar, K., Pandolfi, M., Putaud, J.-P., Shatalov, V., Solberg, S., Spindler, G., Tarasova, O., Vana, M., Adani, M., Almodovar, P., Berton, E., Bessagnet, B., Bohlin-Nizzetto, P., Boruvkova, J., Breivik, K., Briganti, G., Cappelletti, A., Cuvelier, K., Derwent, R., D'Isidoro, M., Fagerli, H., Funk, C., Garcia Vivanco, M., González Ortiz, A., Haeuber, R., Hueglin, C., Jenkins, S., Kerr, J., de Leeuw, F., Lynch, J., Manders, A., Mircea, M., Pay, M., Pritula, D., Putaud, J.-P., Querol, X., Raffort, V., Reiss, I., Roustan, Y., Sauvage, S., Scavo, K., Simpson, D., Smith, R., Tang, Y., Theobald, M., Tørseth, K., Tsyro, S., van Pul, A., Vidic, S., Wallasch, M., and Wind, P.: Air Pollution trends in the EMEP region between 1990 and 2012., Tech. Rep. Joint Report of the EMEP Task Force on Measurements and Modelling (TFMM), Chemical Co-ordinating Centre (CCC), Meteorological Synthesizing Centre-East (MSC-E), Meteorological Synthesizing Centre-West (MSC-W) EMEP/CCC Report 1/2016, Norwegian Institute for Air Research, Kjeller, Norway, URL http://www.unece.org/fileadmin/DAM/env/documents/2016/AIR/Publications/Air_pollution_trends_in_the_EMEP_region.pdf, 2016.

EMEP/EEA: EMEP/EEA air pollutant emission inventory guidebook - 2013, 12/2013, European Environment Agency, EEA, URL http://www.eea.europa.eu/publications/emep-eea-guidebook-2013, 2013a.

EMEP/EEA: EMEP/EEA air pollutant emission inventory guidebook - 2016, 21/2016, European Environment Agency, EEA, URL http://www.eea.europa.eu/publications/emep-eea-guidebook-2016, 2013b.

Gauss, M. and Jonson, J.: Emissions from international shipping, in: Transboundary particulate matter, photo-oxidants, acidifying and eutrophying components. EMEP Status Report 1/2016, pp. 103–109, The Norwegian Meteorological Institute, Oslo, Norway, 2016.

IIASA: The GAINS Model, URL http://www.iiasa.ac.at/web/home/research/researchPrograms/air/GAINS.en.html, 2014.

Jalkanen, J.-P., Johansson, L., and Kukkonen, J.: A comprehensive inventory of ship traffic exhaust emissions in the European sea areas in 2011, Atmos. Chem. Physics, 16, 71–84, doi:10.5194/acp-16-71-2016, URL http://www.atmos-chem-phys.net/16/71/2016/acp-16-71-2016.pdf, 2016.

Kuenen, J. J. P., Visschedijk, A. J. H., Jozwicka, M., and Denier van der Gon, H. A. C.: TNO-MACC-II emission inventory; a multi-year (2003–2009) consistent high-resolution European emission inventory for air quality modelling, Atmos. Chem. Physics, 14, 10 963–10 976, doi:10.5194/acp-14-10963-2014, URL http://www.atmos-chem-phys.net/14/10963/2014/acp-14-10963-2014.html, 2014.

MACC-III: Report on the update of global and European anthropogenic emissions., Tech. Rep. COPERNICUS Grant agreement 633080, MACC-III (Monitoring Atmospheric Composition and Climate, 2015.

Mareckova, K., Pinterits, M., Tista, M., Ullrich, B., and Wankmüller, R.: Inventory review 2017. Review of emission data reported under the LRTAP Convention and NEC Directive. Stage 1 and 2 review. Status of gridded and LPS data, EMEP/CEIP 1/2017, EEA/CEIP Vienna, 2017.

Sigmundsson, F., Hooper, A., Hreinsdöttir, S., Vogfjörd, K., Ófeigsson, B., Heimisson, E. R., Dumont, S., Parks, M., Spaans, K., Gudmundsson, G. B., Drouin, V., Árnadöottir, T., Jónsdöttir, K., Gudmundsson, M. T., Högnadöottir, T., Fridriksdöottir, H., Hensch, M., Einarsson, P., Magnöusson, E., Samsonov, S., Brandsdöttir, B., White, R. S., Ágústsdöttir, T., Greenfield, T., Green, R., Hjartardöttir, A. R., Pedersen, R., Bennett, R. A., Geirsson, H., Femina, P. L., Björnsson, H., Pálsson, F., Sturkell, E., Bean, C. J., Möllhoff, M., Braiden, A., and Eibl, E.: Segmented lateral dyke growth in a rifting event at Bárðarbunga volcanic system, Iceland, Nature, 517, 191–195, doi:doi:10.1038/nature14111, 2015.

UNECE: Guidelines for reporting emission data under the Convention on Long-range Transboundary Air Pollution, Tech. Rep. ECE/EB.AIR/130, UNECE, URL `http://www.ceip.at/fileadmin/inhalte/emep/2014_Guidelines/ece.eb.air.125_ADVANCE_VERSION_reporting_guidelines_2013.pdf`, 2014.

Part II

Research Activities

CHAPTER 4

EMEP MSC-W model runs using the EMEP emissions in fine resolution - comparison to observations

Sverre Solberg, Hilde Fagerli and Svetlana Tsyro

This year countries have for the first time reported gridded emission in $0.1° \times 0.1°$ longitude-latitude resolution. In this chapter we compare the results of the EMEP MSC-W model run on $0.1° \times 0.1°$ resolution (using these new emissions) to the previous standard setup with 50km $\times$ 50km emissions and model resolution.

Clearly, both changes in the distribution of emissions, changes in the resolution of the meteorology and changes due to different resolution of the model will affect the model results.

4.1 Model setup

The model calculations for 2015 were done for two main grids and domains: the new lat x lon map projection with $0.1° \times 0.1°$ resolution with 34 vertical layers (denoted $\text{EMEP}_{0.1}$) and the 'old' 50 km $\times$ 50 km resolution using the polar stereographic map projection with 20 vertical layers (denoted EMEP_{50km}).

In order to be able to distinguish the effect of the changes of the vertical structure of the model from e.g. changes in emission resolution, a model run using $0.1° \times 0.1°$ resolution, but with the same vertical structure as the 50 km $\times$ 50 km model run (20 vertical layers instead of 34, and with the height of the lowest level of ca. 90 m), denoted $\text{EMEP}_{0.1_L20}$, was performed.

Emissions

22 of the 48 countries (within the EMEP domain) reported sectoral gridded emissions in the new grid in 2017. For remaining areas missing emissions are gap-filled and spatially distributed by expert estimates. For the 50 km $\times$ 50 km model runs, we have used a set of emissions with the same national totals as reported this year, but distributed on the 50 km $\times$

Component	N_{stat}	Bias, % 50km	Bias, % 0.1_{L20}	Bias, % 0.1	Corr 50km	Corr 0.1_{L20}	Corr 0.1
NO_2 (μg(N) m^{-3})	65	-42	-42	-32	0.66	0.69	0.69
SO_2 (μg(S) m^{-3})	54	-5	3	10	0.46	0.55	0.47
SO_4^{2-} sea salt inc (μg(S) m^{-3})	33	-19	-21	-16	0.84	0.85	0.83
NH_3 (μg(N) m^{-3})	16	16	11	25	0.75	0.90	0.90
NH_4^+ (μg(N) m^{-3})	19	-6	-15	-10	0.71	0.69	0.70
NH_3+NH_4^+ (μg(N) m^{-3})	32	9	9	21	0.84	0.75	0.74
NO_3^- (μg(N) m^{-3})	20	36	20	26	0.80	0.77	0.79
NO_3^-+HNO_3 (μg(N) m^{-3})	38	17	17	18	0.87	0.88	0.90
SO_4^{2-} wd (μg(S)m^{-2})	51	-16	-13	-11	0.53	0.70	0.67
NH_4^+ wd (μg(N)m^{-2})	51	2	-1	-2	0.44	0.48	0.46
NO_3^- wd (μg(N)m^{-2})	52	-6	-3	-3	0.56	0.64	0.65
Precipitation	53	8	10	10	0.88	0.89	0.89
Ozone max	111	2	4	4	0.80	0.76	0.76
Ozone mean	111	10	12	9	0.66	0.70	0.68
$PM_{2.5}$	30	-6	-8	-1	0.84	0.85	0.84
PM_{10}	41	-15	-15	-10	0.71	0.76	0.74

Table 4.1: Comparison of model results and observations for 2015. Annual averages over all EMEP sites with measurements. N_{stat}= number of stations, wd=wet deposition, Corr = spatial correlation coefficient r (calculated based on the yearly mean of each station). The bias is calculated as (model-observations)/observation, where the mean of the annual averages for the stations are used. For ozone max, the annual mean of the daily maximum is used. Only stations which has observations for at least 75% of the days are used (25% of common days with precipitation for model and measurements, for wet depositions and precipitation), and stations that are situated more than 500 m higher than the topographic height in the EMEP MSC-W model grid are excluded. Results are shown for both 50×50km^2 (50) and $0.1^\circ\times0.1^\circ$(0.1) resolution (34 vertical layers).

50 km base grid from last year. See chapter 3.5 for more details about the gridding of the emissions.

4.2 Short overview: comparison to EMEP background observations

In Table 4.1, the model runs $EMEP_{0.1}$, $EMEP_{0.1_L20}$ and $EMEP_{50km}$ have been compared to EMEP background observations. There are no significant differences in model annual mean biases and spatial correlations between those calculations, with a few exceptions. The primary components SO_2, NO_2 and NH_3 show somewhat higher surface concentrations in $EMEP_{0.1}$, mainly due to the decreased surface level. For SO_2 and NO_2, the spatial correlations are almost unchanged, but for NH_3 the spatial correlation improves from r=0.75 to r=90. Interestingly, spatial correlation for the sum of NH_3+NH_4 decreases (from r=0.84 to r=0.74) while it remains almost unchanged for NH_4^+. Because the sites used are not the same for NH_3, NH_4^+ and sum of NH_3+NH_4, it is hard to tell the reason for this behaviour, and reducing the collection of

observations to only those that are available for all components would make the collection of stations very small.

It is also worth to note that the correlation (and to some extent the bias) of the wet depositions consistently improves in $\text{EMEP}_{0.1}$ compared to EMEP_{50km} (especially for sulfur and oxidized nitrogen). This is also true for $\text{EMEP}_{0.1_L20}$, while the correlations for precipitation is basically the same in the three sets of data. This indicates that it is the improved resolution of the emissions that brings about these improvements.

4.3 Comparison to Airbase data; primary components

In this section we have compared the EMEP_{50km} and $\text{EMEP}_{0.1}$ model runs to the Airbase data, with the aims to investigate: (i) whether this comparison can tell us something about the quality of the new gridded emissions ($0.1^\circ \times 0.1^\circ$) and (ii) if the results from $\text{EMEP}_{0.1}$ improves compared to measurements for the primary components.

In the comparison to Airbase data, we have chosen not to include traffic stations (due to the somewhat coarse resolution of the model calculations, a comparison to traffic stations is not meaningful). Furthermore, we have categorized the Airbase data into two sets of data:

Rural (station type background and area type rural)

Urban (station type background or industrial and area type suburban or urban)

Clearly, the model cannot be expected to reproduce urban measurements. However, including those measurements help us to determine whether the emission sources are placed correctly with respect to each other - when the aim is to investigate the quality of the gridding of the emissions. There are a lot of caveats of this approach, so we will mainly look at the large picture, and sometimes only use the 'rural' part of the data set.

NH_3 measurements are not available from Airbase, so in the following section we will only analyze results for SO_2 and NO_2 and focus on the spatial correlation.

NO_2

The main source of NO_x is traffic, which is a low level source, and one would therefore expect high correlations between emissions and surface concentrations of NO_2. Thus one would expect that improved spatial distribution of NO_x emissions should result in improved spatial distribution of NO_2 concentrations.

In Figure 4.1, spatial correlation between model runs of EMEP_{50km} and $\text{EMEP}_{0.1}$ and observations (urban+rural) for each country is presented. For NO_2, there is a clear improvement for almost all countries, both for those countries that submitted gridded emission data themselves and for those countries where expert estimates have been used. There are some exceptions; for Poland, Portugal, Romania, Croatia and Serbia the spatial correlation get worse. For Slovakia, the correlation with measurements is negative both for EMEP_{50km} and $\text{EMEP}_{0.1}$. For Bulgaria, the correlation is very low (r=0.19). For most countries, however, the correlation between observations and $\text{EMEP}_{0.1}$ is high, which gives confidence to the new gridded emissions. Figure 4.2 confirms the improved model results for $\text{EMEP}_{0.1}$ compared to EMEP_{50km}, both spatial correlation and bias improves when compared to Airbase data, both for the set of rural+urban sites and the set with only rural data.

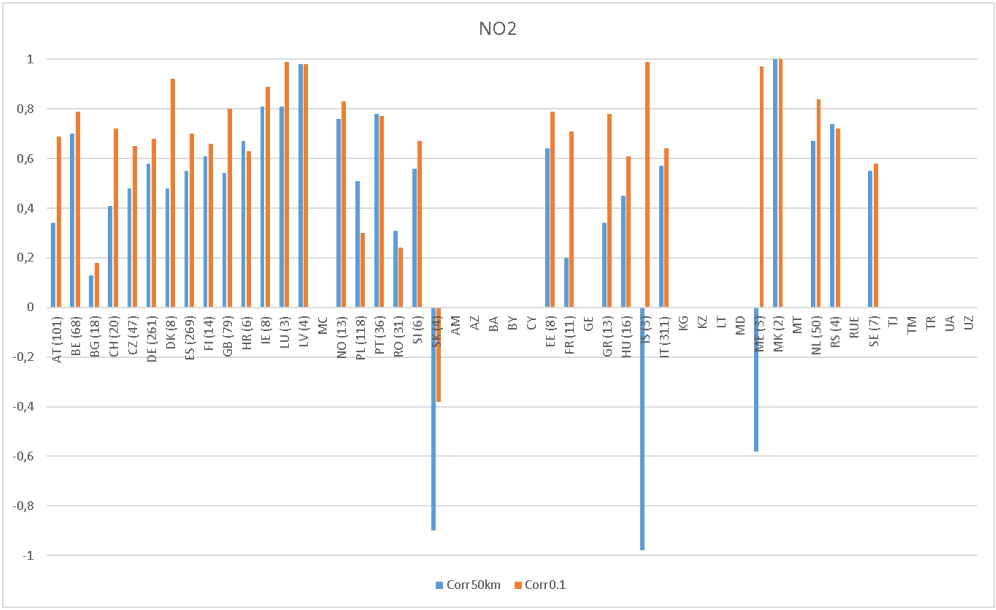

(a) NO_2

Figure 4.1: Spatial correlation coefficient for annual averages of model results (50×50km^2 and $0.1\times0.1^\circ$, 34 vertical layers) versus Airbase observations for NO_2. The number of stations used in the comparison for each country is given in parentheses. The countries AT to SK reported new gridded emissions.

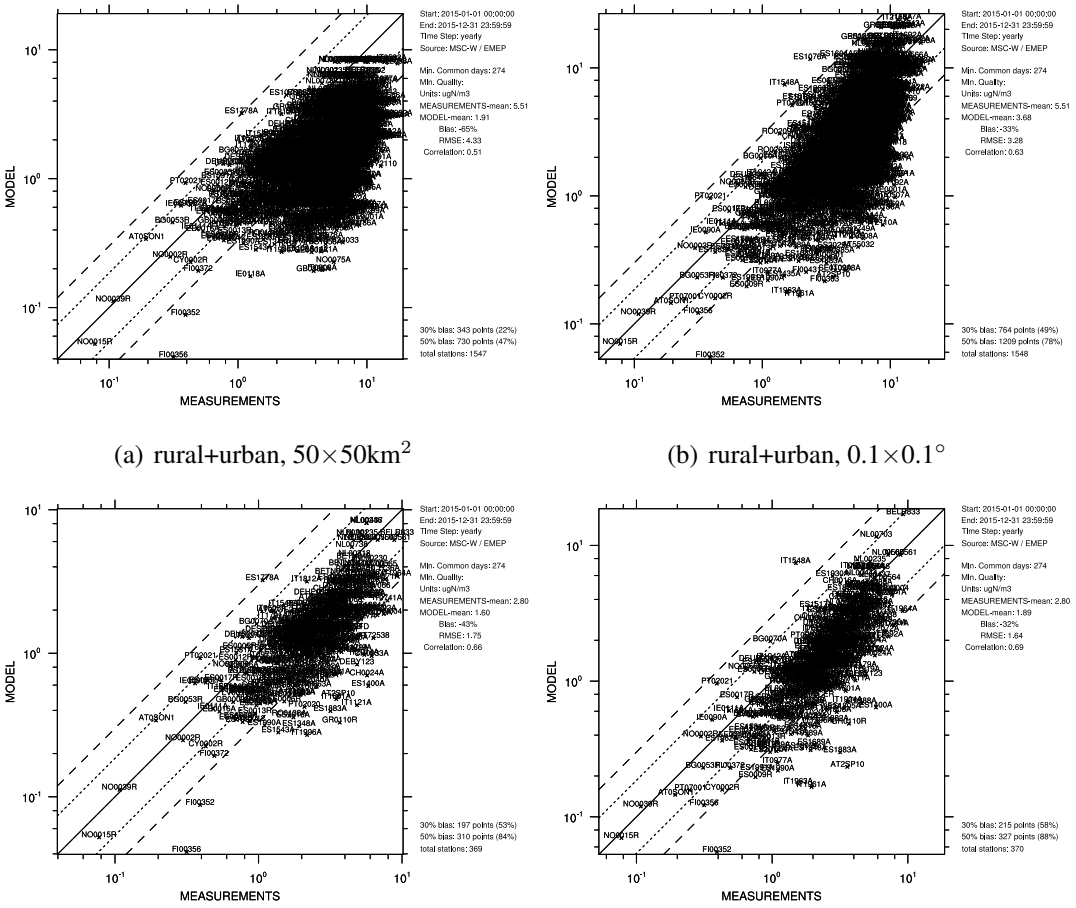

(a) rural+urban, 50×50km^2

(b) rural+urban, $0.1\times0.1^\circ$

(c) rural, 50×50km^2

(d) rural, $0.1\times0.1^\circ$

Figure 4.2: Comparison of $EMEP_{50km}$ and $EMEP_{0.1}$ to Airbase data for NO_2 (towards only rural measurements and all (rural + urban) Airbase measurements).

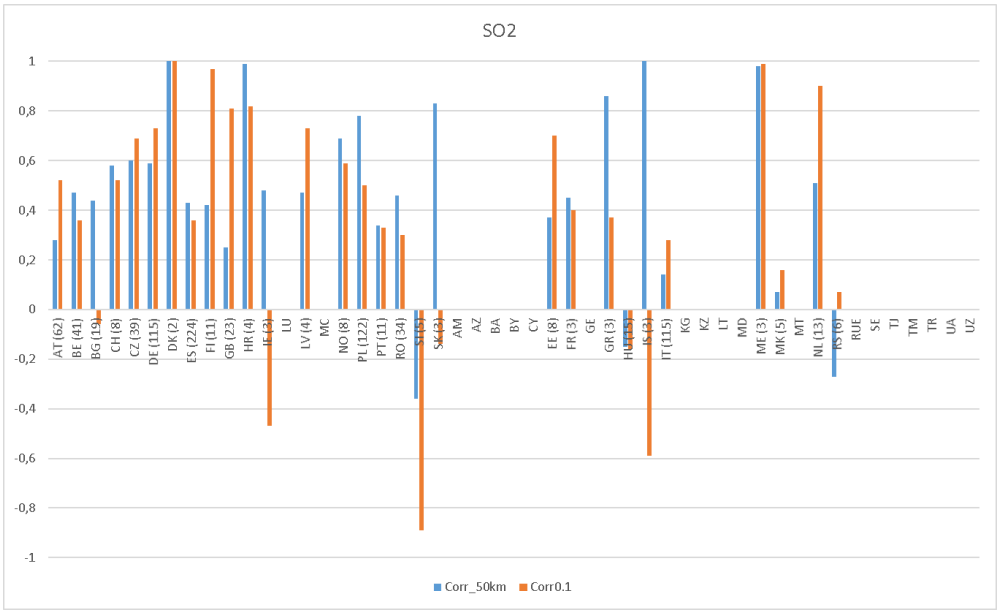

(a) SO_2

Figure 4.3: Spatial correlation coefficient for annual averages of model results (50×50km^2 and $0.1\times0.1^\circ$, 34 vertical layers) versus Airbase observations for NO_2. The number of stations used in the comparison for each country is given in parentheses. The countries AT to SK reported new gridded emissions.

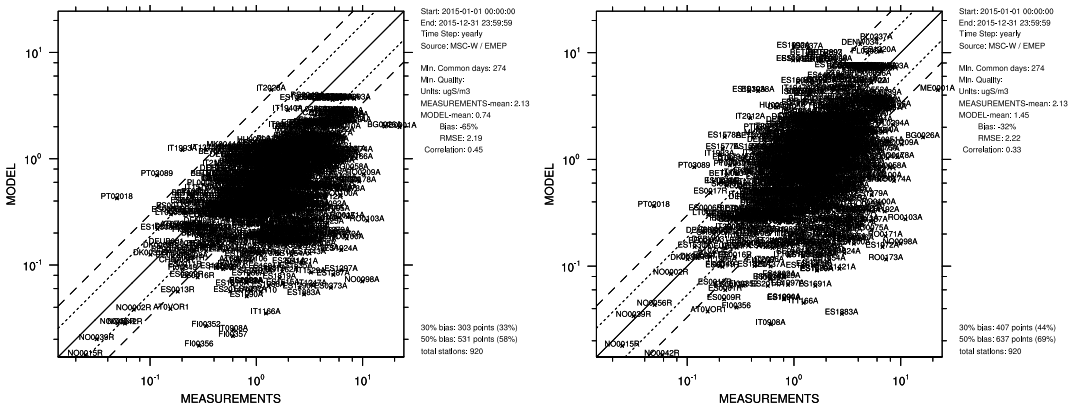

(a) rural+urban, 50×50km^2

(b) rural+urban, $0.1\times0.1^\circ$

(c) rural, 50×50km^2

(d) rural, $0.1\times0.1^\circ$

Figure 4.4: Comparison of $EMEP_{50km}$ and $EMEP_{0.1}$ to Airbase data for SO_2 (towards only rural measurements and all (rural + urban) Airbase measurements).

SO_2

Because the emission sources of SO_2 to a large extent are higher level sources (not surface based), the correlation of emissions and surface concentrations is less evident than for NO_x. From Figure 4.3 it can be seen that the results for SO_2 are indeed mixed (also when comparing to only rural or urban sites, not shown). For some countries, like Finland, Great Britain or the Netherlands, the correlation improves a lot. For other countries, like Bulgaria, Poland, Slovenia, Slovakia or Greece, the correlation decreases considerably. When compared to all Airbase (rural + urban) measurements, the spatial correlation actually decrease, while when compared to only rural Airbase measurements, the bias and spatial correlation improves somewhat (Figure 4.4). It is difficult to explain why the results vary so much without going into details for each country (looking at where the measurements sites are situated, which grid cells the large emissions sources are allocated to etc.).

4.4 Comparison to Airbase and EMEP data; secondary components

Ozone

The model results have been compared with ozone monitoring data from the EMEP data base (EBAS) and Airbase. This included of the order of 150 EMEP sites, 500 rural Airbase sites and 1200 urban and suburban Airbase sites. The traffic sites were not included in the analyses. Stations located higher than 1000 m asl were not included in these plots to avoid problems with model data in complex terrain.

The country based bar plots (Figure 4.5) and the scatter plots (Figure 4.6) all show systematically better agreement with the measured annual mean concentration for the $EMEP_{0.1}$ compared to the $EMEP_{50km}$. This applies to the rural Airbase data as well as the urban Airbase data (Figure 4.6). The bias is smaller and the correlation coefficient is higher, except for a very few countries. This is in line with the results seen for NO_2 which is to be expected since the annual mean ozone concentration is likely closely linked to the annual mean NO_2 through the local titration effect.

This is further confirmed by the fact that the degree of change in performance for ozone going from one model to the other closely reflects that for NO_2 (Figure 4.1 vs Figure 4.5) for the individual countries. Large improvements in $EMEP_{0.1}$ relative to $EMEP_{50km}$ for the annual mean ozone is seen in Austria, Switzerland and Denmark and the same is seen for NO_2. Poland on the other hand show somewhat poorer performance for both NO_2 and O_3. One should be a bit careful with these simple relationships though, since the location of the O_3 sites not necessarily are the same as the NO_2 sites.

Thus, the general improvement in modelling the annual mean O_3 when taking Airbase data into consideration likely reflects the direct (titration) effect of the finer spatial resolution of the new emission data. For the rural EMEP data, however (Table 4.1), there is very little difference in the annual mean O_3 between $EMEP_{50km}$ and $EMEP_{0.1}$. This discrepancy between the results for the EMEP and the rural Airbase data likely reflects that the EMEP data in general are found at more clean locations and less influenced by local NO_x emissions than the rural Airbase sites. Several of the Airbase sites classified as rural were also classified as being near a city.

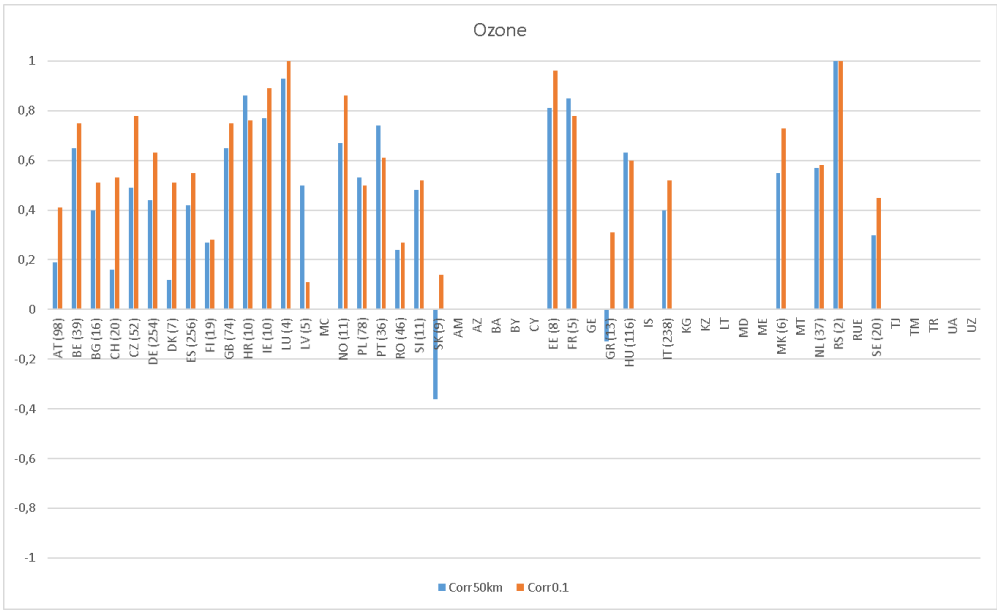

(a) O_3

Figure 4.5: Spatial correlation coefficient for annual averages of model results (50×50km^2 and $0.1\times0.1°$, 34 vertical layers) versus Airbase observations for ozone. The number of stations used in the comparison for each country is given in parentheses. The countries AT to SK reported new gridded emissions.

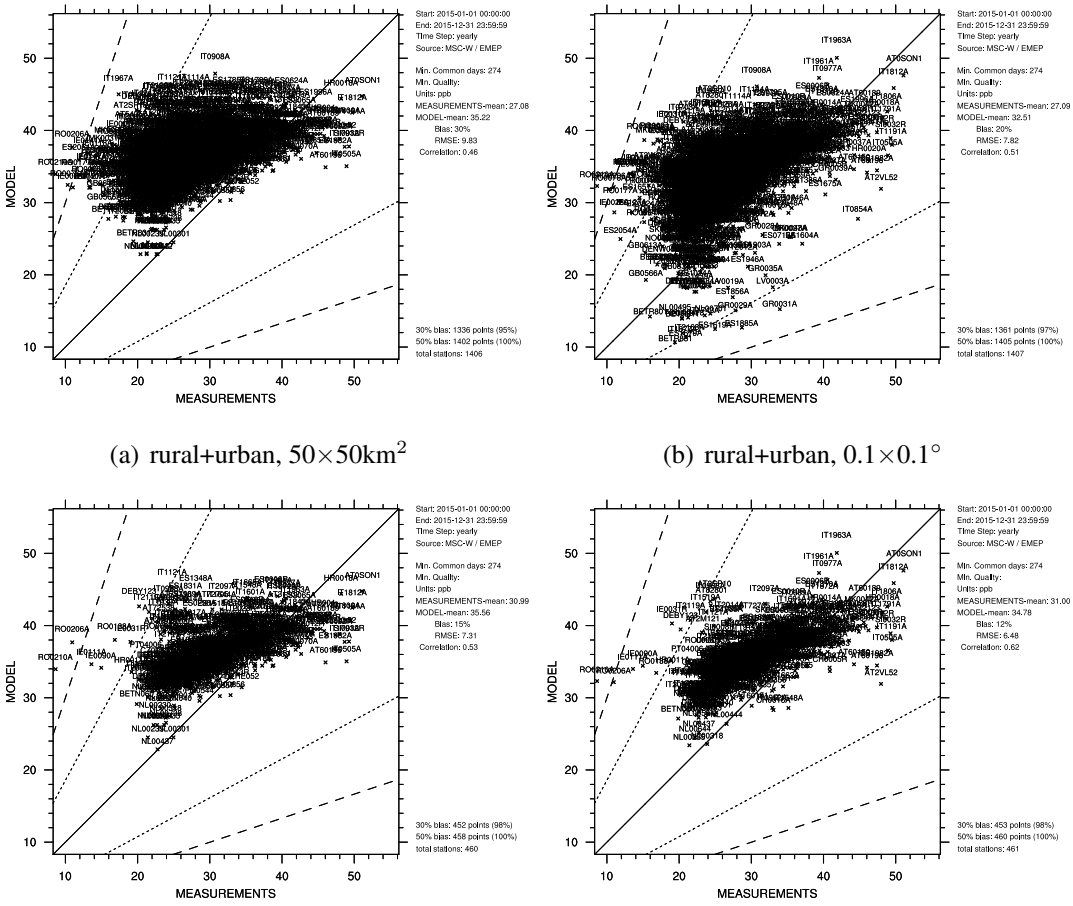

(a) rural+urban, 50×50km^2

(b) rural+urban, $0.1\times0.1°$

(c) rural, 50×50km^2

(d) rural, $0.1\times0.1°$

Figure 4.6: Comparison of EMEP_{50km} and $\text{EMEP}_{0.1}$ to Airbase data for yearly mean of O_3 (towards only rural measurements and all (rural + urban) Airbase measurements).

The better agreement for the annual mean ozone concentration in $\text{EMEP}_{0.1}$ compared to EMEP_{50km} is encouraging and confirms the positive effect of the finer resolution of the emission data. It furthermore gives confidence that the $\text{EMEP}_{0.1}$ model could be used to predict quantities related to long-term exposure (or deposition) on a better resolution and more correct than the EMEP_{50km} model.

The selection of ozone metric is, however, critical for this kind of model evaluation. Since ozone is controlled by a number of processes with strongly varying influences over the year, the annual mean concentration is of less relevance when evaluating the influence of photochemistry in general and the high ozone episodes in particular. In the following we are focusing on the ozone episodes and have thus based the evaluation on d8hMAX - the daily maximum running 8h mean concentration. This metric avoids the problems of modelling the night-time values that often are very locally determined (based on topography etc).

For each day in 2015 we calculated the d8hMAX for each station from the measured and modelled data. The model data were based on the grid square containing the station without any interpolation of neighbouring grid values. Furthermore, for each station we only used the hours with valid measurements, i.e. the model data were screened so that the statistics were based on exactly the same hours of the day as the observations to avoid any spurious results caused by missing data. Then, for each day through the year we calculated the spatial linear correlation coefficient (r) and the mean difference (modelled-observed) based on the modelled and measured d8hMAX values for all sites that day. By this procedure we got daily statistics for the model performance (correlation and bias) through all of 2015.

The daily statistics explained above were grouped into three observation based groups and the three model based groups. The three observational groups included i) EMEP rural, ii) Airbase + EMEP rural and iii) Airbase suburban + urban sites, respectively. The three model groups included EMEP_{50km}, $\text{EMEP}_{0.1}$ and $\text{EMEP}_{0.1_L20}$, respectively. Results showing the correlation and mean bias for these 3 x 3 combinations where the statistics are grouped in months by standard box-whisker plots are shown in Figures 4.7, 4.8 and 4.9.

The results show some general characteristics. Firstly, the EMEP rural monitoring data show better agreement with the model results than the combined Airbase + EMEP rural data. Secondly, the EMEP_{50km} results agree slightly better with the rural monitoring data than the $\text{EMEP}_{0.1}$ results except in winter when $\text{EMEP}_{0.1}$ is better (and when $\text{EMEP}_{0.1_L20}$ is even better when measured by correlation). The differences are not large, though. It should be noted, though, that for ozone, summer is the main season with consequences for human health and vegetation. For the Airbase suburban and urban data the EMEP_{50km} shows a considerably better correlation than the $\text{EMEP}_{0.1}$ whereas the bias is smaller in $\text{EMEP}_{0.1}$. Thirdly, the negative bias (underestimation) in summer for suburban and urban sites is considerably smaller in the $\text{EMEP}_{0.1_L20}$ compared to the $\text{EMEP}_{0.1}$. Finally, there is a systematic seasonal cycle in model performance in general: the correlation is highest in summer and lowest in spring, whereas the bias is negative (underestimation by the models) in summer and positive else in the year.

It should be stated that refining the spatial scale down to 0.1° is primarily expected to improve the calculation of the primary species (NOx, PM etc) whereas ozone is considered a large-scale regional issue. Thus, it's reassuring to see that the difference in model performance for the EMEP rural data is not large. That the models agree better with the EMEP rural data compared to the Airbase rural data is to be expected since the EMEP data in principle only includes rural background stations whereas the Airbase data contain some sites classified as near city (although still rural).

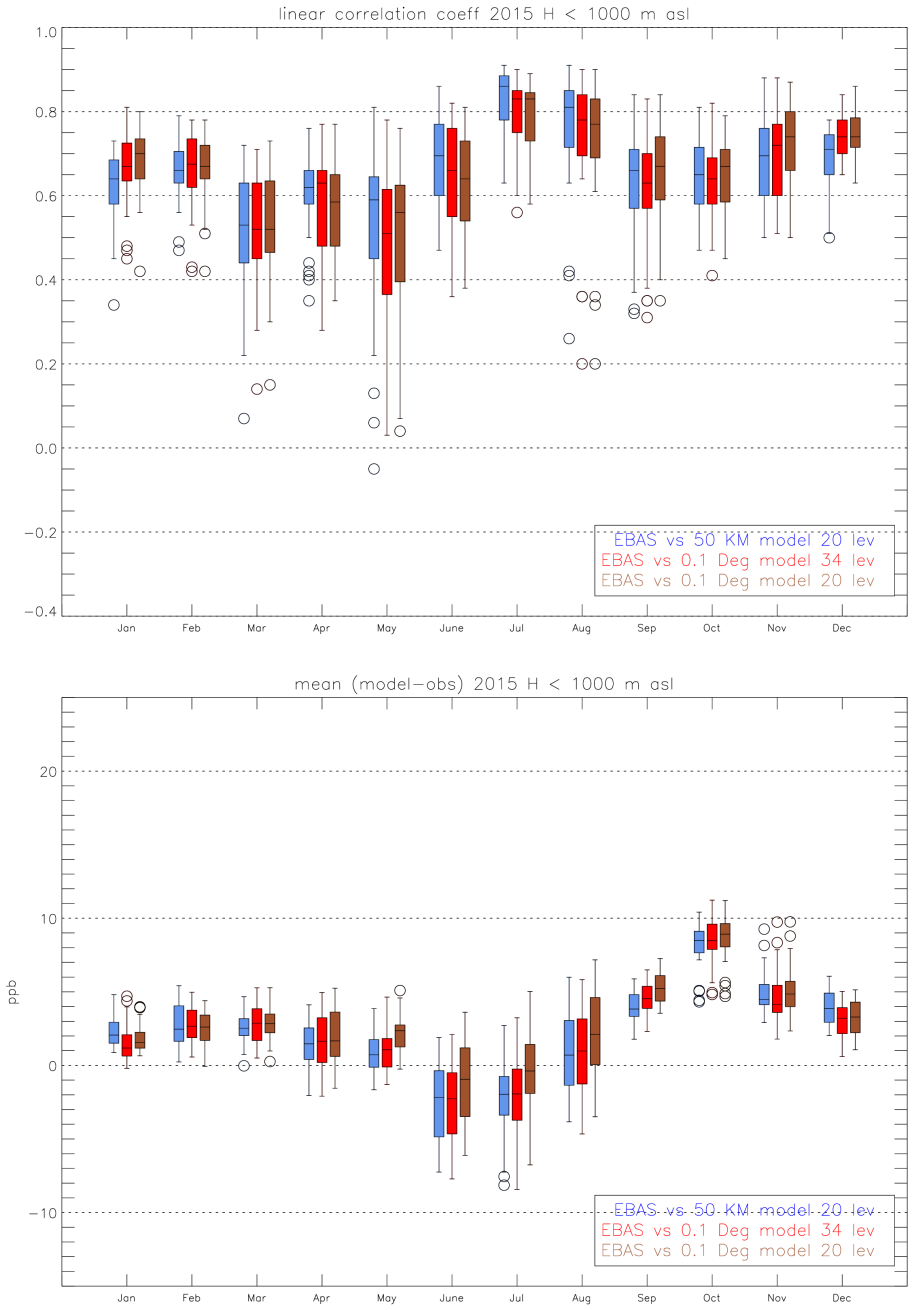

Figure 4.7: Box and whisker plots of the spatial linear correlation coefficient (r) and the mean difference based on EMEP rural ozone data (see text for details). The boxes enclose the 25 to 75 percentile and the whiskers extend out to the min and max values or to 1.5 times the 25 and 75 percentiles, if there is data beyond this range. Outliers are identified with circles. The median is indicated inside the box.

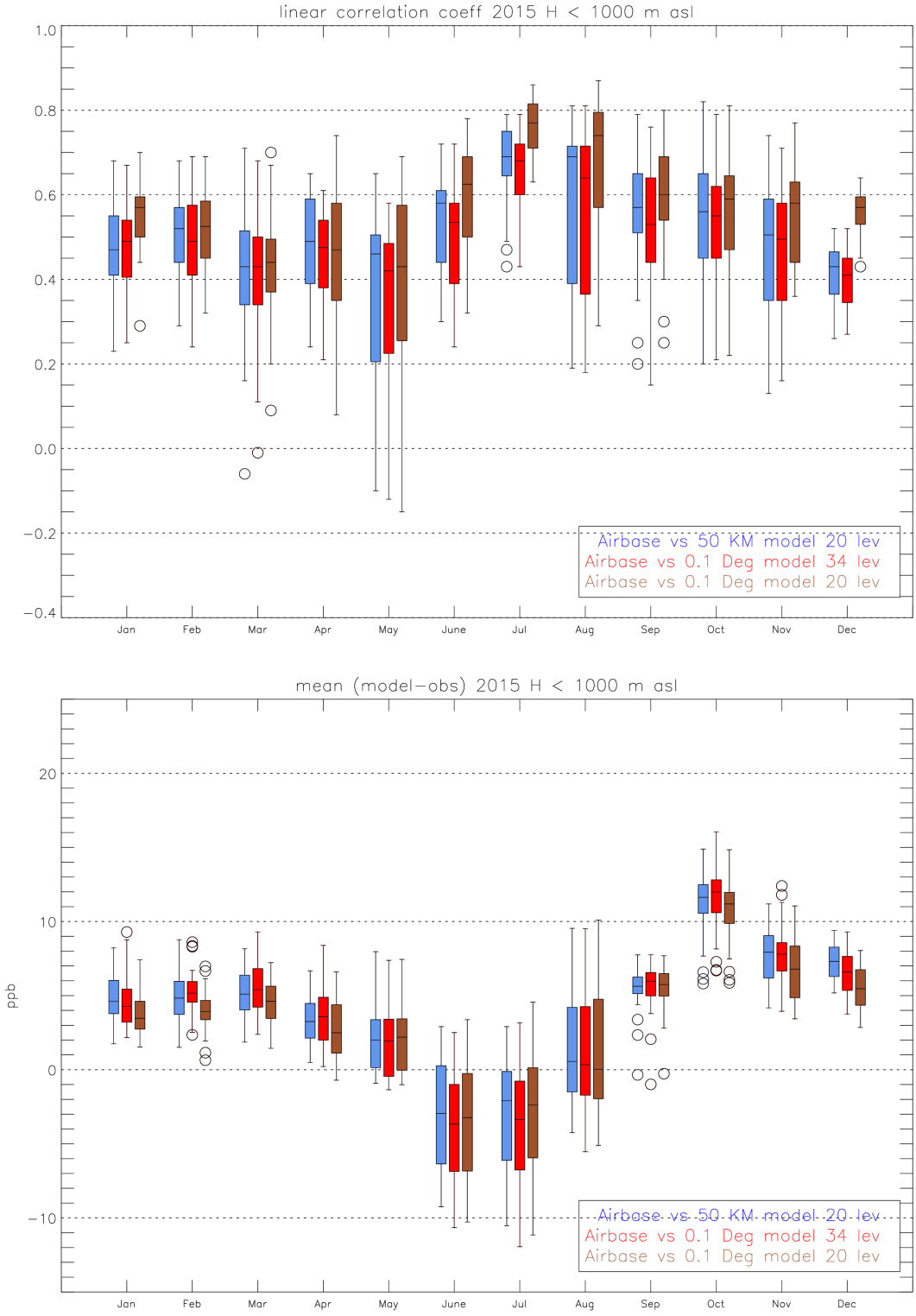

Figure 4.8: Box and whisker plots of the spatial linear correlation coefficient and the mean difference based on Airbase + EMEP rural ozone data.

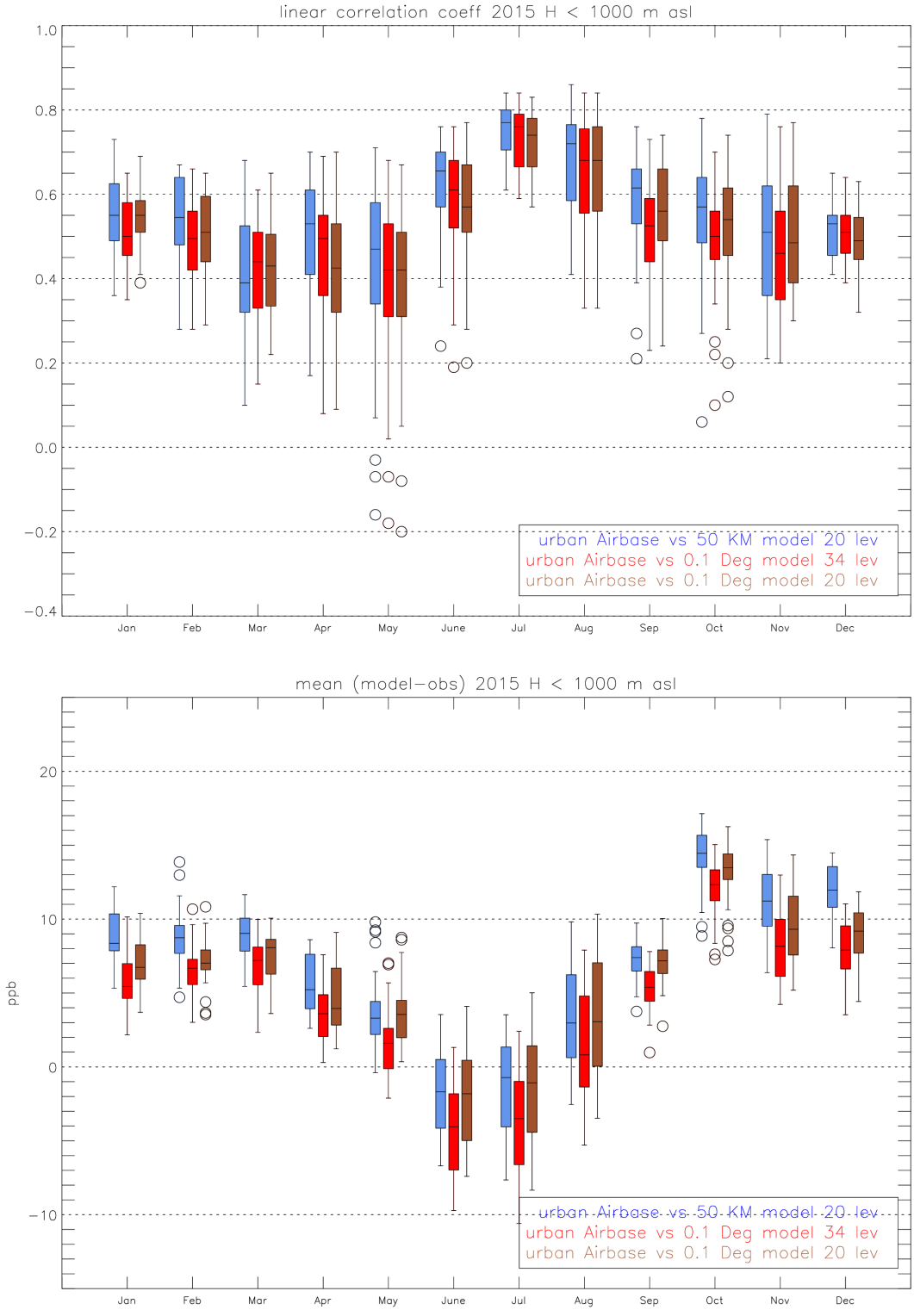

Figure 4.9: Box and whisker plots of the spatial linear correlation coefficient and the mean difference based on Airbase suburban and urban ozone data.

The differences in model performance for suburban and urban sites is, however, somewhat surprising as one would expect that the finer scale models ($EMEP_{0.1}$ and $EMEP_{0.1_L20}$) should perform better than the coarser $EMEP_{50km}$ at these sites. For the primary pollutants a clear improvement in model agreement (spatial correlation) is seen, as discussed above. On the other hand, the main episodes associated with high levels of primary pollutants are very different to the main episodes of elevated ozone and a range of processes could be the reason for the somewhat poorer model performance for the lat x lon model compared to the $EMEP_{50km}$ for ozone; VOC emissions (biogenic and anthropogenic), land use data, vertical resolution etc. The lower concentrations (as seen by the bias) in the $EMEP_{0.1}$ having 34 layers is likely caused by the stronger titration in that model due to the finer vertical resolution.

The marked seasonal pattern in model performance is partly as expected. We do expect a better performance in summer since ozone is to a larger extent controlled by internal emissions and photochemistry in summer as opposed to other seasons when boundary conditions and intercontinental transport processes become more important. The systematic underestimation of the ozone levels seen particularly in $EMEP_{0.1}$ as a negative bias in summer is somewhat worrying and is also seen when inspecting individual time series and maps (not shown here). That the negative bias in summer is considerably less in the $EMEP_{0.1_L20}$ compared to the $EMEP_{0.1}$ suggests that it could be worthwhile to look further into the vertical resolution and the boundary layer assumptions in the 34 layer model. It should be said that the model version using 34 layers is somewhat experimental for species that depends strongly on dry deposition such as ozone and that improvements in the vertical gradient algorithms may be required.

Summing up, one could say that this comparison has shown that the $EMEP_{0.1_L20}$ overall is the model that performs the best of these three model versions for ozone d8hMAX.

PM_{10} and $PM_{2.5}$

As expected, the comparison of the results from $EMEP_{50km}$, $EMEP_{0.1_L20}$ and $EMEP_{0.1}$ to EMEP background observations are relatively similar (Table 4.1). The spatial correlation for PM_{10} improves somewhat for the fine resolution runs compared to 50 km $\times$ 50 km resolution (from r=0.71 to r=0.74-0.76), while for $PM_{2.5}$ the changes in correlation is small. For both components the bias is smaller in the model run where the height of the lowest level is decreased ($EMEP_{0.1}$) compared to the other runs.

This comparison has been made based on daily measurement data with a requirement of 75% data coverage (or 274 days) and the corresponding scatter-plots can be found in Tsyro et al. (2017). Several sites measured PM less frequently e.g. performing weekly sampling, during the whole of 2015, and were not included in the evaluation results in Table 4.1 and Tsyro et al. (2017). In Figure 4.14 weekly PM measurements are also included in order to incorporate more sites (for example Northern Europe is better represented as two Norwegian sites are included), but overall the general pattern is the same as when using the reduced data set in Table 4.1.

Much more stations with PM measurements are incorporated in the Airbase database. This allowed comparison of the model results with PM observations in the individual countries and also separately at rural and sub-urban/urban sites.

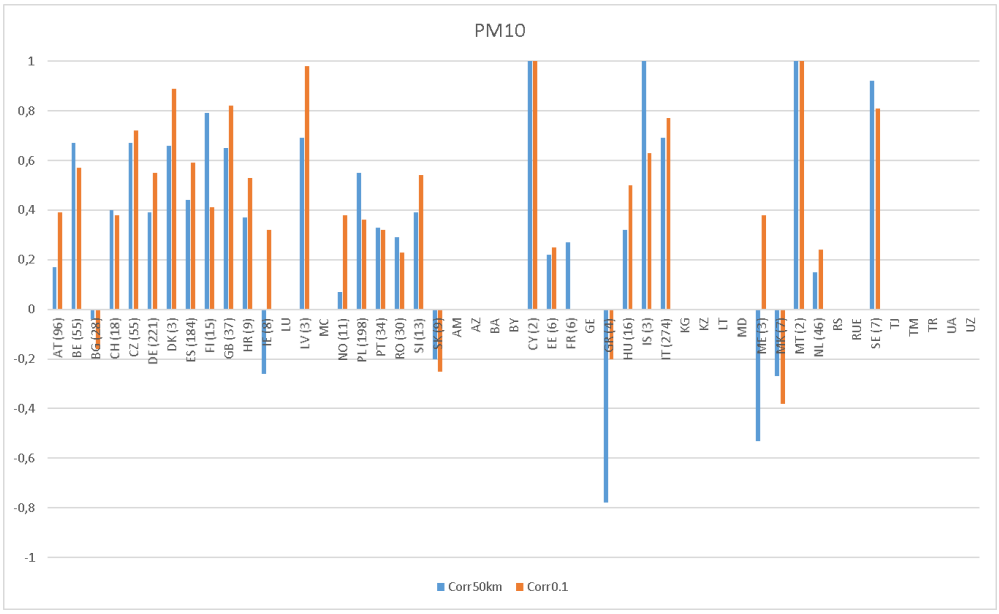

(a) PM_{10}

Figure 4.10: Spatial correlation coefficient for annual averages of model results (50×50km^2 and $0.1\times0.1^\circ$, 34 vertical layers) versus Airbase observations for PM_{10}. The number of stations used in the comparison for each country is given in parentheses. The countries AT to SK reported new gridded emissions.

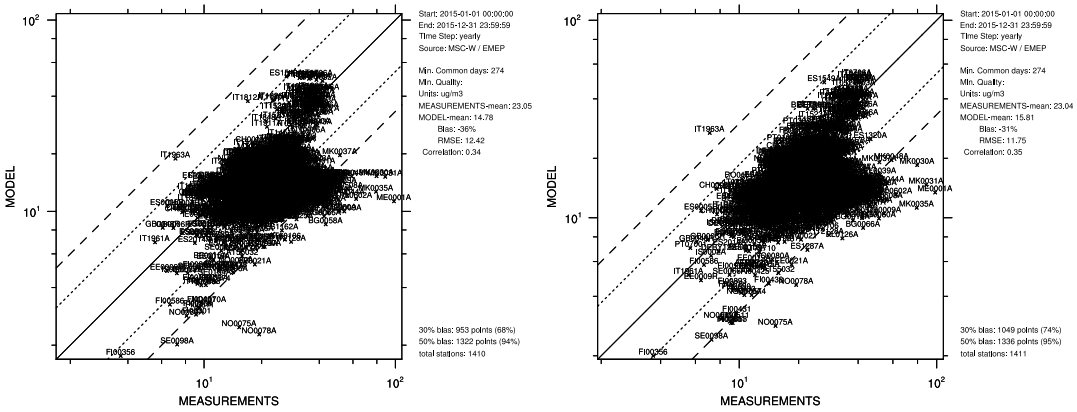

(a) rural+urban, 50×50km^2

(b) rural+urban, $0.1\times0.1^\circ$

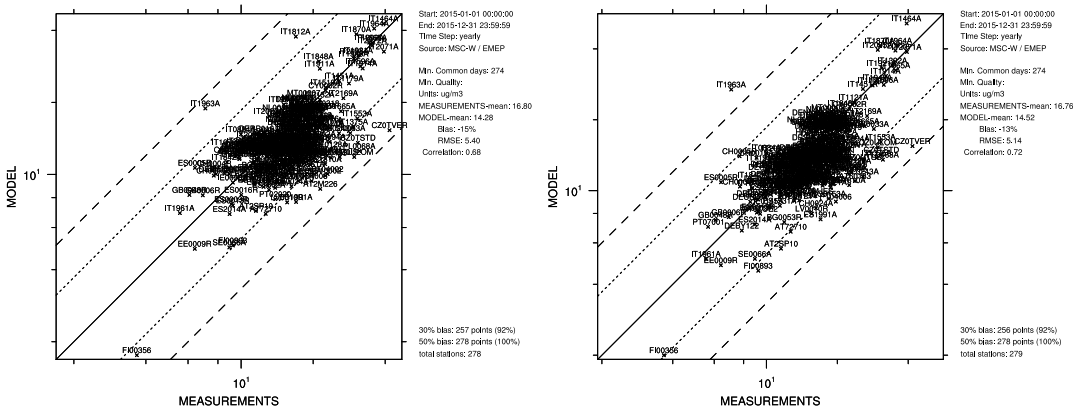

(c) rural, 50×50km^2

(d) rural, $0.1\times0.1^\circ$

Figure 4.11: Comparison of $EMEP_{50km}$ and $EMEP_{0.1}$ to Airbase data for yearly mean of PM_{10} (considering only rural measurements and all (rural + urban) Airbase measurements).

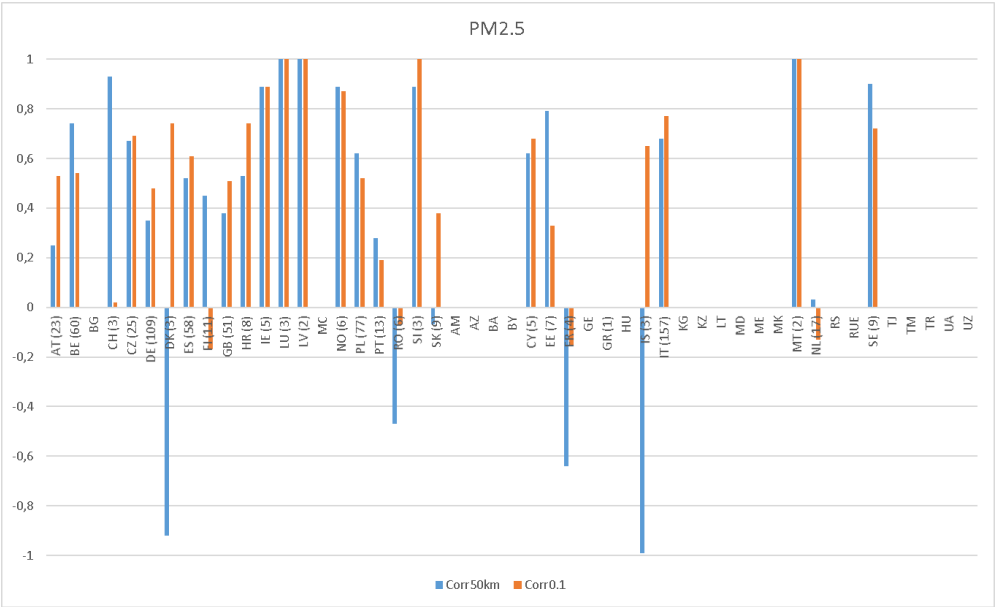

(a) $PM_{2.5}$

Figure 4.12: Spatial correlation coefficient for annual averages of model results (50×50km^2 and $0.1\times0.1^\circ$, 34 vertical layers) versus Airbase observations for $PM_{2.5}$. The number of stations used in the comparison for each country is given in parentheses. The countries AT to SK reported new gridded emissions.

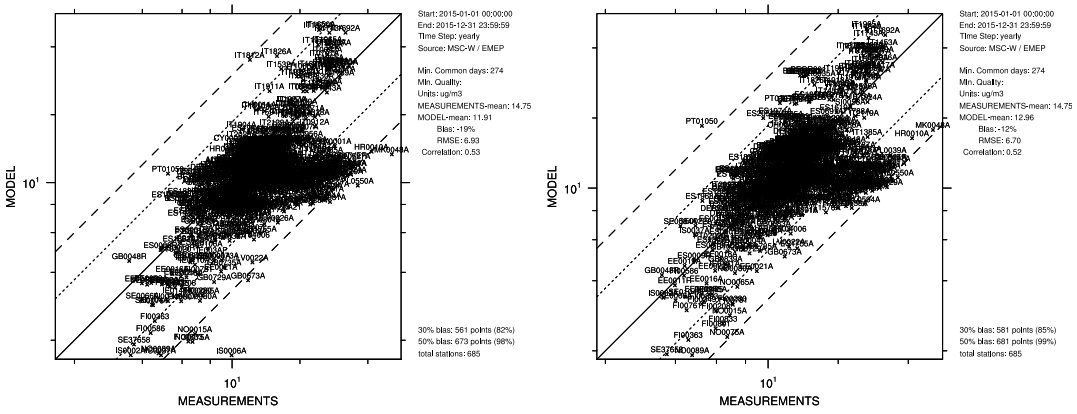

(a) rural+urban, 50×50km^2

(b) rural+urban, $0.1\times0.1^\circ$

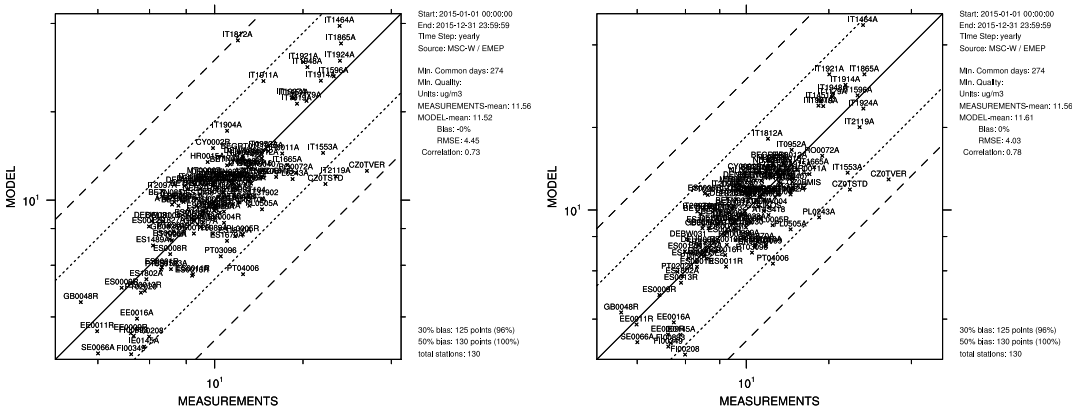

(c) rural, 50×50km^2

(d) rural, $0.1\times0.1^\circ$

Figure 4.13: Comparison of $EMEP_{50km}$ and $EMEP_{0.1}$ to Airbase data for yearly mean of $PM_{2.5}$ (considering only rural measurements and all (rural + urban) Airbase measurements).

Averaged over all sites, we find decreases in the negative biases for PM_{10} and $PM_{2.5}$ in the $EMEP_{0.1}$ run compared to the $EMEP_{50km}$ run (Figures 4.11 and 4.13). As expected, the comparison to only rural stations are relatively similar for the different resolutions, and it is mainly when including also sub-urban/urban sites that the correlation and bias improves in the fine resolution run.

The PM_{10} concentrations produced in the $EMEP_{0.1}$ calculations show better agreement with Airbase observations in most of individual EU countries, both in terms of bias (not shown here) and spatial correlation (Figure 4.10) compared to the results from $EMEP_{50km}$. A certain improvement in terms of bias and correlation can also be seen for modelled $PM_{2.5}$, although the results are more mixed (Figure 4.12).

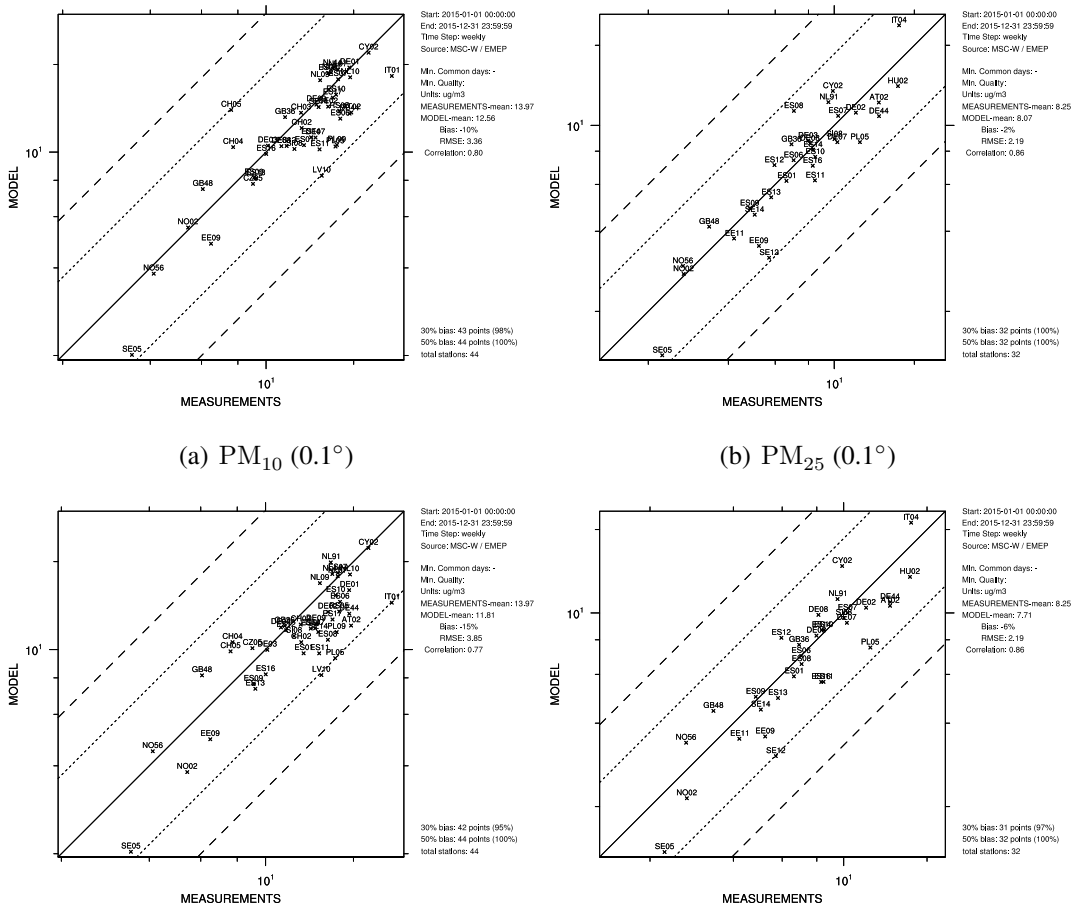

(a) PM_{10} (0.1°) (b) PM_{25} (0.1°)

(c) PM_{10} (50km) (d) PM_{25} (50km)

Figure 4.14: Scatter plots for PM_{10} and $PM_{2.5}$ for 2015: upper - the $EMEP_{0.1}$ run; lower - the $EMEP_{50km}$ run (based on weekly averaged data).The statistics are calculated based for annual mean modelled and measured concentrations.

Finally, we show the maps of exceedance days for PM_{10} and $PM_{2.5}$ derived from the $EMEP_{50km}$ calculation on Figure 4.15, which can be compared with the corresponding results from the $EMEP_{0.1}$ (Figure 2.9). The geographical pattern and the overall numbers are quite similar, but better resolved $EMEP_{0.1}$ run provides a more nuanced picture of PM exceedances.

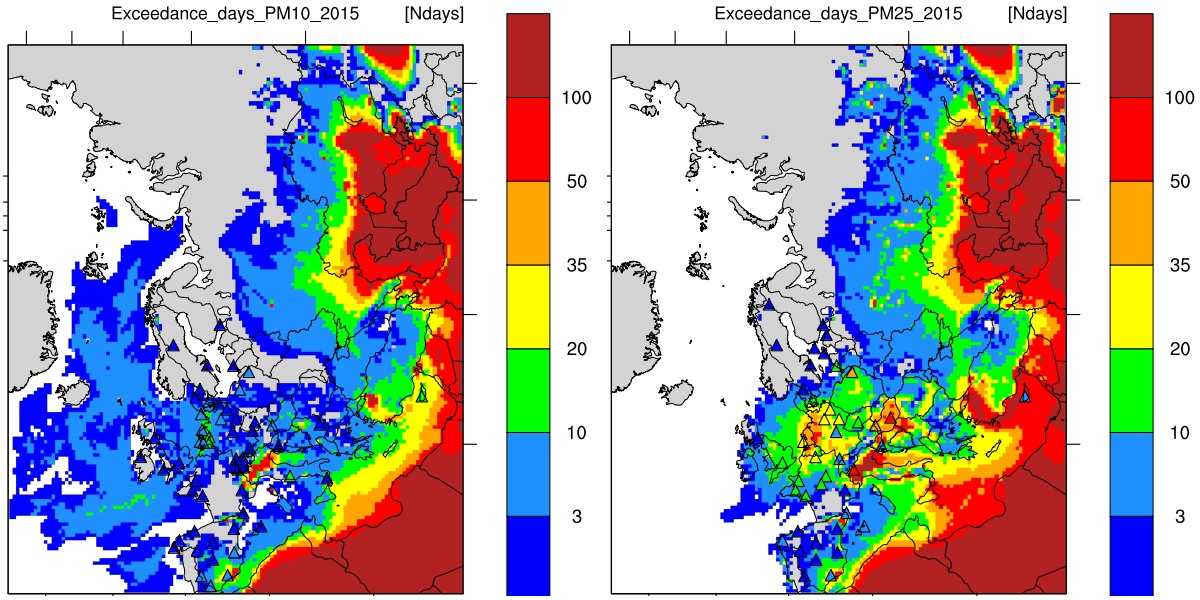

(a) PM_{10} (b) PM_{10}

Figure 4.15: Calculated with the $EMEP_{50km}$ setup and observed (triangles) number of days with exceedances in 2015: PM_{10} exceeding 50 μg m^{-3} (upper) and $PM_{2.5}$ exceeding 25 μg m^{-3} (lower).

4.5 Summary and conclusions

In this chapter we have compared three sets of model runs to EMEP and Airbase observations; the 'old' 50 km×50 km resolution model and two sets of 0.1°×0.1° resolution (20 vertical layers and 34 vertical layers, respectively). For NO_2, the model results on fine resolution are clearly improved, even on a country level, providing confidence in the new gridded emissions of NO_x. For SO_2, the results are more mixed. For some countries the spatial correlation improves a lot, while for other countries the correlation decreases considerably. It is difficult to explain why the results are so variable without going into details for each country, which have not been attempted here.

In general, the results for secondary components show less changes than the primary components when going down in scale. An interesting exception is the wet depositions of sulfate and nitrate where the spatial correlation improves notably. Some improvements in spatial correlation can be seen for PM_{10}, both when compared with EMEP and Airbase data, while for PM_{25} this is less clear. For both PM_{10} and PM_{25}, the bias between model results and measurements becomes somewhat smaller in the fine scale calculations (around 0%), partly related to the decrease of height of the lowest model layer.

The modelled annual mean of ozone show better spatial correlation towards both EMEP and Airbase measurements for the fine scale model runs, even on a country level. The general improvement in modelling the annual mean O_3 likely reflects the direct (titration) effect of the finer spatial resolution of the new emission data. It furthermore gives confidence that the $EMEP_{0.1}$ model could be used to predict quantities related to long-term exposure (or deposition) on a better resolution and more correct than the $EMEP_{50km}$ model.

For the ozone metric d8hMAX (the daily maximum running 8h mean concentration) the results are more mixed, but showing that $EMEP_{0.1_L20}$ overall is the model that performs the

best of these three model versions. The latter result indicates that it would be worthwhile looking further into the vertical resolution definitions and the boundary layer assumptions in the fine resolution model.

References

Tsyro, S., Gauss, M., Hjellbrekke, A.-G., and Aas, W.: PM10, PM2.5 and individual aerosol components, Supplementary material to EMEP Status Report 1/2017, available online at www.emep.int, The Norwegian Meteorological Institute, Oslo, Norway, 2017.

CHAPTER 5

Local Fractions in the EMEP MSC-W model

Peter Wind and Bruce Rolstad Denby

5.1 Introduction

In the 2016 EMEP report (Denby and Wind 2016) a methodology was described concerning the subgrid downscaling of EMEP gridded concentrations, called "urban EMEP" or "uEMEP". The methodology consists of essentially two parts. The first is to determine the contribution of local emissions, from each individual EMEP grid, to the local and surrounding grid concentrations, called the "Local Pollutant". The second part makes use of this information to redistribute the locally generated pollutant to subgrids within each EMEP grid. In this chapter we will describe the first part of the uEMEP methodology more in detail, as this has been further developed to be more generally applicable and to provide additional information concerning source contributions from regions surrounding any grid cell at little extra computational cost.

We define a "Local Fraction", as the fraction of a pollutant originating from a particular source in a specific grid. The purpose of calculating this new quantity in the model is threefold:

- Downscaling. As shown in the uEMEP project (Denby and Wind 2016), a distinction between background and locally produced pollutants, opens the way to a consistent description of fine scale/urban processes in a background of long-range transported pollutants.
- Improved modelling. The knowledge of the origin of a pollutant can be used for refining the description of different processes. For instance the vertical profile of a background pollutant would typically be decreasing closer to the surface, while the opposite can be expected if the pollutant is emitted locally. Also when emissions are not evenly distributed, as is the case for roads and point sources, the chemical composition can

have strong local gradients at the subgrid scales. To model the associated non-linearities a distinction between locally produced and background concentrations is a prerequisite.

- Local source-receptor maps. Local fractions can be computed for a large number of different sources; as will be shown below, several sources in every gridcell can be traced. This allows the production of local source-receptor maps "on demand" in one single run.

The first two applications are related to the subgrid redistribution modelling which will not be discussed further. In this chapter we will focus on the last application.

5.2 Calculation of Local Fractions

We define our Local Fractions (Lf), as a number between zero and one, given by the fraction of a pollutant which has its origin in a particular source in a specific grid labeled s:

$$Lf_s = \frac{\text{Local Pollutant (s)}}{\text{Total Pollutant}} = \frac{Lp_s}{Tp} \tag{5.1}$$

Where Total Pollutant is abbreviated Tp. What is actually included in the Local Pollutant (Lp), will be described below. In a time splitting framework the different physical processes are included sequentially, and we will show how the Local Pollutants vary during each of them.

5.2.1 Emissions

The Local Pollutant and Local Fraction can be associated with a particular emission source (E_s) in a specific grid and will increase accordingly (for simplicity we do not display the parameters associated with position):

$$Lp_s(t + \Delta t) = Lp_s(t) + E_s(t)\Delta t \tag{5.2}$$

$$Lf_s(t + \Delta t) = \frac{Lp_s(t + \Delta t)}{Tp(t + \Delta t)} \tag{5.3}$$

For instance s could refer to emissions of particulate matter from sector 7, Tp would be the total concentration of particulate matter, and Lf_s would then represent the fraction by which the total concentrations would be reduced if the emissions from sector 7 would be removed (assuming linearity).

5.2.2 Advection

So far only one gridcell has been considered. Transport of pollutants will mix pollutants from different origins. We will trace the Local Pollutant from every horizontal gridcell separately. We need then two sets of position indices, one for the origin and one for the actual position:

$$Lf_{s,x_s,y_s}(x, y, z, t) \tag{5.4}$$

Where x_s and y_s are the horizontal coordinate of the source, and x, y and z are the actual coordinates of the pollutant. For large grids, this would represent a very large amount of data.

One key point to keep the calculation at a reasonable cost, is to limit x_s and y_s to be within a preset distance of the source:

$$Lf_{s,\Delta x_s,\Delta y_s}(x,y,z,t) \tag{5.5}$$

Where Δx_s and Δy_s are the distances to the source.

If we consider a flux of pollutant, $F(x,y,z,t)$ (assumed positive), from a gridcell x to $x+1$, the Local Pollutant at $x+1$ will vary according to

$$Lp_{s,\Delta x_s,\Delta y_s}(x{+}1,y,k,t{+}\Delta t) = Lp_{s,\Delta x_s,\Delta y_s}(x{+}1,y,z,t){+}F(x,y,z,t)Lf_{s,\Delta x_s+1,\Delta y_s}(x,y,z,t) \tag{5.6}$$

The local fractions are then updated according to 5.1

$$Lf_{s,\Delta x_s+1,\Delta y_s}(x+1,y,z,t) = \frac{Lp_{s,\Delta x_s+1,\Delta y_s}(x+1,y,z,t+\Delta t)}{Tp(x+1,y,z,t+\Delta t)} \tag{5.7}$$

The fluxes and Total Pollutants, are not explicitly dependent on the source s, and are normally available quantities in the model.

If the flux is exiting the gridcell x, the local fractions at x do not have to be updated, since it can be assumed that the same fraction of Local and Total pollutants are removed.

5.2.3 General expression

The general formula for the update of the Total Pollutant is:

$$Lp(t+\Delta t) = Lp(t) + \sum_{X_v} \frac{\partial Lp}{\partial X_v}\frac{\partial X_v}{\partial t}\Delta t \tag{5.8}$$

Where the X_v are the variables that influence the pollutants, and $\frac{\partial Lp}{\partial X_v}$ represent the sensitivity of the Local Pollutant to that variable. For instance in 5.6 $\frac{\partial X_v}{\partial t}\Delta t$ would be the flux, and the sensitivity is translated to $Lf_{s,\Delta x_s,\Delta y_s}(x,y,z,t)$.

5.2.4 Diffusion

For diffusion, it would be possible to use the formula 5.8 but since diffusion is relatively inexpensive to calculate, it is simpler to compute the effect of diffusion directly on every Local Pollutant:

$$Lf_{s,\Delta x_s,\Delta y_s}(x,y,:,t+\Delta t) = \frac{\text{Diffusion}(Lp_{s,\Delta x_s,\Delta y_s}(x,y,:,t))}{\text{Diffusion}(Tp(x,y,:,t))} \tag{5.9}$$

Where “Diffusion()” is the numerical operator that computes the diffusion in the model and the colon ’:’ indicates its operation over the entire vertical grid column. This ensures a consistent treatment of the Local Fractions, whatever numerical procedure is applied for the diffusion.

5.2.5 Deposition

For deposition, we can assume that the same fraction of Local and Total pollutants are removed. Therefore the Local Fractions will not vary during the deposition process:

$$Lf^{\text{deposition}}(t + \Delta t) = Lf(t) \tag{5.10}$$

In the future we may adapt the deposition velocities to the values of the Local Fractions, but this is not the case in the current version of the model.

5.2.6 Chemistry

To fully follow the pollutants through all the chemical reactions would, in principle, require a reference to all the sources and grids independently. It is possible to reduce the size of the problem if linearity is assumed. This has been done by other groups, see for instance (Kranenburg et al. 2013). The description of all the chemical reactions is the most computation intensive part of the EMEP MSC-W model. A consistent chemical treatment of Local Pollutants, would require to almost multiply this time by the number of Local Pollutants considered, i.e. the size of $(s, \Delta x_s, \Delta y_s)$. In order to keep the calculation at an affordable cost, we will in this version limit the description to a few pollutants, where the Local Fractions are not (or little) modified by chemical processes: Primary Particles, NH_3 NO_x and SO_x. As we will show in the next section, even if the NH_3, NO_x and SO_x are heavily involved in chemical reactions, the local fractions remain relatively constant.

5.2.7 Computational aspects

The transformation involved for the calculation of local fractions as presented above, are all relatively simple. The most calculation intensive parts of the model (calculation of fluxes, chemical transformations, deposition processes) are not explicitly performed for every Local Pollutant, but only once for the total concentrations. This also means that there are no fundamental changes in code involved, only a few updates of Local Fractions to include. Storing all the Local Fractions is memory demanding; however the data is distributed among the compute nodes, meaning that it is possible to increase the available memory by increasing the number of nodes. Calculation of the Local fractions only needs information from the nearest neighbors and are therefore well suited for parallelization. At present in our implementation, writing the Local Fractions results to disc is not done efficiently and may in some cases take most of the time. If only average results over the entire run are required (instead of every hour) this is not a limitation.

The additional computation time will be proportional to the number of sources considered and the size of the local area. For instance a run over 5 days on 60 processors takes 80 seconds without the Local Fraction routines. If we include 14 different combinations of pollutants and sectors, and a local area of 21x21 gridcells the computation will take 440 seconds (of which 50 seconds are used to write out the results at the end of the run). If only the total for all sectors for 4 pollutants and an area of 11x11 is required, then the time is reduced to 116 seconds.

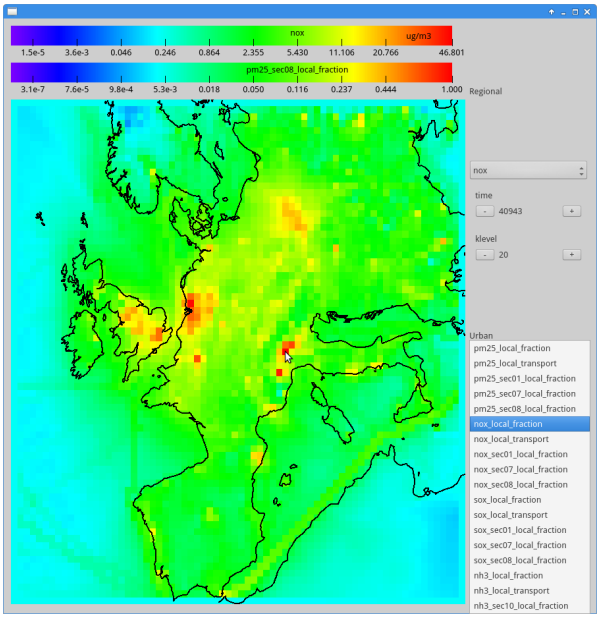

(a) NO_x concentrations. Any point on the map can be chosen with the cursor. On the right the sector and pollutant of interest for that point can be chosen

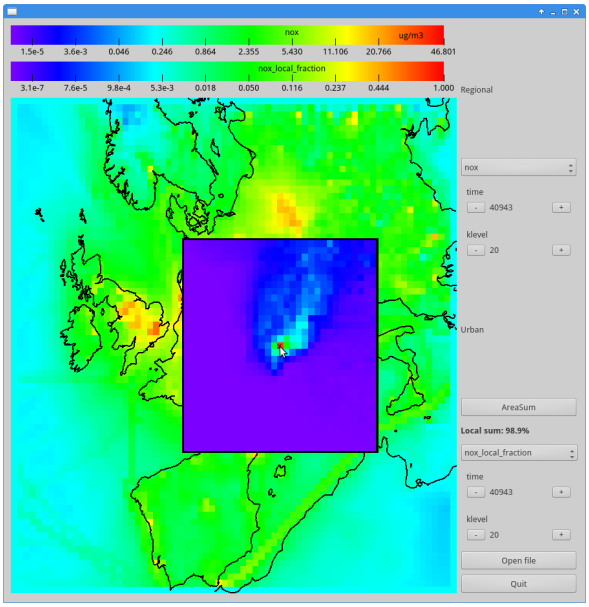

(b) Local Fractions of NO_x from all sectors, showing the origin of the pollutant

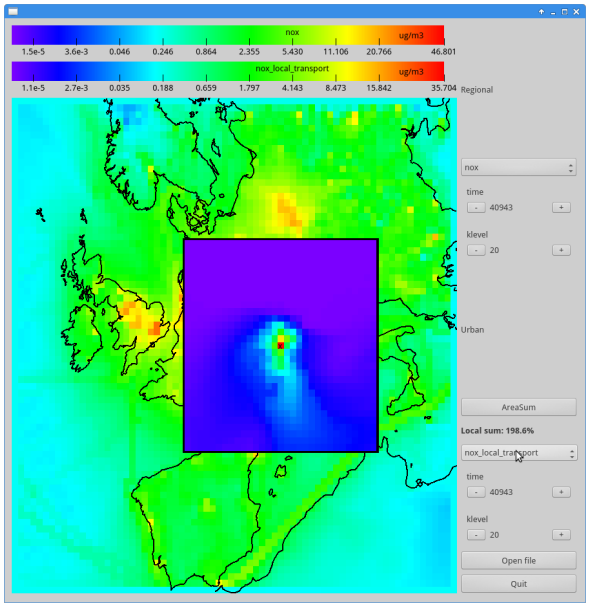

(c) Transport of NO_x *from* that point to the surrounding area.

Figure 5.1: Illustration of visualization tool. (b) Local Fractions centered at the chosen point, showing the fractions of NO_x coming from different sources *to* the chosen point. The sum of all the fractions accounts for 98.9% of the total NO_x concentrations at a that point. (c) Receptor map for pollutants emitted at the chosen point obtained by reversing the Local Fractions. This map can also be reproduced using the difference between two traditional runs with or without NO_x emissions at the reference point

5.3 Examples and validation

The focus in this section is to illustrate the results that can be obtained with the new method. Therefore some details concerning the exact description of the model setup (emissions, positions etc.) are omitted.

The model can produce the Local Fractions for different emitted pollutants ($PPM_{2.5}$, PPM_{coarse}, SO_x, NO_x or NH_3) and are also partitioned into individual requested sector categories. When Local Fractions are known for every gridcell, this information can be reversed to show the destination of the pollutants. A single model run will then give the contribution from (and to) *any* gridcell within a given distance around that gridcell. The size of this area can also be chosen.

It is difficult to show the results in a figure, as the data has too many dimensions (2 horizontal dimensions for the source, 3 dimensions for the receptor gridcell, time, sector and pollutant). A Python code has been made that allows visualization of these data interactively. A map of concentrations is given, and the user can click on the map to get a new map with the sources or destinations of one pollutant at that position. Figure 5.1 provides an example of what this tool can do.

In order to validate the new method, we compare two sets of runs:

- Results obtained by running the model twice and taking the difference of the concentrations. The second run being with emissions in the relevant gridcell removed. This is the more standard source receptor methodology ("SR method")
- Results obtained in one single run using the Local Fractions and Local Pollutants ("Lf method")

The advection scheme in the EMEP MSC-W model, is based on the fourth order Bott's scheme (Bott 1989). This scheme is non local and is not well suited to reproduce the changes in the immediate vicinity of emission changes. By this we mean that using the fourth order scheme will give a different result compared to a "tagging" method (for instance (Kranenburg et al. 2013)). For this reason all the runs shown in this section are performed using a simpler zero order advection scheme. In normal mode, the fourth order advection scheme is used, and the Local Fractions will make use of the actual fourth order fluxes and still give a consistent result. In this sense we can say that for the very short distances, the "Lf method" can be more accurate than the "SR method".

Figures 5.2 and 5.3 show a comparison of the results using these two methods. The "SR method" requires two runs for every emitter, while the "Lf method" give results for all emitters in one single run. Figure 5.2 compares the concentrations at the source gridcell, while Figure 5.3 shows the results in the twenty five gridcells surrounding Oslo.

The two methods show almost identical results. $PPM_{2.5}$ does not undergo any chemical transformation in the model. This demonstrates that the new method captures all the other processes, and the local pollutants are transformed in exactly the same way as the original pollutants.

Figure 5.4 shows a comparison between the "Lf" and "SR method" for NO_x in a region around Oslo. The local fractions correctly describe the trends, but some discrepancies can be observed. NO_x undergoes several chemical transformations. The Local Fractions assume that the Local fraction of NO_x is transformed in the same proportions as the total NO_x. Since the Local fractions can have a different mix of NO and NO_2, these will in reality lead to a shift in the chemical reactions which is not captured by the "LF method".

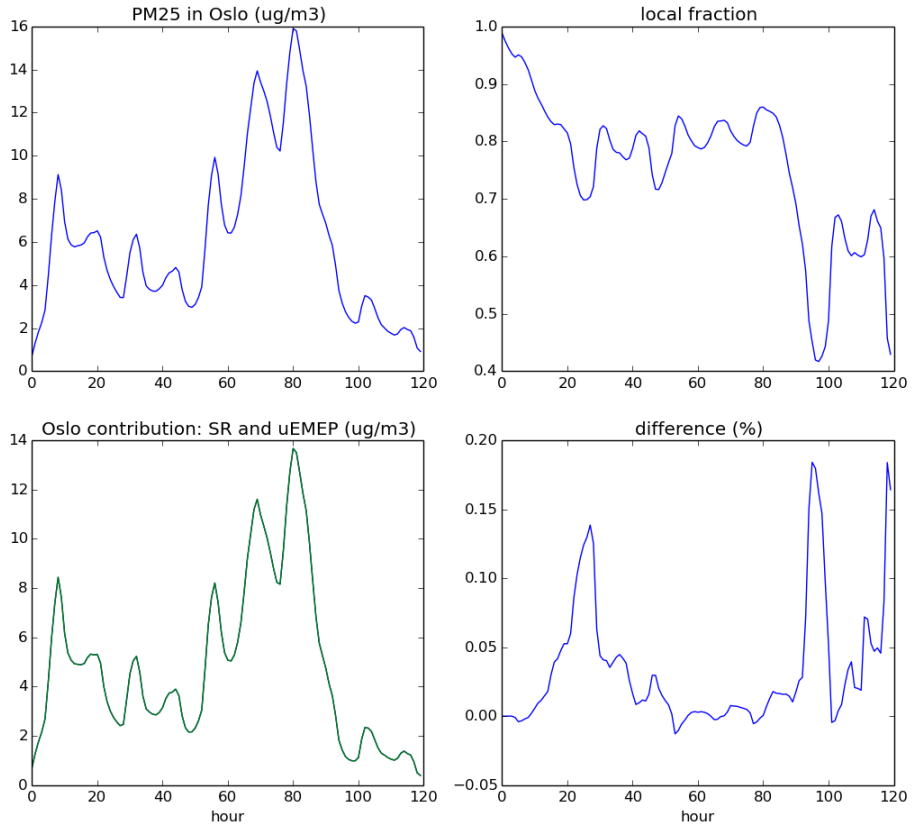

Figure 5.2: Concentrations of primary particles ($PPM_{2.5}$) in Oslo. 120 hours simulations in February. Upper left: absolute concentrations. Upper right: fraction with origin in the same gridcell. Lower left: in blue conventional difference between two runs ("SR method"), in green (superposed) new Local Fraction method ("Lf method"). Lower right: difference between the two methods.

Figure 5.5 shows a comparison between the "Lf" and "SR method" for NH_3 in a region in the Netherlands. Although NH_3 is involved in chemical reactions, these will transform Local and total NH_3 in the same proportions, and the resulting Local Fractions will be accurate.

5.4 Conclusions and future development

The calculation of local pollutants in the EMEP MSC-W model ("Lf method"), as described in this chapter, was initially intended to provide the required information for downscaling of concentrations used in the uEMEP subgrid redistribution method. However, further development of the "Lf method" has shown it can provide very similar information as more standard source receptor approaches ("SR method") but at a much lower computational cost. There are limitations concerning this method. Firstly the region around each grid cell where the calculation can be made is limited. Within this region it is possible to specify which source sector and which grid contributes to, or from, another grid but it is not possible to specify how much a specific grid source outside of this area contributes. This information is not calculated by the method. There is also a limitation concerning chemical processes as these are non-linear

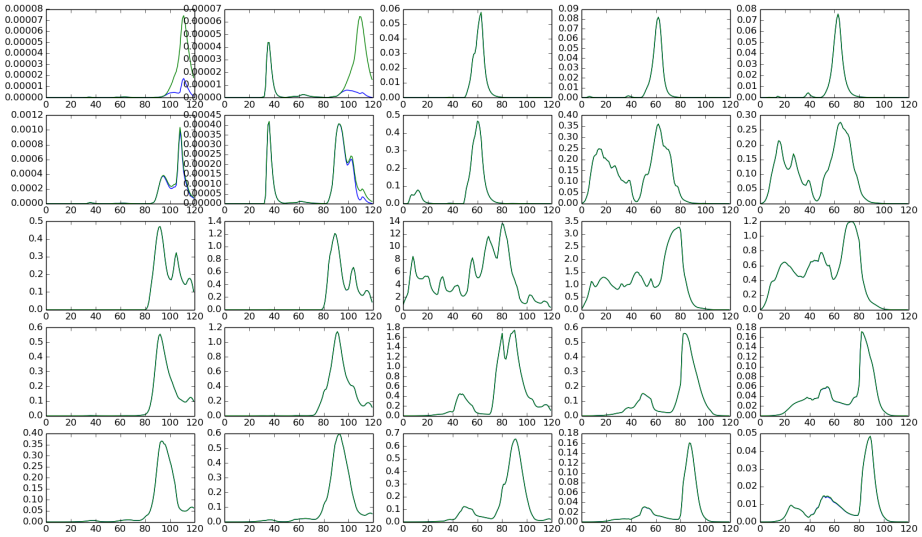

Figure 5.3: Concentrations of primary particles ($PPM_{2.5}$) in the 25 gridcells around Oslo (each panel corresponds to one gridcell, Oslo in the middle). 120 hours simulations in February. In blue conventional difference between two runs ("SR method"), in green new Local Fraction method

and this will require further development. If hourly concentrations and local fractions are to be calculated over large regions for several source sectors then this can also present a memory problem, slowing down the calculations. Further optimization of the method and its use is required.

The extent of the calculation grid used in the Lf method can be chosen by the user for any particular need. When the Lf method is used for subgrid downscaling then only a 3x3 grid is required, making the method very efficient. If the user is interested in determining the contribution of one nearby city, or cities, to a grid cell or region then the calculation grid needs to be large enough to include these cities and regions.

The development of a visualization tool provides an easily accessible visual impression of the source contributions around any grid cell. Further development of this tool is envisaged, such as online availability and the ability to define non-rectangular regions, e.g. city boundaries or regional borders, within which the source contribution calculation can be made.

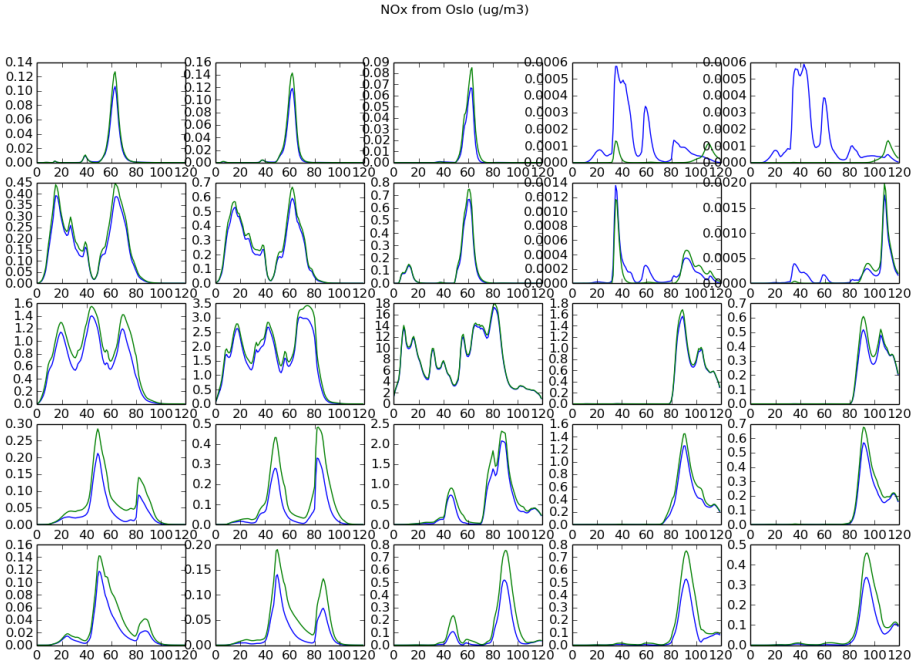

Figure 5.4: Concentrations of NO_x in the 25 gridcells around Oslo (Oslo in the middle). 120 hours simulations in February. In blue conventional difference between two runs ("SR"), in green new Local Fraction method ("Lf"). NO_x is here defined as NO + NO_2 in units of $\mu g/m^{-2}$ as NO_2

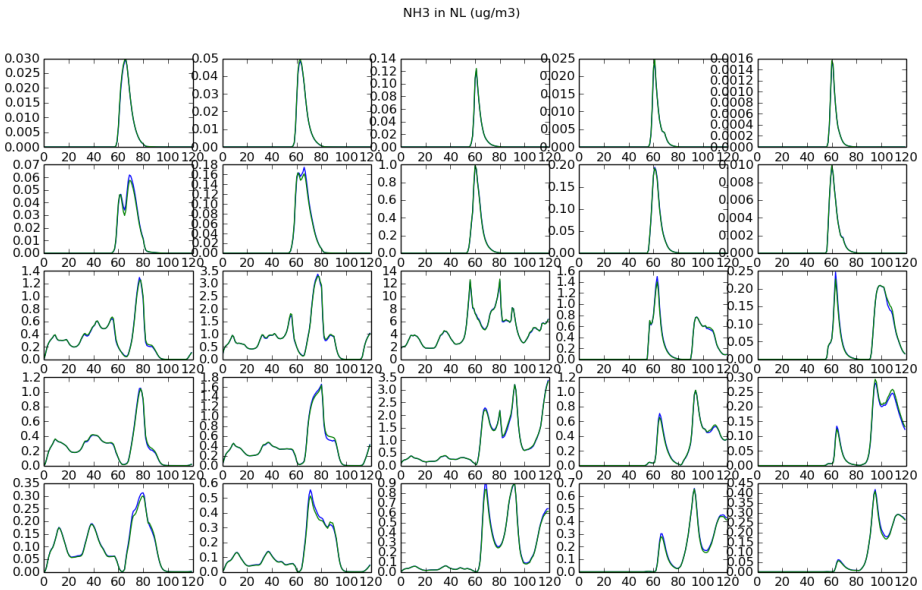

Figure 5.5: Concentrations of NH_3 in the 25 gridcells in the Netherlands (reference source in the middle). 120 hours simulations in February. In blue conventional difference between two runs ("SR"), in green new Local Fraction method ("Lf")

References

Bott, A.: A positive definite advection scheme obtained by non-linear re-normalization of the advection fluxes, Mon. Weather Rev., 117, 1006–1015, 1989.

Denby, B. and Wind, P.: Development of a downscaling methodology for urban applications (uEMEP), in: Transboundary particulate matter, photo-oxidants, acidifying and eutrophying components. EMEP Status Report 1/2016, pp. 75–88, The Norwegian Meteorological Institute, Oslo, Norway, 2016.

Kranenburg, R., Segers, A. J., Hendriks, C., and Schaap, M.: Source apportionment using LOTOS-EUROS: module description and evaluation, Geoscientific Model Dev., 6, 721–733, doi:10.5194/gmd-6-721-2013, 2013.

CHAPTER 6

Comparison of model calculations with ACSM data

Wenche Aas, Svetlana Tsyro, Maria Cruz Minguillón, Patrick Schlag, Laurent Poulain and Liine Heikkinen

6.1 Introduction

Information on particulate matter (PM) chemical composition is essential for source allocation and for investigating effects of PM on human health and on climate.

Within EMEP, PM chemical composition data has typically been based on off-line analysis and has a daily to weekly time resolution, as well as certain species (e.g. ammonium nitrate and organic carbon) are prone to sampling artefacts, causing biased concentrations. For a more accurate characterization of PM components within EMEP, and for an extended model evaluation and better understanding of the differences between calculated and observed levels, the need for "artefact-free" sampling and analytical methods that provide high time resolution data has been emphasised (Aas et al. 2012).

The last decade, high time resolution instruments less affected by artefacts have become available for the wider monitoring community. In particular, the Aerosol Chemical Speciation Monitor (ACSM, Aerodyne Inc.) is shown to be a robust instrument, suitable for long-term measurements at rural background sites, situated too far away for frequent maintenance. The ACSM provides high time resolved (30 min) information on the chemical composition of non-refractory submicron PM (PM_1), measuring concentrations of organic mass, nitrate, sulfate, ammonium and chloride (Ng et al. (2011), Fröhlich et al. (2013)). Lately also measurements of non-refractory $PM_{2.5}$ chemical composition have been made.

The European Research Infrastructure ACTRIS for the observations of Aerosol, Clouds, and Trace gases has been developing harmonised measurement procedures and protocols for the ACSM instrument, and data reporting guidelines for submitting these observations to EBAS (http://ebas.nilu.no/) has been defined, so that these measurements have now become available to a wider community.

In 2012, ACTRIS initiated a long-term (> 1 year) measurement period with ACSM instruments, coordinated with the EMEP intensive measurement periods in June 2012 and January 2013. However, the measurements with ACSM in Europe were not limited to this period and continued after 2013. Bressi et al. (2017) have presented an overview of aerosol particle chemistry from ACSM measurements from totally 20 sites with at least one year of measurements in the period from June 2011 to May 2015.

In this report, we focus on the years 2012 and 2013, and use data collected at four sites representative of rural/regional background in the Northern (FI0050 for March 2012-December 2013), mid-latitude (NL0044 for July 2012-July 2013 and DE0044 for June 2012-December 2013) and Southern Europe (ES1778 for June 2012-August 2013). At those sites, the measurements of particle chemical composition in a size fraction PM_1 were performed using same type of instrumentation (i.e. Q-ACSM as documented in Bressi et al. (2017)). The measurements from Cabauw (NL0044) and Montseny (ES1778) are also thoroughly discussed in studies by Schlag et al. (2016) and Minguillón et al. (2015).

This is the first attempt to use the ACSM data together with the EMEP MSC-W Model, and the aim is to investigate especially diurnal variations in the chemical composition of PM_1 at these four selected sites.

6.2 Results

6.2.1 Mean chemical composition

Concentrations and chemical composition of ambient PM varies widely, depending on size fraction and geographical location at the European continent (Putaud et al. (2010); Tørseth et al. (2012); Bressi et al. (2017)). Figure 6.1 presents observed and calculated mass of submicron non-refractory PM (NR-PM_1), i.e. the sum of SO_4^{2-}, NO_3^-, NH_4 and organic mass, averaged over 2012-2013 intensive measurement period (note that chloride is not included in this study as the model does not account for chloride chemistry). Figure 6.1 shows that the mean observed NR-PM_1 was highest at Melpitz (DE0044) in south-eastern Germany, closely followed by Cabauw (NL0044) in the Netherlands. The NR-PM_1 levels were somewhat lower in the north-east of Spain (ES1778), and the lowest NR-PM_1 concentrations were observed in southern Finland (FI0050). This is in accordance to the results presented by Bressi et al. (2017), whose study covers a longer time period (over 6 years for all considered sites). Model calculated 2-year average NR-PM_1 concentrations are quite close to the observed levels. The relatively larger model underestimation of NR-PM_1 at DE0044 and FI0050 was due to a significant underestimation of organic mass (OM). On the other hand, the model overestimated the secondary inorganic aerosol (SIA) components, except for FI0050. This SIA overestimation compensates to a large degree for the model's OM underestimation, causing the close comparability to the total NR-PM_1 mass.

The relative importance of SIA was highest in the Netherlands (almost 70%), where nitrate contributes with about 40% to the observed NR-PM_1 mass, as previously shown by Schlag et al. (2016). The model calculates approximately the same relative contribution of the SIA components (ca. 80%) and organic mass at Melpitz (DE0044) and Cabauw (NL0044), whereas the observations show that organic mass is more important at DE0044, contributing with 45% versus 32 % at NL0044. At the Spanish site Montseny (ES1778), the relative importance of organic mass is even higher (57% of observed NR-PM_1 mass), and whereas at

the Finnish site (FI0050), the NR-PM_1 is dominated by organic mass (67% of the observed NR-PM_1). These findings are in line with the extended dataset analysis by Bressi et al. (2017). Thus, the model is doing a good job calculating the relative composition of NR-PM_1 at FI0050 (though it underestimates the absolute concentrations). At the other sites, the modelled contributions of SIA components are over-predicted.

It should be noted that the measurements of nitrate with ACSM might include organic nitrate. Contribution of organic-nitrate to the nitrate signal is difficult to assess, as very few studies focused on this topics (Farmer et al. (2010); Schlag et al. (2016)). Organic nitrate is not accounted for in the model. Moreover, the discrepancy between measured and modelled sulfate at Cabauw might be related to the underestimation of the measured SO_4^{2-} due to calibration issues (Schlag et al. 2016).

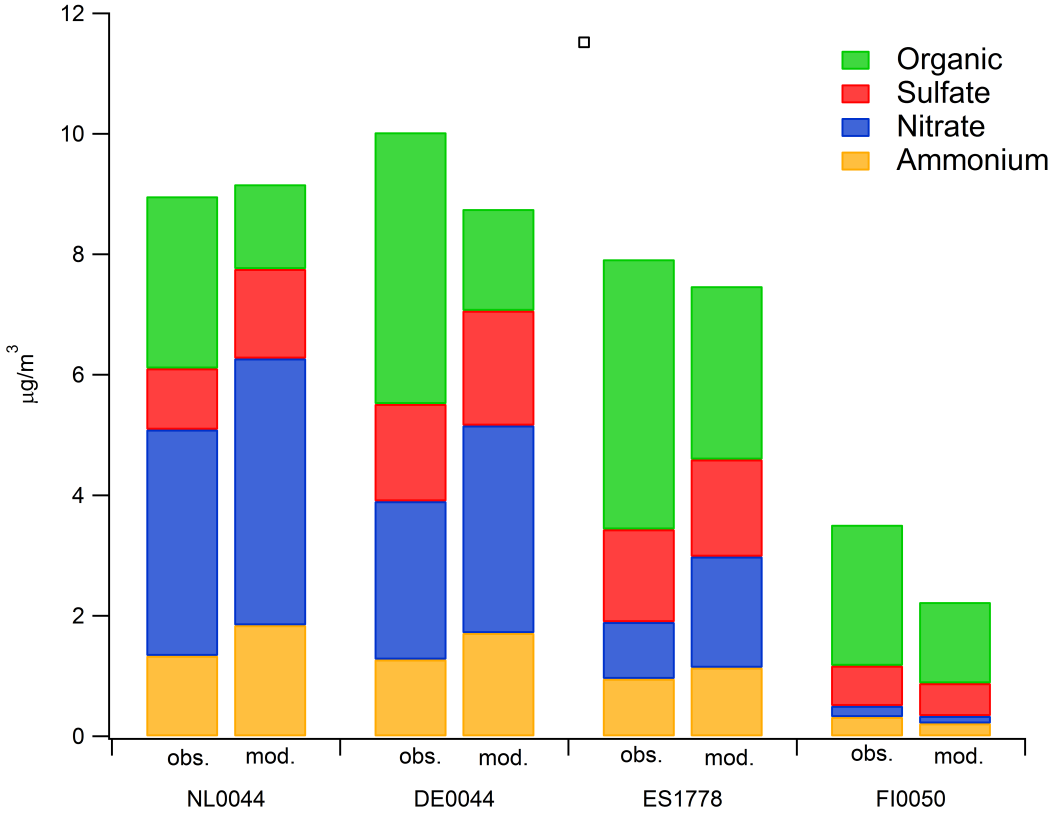

Figure 6.1: Measured (obs) and calculated (mod) chemical composition of non-refractive PM_1 over 2012-2013 intensive period.

6.2.2 Mean diurnal profiles

High time resolution ACSM measurements offer a good opportunity to study diurnal variations of PM_1 components, and facilitate the evaluation of the model's ability to reproduce those, which may give better insights in the accuracy of model calculations and indicate which further improvements are needed.

Figure 6.2 shows the measured and model results for diurnal variations of the main aerosol components. Similar patterns of diurnal profiles were observed at the Dutch (NL0044) and

German (DE0044) sites, with pronounced diurnal variation of NO_3^- and organic mass characterized by a minimum in the early afternoon and increased night-time levels. The model reproduced the observed variation patterns, though there are also some discrepancies. For instance, it accurately calculates the daytime NO_3^-, but over-predicts its night-time levels, which points to an over-production of NO_3^- aerosol during late evening/night hours and also to too weak pollutants dispersion at night/early morning. Higher night-time NO_3^- is commonly seen in regions with relatively high influence of NO_x emissions, favouring NO_3^- night-time production, whereas during daytime the volatility of ammonium nitrate increases. This is more pronounced during summer than winter, as seen in Figure 6.3 and discussed by Bressi et al. (2017), Schlag et al. (2016) and Poulain et al. (2011). Similar to NO_3^-, the levels of volatile organics drop during daytime due to their evaporation and rise during night due to VOC condensation (Bressi et al. (2017); Schlag et al. (2016); Poulain et al. (2011)). In addition, the reason for night-time elevated levels of organics can partly be attributed to domestic heating in the evenings, especially during winter (Figure 6.3).

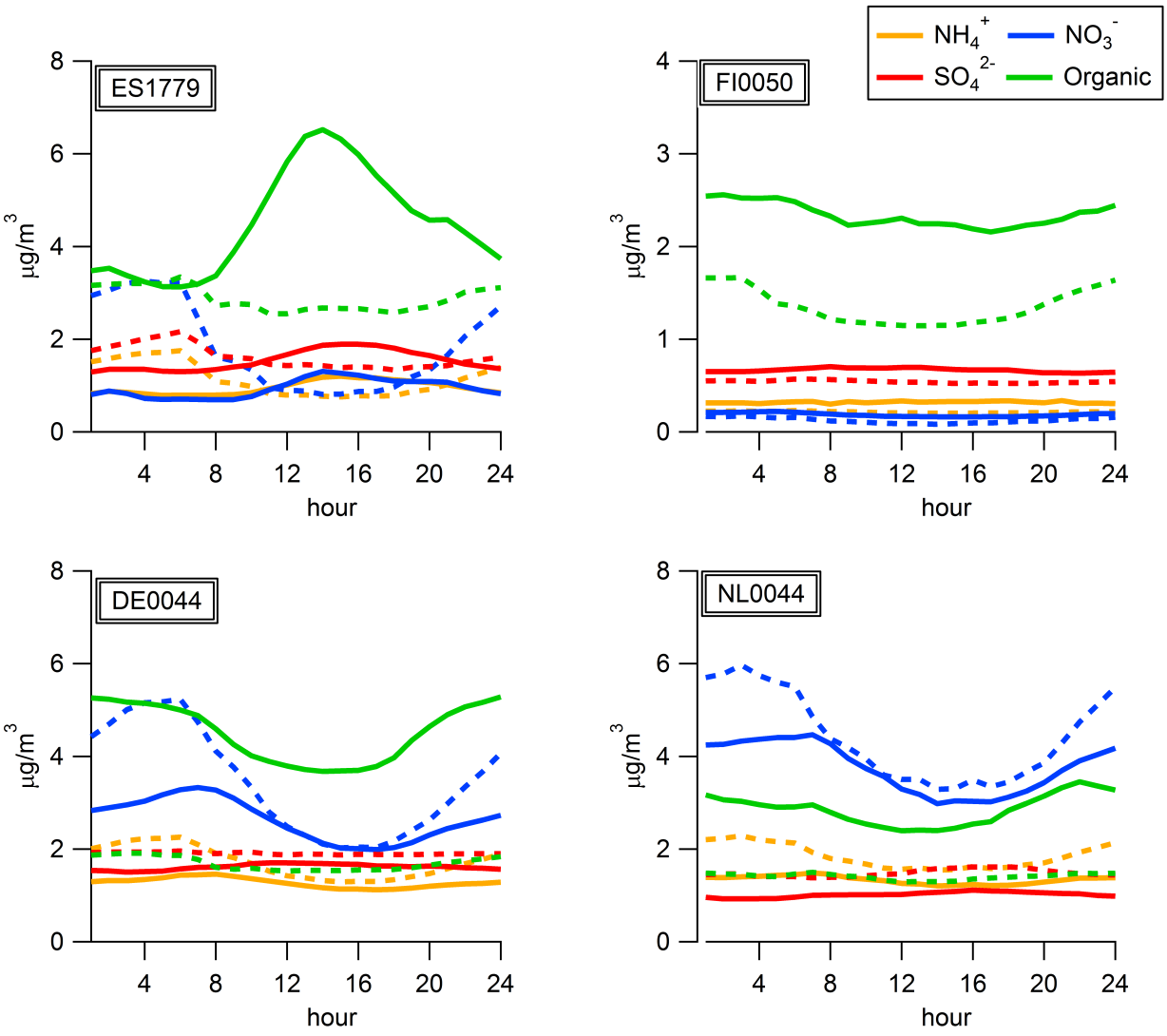

Figure 6.2: Mean observed and calculated diurnal variation of SO_4^{2-}, NO_3^-, NH_4 and organic aerosols for the 2012-2013 intensive measurement period. Solid lines represent the observations and dashed lines the model.

Sulfate shows little variations at NL0044 and DE0044; a small bump in the afternoon may be attributed to higher photochemical activity enhancing oxidation of SO_2. The model results are in good agreement with the observations, though it calculates a somewhat flatter SO_4^{2-} diurnal profile for DE0044. The diurnal pattern of NH_4 resembles that of NO_3^- and SO_4^{2-}, depending of its association. The model calculates somewhat larger diurnal variation for NH_4 with too strong night-time increase due to its over-prediction of night-time ammonium nitrate.

At the Finnish site Hyytiälä / SMEAR II (FI0050), hardly any diurnal variations are seen either in the observation or in the model for the SIA components. This is due to the site's location far from the SIA sources (Hari and Kulmala 2005), and NH_4 is mainly associated with SO_4^{2-}, whereas ammonium nitrate levels are low, hence evaporation and condensation processes are of less importance. The pattern of diurnal variation of organic mass is similar to that at DE0044 and NL0044, although less pronounced. This could be due to comparably lower daytime temperatures and thus less evaporation of volatile organics. The model results are in good correspondence with the ACSM data.

Montseny (ES1778) differs distinctly from the other sites with its daytime peaks for all the observed components. This is not seen in the model results, which calculates the opposite diurnal profile with elevated concentrations at night/early morning hours (maximum at 5-6 am).

Montseny is situated upwind of the metropolitan area of Barcelona and receives polluted air from this region when the afternoon breeze from the Mediterranean carries this air pollution to the inland. The high organic aerosol (OA) concentrations during daytime in summer (Figure 6.3) reflect the efficient secondary organic aerosol (SOA) formation under Mediterranean conditions, as discussed by Minguillón et al. (2015). The model appears to have problems reproducing this diurnal cycle, probably because the meteorological driver in the EMEP MSC-W model does not capture this regional phenomena, but to be certain this needs further investigation.

6.2.3 Seasonal diurnal profiles

Better understanding of the effects of varying emissions and chemical processes can be obtained by studying diurnal profiles of PM species in different seasons, as presented in Figure 6.3. The annual diurnal patterns for SIA and organics already discussed, can also be recognized for certain seasons. The most pronounced diurnal variations are typically seen in summer and spring, whereas variability in winter is in general minor. Seasonal diurnal profiles varies between sites and species.

At FI0050, hardly any difference can be seen in diurnal profiles of the different components between seasons, and the variability is small, although observed organic mass shows increased levels and a daytime minimum in summer. At ES1778, a particular diurnal profile with a daytime maximum for all components is seen in all seasons, and especially pronounced in summer. In winter, NO_3^- and organics appear to remain elevated until late evening, probably due to the effect of local NO_x emissions.

At NL0044 and DE0044, the main features of diurnal profiles are quite similar between the seasons (see discussion in 6.2.2), although the relative levels of aerosol species vary. Similar to ES1778, slightly enhanced levels of organic and NO_3^- aerosols are seen at these sites in winter afternoon/evening hours, which probably associated with residential heating and traffic sources.

The model's ability to reproduce the observed diurnal profiles are rather variable for different components and sites. Model results for FI0050 correspond quite well with the observed profiles for all seasons, although the calculated organic aerosol is too low. For ES1778, the model fails to reproduce the observed daytime maxima (as first pointed out in 6.2.2), only in summertime do the modelled profiles of SO_4^{2-} and NH_4 approach the observed ones. For NL0044 and DE0044, the model results show somewhat less pronounced diurnal variation for the organic aerosol (which is particularly underestimated in winter and spring). On the other hand, it overestimates the diurnal variation of NO_3^-, particularly in autumn and winter.

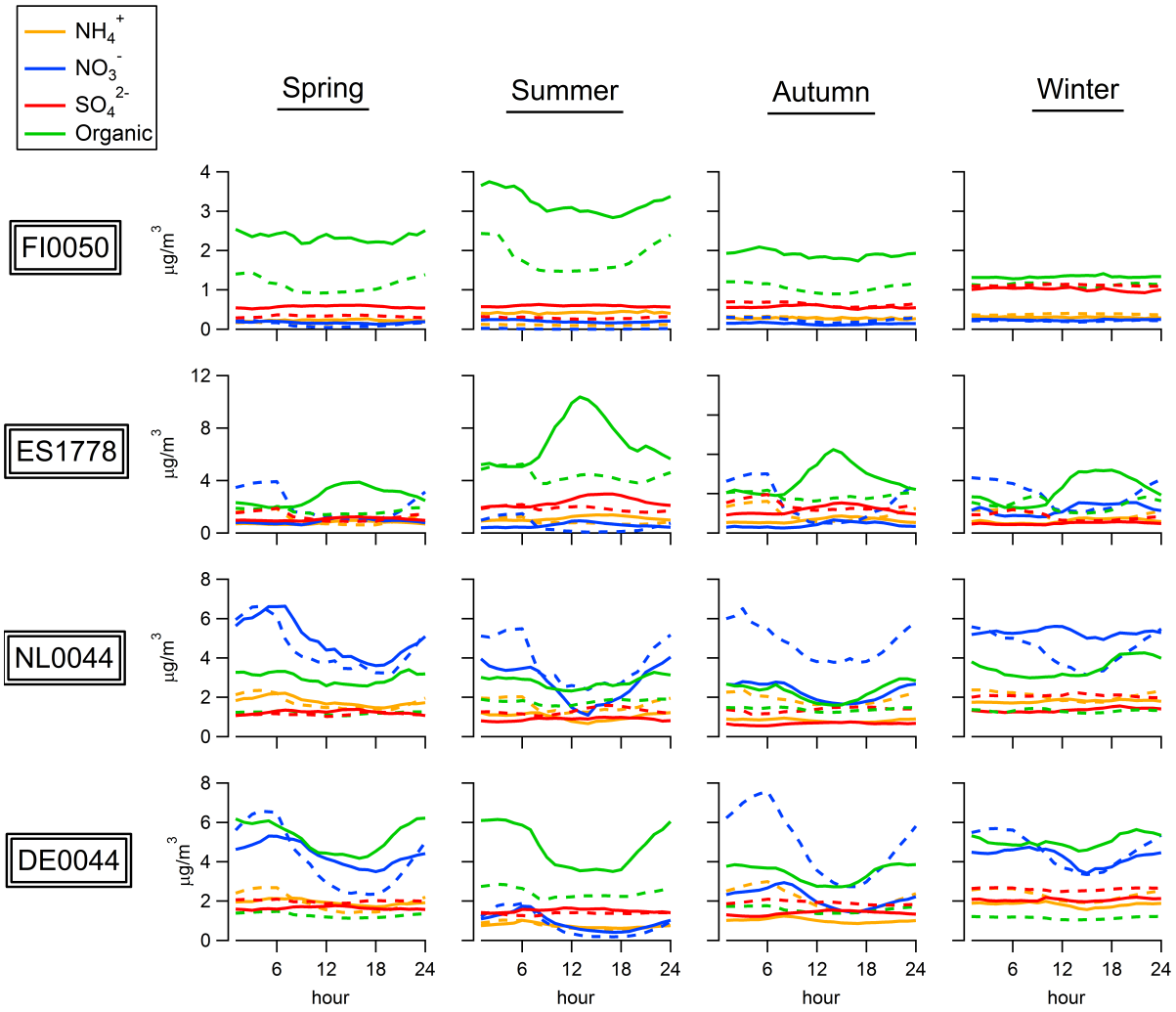

Figure 6.3: Seasonal mean observed and calculated diurnal variation of SO_4^{2-}, NO_3^-, NH_4 and organic aerosols for the 2012-2013 intensive measurement period. Solid lines represent the observations and dashed lines the model.

6.3 Recommendations and future work

The present chapter briefly illustrates the possibilities associated with ACSM measurements for characterization of the ambient aerosol at high time resolution in Europe, and for model validation.

Future studies should include more sites for a better spatial assessment of the ambient aerosol chemical composition across Europe, and extending existing multiyear time series obtained by ACSM should be prioritized to assure robust results.

An obvious next step is to use the source apportioned fractions of the organic mass, obtained by positive matrix factorization (PMF), to compare with source profiles in regional atmospheric transport models, as was done with the observations from the Aerosol Mass Spectrometers (AMS) used during the EUCAARI-EMEP measurement campaign in 2008 and 2009 (Crippa et al. (2014), Fountoukis et al. (2014)).

PMF analysis from ACSM measurements should be combined with other source apportionment studies. One challenge is to get a regional dataset with a standardized and comparable PMF analysis from all the sites. In the new COST Action CA16109 COLOSSAL, harmonized processing and interpretation of the data from these instruments across Europe is one of the main objectives, and this will be very useful products for air quality modelers and policy makers.

References

Aas, W., Tsyro, S., Bieber, E., Bergström, R., Ceburnis, D., Ellermann, T., Fagerli, H., Frölich, M., Gehrig, R., Makkonen, U., Nemitz, E., Otjes, R., Perez, N., Perrino, C., Prévôt, A. S. H., Putaud, J.-P., Simpson, D., Spindler, G., Vana, M., and Yttri, K. E.: Lessons learnt from the first EMEP intensive measurement periods, Atmos. Chem. Physics, 12, 8073–8094, doi:10.5194/acp-12-8073-2012, 2012.

Bressi, M., Cavalli, F., Putaud, J. P., Prevot, A. S. H., et al.: A European aerosol phenomenology - 6: high-time resolution chemical characteristics of submicron particulate matter across Europe, In preparation, 2017.

Crippa, M., Canonaco, F., Lanz, V. A., Äijälä, M., Allan, J. D., Carbone, S., Capes, G., Ceburnis, D., Dall'Osto, M., Day, D. A., DeCarlo, P. F., Ehn, M., Eriksson, A., Freney, E., Hildebrandt Ruiz, L., Hillamo, R., Jimenez, J. L., Junninen, H., Kiendler-Scharr, A., Kortelainen, A.-M., Kulmala, M., Laaksonen, A., Mensah, A. A., Mohr, C., Nemitz, E., O'Dowd, C., Ovadnevaite, J., Pandis, S. N., Petäjä, T., Poulain, L., Saarikoski, S., Sellegri, K., Swietlicki, E., Tiitta, P., Worsnop, D. R., Baltensperger, U., and Prévôt, A. S. H.: Organic aerosol components derived from 25 AMS data sets across Europe using a consistent ME-2 based source apportionment approach, Atmospheric Chemistry and Physics, 14, 6159–6176, doi:10.5194/acp-14-6159-2014, URL http://www.atmos-chem-phys.net/14/6159/2014/, 2014.

Farmer, D. K., Matsunaga, A., Docherty, K. S., Surratt, J. D., Seinfeld, J. H., Ziemann, P. J., and Jimenez, J. L.: Response of an aerosol mass spectrometer to organonitrates and organosulfates and implications for atmospheric chemistry, Proceedings of the National Academy of Sciences, 107, 6670–6675, doi:10.1073/pnas.0912340107, URL http://www.pnas.org/content/107/15/6670.abstract, 2010.

Fountoukis, C., Megaritis, A. G., Skyllakou, K., Charalampidis, P. E., Pilinis, C., Denier van der Gon, H. A. C., Crippa, M., Canonaco, F., Mohr, C., Prévôt, A. S. H., Allan, J. D., Poulain, L., Petäjä, T., Tiitta, P., Carbone, S., Kiendler-Scharr, A., Nemitz, E., O'Dowd, C., Swietlicki, E., and Pandis, S. N.: Organic aerosol concentration and composition over Europe: insights from comparison of regional model predictions with aerosol mass spectrometer factor analysis, Atmospheric Chemistry and Physics, 14, 9061–9076, doi:10.5194/acp-14-9061-2014, URL https://www.atmos-chem-phys.net/14/9061/2014/, 2014.

Fröhlich, R., Cubison, M. J., Slowik, J. G., Bukowiecki, N., Prévôt, A. S. H., Baltensperger, U., Schneider, J., Kimmel, J. R., Gonin, M., Rohner, U., Worsnop, D. R., and Jayne, J. T.: The ToF-ACSM: a portable aerosol chemical speciation monitor with TOFMS detection, Atmospheric Measurement Techniques, 6, 3225–3241, doi:10.5194/amt-6-3225-2013, URL https://www.atmos-meas-tech.net/6/3225/2013/, 2013.

Hari, P. and Kulmala, M.: Station for Measuring Ecosystem - Atmosphere Relations (SMEAR II), Boreal Env. Res., 10, 315–322, 2005.

Minguillón, M., Ripoll, A., Pérez, N., Prévôt, A., Canonaco, F., Querol, X., and Alastuey, A.: Chemical characterization of submicron regional background aerosols in the western

Mediterranean using an Aerosol Chemical Speciation Monitor, Atmospheric Chemistry and Physics, 15, 6379–6391, doi:10.5194/acp-15-6379-2015, URL https://www.atmos-chem-phys.net/15/6379/2015/, 2015.

Ng, N. L., Herndon, S. C., Trimborn, A., Canagaratna, M. R., Croteau, P. L., Onasch, T. B., Sueper, D., Worsnop, D. R., Zhang, Q., Sun, Y. L., and Jayne, J. T.: An Aerosol Chemical Speciation Monitor (ACSM) for Routine Monitoring of the Composition and Mass Concentrations of Ambient Aerosol, Aerosol Science and Technology, 45, 780–794, doi:10.1080/02786826.2011.560211, URL http://dx.doi.org/10.1080/02786826.2011.560211, 2011.

Poulain, L., Spindler, G., Birmili, W., Plass-Dülmer, C., Wiedensohler, A., and Herrmann, H.: Seasonal and diurnal variations of particulate nitrate and organic matter at the IfT research station Melpitz, Atmospheric Chemistry and Physics, 11, 12 579–12 599, doi:10.5194/acp-11-12579-2011, URL https://www.atmos-chem-phys.net/11/12579/2011/, 2011.

Putaud, J. P., Van Dingenen, R., Alastuey, A., Bauer, H., Birmili, W., Cyrys, J., Flentje, H., Fuzzi, S., Gehrig, R., Hansson, H. C., Harrison, R. M., Herrmann, H., Hitzenberger, R., Huglin, C., Jones, A. M., Kasper-Giebl, A., Kiss, G., Kousa, A., Kuhlbusch, T. A. J., Loschau, G., Maenhaut, W., Molnar, A., Moreno, T., Pekkanen, J., Perrino, C., Pitz, M., Puxbaum, H., Querol, X., Rodriguez, S., Salma, I., Schwarz, J., Smolik, J., Schneider, J., Spindler, G., ten Brink, H., Tursic, J., Viana, M., Wiedensohler, A., and Raes, F.: A European aerosol phenomenology-3: Physical and chemical characteristics of particulate matter from 60 rural, urban, and kerbside sites across Europe, Atmos. Environ., 44, 1308–1320, 2010.

Schlag, P., Kiendler-Scharr, A., Blom, M. J., Canonaco, F., Henzing, J. S., Moerman, M., Prévôt, A. S. H., and Holzinger, R.: Aerosol source apportionment from 1-year measurements at the CESAR tower in Cabauw, the Netherlands, Atmospheric Chemistry and Physics, 16, 8831–8847, doi:10.5194/acp-16-8831-2016, URL https://www.atmos-chem-phys.net/16/8831/2016/, 2016.

Tørseth, K., Aas, W., Breivik, K., Fjæraa, A. M., Fiebig, M., Hjellbrekke, A. G., Lund Myhre, C., Solberg, S., and Yttri, K. E.: Introduction to the European Monitoring and Evaluation Programme (EMEP) and observed atmospheric composition change during 1972–2009, Atmos. Chem. Physics, 12, 5447–5481, doi:10.5194/acp-12-5447-2012, URL http://www.atmos-chem-phys.net/12/5447/2012/, 2012.

CHAPTER 7

Equivalent Black Carbon from fossil fuel and biomass burning sources at European rural background sites assessed by high time resolution measurements and modelling

Karl Espen Yttri, Stephen Matthew Platt, Markus Fiebig, David Simpson, Erik Swietlicki, Johan Martinsson, Milan Vana, Adeala Holubova Smejkalova, Jean-Philippe Putaud, Fabrizia Cavalli, Nikos Mihalopoulos, Giorgos Kouvarakis

7.1 Introduction

Separation of equivalent black carbon (EBC) into fossil fuel (EBC_{ff}) and biomass burning (EBC_{bb}) sources is possible by multi-wavelength measurement of the absorption coefficient (Sandradewi et al. 2008), and is based on the assumption that aerosol particles emitted from biomass burning absorb relatively more in near UV than in IR, compared to aerosol particles from combustion of fossil fuels. For the AE33 aethalometer (Magee Scientific) this separation is an online feature. Being robust, easy to operate and available at relatively low cost, the multi wavelength aethalometer holds the potential to be an important tool for source apportionment (SA) of carbonaceous aerosol.

Only a few studies have reported using a multi wavelength aethalometer for SA of EBC in the European rural background environment, and for an extended period of time (e.g. Herich et al. 2011). With an increasing number of such instruments in use at European rural background sites and a substantial focus on BC and its sources, it appears timely to validate the instruments ability to do SA of EBC at a range of sites that varies in BC concentration as well as BC source composition. Influence by other light absorbing aerosol particles than those originating from vehicular traffic and biomass burning, e.g. hematite containing mineral dust and coal, is not widely explored, but ought to be if multi-wavelength aethalometers are to be implemented in monitoring networks for source apportionment purposes.

A joint EMEP TFMM and ACTRIS intensive measurement period (IMP) focusing on SA of EBC is suggested for winter 2018 to start the validation work briefly outlined. An outline of this IMP has been made available to the EMEP community, and the interested reader can find more information by following this link: `http://www.nilu.no/projects/ccc/tfmm/Winter%20intensive%20measurement%20period.pdf`.

In this chapter, EBC_{ff} and EBC_{bb} have been calculated for four EMEP sites along a north to south transect for 2015, obtained using a slight modification of the approach described by Sandradewi et al. (2008), and by the EMEP model for comparison. Our purpose is to demonstrate the high time resolution signal of EBC_{ff} and EBC_{bb} from a multi-wavelength aethalometer, which can be used for model validation, and how the biomass burning tracer levoglucosan can be used for validation of the EBC_{bb} signal, in addition to provide a snapshot of the EBC_{bb} and EBC_{ff} signal across Europe. This chapter serves as a pilot for the suggested EMEP/ACTRIS IMP.

7.2 Methodology

7.2.1 Observations and the multi-wavelength PMF approach

EBC data submitted to the EBAS database (ebas.nilu.no) was converted to aerosol absorption coefficient (b_{abs}) data according to Equation 7.1 for each of the 7 wavelengths (λ) of the aethalometer, using the internal mass absorption coefficient (MAC), $\sigma_{abs}(\lambda)$, values specified by the manufacturer for each aethalometer model (Table 7.1).

$$b_{abs}(\lambda) = EBC(\lambda) \times \sigma_{abs}(\lambda) \times C_0 \tag{7.1}$$

A C_0 (loading correction coefficient) value of 3.5 (WMO 2016) was applied for the AE31 model, and 2.57 for the AE33, to obtain corrected MAC values. The C_0 value for the AE33 is explained as follows: a default value of 1.57, automatically accounted for by the instrument, explains the difference in filter medium matrix scattering between the AE33 and the AE31, whereas an additional factor of 1.64 is used to level with the corrected MAC values seen for AE31. It is apparent that a C_0 value of 1.57 is not sufficient to correct the data with respect to the scattering and the shadowing effect, whereas the additional 1.64 yet should be considered as temporarily and needs further evaluation and a consensus. Site specific MAC values (Table 7.2) were calculated according to Equation 7.2, using parallel measurements of EC obtained by thermal-optical analysis, operated according to the EUSAAR-2 temperature program, and b_{abs}.

$$\sigma_{abs}(\lambda) = b_{abs}(\lambda)/EC \tag{7.2}$$

The calculated MAC values in Table 7.2, i.e. across all 7 wavelengths, were on average 1.7 $\pm$ 0.3 (Kosetice) to 2.1 $\pm$ 0.2 (Finokalia) times higher than the corrected internal MAC values (Table 7.1). This reflects the use of thermal-optical analysis for calculated MACs versus non-thermal-optical for the internal MACs.

The choice of the absorption Angström exponent (AAE) is decisive for the separation of EBC into EBC_{bb} and EBC_{ff}. Wood burning emissions have an AAE ranging from 1.5 to 2.5, whereas it is about 1 for fossil fuel emissions. EBC_{bb} and EBC_{ff} were apportioned using positive matrix factorization (PMF) and ME2 via the SOFI toolkit (Canonaco et al. 2013). Selecting a two-factor solution, we constrain the slope of the wavelength dependence of one

factor to 1.0±0.25 (representing EBC_{ff} and allow the PMF solver to find the remaining factor (assumed to represent EBC_{bb}), though a combination of sources may be possible). Thus, we emulate the Sandradewi et al. (2008) approach, using the more powerful PMF solver to apportion the sources without strong a priori assumptions on the AAE. PMF generated factor profiles are used to determine site specific AAEs (Table 7.3). This approach ensures an optimized solution for each participating site and ought to be superior to assuming one factor for each of the two sources being valid for all of Europe.

Table 7.1: Internal MAC values (Unit: m^2 g^{-1}) for AE31 and AE 33 provided by the instrument manufacturer along with the corresponding C_0 values used to calculate the corrected internal MAC values.

AE31	**370 nm**	**470 nm**	**520 nm**	**590 nm**	**660 nm**	**880 nm**	**950 nm**
Internal MAC	39.5	31.1	28.1	24.8	22.2	16.6	15.4
C_0	3.5	3.5	3.5	3.5	3.5	3.5	3.5
Corr. Int. MAC	11.3	8.9	8.0	7.1	6.3	4.7	4.4
AE33	**370 nm**	**470 nm**	**520 nm**	**590 nm**	**660 nm**	**880 nm**	**950 nm**
Internal MAC	18.5	14.5	13.1	11.6	10.4	7.8	7.2
C_0	2.57	2.57	2.57	2.57	2.57	2.57	2.57
Corr. Int. MAC	11.3	8.9	8.0	7.1	6.3	4.7	4.4

Table 7.2: Calculated site specific MAC values (Unit: m^2 g^{-1}). Based on concurrent measurements of EC (EUSAAR-2;Cavalli et al. (2010)) and b_{abs}.

	370 nm	**470 nm**	**520 nm**	**590 nm**	**660 nm**	**880 nm**	**950 nm**
Vavihill	26.0±11.0	18.3±7.5	15.7±6.4	13.5±5.4	11.7±4.7	8.2±3.2	7.8±3.1
Kosetice	25.7±3.5	16.7±2.2	13.4±1.8	11.5±1.6	10.2±1.4	6.7±1.0	5.9±0.9
Ispra	23.6±4.3	17.2±3.5	14.5±3.1	12.6±2.9	11.4±2.7	8.1±2.1	7.4±2.0
Finokalia	27.8±9.2	20.4±7.0	17.5±6.2	14.9±5.3	12.8±4.5	9.0±3.1	8.5±2.9

Table 7.3: Site-specific absorption Angström exponents for fossil fuel and biomass burning particles derived from positive matrix factorization.

	Vavihill	**Kosetice**	**Ispra**	**Finokalia**
AAE_{ff}	0.90±0.01	0.96±0.00	0.94±0.00	0.92±0.00
AAE_{bb}	1.78±0.05	1.81±0.02	2.21±0.06	2.96±0.23

The resulting EBC_{bb} output was evaluated by comparison with the source specific biomass burning tracer levoglucosan (only available for one site). ^{14}C-analysis of EC, separating EC into a modern and a fossil carbon fraction, could have evaluated both EBC_{bb} and EBC_{ff}, but was not available, whereas additional species, e.g. picene and Fe, would be needed to assess the potential influence of coal and hematite containing mineral dust.

7.2.2 Modelling EC

The EMEP MSC-W model has been run in two configurations:

EMEP01 - uses the new 0.1 × 0.1 degree EMEP modelling system, with officially provided emissions of $PM_{2.5}$. The split into EC components is based upon emep-default splits, as provided by IIASA some years ago. The model version used here was with 20 vertical layers.

EECCA/MACC - uses the 'traditional' polar-stereographic grid (50km at 60°N), and MACC-III $PM_{2.5}$ emissions (Kuenen et al. 2014, MACC-III 2015). The emissions are from an earlier year, 2011, but the split into EC_{ff}, EC_{bb} was made from consistent MACC data also provided by JJP Kuenen (TNO, pers. comm. 2017).

Thus, EMEP01 has higher spatial resolution, but EECCA/MACC probably has a more consistent estimate of the EC fractions than we have in the EMEP defaults. Also, the EMEP01 system is fairly new, and work is still needed to evaluate the behaviour of for example parameters associated with boundary layer meteorology or other aspects. The two model setups should therefore be considered as two different but valid efforts to model EC for this comparison.

7.3 Seasonal and annual observations

The spatial resolution of the annual mean EBC levels (Table 7.4) closely resembles that previously seen for EC in the European rural background environment (Yttri et al. 2007). The elevated levels at Ispra (1.16 $\mu g\ m^{-3}$), situated in the polluted Po Valley in Northern Italy, were nearly three times higher than at the eastern European site Kosetice (0.42 $\mu g\ m^{-3}$) in the Czech Republic, which in turn was approximately 2 times higher than at the eastern Mediterranean site Finokalia (0.24 $\mu g\ m^{-3}$) at the Greek Island of Crete and at the Scandinavian site Vavihill (0.21 $\mu g\ m^{-3}$) in Southern Sweden.

Table 7.4: Annual mean concentrations of EBC, EBC_{ff} and EBC_{bb} ($\mu g\ m^{-3}$) and relative contributions of EBC_{ff} and EBC_{bb} to EBC (%) for 2015, listed from North to South.

Site (Country)	EBC µg m^{-3}	EBC_{ff} µg m^{-3}	EBC_{bb} µg m^{-3}	EBC_{ff}/EBC %	EBC_{bb}/EBC %
Vavihill (Sweden)	0.21 ± 0.27	0.11 ± 0.13	0.10 ± 0.16	57 ± 19	43 ± 19
Kosetice (Czech Rep)	0.42 ± 0.30	0. 22 ± 0.19	0.20 ± 0.18	54 ± 22	46 ± 22
Ispra (Italy)	1.16 ± 1.16	0.75 ± 0.76	0.41 ± 0.46	72 ± 23	28 ± 23
Finokalia (Greece)	0.24 ± 0.15	0.20 ± 0.13	0.04 ± 0.04	82 ± 13	18 ± 13

Fossil fuel sources were the major fraction of EBC annually at all four sites (54-82%), and by a noticeably margin at the two southernmost sites (82±13% and 72±23%) (Table 7.4). At the Eastern European (EBC_{bb} = 46±22%) and the Scandinavian (EBC_{bb} = 43±19%) sites, the difference was less pronounced, and the EBC_{bb} fraction nearly equaled that of EBC_{ff}.

EBC_{bb} levels were elevated in the heating season and low in summer, which shows that residential heating was the major source of EBC_{bb}. A certain influence of agricultural waste burning and wild fires in the transition seasons and in summer is likely, but must be studied in more detail for a quantitative estimate. The seasonality was particularly pronounced at Ispra. All sites, except Finokalia, experienced months where $EBC_{bb}/EBC > EBC_{ff}/EBC$. Indeed, EBC_{bb} exceeded EBC_{ff} for six months at Kosetice, four at Vavihill and for one month at Ispra. Note that EBC was elevated for these months. As a continental site, situated 534 masl, Kosetice and its surroundings, along with the Scandinavian site Vavihill, nearby settlements likely experience a higher need for residential heating than the two southernmost sites included in the current study. Indeed, the number of heating degree-days at Kosetice and Vavihill was 1.4 times higher than at Ispra and 3.7 times higher than at Finokalia.

Finokalia deviated slightly from the pattern described, as EBC_{bb} concentrations increased substantially in August. This finding is in line with Sciare et al. (2008) for EC and non-sea salt potassium at Finokalia, which associated the peak in August (and March/April) with long-range transport of agricultural waste burning emissions from countries surrounding the Black Sea. Sciare et al. (2008) separated EC into a biomass and a non-biomass burning category, and found that the latter category dominated, with biomass burning accounting for 20±10% of EC annually. This finding is highly similar to the annual estimate provided in the current study: i.e. EBC_{bb} constituted 17±13% of EBC. Note that in the present study, we force the real world situation into a two-source solution, which we know is incorrect, partly because hematite containing mineral dust will cause absorption at certain sites, such as at Finokalia. Indeed, Sciare et al. (2008) found that 12.6±3.5% of the aethalometer light absorption could be attributed to hematite at Finokalia annually, and more than 50% during events (Vrekoussis et al. 2005). To reduce uncertainties in the source apportionment of EBC by the multi-wavelength aethalometer approach, the influence of light absorbing mineral dust should be accounted for, e.g. by finding higher order PMF solutions.

Sciare et al. (2008) stated that coal should be a significant contributor to background EC in the Eastern Mediterranean, as previously shown for SO_2. Likewise, coal is used for residential heating in Eastern Europe, including in the Czech Republic where Kosetice is situated. As for hematite containing mineral dust, we do not yet know how coal fits into the two-source solution used. There are studies, which suggest that the AAE of coal closely resembles that of biomass burning (Sun et al. 2017), thus EBC_{bb} might not be exclusively associated with biomass burning, and hence is the separation of EBC into a fossil fuel and a biomass burning source not as exclusive as desirable in coal influenced areas. If the coal emission mainly originates from small domestic installations used for residential heating, it can be speculated that its temporal resolution closely resembles that of wood burning for residential heating and is thus not well separated from biomass burning emissions in the PMF analysis.

The seasonality of EBC_{ff} showed some resemblance with that of EBC_{bb} at the sites Vavihill, Kosetice and Ispra (Figure 7.1), whereas the monthly mean concentration variability was slightly less pronounced than for EBC_{bb}, indicating influence of sources such as vehicular traffic, which is assumed less seasonal dependent.

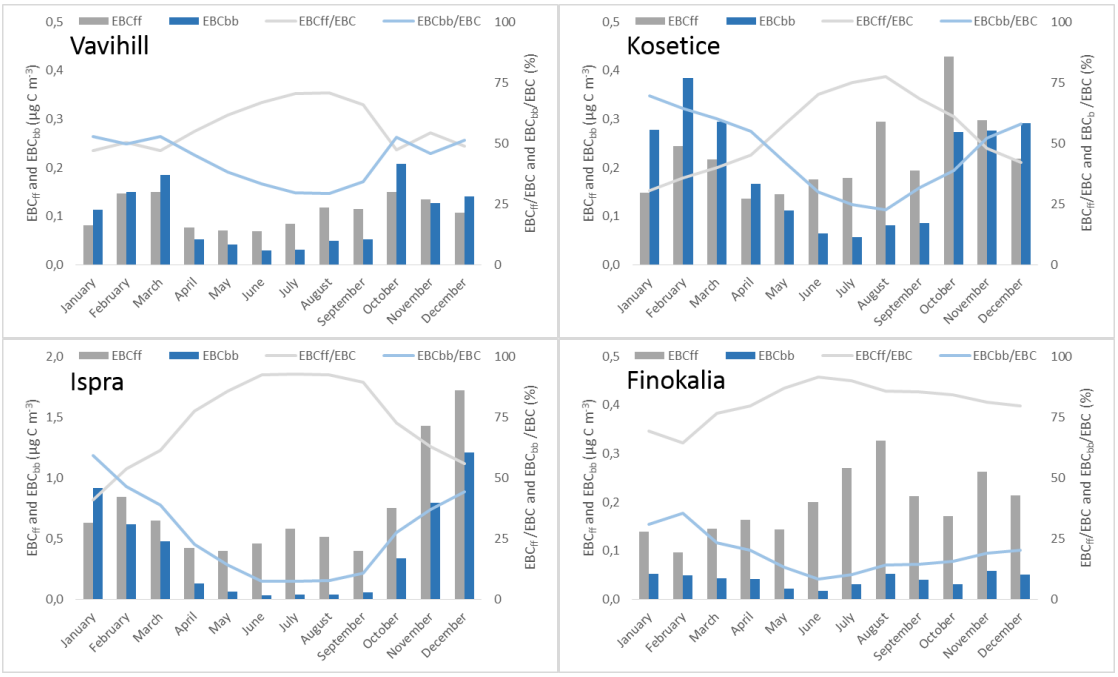

Figure 7.1: Monthly mean concentration of EBC_{ff} and EBC_{bb} ($\mu g\ m^{-3}$) and relative contribution of EBC_{ff} and EBC_{bb} to EBC (%) at Vavihill, Kosetice, Ispra and Finokalia in 2015.

7.4 Observed diurnal variability

Diurnal variability of EBC_{ff} and EBC_{bb} was observed at most sites, annually and/or seasonally, being most pronounced at Ispra (Figure 7.2a,b), and to some extent at Kosetice. At Ispra, the diurnal pattern of EBC_{ff} clearly reveals the influence of the morning and the afternoon vehicular rush hours, peaking around 07:00 - 09:00 and 16:00 - 18:00. These peaks appear at a time that suggests that the source is of local origin. It is likely though that such a pattern is representative for large parts of the rural environment in the densely populated Po Valley. The actual pattern varies as a function of season and was more pronounced in winter and fall than in spring and summer. To what extent this is largely due to less emission from local vehicular traffic in spring/summer or meteorological conditions remains to be studied in more detail. The less pronounced signs of diurnal patterns of EBC_{ff} at Vavihill, and particularly at Finokalia, suggests less impact from local sources and more from regional ones. Martinsson et al. (2017) showed that EBC_{ff} peaked at 08:00 - 10:00 and 17:00 - 19:00 at Vavihill, arguing that a combination of its rural location and that emissions might originate from the major cities in the region, was the reason why peaks occurred later than expected rush hour. A similar pattern was observed in the current study (not shown).

The diurnal variability of EBC_{bb} observed at Ispra (Figure 7.2b) and Kosetice (Figure 7.2c) was highly pronounced, and quite comparable between the two sites, suggesting minor differences in residential heating practice across Europe and between seasons. EBC_{bb} peaked in the evening between 20:00 and 22:00, and the peak was typically broader than that seen for EBC_{ff} (considering both the morning and the afternoon peak of EBC_{ff}), starting as early as 15:00 to 16:00. After peaking, the concentration gradually declined until the afternoon the next day, suggesting that biomass burning commences in early evening, but continues to some extent through the night and early morning. As for EBC_{ff}, at Ispra in particular, this suggest a noticeably influence from local sources for EBC_{bb}. The diurnal variability observed for

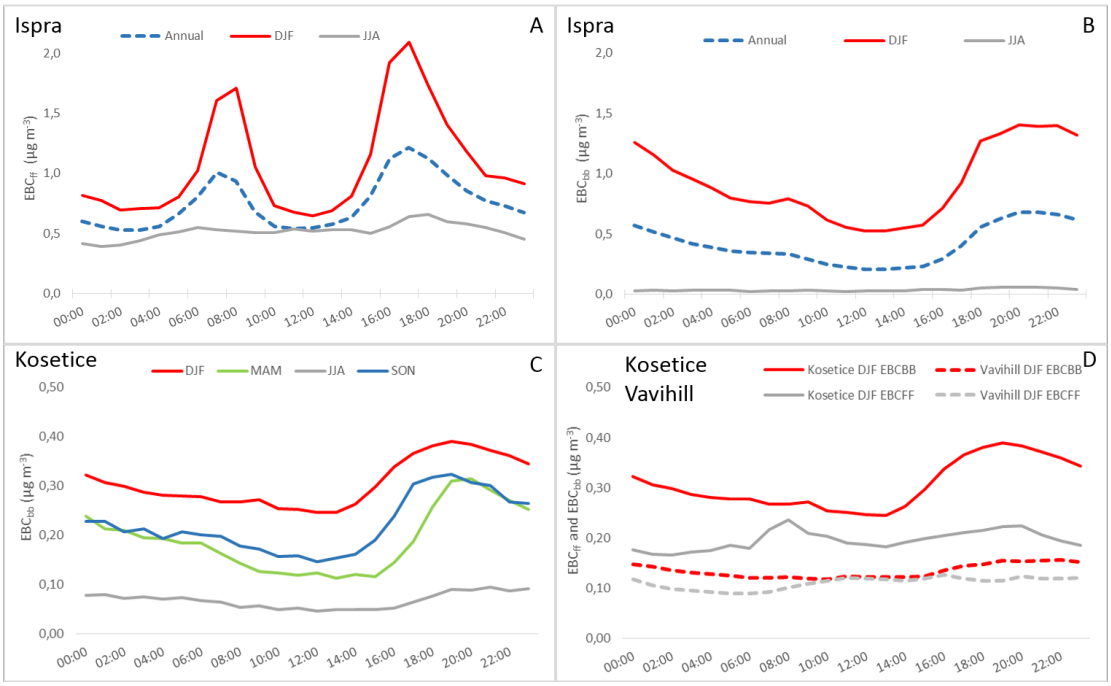

Figure 7.2: a) Diurnal variability of EBC_{ff} at Ispra annually, in winter (DJF), and summer (JJA); b) Diurnal variability of EBC_{bb} at Ispra annually, in winter (DJF), and summer (JJA); c) Diurnal variability of EBC_{bb} at Kosetice as a function of season; d) Diurnal variability of EBC_{ff} and EBC_{bb} at Kosetice and Vavihill in winter (DJF). Unit: (μg m^{-3}).

EBC_{bb} at Vavhill was rather similar to that seen for Ispra and Kosetice, but saw a broad based peak during the morning in spring and fall, which extended further into the day than that seen for Ispra in Figure 7.2b. Finokalia was characterized by a general lack of pronounced diurnal variability, as for EBC_{ff}, and suggests that regional sources dominated.

When the heating season peaks, we find that EBC_{bb} is higher than EBC_{ff} during the entire day, as seen for Kosetice and Vavihill in winter (DJF) (Figure 7.2d) or for large parts of the day, typically the afternoon and the night, as seen for Kosetice and Vavihill in spring and fall and for Ispra in winter. For Kosetice and Vavihill, $EBC_{bb} \geq EBC_{ff}$ for more than one third of the hours of the day (i.e. during night) even when considering data for the entire year.

7.5 Validation of the multi-wavelength PMF approach

The AAE_{ff} values derived from PMF all showed minor variability, ranging from 0.90 at Vavihill to 0.96 at Kosetice. The AAE_{bb} values were highly similar at Vavihill (1.78) and Kocetice (1.81) and to some extent at Ispra (2.21), whereas it was substantially higher at Finokalia (2.96) (Table 7.3). With the exception of Finokalia, the AAE_{ff} and AAE_{bb} values closely resembles that reported in the literature (e.g. Bond et al. 2007, Martinsson et al. 2017). We speculate that the high AAE_{bb} at Finokalia might be influenced by mineral dust, as the site experiences dust outbreaks from the African continent. The AAE is inversely related to the average aerosol particles size, hence the smaller the particles, the larger the exponent, thus AAE will likely go down for mineral dust due to the larger particles size. However, larger AAE values (2.9) have been reported for Saharan dust aerosol (Fialho et al. 2005, Bergstrom et al. 2007), and are attributed to the spectral dependency of dust absorption.

The output of the PMF approach is partly validated by the diurnal and seasonal variation observed in the EBC_{bb} factors. In future studies, PMF diurnal and seasonal variation in the output time series could be used as selection criteria for more optimum solutions following the approach of Elser et al. (2016). Here, the PMF output is quality assured via comparison of the EBC_{bb} factor time series to levoglucosan at Vavihill and to the output of the Sandradewi approach. Levoglucosan data for Vavihill is available as supplementary material from Martinsson et al. (2017). Figure 7.3 shows that the PMF EBC_{bb} factor time series shows reasonable agreement with the levoglucosan time series and captures the strongest episodes very well. Linear regression (Figure 7.3, inset) yields a Pearson's r = 0.86. The comparison of levoglucosan and the PMF derived EBC_{bb} thus strongly supports the source apportionment result for this site and the PMF approach in general. Figure 7.4 also shows a comparison of the PMF ECB_{bb} profile with ECB_{bb} according to the Sandradewi approach, using AAE_{ff} of 1.1 and AAE_{bb} of 1.8 as input for the Sandradewi approach. Again, the comparison is favourable. Note that while the agreement between levoglucosan and ECB_{bb} is better (Pearson's r = 0.90) from the Sandradewi approach than the PMF approach, negative values for EBC_{ff} (Figure 7.4) are obtained. This suggests that the Sandradewi model yields a poorer description of the observed data overall compared to the PMF based approach.

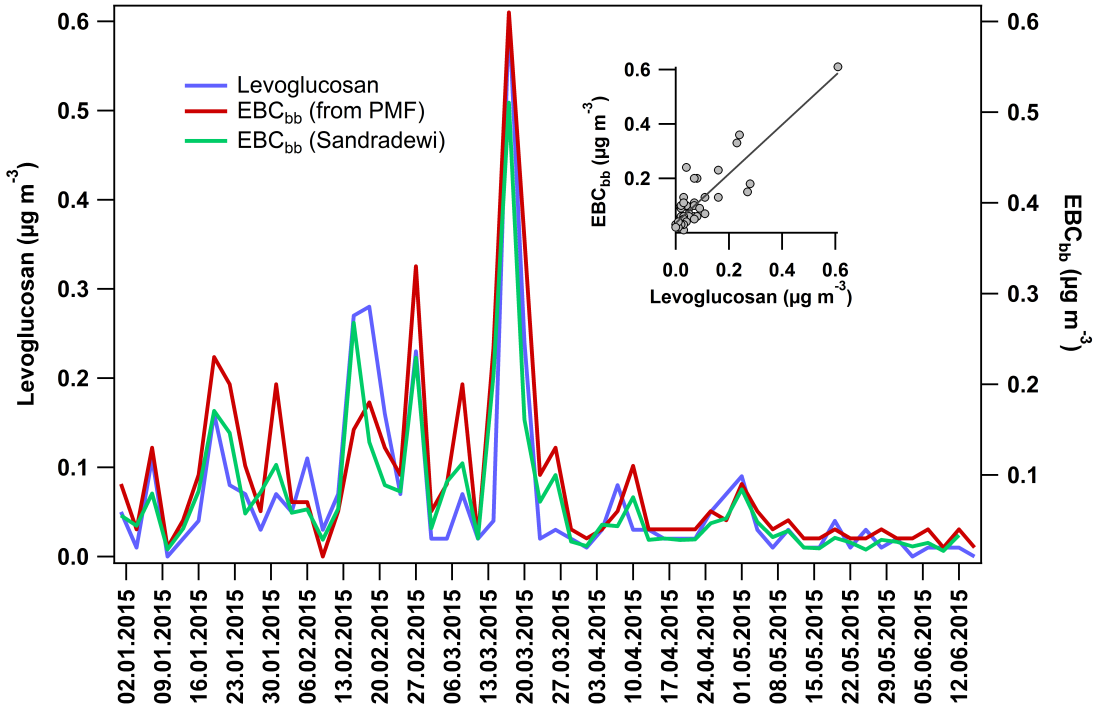

Figure 7.3: PMF-derived EBC_{bb} from PMF (red), Sandradewi approach derived EBC_{bb} (green) and levoglucosan (blue) vs time for the Vavihill site, Sweden. The inset shows a linear regression of EBC_{bb} from PMF vs levoglucosan.

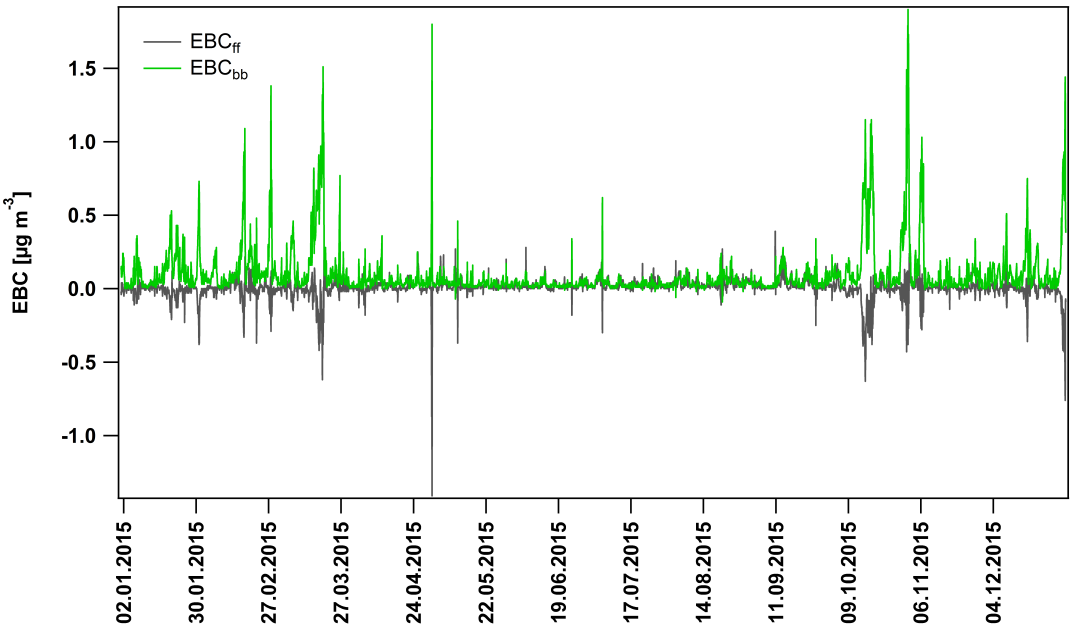

Figure 7.4: EBC_{bb} (green) and EBC_{ff} (black) from the Sandradewi approach for the Vavihill site, Sweden.

7.6 Comparison of EMEP model with observational derived results

Figures 7.5 and 7.6 compare daily mean values of modelled and observed EC components at all four sites. For Ispra and Kosetice the results are rather good in most cases, with Pearson's correlation coefficients of $r \approx 0.6$–0.8. The relative levels of biomass-burning ('bb') and fossil-fuel ('ff') EC are also quite well captured. For Kosetice, the EECCA/MACC model setup provides somewhat better results than the EMEP01 case for ff and total ('tot'), though EMEP01 performs better for bb. For Ispra, the EMEP01 case provides somewhat better agreement.

For Vavihill the results are mixed. The EC_{ff} component is captured well by the model ($r = 0.81$ for the EECCA/MACC case, 0.66 for EMEP01). The results for EC_{bb} are somewhat worse ($r = 0.40$ and 0.58 respectively), and substantially underpredicted.

The results for Finokalia are also mixed, but still r-values of around 0.5–0.6 are obtained for both EC_{ff} and EC_{bb}. The model's EC_{ff} is much lower than the observed with both model setups, however. This could be an emissions issue; for example, assumptions concerning the split of EC with respect to $PM_{2.5}$ are derived from data for Greece as a whole, may be especially uncertain for this Mediterranean island.

The results presented here for all sites are however roughly in line with those obtained in previous studies where the model was compared to the results of tracer-based source-apportionment. These studies also highlighted problems with underestimates of the biomass-burning emissions in most countries (e.g. Simpson et al. 2007, Genberg et al. 2011, 2013, Denier van der Gon et al. 2015).

Figure 7.7 presents the diurnal variations of the modelled and observed EC components at Kosetice and Ispra. This plot makes the general underestimate of EC concentrations clear,

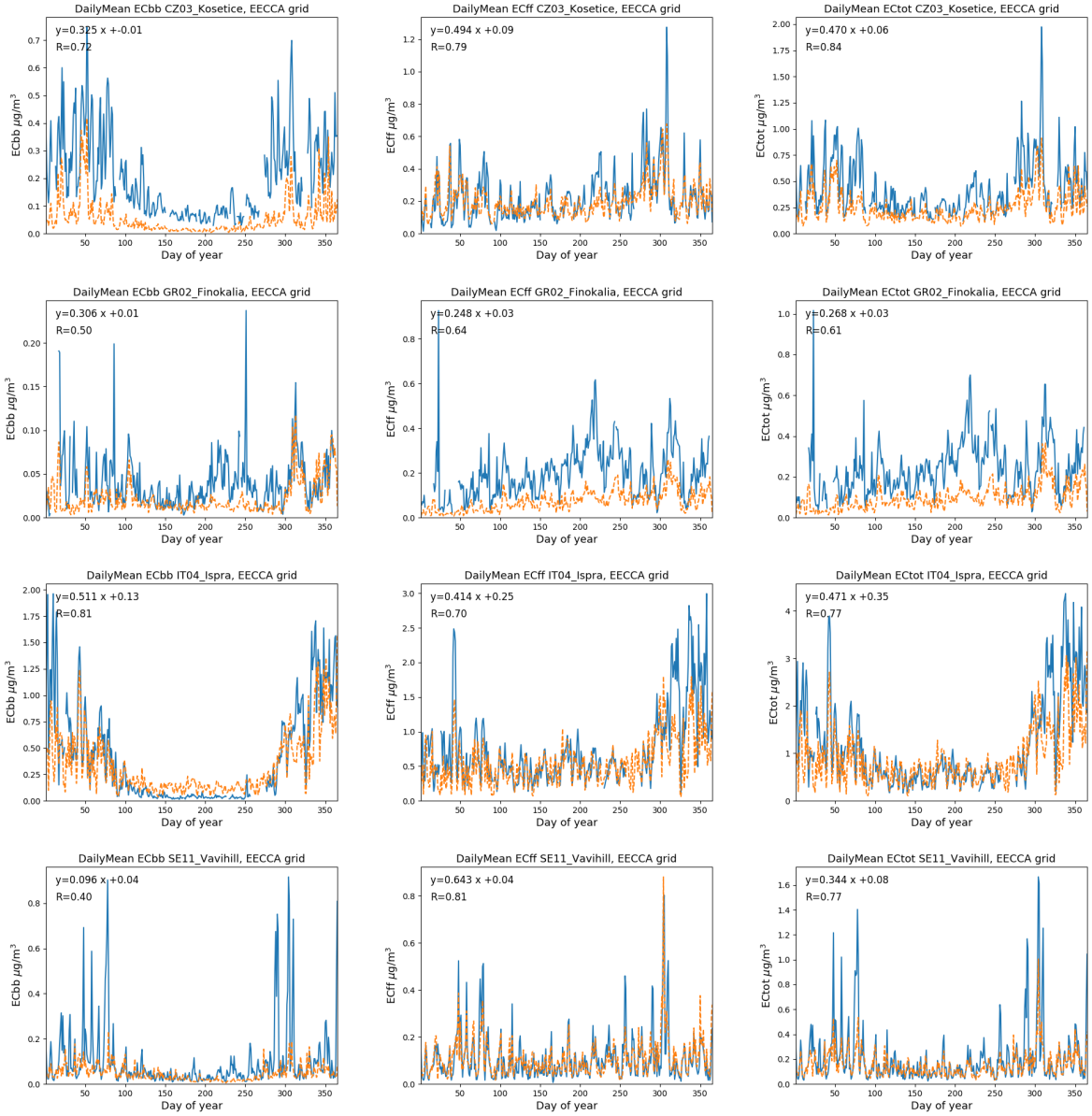

Figure 7.5: Comparison of modelled EC components (orange, dashed) against EBC components (blue, solid). Components are: bb (left), ff (centre), and tot (right). Results are daily means from EECCA/MACC (ca. 50 km) model run, 2015. Note: each plot has own y-axis. Unit: (μg m^{-3}).

but results are very mixed. At Kosetice, both model setups result in very low EC compared to the observed EBC_{bb}, but the modelled EC_{ff} matches observed EBC_{ff} quite well with the EECCA/MACC setup. At Ispra the EECCA/MACC case also seems to give better concentration levels than the EMEP01 case.

As noted above, the difference between the EECCA/MACC and EMEP01 cases is not just one of resolution, but also of the underlying inventory (EMEP or MACCIII). Probably the most important issue is that the base inventories are for $PM_{2.5}$, but that very different assumptions are made to estimate the EC_{ff} and EC_{bb} fractions from these $PM_{2.5}$ values. Another major problem is that these EC_{ff} +EC_{bb} fractions are only available at national scale, which means that estimates of the spatial distribution of EC emissions are very uncertain. Clearly,

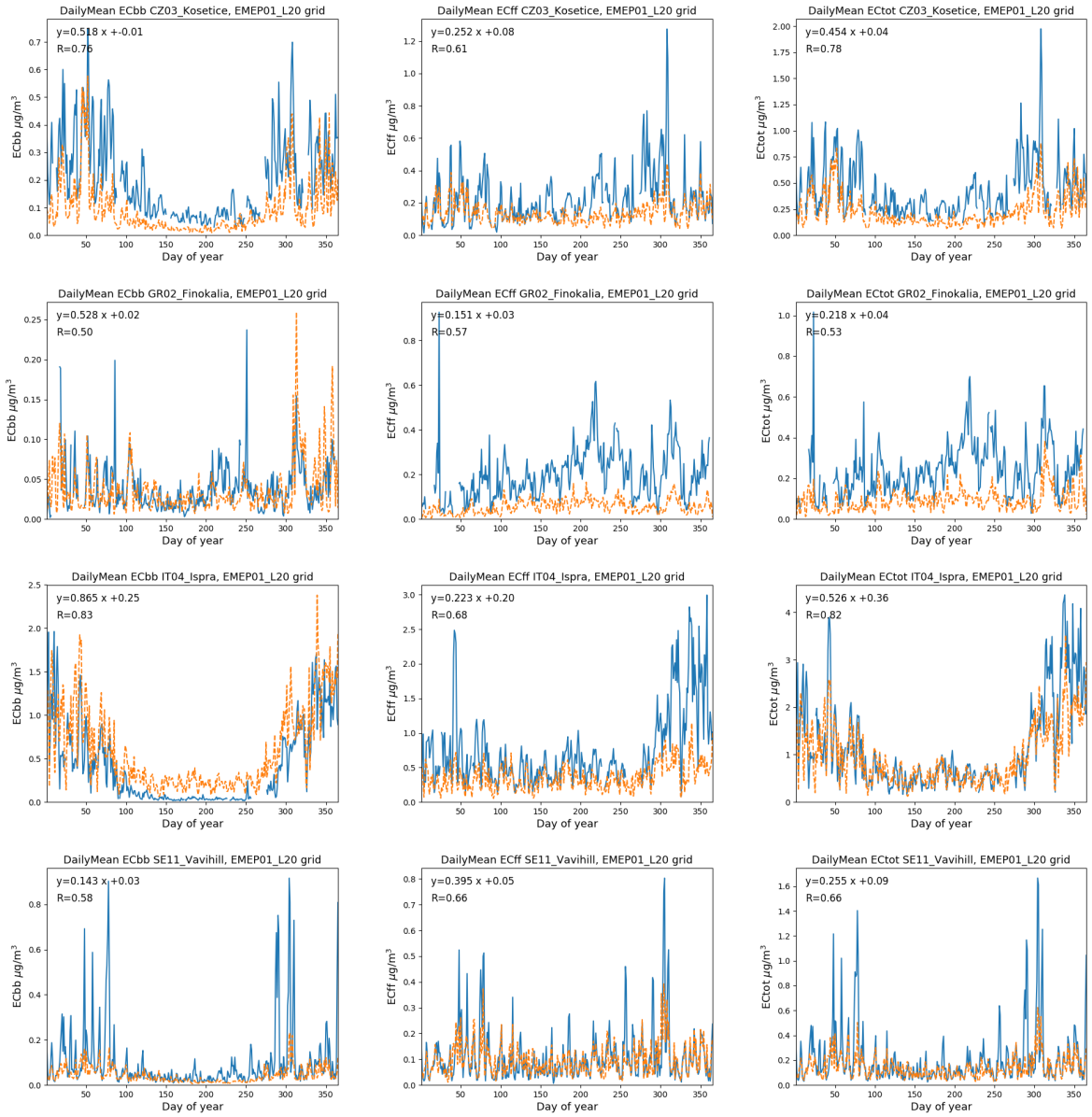

Figure 7.6: Comparison of modelled EC components (orange, dashed) against EBC components (blue, solid). Components are: bb (left), ff (centre), and tot (right). Results are daily means from the EMEP01 (0.1°) model run, 2015. Note: each plot has own y-axis. Unit: (μg m^{-3}).

this type of modelling work and evaluation would benefit from explicit inventories of EC_{ff} and EC_{bb} (and further of coal versus oil emissions, etc.)

However, despite these caveats, it is clear that these new EBC data are a very valuable source of new information on the sources of EC at each site.

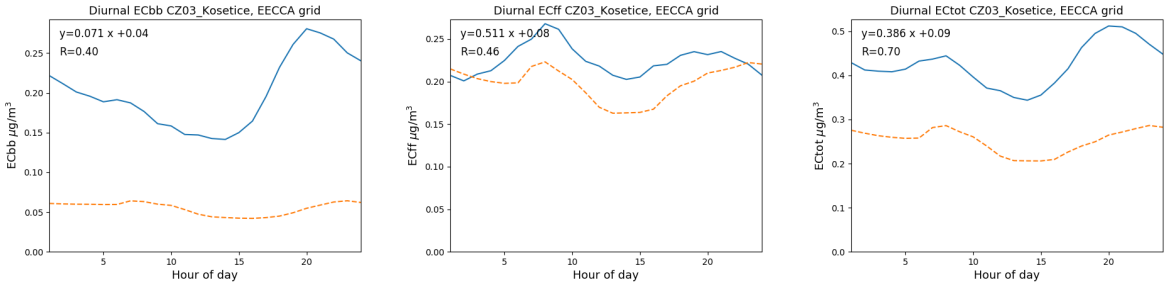

(a) Kosetice - EECCA/MACC

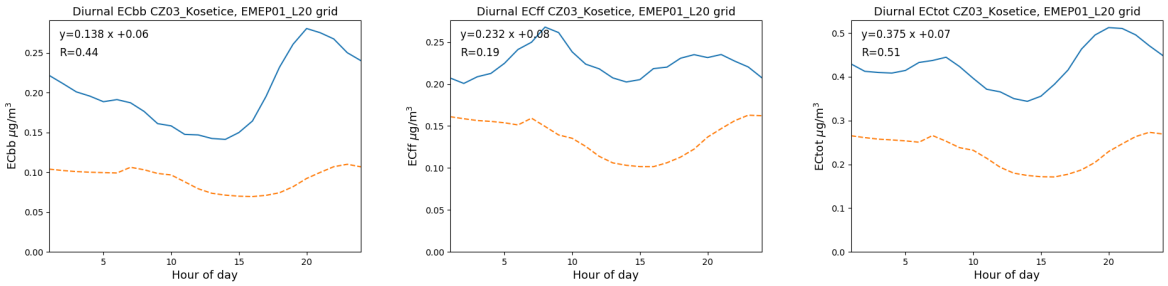

(b) Kosetice - EMEP01

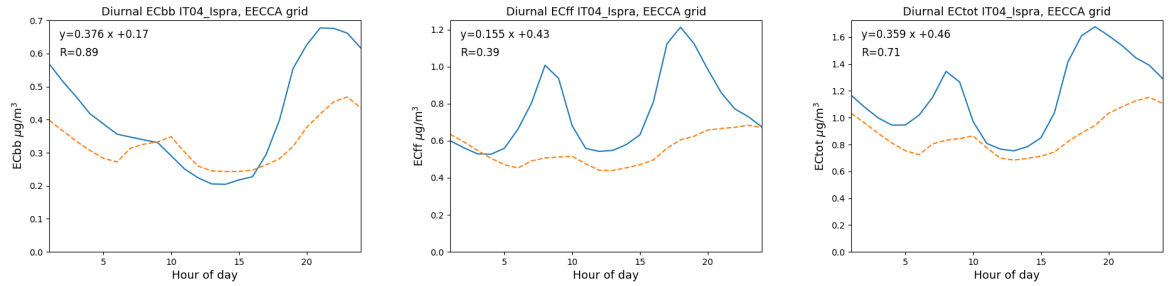

(c) Ispra - EECCA/MACC

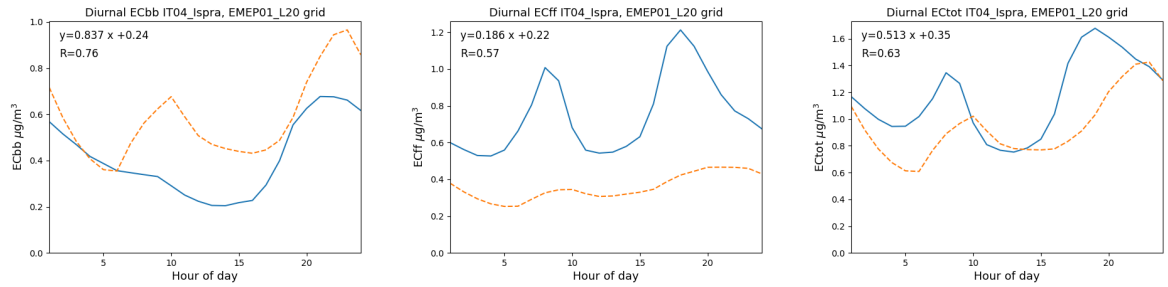

(d) Ispra - EMEP01

Figure 7.7: Comparison of diurnal variation at Kosetice and Ispra from two model versions. Notation as Fig. 7.5. Unit: (μg m^{-3}).

References

Bergstrom, R. W., Pilewskie, P., Russell, P. B., Redemann, J., Bond, T. C., Quinn, P. K., and Sierau, B.: Spectral absorption properties of atmospheric aerosols, Atmospheric Chemistry and Physics, 7, 5937–5943, doi:10.5194/acp-7-5937-2007, URL https://www.atmos-chem-phys.net/7/5937/2007/, 2007.

Bond, T. C., Bhardwaj, E., Dong, R., Jogani, R., Jung, S. K., Roden, C., Streets, D. G., and Trautmann, N. M.: Historical emissions of black and organic carbon aerosol from energy-related combustion, 1850-2000, Global Biogeochem. Cycles, 21, GB2018, 2007.

Canonaco, F., Crippa, M., Slowik, J. G., Baltensperger, U., and Prévôt, A. S. H.: SoFi, an IGOR-based interface for the efficient use of the generalized multilinear engine (ME-2) for the source apportionment: ME-2 application to aerosol mass spectrometer data, Atmospheric Measurement Techniques, 6, 3649–3661, doi:10.5194/amt-6-3649-2013, URL http://www.atmos-meas-tech.net/6/3649/2013/, 2013.

Cavalli, F., Viana, M., Yttri, K. E., Genberg, J., and Putaud, J.-P.: Toward a standardised thermal-optical protocol for measuring atmospheric organic and elemental carbon: the EUSAAR protocol, Atmospheric Measurement Techniques, 3, 79–89, doi:10.5194/amt-3-79-2010, URL http://www.atmos-meas-tech.net/3/79/2010/, 2010.

Denier van der Gon, H. A. C., Bergström, R., Fountoukis, C., Johansson, C., Pandis, S. N., Simpson, D., and Visschedijk, A. J. H.: Particulate emissions from residential wood combustion in Europe - revised estimates and an evaluation, Atmos. Chem. Physics, pp. 6503–6519, doi:doi:10.5194/acp-15-6503-2015, URL http://www.atmos-chem-phys.net/15/6503/2015/, 2015.

Elser, M., Huang, R.-J., Wolf, R., Slowik, J. G., Wang, Q., Canonaco, F., Li, G., Bozzetti, C., Daellenbach, K. R., Huang, Y., Zhang, R., Li, Z., Cao, J., Baltensperger, U., El-Haddad, I., and Prévôt, A. S. H.: New insights into $PM_{2.5}$ chemical composition and sources in two major cities in China during extreme haze events using aerosol mass spectrometry, Atmospheric Chemistry and Physics, 16, 3207–3225, doi:10.5194/acp-16-3207-2016, URL https://www.atmos-chem-phys.net/16/3207/2016/, 2016.

Fialho, P., Hansen, A., and Honrath, R.: Absorption coefficients by aerosols in remote areas: a new approach to decouple dust and black carbon absorption coefficients using seven-wavelength Aethalometer data, Journal of Aerosol Science, 36, 267 – 282, doi:http://dx.doi.org/10.1016/j.jaerosci.2004.09.004, URL http://www.sciencedirect.com/science/article/pii/S0021850204003398, 2005.

Genberg, J., Hyder, M., Stenström, K., Bergström, R., Simpson, D., Fors, E., Jönsson, J. Å., and Swietlicki, E.: Source apportionment of carbonaceous aerosol in southern Sweden, Atmos. Chem. Physics, 11, 11 387 – 11 400, doi:10.5194/acp-11-11387-2011, URL http://www.atmos-chem-phys-discuss.net/11/13575/2011/, 2011.

Genberg, J., Denier van der Gon, H. A. C., Simpson, D., Swietlicki, E., Areskoug, H., Beddows, D., Ceburnis, D., Fiebig, M., Hansson, H. C., Harrison, R. M., Jennings, S. G., Saarikoski, S., Spindler, G., Visschedijk, A. J. H., Wiedensohler, A., Yttri, K. E., and Bergström, R.: Light-absorbing carbon in Europe - measurement and modelling, with a

focus on residential wood combustion emissions, Atmospheric Chemistry and Physics, 13, 8719–8738, doi:10.5194/acp-13-8719-2013, URL http://www.atmos-chem-phys.net/13/8719/2013/, 2013.

Herich, H., Hueglin, C., and Buchmann, B.: A 2.5 year's source apportionment study of black carbon from wood burning and fossil fuel combustion at urban and rural sites in Switzerland, Atmospheric Measurement Techniques, 4, 1409–1420, doi:10.5194/amt-4-1409-2011, URL http://www.atmos-meas-tech.net/4/1409/2011/, 2011.

Kuenen, J. J. P., Visschedijk, A. J. H., Jozwicka, M., and Denier van der Gon, H. A. C.: TNO-MACC-II emission inventory; a multi-year (2003–2009) consistent high-resolution European emission inventory for air quality modelling, Atmos. Chem. Physics, 14, 10 963–10 976, doi:10.5194/acp-14-10963-2014, URL http://www.atmos-chem-phys.net/14/10963/2014/acp-14-10963-2014.html, 2014.

MACC-III: Report on the update of global and European anthropogenic emissions., Tech. Rep. COPERNICUS Grant agreement 633080, MACC-III (Monitoring Atmospheric Composition and Climate, 2015.

Martinsson, J., Abdul Azeem, H., Sporre, M. K., Bergström, R., Ahlberg, E., Öström, E., Kristensson, A., Swietlicki, E., and Eriksson Stenström, K.: Carbonaceous aerosol source apportionment using the Aethalometer model – evaluation by radiocarbon and levoglucosan analysis at a rural background site in southern Sweden, Atmospheric Chemistry and Physics, 17, 4265–4281, doi:10.5194/acp-17-4265-2017, URL https://www.atmos-chem-phys.net/17/4265/2017/, 2017.

Sandradewi, J., Prevot, A. S. H., Szidat, S., Perron, N., Alfarra, M. R., Lanz, V. A., Weingartner, E., and Baltensperger, U.: Using aerosol light absorption measurements for the quantitative determination of wood burning and traffic emission contributions to particulate matter, Environ. Sci. Technol., 42, 3316–3323, doi:10.1021/es702253m, 2008.

Sciare, J., Oikonomou, K., Favez, O., Liakakou, E., Markaki, Z., Cachier, H., and Mihalopoulos, N.: Long-term measurements of carbonaceous aerosols in the Eastern Mediterranean: evidence of long-range transport of biomass burning, Atmospheric Chemistry and Physics, 8, 5551–5563, doi:10.5194/acp-8-5551-2008, URL https://www.atmos-chem-phys.net/8/5551/2008/, 2008.

Simpson, D., Yttri, K., Klimont, Z., Kupiainen, K., Caseiro, A., Gelencsér, A., Pio, C., and Legrand, M.: Modeling Carbonaceous Aerosol over Europe. Analysis of the CARBOSOL and EMEP EC/OC campaigns, J. Geophys. Res., 112, D23S14, doi:10.1029/2006JD008158, 2007.

Sun, J., Zhi, G., Hitzenberger, R., Chen, Y., Tian, C., Zhang, Y., Feng, Y., Cheng, M., Zhang, Y., Cai, J., Chen, F., Qiu, Y., Jiang, Z., Li, J., Zhang, G., and Mo, Y.: Emission factors and light absorption properties of brown carbon from household coal combustion in China, Atmospheric Chemistry and Physics, 17, 4769–4780, doi:10.5194/acp-17-4769-2017, URL https://www.atmos-chem-phys.net/17/4769/2017/, 2017.

Vrekoussis, M., Liakakou, E., KoÃğak, M., Kubilay, N., Oikonomou, K., Sciare, J., and Mihalopoulos, N.: Seasonal variability of optical properties of

aerosols in the Eastern Mediterranean, Atmospheric Environment, 39, 7083 – 7094, doi:http://dx.doi.org/10.1016/j.atmosenv.2005.08.011, URL http://www.sciencedirect.com/science/article/pii/S1352231005007454, 2005.

WMO: WMO/GAW Aerosol measurement procedures, guidelines and recommendations, gAW Report No. 227/WMO-No. 1177, http://library.wmo.int/opac/doc_num.php?explnum_id=3073, ISBN 978-92-63-11177-7, 2016.

Yttri, K., Aas, W., Bjerke, A., Ceburnus, D., Dye, C., Emblico, L., Facchini, M., Forster, C., Hanssen, J., Hansson, H., Jennings, S., Maenhaut, W., and Tørseth, K.: Elemental and organic carbon in PM_{10}: A one year measurement campaign within the European Monitoring and Evaluation Programme EMEP, Atmos. Chem. Physics, 7, 56 711–5725, 2007.

Part III

Technical EMEP Developments

CHAPTER 8

Updates to the EMEP MSC-W model, 2016-2017

David Simpson, Robert Bergström, Hannah Imhof and Peter Wind

This chapter summarises the changes made to the EMEP MSC-W model since Simpson et al. (2016), and along with changes discussed in Simpson et al. (2013, 2015) and Tsyro et al. (2014), updates the standard description given in Simpson et al. (2012). The model version used for reporting this year is denoted rv4.15. Table 8.2 summarises the changes made in the EMEP model since the version documented in Simpson et al. (2012).

8.1 Chemical mechanism

The new 'EmChem16' chemical mechanism was developed mainly up to the year 2016, and is a preliminary modernisation of the previously used EmChem09 (2009-era) scheme. The main features of the update are:

1. The EmChem09 isoprene chemistry (which was based upon Paulson and Seinfeld 1992) has been replaced by the more recent 'CheT2' scheme of Squire et al. (2015). This scheme, traceable to the Master Chemical Mechanism (MCM, Jenkin et al. 2015, and refs therein), accounts for some of the recent findings concerning isoprene chemistry (e.g. Archibald et al. 2010), for example giving more HOx regeneration in low-NOx high isoprene conditions. (Thanks are due to A. Archibald, University of Bristol, and M.E. Jenkin, Atmospheric Chemistry Services, for making this scheme available to EMEP.)

2. Simple gas-phase mechanisms were added for two explicit monoterpenes (MT), α-pinene, β-pinene, plus an additional species, XTERP, representing a mix of remaining MT. Each MT species is assumed to react with OH to produce a peroxy radical (TERPO2), which further reacts following a scheme based upon CAM-chem (Lamarque et al. 2012). Additionally, an instantaneous production of inert SOA, proportional to MT emissions, is assumed to arise from sesqui-terpenes.

3. Many rate-coefficients have been updated to those of the latest MCM scheme, MCM-v3.3.1 (Jenkin et al. 2015), and a bug fixed for the rate of PAN formation. As part of this update, and in order to improve the model's applicability to global atmospheric modelling, the species HO_2NO_2 was added to EmChem16.

EmChem16 should be seen as an interim update, with a view to a more finished version as EmChem17 or EmChem18. The main aim of this work is to provide a code which is comparable to that of MCMv3.3.1. Ongoing work is comparing these schemes (and others) in detail, and this will likely result in further changes.

8.2 Deposition

Dry deposition of gases is modelled using deposition velocities and a resistance approach (for details see Simpson et al. 2012). The model makes use of tabulated gaseous diffusivities, effective solubilities and reactivity factors for the depositing gases, loosely based upon the scheme of Wesely (1989).

During 2017, some of these parameters have been updated, based on new solubility data (Sander 2015) and suggestions presented in Zhang et al. (2002, 2003). For a few species the diffusivities have also been revised (based on Massman 1998, Tang et al. 2014, 2015).

Notable changes compared to Table S18 of Simpson et al. (2012) include modified diffusivities for ozone, aldehydes, hydroperoxides and PAN; lower effective solubility for formaldehyde; higher reactivity factors for NO2, PAN, aldehydes and organic hydroperoxides. Table 8.1 presents the revised parameters as used in the EmChem16 scheme.

Deposition parameters for a large number of organic compounds were further added, in order to provide more realistic accounting for deposition when the more-extensive 'CRI' chemical mechanisms are in use.

Finally, the model code was improved to consistently make use of the gas and particle fractions of each compound in both the wet and dry deposition calculations.

8.3 Land-cover and biogenic VOC

Land-cover in the EMEP model is required for two main roles:

(a) for the deposition calculations (which also includes stomatal uptake), which affect for example the relation between near-surface (3 m) and grid-average concentration.

(b) for biogenic volatile organic compound (BVOC) emissions.

As described in Simpson et al. (2012), the EMEP model uses fine-scale (5km resolution) European data which merges the CORINE land-cover maps (de Smet and Hettelingh 2001) with data and from the Stockholm Environment Institute at York (SEIY) which had more detail on agricultural land-cover (*ibid.*). The merged data-set was provided to MSC-W by the EMEP Coordinating Centre for Effects (Max Posch, CCE, pers. comm).

This CCE/SEI merge is still the default land-cover over Europe, but as from EMEP model rv4.12 we now use a different global land-cover map for regions outside the CCE/SEI domain. The previous data, from the 'GLC-2000' land-cover data-set (`http://bioval.jrc.ec.europa.eu/products/glc2000/glc2000.php`), have now been replaced

Table 8.1: Properties of gases for EmChem16 dry deposition calculations: diffusivity ratio for a gas i, $D_r = D_{H2O}/D_i$, solubility index H^* (based on effective Henry's Law constants), and reactivity index f_0. Update of Wesely (1989), based largely on Zhang et al. (2002) and references in Notes.

Gas	D_r	H^*	f_0
SO2[†]	1.9	1.0×10^5	0.0
O3	1.51[a]	1.0×10^{-2}	1.0
NO2	1.6[b]	1.0×10^{-2}	0.5[c]
HNO3[d]	1.9	1.0×10^{14}	0.0
HCHO	1.4[e]	3.2×10^{3}[f]	0.2[g]
CH3CHO[h]	2.1[h]	13[f]	0.05[g]
CH3OOH[i]	1.9[e]	3.0×10^{2}[f]	0.2[j]
NH3	1.1[k]	1.0×10^{5}[l]	0.0
PAN[m]	2.8[e]	3[f]	0.5[n]
HONO	1.6[b]	2.6×10^{5}[g]	0.5[o]

Notes: (†) the parameters for SO2 are used also for H2O2 dry deposition in EmChem16; (a) based on Massman (1998) – the diffusion coefficient of ozone in air has not been measured and has a large uncertainty (Tang et al. 2014); (b) The diffusivity has a large uncertainty (Tang et al. 2014); (c) increased from 0.1 (based on the discussion in Zhang et al. (2002) but using a somewhat lower f_0 than their corresponding β-value of 0.8); (d) used also for HO2NO2; (e) D_r is based on an average of three different estimation methods provided by the US EPA; (f) based on Sander (2015); (g) based on Zhang et al. (2002); (h) used also for heavier aldehydes in EmChem16 (the D_r value is probably a bit too high for acetaldehyde); (i) used also for ethyl hydroperoxide, D_r based on estimated diffusion coefficients using the FSG-method (Fuller et al. 1966); (j) increased from 0.1 (Zhang et al. 2002, use a much higher corresponding β-value of 0.8); (k) based on Tang et al. (2014); (l) H^* increased compared to Wesely value, reflecting European pH conditions; (m) used also for MPAN in EmChem16; (n) increased from 0.1 (based on Zhang et al. 2002, that use a β-value of 0.6); (o) increased from 0.1 (note that Zhang et al. 2002, assume a very efficient deposition of HONO, with a β-value of 2.0);

by data based mainly upon the Community Land Model (`http://www.cgd.ucar.edu/models/clm/`, Oleson et al. 2010, Lawrence et al. 2011).

Both the GLC and CLM data-sets have pros and cons. The GLC data has the advantage that non-vegetated areas such as water, ice, and urban are explicitly delineated, and also that the density of vegetation is indicated to some extent with qualifiers such as 'sparse'. The two main disadvantages of the GLC data for our purposes are that (i) many categories consist of mixes of e.g. coniferous and deciduous forest, and (ii) there is no distinction between ecosystem zones, e.g. no indication if a forest is boreal, temperate or tropical.

The CLM database on the other had has clearly delineated types of forest, grouped as boreal, temperate, and tropical, and thus these are easier to handle when assigning typical foliar biomass or emissions rates. The CLM data also underlies much of the work being done with the MEGAN database (Guenther et al. 2012), so comparison of emissions between our work and MEGAN is simplified.

For this work we have merged the GLC2000 and CLM data-sets through the following procedure:

1. GLC2000 is used to define water, ice, urban and bare surfaces, and then 'high' and 'low' vegetation (HV, LV).
2. Where high vegetation is labelled as sparse, we allocate 50% as HV, 50% as LV.
3. Where low vegetation is labelled as sparse, we allocate 50% as LV, 50% as bare.
4. For each grid square we then allocate the HV and LV vegetation according to CLM categories.

8.4 Local fractions

As noted in chapter 5 the EMEP model can now track the fraction of specific pollutants and sources within each each grid-square. For more details see chapter 5.

8.5 Other improvements

- GNFR emissions and SNAP emissions can be combined.
- Hourly emission time-factors can be specified separately for individual countries or regions (provided those emissions are defined with an individual code). Can be useful for instance if time factors for traffic in a specific city are known in more details than the default values.
- The model fully support Lambert conical conformal projection.
- Smoother interpolation of input data. In cases where the model grid has finer resolution than the input data, interference patterns could occur. The newer version avoid these problems.
- For nested runs, an option is added to save only the data at the boundaries of the inner grid. This dramatically reduces the size of the data files and the disk space requirements.

Table 8.2: Summary of major EMEP MSC-W model versions from 2012–2017. Extends Table S1 of Simpson et al. 2012

Version	Update	Ref[(a)]
rv4.15	EmChem16 scheme	This Report
rv4.14	Updated chemical scheme	This Report
rv4.12	New global land-cover and BVOC	This Report
rv4.10	Public domain (Oct. 2016)	R2016
rv4.9	Updates for GNFR sectors, DMS, sea-salt, dust, S_A and γ, N_2O_5	
rv4.8	Public domain (Oct. 2015) ShipNOx introduced	R2015
rv4.7	Used for reporting, summer 2015 : New calculations of aerosol surface area; ; New gas-aerosol uptake and N2O5 hydrolysis rates ; Added 3-D calculations pf aerosol extinction and AODs; ; Emissions - new flexible mechanisms for interpolation and merging sources ; Global - monthly emissions from ECLIPSE project ; Global - LAI changes from LPJ-GUESS model ; WRF meteorology (Skamarock and Klemp 2008) can now be used directly in EMEP model.	R2015
rv4.6	Used for Euro-Delta SOA runs Revised boundary condition treatments ; ISORROPIA capability added	R2015
rv4.5	Sixth open-source (Sep 2014) Improved dust, sea-salt, SOA modelling ; AOD and extinction coefficient calculations updated ; Data assimilation system added ; Hybrid vertical coordinates replace earlier sigma ; Flexibility of grid projection increased.	R2014
rv4.4	Fifth open-source (Sep 2013) ; Improved dust and sea-salt modelling ; AOD and extinction coefficient calculations added ; gfortran compatibility improved	R2014, R2013
rv4.3	Fourth public domain (Mar. 2013) ; Initial use of namelists ; Smoothing of MARS results ; Emergency module for volcanic ash and other events; Dust and road-dust options added as defaults ; Advection algorithm changed	R2013
rv4.0	Third public domain (Sep. 2012) As documented in Simpson et al. (2012)	R2013
v2011-06	Second public domain (Aug. 2011)	
rv3	First public domain (Sep. 2008)	

Notes: (a) R2015 refers to EMEP Status report 1/2015, etc.

References

Archibald, A. T., Cooke, M. C., Utembe, S. R., Shallcross, D. E., Derwent, R. G., and Jenkin, M. E.: Impacts of mechanistic changes on HOx formation and recycling in the oxidation of isoprene, Atmos. Chem. Physics, 10, 8097–8118, 2010.

de Smet, P. and Hettelingh, J.-P.: Intercomparison of Current Landuse/Land Cover Databases, in: Modelling and Mapping of Critical Thresholds in Europe. Status report 2001, edited by Posch, M., de Smet, P., Hettelingh, J.-P., and Downing, R., Coordination Centre for Effects, RIVM, Bilthoven, The Netherlands, 2001.

Fuller, E. N., Schettler, P. D., and Giddings, J. C.: A new method for prediction of binary gas-phase diffusion coefficients, Ind. Eng. Chem., 58, 18–27, 1966.

Guenther, A. B., Jiang, X., Heald, C. L., Sakulyanontvittaya, T., Duhl, T., Emmons, L. K., and Wang, X.: The Model of Emissions of Gases and Aerosols from Nature version 2.1 (MEGAN2.1): an extended and updated framework for modeling biogenic emissions, Geoscientific Model Dev., 5, 1471–1492, doi:10.5194/gmd-5-1471-2012, URL `http://www.geosci-model-dev.net/5/1471/2012/`, 2012.

Jenkin, M. E., Young, J. C., and Rickard, A. R.: The MCM v3.3.1 degradation scheme for isoprene, Atmos. Chem. Physics, 15, 11 433–11 459, doi:10.5194/acp-15-11433-2015, 2015.

Lamarque, J. F., Emmons, L. K., Hess, P. G., Kinnison, D. E., Tilmes, S., Vitt, F., Heald, C. L., Holland, E. A., Lauritzen, P. H., Neu, J., Orlando, J. J., Rasch, P. J., and Tyndall, G. K.: CAM-chem: description and evaluation of interactive atmospheric chemistry in the Community Earth System Model, Geoscientific Model Dev., 5, 369–411, doi:10.5194/gmd-5-369-2012, 2012.

Lawrence, D. M., Oleson, K. W., Flanner, M. G., Thornton, P. E., Swenson, S. C., Lawrence, P. J., Zeng, X., Yang, Z.-L., Levis, S., Sakaguchi, K., Bonan, G. B., and Slater, A. G.: Parameterization Improvements and Functional and Structural Advances in Version 4 of the Community Land Model, J. Adv. Mod. Earth Sys., 3, doi:10.1029/2011MS000045, 2011.

Massman, W.: A review of the molecular diffusivities of H2O, CO2, CH4, CO, O-3, SO2, NH3, N2O, NO, AND NO2 in air, O-2 AND N-2 near STP, Atmos. Environ., 32, 1111–1127, 1998.

Oleson, K., Lawrence, D., Bonan, G., Flanner, M., Kluzek, E., Lawrence, P., Levis, S., Swenson, S., Thornton, P., Dai, A., Decker, M., Dickinson, R., Feddema, J., Heald, C., Hoffman, F., Lamarque, J., Mahowald, N., Niu, G., Qian, T., Randerson, J., Running, S., Sakaguchi, K., Slater, A., Stockli, R., Wang, A., Yang, Z., Zeng, X., and Zeng, X.: Technical Description of version 4.0 of the Community Land Model (CLM), NCAR Technical Note NCAR/TN-478+STR, National Center for Atmospheric Research, National Center for Atmospheric Research, Boulder, CO, 2010.

Paulson, S. E. and Seinfeld, J.: Development and evaluation of a photooxidation mechanism for isoprene, J. Geophys. Res., 97, 20 703–20 715, 1992.

Sander, R.: Compilation of Henry's law constants (version 4.0) for water as solvent, Atmospheric Chemistry and Physics, 15, 4399–4981, doi:10.5194/acp-15-4399-2015, URL https://www.atmos-chem-phys.net/15/4399/2015/, 2015.

Simpson, D., Benedictow, A., Berge, H., Bergström, R., Emberson, L. D., Fagerli, H., Hayman, G. D., Gauss, M., Jonson, J. E., Jenkin, M. E., Nyíri, A., Richter, C., Semeena, V. S., Tsyro, S., Tuovinen, J.-P., Valdebenito, A., and Wind, P.: The EMEP MSC-W chemical transport model – technical description, Atmos. Chem. Physics, 12, 7825–7865, doi:10.5194/acp-12-7825-2012, 2012.

Simpson, D., Tsyro, S., Wind, P., and Steensen, B. M.: EMEP model development, in: Transboundary acidification, eutrophication and ground level ozone in Europe in 2011. EMEP Status Report 1/2013, The Norwegian Meteorological Institute, Oslo, Norway, 2013.

Simpson, D., Tsyro, S., and Wind, P.: Updates to the EMEP/MSC-W model, in: Transboundary particulate matter, photo-oxidants, acidifying and eutrophying components. EMEP Status Report 1/2015, pp. 129–138, The Norwegian Meteorological Institute, Oslo, Norway, 2015.

Simpson, D., Nyíri, A., Tsyro, S., Valdebenito, Á., and Wind, P.: Updates to the EMEP/MSC-W model, in: Transboundary particulate matter, photo-oxidants, acidifying and eutrophying components. EMEP Status Report 1/2016, The Norwegian Meteorological Institute, Oslo, Norway, 2016.

Skamarock, W. C. and Klemp, J. B.: A time-split nonhydrostatic atmospheric model for weather research and forecasting applications, J. Comp. Phys., 227, 3465–3485, doi:10.1016/j.jcp.2007.01.037, 2008.

Squire, O. J., Archibald, A. T., Griffiths, P. T., Jenkin, M. E., Smith, D., and Pyle, J. A.: Influence of isoprene chemical mechanism on modelled changes in tropospheric ozone due to climate and land use over the 21st century, Atmospheric Chemistry and Physics, 15, 5123–5143, doi:10.5194/acp-15-5123-2015, URL http://www.atmos-chem-phys.net/15/5123/2015/, 2015.

Tang, M. J., Cox, R. A., and Kalberer, M.: Compilation and evaluation of gas phase diffusion coefficients of reactive trace gases in the atmosphere: volume 1. Inorganic compounds, Atmospheric Chemistry and Physics, 14, 9233–9247, doi:10.5194/acp-14-9233-2014, URL https://www.atmos-chem-phys.net/14/9233/2014/, 2014.

Tang, M. J., Shiraiwa, M., Pöschl, U., Cox, R. A., and Kalberer, M.: Compilation and evaluation of gas phase diffusion coefficients of reactive trace gases in the atmosphere: Volume 2. Diffusivities of organic compounds, pressure-normalised mean free paths, and average Knudsen numbers for gas uptake calculations, Atmospheric Chemistry and Physics, 15, 5585–5598, doi:10.5194/acp-15-5585-2015, URL https://www.atmos-chem-phys.net/15/5585/2015/, 2015.

Tsyro, S., Karl, M., Simpson, D., Valdebenito, A., and Wind, P.: Updates to the EMEP/MSC-W model, in: Transboundary particulate matter, photo-oxidants, acidifying and eutrophying components. EMEP Status Report 1/2014, pp. 143–146, The Norwegian Meteorological Institute, Oslo, Norway, 2014.

Wesely, M.: Parameterization of surface resistances to gaseous dry deposition in regional scale numerical models, Atmos. Environ., 23, 1293–1304, 1989.

Zhang, L., Moran, M., Makar, P., Brook, J., and Gong, S.: Modelling gaseous dry deposition in AURAMS: a unified regional air-quality modelling system, Atmos. Environ., 36, 537–560, 2002.

Zhang, L., Brook, J., and Vet, R.: A revised parameterization for gaseous dry deposition in air-quality models, Atmos. Chem. Physics, 3, 2067–2082, 2003.

CHAPTER 9

Development in the monitoring network, data quality and database infrastructure

Wenche Aas, Anne Hjellbrekke, Richard Olav Rud, Sverre Solberg and Kjetil Tørseth

9.1 Compliance with the EMEP monitoring strategy

The monitoring obligations in EMEP is described in the Monitoring Strategy for 2010-2019 (UNECE (2009), Tørseth et al. (2012)). The complexity in the monitoring program with respect to the number of variables and sites, whether it is a level 1 or level 2 parameter, and the required time resolution (hourly, daily, weekly), makes it challenging to assess whether a country is in compliance or not. CCC has developed an index to illustrate to what extent the Parties comply.

For the level 1 parameters an index is defined, calculated based on what has been reported compared to what is expected. It is recommended to have one EMEP site pr 50.000 km^2, but this target number is adjusted for very large countries (i.e. KZ, RU, TR and UA). The components and number of variables to be measured in accordance to the strategy is as follows: major inorganic ions in precipitation (10 variables), major inorganic components in air (13 variables), ozone (1 variable), PM mass (2 variables) and heavy metals in precipitation (7 variables). For heavy metals, the sampling frequency is weekly, and for the other components it is daily or hourly (ozone). Based on the relative implementation of the different variables, the index has been given the following relative weights: Inorganics in precipitation: 30%, inorganics in air: 30%, ozone: 20%, PM mass: 10%, heavy metals: 10%.

Figure 9.1 summarises the compliance in 2015 compared to 2000, 2005 and 2010. The countries are sorted from left to right with increasing index for 2015. Slovenia has full score as they measure all the required parameters with satisfactory sampling frequency. Estonia, The Netherlands, Slovakia, Denmark, and Switzerland have almost complete program with

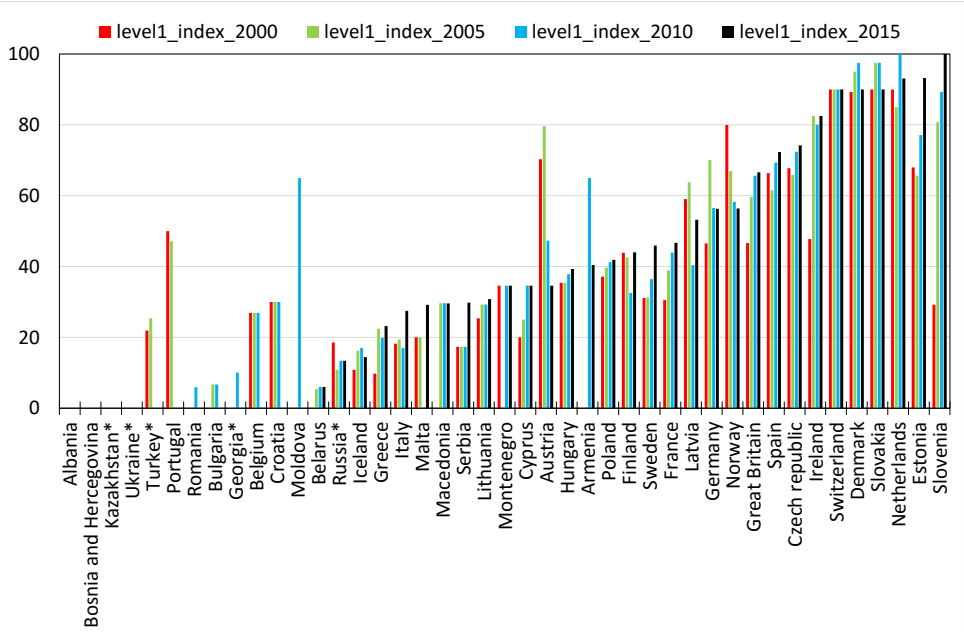

Figure 9.1: Index for implementation of the EMEP monitoring strategy, level 1 based on what has been reported for 2000, 2005, 2010 and 2015. * means adjusted land area

an index of 90% or higher. Small countries with requirements of less number of level 1 sites seem to comply easier than large countries.

Since 2010, 42% of the Parties have improved their monitoring programme, while 28% have a decrease. Improvements are seen in e.g. France and Great Britain. Some new Parties have begun monitoring, such as Macedonia and Armenia, while others have stopped reporting/measuring, e.g. Portugal, Croatia and Turkey. In Figure 2.4 in Chapter 2.2, the geographical distribution of level 1 sites is mapped for 2015. In large parts of Europe implementation of the EMEP monitoring strategy is far from satisfactory.

For the level 2 parameters, an index based system has not been defined, but mapping the site distribution illustrate the compliance to the monitoring strategy. 56 sites reported at least one of the required EMEP level 2 parameters relevant to this report (aerosols (46 sites), photo-oxidants (23 sites) and trace gases (10 sites)). The sites with measurements of POPs and heavy metals are covered in the EMEP status reports 2 and 3. Figure 9.2 shows that level 2 measurements of aerosols have better spatial coverage than oxidant precursors (VOC + methane) and trace gases. Few sites have a complete measurement program, and only 9 sites have a complete aerosol program. Nevertheless, regarding the aerosol monitoring, there have been large improvements in the spatial coverage and the data quality over the last decade. Standardization and reference methodologies have been developed, and the reporting has improved significantly with much more metadata information available. For oxidant precursors and trace gases, there are ongoing improvement in the measurement capabilities resulting from recent development in research projects such as ICOS (Integrated Carbon Observation System), InGOS (Integrated non-CO_2 Greenhouse gas Observation Sys-

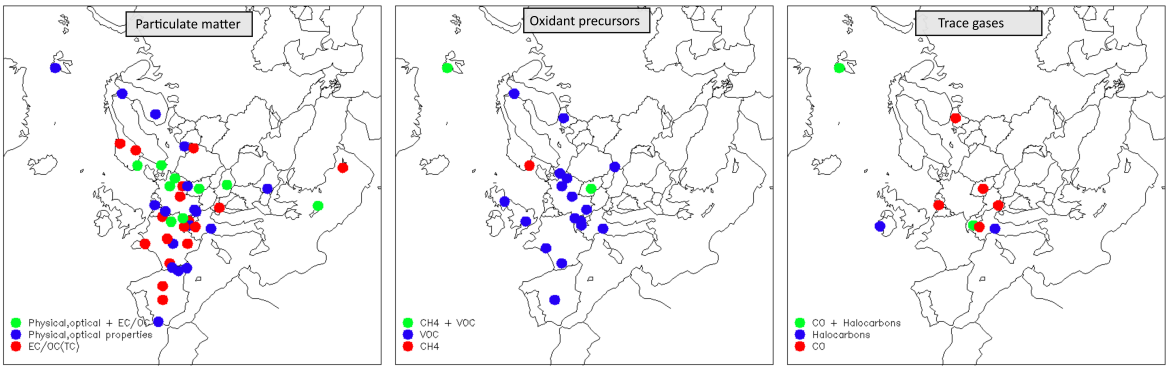

Figure 9.2: Sites measuring and reporting EMEP level 2 parameters for the year 2015

tem) and ACTRIS (Aerosols, Clouds, and Trace gases Research InfraStructure Network) in co-operation with the WMO Global Atmospheric Watch Programme (GAW).

9.2 Updates in reporting templates and guidelines

In addition to the requirements of variables to be measured as defined in the EMEP monitoring strategy discussed above, it is important that the data are reported in time to ensure that they can be quality assured and included in the database. This allows them to be included in the annual model validation, interpretations for the EMEP status reports, as well as other regional assessments and studies carried out beyond EMEP.

Figure 9.3 shows the status of the submission of data for 2015 and to what extent the data were reported in time. It is obvious that large volumes of data are reported late and some not at all. Of the 33 Parties reporting either level 1 or level 2 data, about 60% reported in time within the deadline of 31 July 2016.

To improve the timelines and quality of the data reporting, an online data submission and validation tool was launched in spring 2016 (http://ebas-submit-tool.nilu.no). This tool gives data submitters a possibility to check and correct their files before submitting them. The tool gives information on how to best troubleshoot errors in the file, including information on how to format the data files, as well as offering the user a way to plot data. The tool is designed to give the data submitters direct feedback on the formatted NASA Ames files and to deliver files through online data submission.

The format checker is directly linked to all (ca 40) data format templates located at http://ebas-submit.nilu.no/ and the ftp server designed for incoming data. The tool aims to:

- Check the consistency of their NASA Ames file.
- Upload data to EBAS submissions in case it passes the check.

EMEP data should from now on be submitted using this submission tool, unless otherwise have been agreed upon. There are many users that check their files using the submission tool, more than 700 users the last year, and this has improved the correctness of the data files significantly. However, relatively few users are submitting their files via the submission tool, but use e-mail or ftp instead. Since October 2016 until August 2017, about 10% of the EMEP measurements for 2015 were delivered using the submission tool. The highest shares of data submitted using the submission tool are from France, Germany, Austria and Finland.

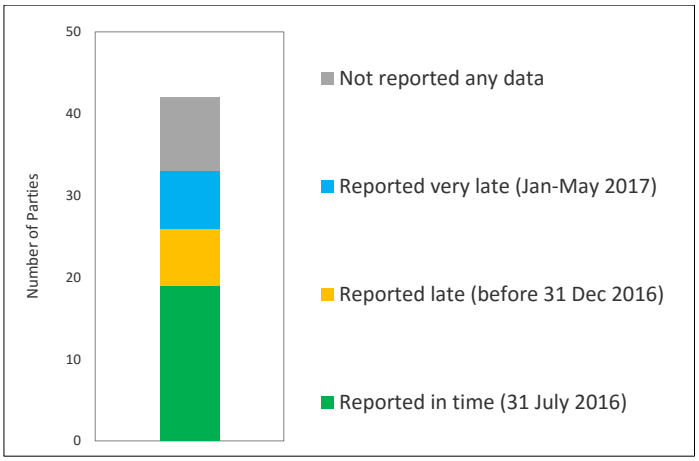

Figure 9.3: Submission of 2015 data to EMEP/CCC.

9.3 Data Quality

In October 2016, EMEP/CCC arranged a workshop in co-operation with ACTRIS on quality assurance and data reporting. The workshop discussed revisions of the data quality objective (DQO), field and lab methods, and how to report relevant data quality measures.

It was decided that the DQO for inorganic ions should be updated and be in line with the guidelines of the Global Atmospheric Watch (GAW) Programme, to 5% for sulfate and nitrate, while 7% for ammonium. Whether these DQO are met is controlled in the annual laboratory intercomparison by EMEP. These results should be reported, defined as QA (quality assurance) measures, in the reporting templates. QA measures can be an on-site or off-site intercomparison, round-robin or an on-site audit. The documentation is imported in the database and thus also exported to the data users. The metadata for QA measures are administrated by CCC or external institutes and calibration centres, i.e. by WMO/GAW and ACTRIS. The data providers need to check and download relevant information from these sites, and links to these are given in the reporting templates.

The measurement guidelines and standard operating procedures (SOPs) defined as reference for the EMEP program has usually been given in the EMEP Manual for Sampling and Analysis (EMEP 2014). However, several of the new developments and recommendations are done by other networks and programmes (i.e. WMO/GAW, ACTRIS, CEN) in co-operation with the EMEP TFMM. Regular updates of the whole EMEP Manual is therefore impractical. EMEP/CCC will rather publish individual guidelines, which is developed by TFMM or other communities on the submission web page and clearly state which guidelines and SOPs are recommended for the EMEP network. As an example, the methods for measuring NO_2 by selective monitors have now been improved and can be recommended to be used as reference for the EMEP Programme. Guidelines are found at http://ebas-submit.nilu.no/Standard-Operating-Procedures.

The data reporting templates include measurement uncertainty. It is, however, somewhat unclear how to report measurement uncertainty for several species. A follow up from the workshop in October 2016 was to distribute a questionnaire on how the laboratories calculate

measurement uncertainties, and the use of field blanks. The results show that for EC/OC the template for calculating uncertainty is not used by everyone. This needs to be improved. Further, for the other compounds, where there is not developed any template to calculate this, the TFMM meeting in May 2017 proposed to include at least the analytical uncertainty. Templates and guidelines for how to calculate this will be done by the TFMM community the coming year, and the templates will be updated accordingly.

Within the European Research Infrastructure for the observation of Aerosol, Clouds, and Trace gases (ACTRIS), a very detailed and comprehensive procedure for data quality has been implemented for VOCs. This includes standardized data checks done by EMPA and NILU in parallel, a web tool for documenting all corrections being done and a close collaboration with the original data providers. Although it has taken substantial time and effort to establish this, the experience now is that this procedure has greatly improved the general data quality, the metadata documentation and the monitoring skills of the contributing institutions for VOCs.

In 2017, two new projects under EURAMET, European Metrology Programme for Innovation and Research (EMPIR) were launched, which will potentially give important improvements in data quality and traceability for several measurements relevant to the EMEP Programme. One project deals with aerosol measurements (16ENV07 AEROMET) and the other on NO_2 (16ENV05 MetNO_2). The objectives are to get more accurate and traceable measurements, which will bring greater confidence in identified trends in emissions and air quality, and support the development and implementation of effective, evidence-based mitigation policies needed to reduce pollution levels.

The MetNO_2 (Metrology for nitrogen dioxide) project will develop capabilities for the direct measurement of NO_2 using innovative techniques and direct calibration with more accurate and stable primary reference standards.

The AEROMET (Aerosol metrology for atmospheric science and air quality) project aims to develop and demonstrate methods for traceability and calibration of different aerosol instruments capable of covering the environmentally relevant size ranges from several nm up to 10 μm and the regulatory relevant mass concentrations (0.1 μg m^{-3} to 1000 μg m^{-3}) and number concentrations. An interesting research item in the project, which could be of interest for the EMEP monitoring programme, is to test mobile X-ray spectroscopy techniques in the field.

NILU/EMEP-CCC is involved in both projects, together with a few other EMEP national laboratories, to secure close links with the ongoing efforts of the EMEP monitoring and QA/QC.

References

EMEP: Manual for Sampling and Chemical Analyses, EMEP/CCC Report 1/2014, The Norwegian Institute for Air Research (NILU), Kjeller, Norway, URL http://www.nilu.no/projects/ccc/manual/index.html, 2014.

Tørseth, K., Aas, W., Breivik, K., Fjæraa, A. M., Fiebig, M., Hjellbrekke, A. G., Lund Myhre, C., Solberg, S., and Yttri, K. E.: Introduction to the European Monitoring and Evaluation Programme (EMEP) and observed atmospheric composition change during 1972–2009, Atmos. Chem. Physics, 12, 5447–5481, doi:10.5194/acp-12-5447-2012, URL http://www.atmos-chem-phys.net/12/5447/2012/, 2012.

UNECE: Progress in activities in 2009 and future work. Measurements and modelling (acidification, eutrophication, photooxidants, heavy metals, particulate matter and persistent organic pollutants). Draft revised monitoring strategy., Tech. Rep. ECE/EB.AIR/GE.1/2009/15, UNECE, URL http://www.unece.org/env/documents/2009/EB/ge1/ece.eb.air.ge.1.2009.15.e.pdf, 2009.

CHAPTER 10

Emissions from international shipping

Michael Gauss, Jan Eiof Jonson and Ágnes Nyíri

The use of accurate ship emission data for air quality modelling has become increasingly important as land-based emissions have decreased relative to ship emissions during the last few decades. The trends in ship emissions have been highly non-monotonic and spatially variable, especially during the last ten years. At the same time, obtaining reliable data on emissions from international shipping has always been challenging. In the EMEP status report of last year we gave an overview of the different data sets being considered for modelling at EMEP/MSC-W (Gauss and Jonson 2016). As a follow-up, we discuss in this chapter the choices we have made for our EMEP MSC-W model simulations this year, i.e. for reporting the status of 2015.

10.1 Background

Emissions from shipping activities are major sources of air pollution and depositions in Europe (Jonson et al. 2015). While land-based emissions of SO_x and NO_x have been reduced significantly since 1990 as a result of air quality legislation, emissions from international shipping have decreased less for SO_x, and even increased for NO_x in response to enhanced ship traffic. This has led to a general increase in the relative importance of emissions from shipping, as was illustrated in Gauss and Jonson (2016).

However, the 1st of January 2015 marked a major change in sulphur emissions from shipping within the so-called SECAs (Sulphur Emission Control Areas). Here the maximum allowed sulphur content in marine fuels was reduced from 1% to 0.1%, following a new regulation by the IMO (International Maritime Organization). The regulation also includes the provision that fuel with higher sulphur content may be used under the condition that emission reduction technology is installed that reduces the sulphur content of the exhaust gas to what would correspond to the use of 0.1% sulphur fuel. Within the EMEP model domain, the Baltic Sea and the North Sea are the only seas that are designated as SECA. In other European wa-

ters the regulations are so far unchanged. However, from 2020 a maximum sulphur content of 0.5% in marine fuels will be implemented worldwide (down from the current 3.5%, but in practice average sulphur content is now about 2.5%).

10.2 The FMI data on ship emissions

For the last two years EMEP/MSC-W has been using ship emissions based on the TNO-MACC-III inventory extending up to year 2011 (see discussion in Gauss and Jonson (2016)). Due to the lack of reliable data, no trend in ship emissions was assumed for the years 2012, 2013 and 2014. However, following the implementation of the stricter SECA regulations in January 2015 this assumption is no longer valid.

By courtesy of the Finnish Meteorological Institute (FMI) we have been granted access to a newly developed set of ship emission data for year 2015 (Johansson et al. 2017). The data are based on real ship movements obtained from data collected through the Automatic Identification System (AIS), which is mandatory worldwide for all ships with a gross tonnage of 300 tonnes or more, as well as for all passenger ships regardless of size. The ship movements are combined with vessel specific technical data (ship size, engines installed, speed, etc.) for each individual ship. Emissions are then calculated using the STEAM model as described in Jalkanen et al. (2016).

The 2015 global ship emissions from FMI have been provided as daily data on a 0.1 x 0.1 degrees grid for NO_x, SO_x, CO, and particulate matter. For NMVOC (Non Methane Volatile Organic Compounds) emissions from TNO-MACC-III are used in the EMEP model, as these are not included in the FMI emission inventory. Furthermore, we have aggregated the daily emissions to monthly data. This choice was made after two model sensitivity tests using daily and monthly data, respectively, which showed virtually identical model results.

Table 10.1: Ship emissions from FMI in European sea areas. Sulphur emissions are given as SO_2 and SO_4. PM emissions are sub-divided into Ash, EC and OC, all assumed emitted as $PM_{2.5}$. Differences between FMI and TNO-MACC-III data are given in percent.

	Sulphur Gg SO_2			**NOx** Gg NO_2		**CO** Gg CO		**$PM_{2.5}$** Gg, see caption			
	SO_2	SO_4						Ash	EC	OC	
Baltic Sea	10.3	0.8	*-84%*	321	*18%*	22	*-21%*	1.5	2.0	5.0	*-23%*
North Sea	23.8	1.5	*-84%*	695	*8%*	51	*-24%*	3.4	4.7	11.9	*-26%*
Mediterr. Sea	675	40	*-27%*	1353	*-10%*	94	*-38%*	6.4	8.8	22	*-66%*
Black Sea	68	3.9	*36%*	172	*118%*	13	*63%*	0.9	1.2	3.0	*-15%*

In Table 10.1 the FMI global emissions are listed for the Baltic Sea, the North Sea, the Mediterranean Sea and the Black Sea. Also listed are the percentage differences between the FMI data and the TNO-MACC-III used in last year's reporting (on status of 2014).

Emissions of gaseous SO_2 and particulate SO_4 are listed separately, while the percentage difference between TNO-MACC-III and FMI refers to the sum of the two (in TNO-MACC-III

5% of SO_x is assumed to be emitted as SO_4).

In the FMI 2015 emission data all PM emissions are assumed to be $PM_{2.5}$ (SO_4 is also emitted as particles, but for comparison with TNO-MACC-III these emissions are included under 'Sulphur'). Emissions of ash are assumed to have a high content of metals with a weighted average molecular weight of 42.4, see Moldanová et al. (2009), thus making a non-negligible contribution to PM emissions by mass.

When evaluating the percentage differences it has to be noted that the FMI data are valid for 2015 while the MACC-III data are valid for 2011. The large reductions in sulphur emissions in the Baltic Sea and in the North Sea can thus be explained by the stricter SECA regulations since January 2015. But the estimated sulphur emissions are of the order of 27% lower also in the Mediterranean Sea, while they are 36% higher in the Black Sea. For NO_x the FMI 2015 emissions are moderately higher in the Baltic Sea and in the North Sea, and considerably higher in the Black Sea. In the Mediterranean Sea emissions are somewhat lower. CO emissions are lower in all sea areas except the Black Sea. $PM_{2.5}$ emissions are 15 to 26% lower in the most sea areas except the Mediterranean Sea, where emissions are 66% lower. For all emitted species the percentage difference between the FMI 2015 and the TNO-MACC-III 2011 emissions are higher in the Black Sea than in other sea areas. The reason for this is not fully understood, but could be related to a better representation of the fleet composition in the FMI 2015 inventory, as this data set is based on counting each individual ship as a separate entity based on ship size, age and engines installed.

10.3 The way ahead

International shipping is now a major source of air pollution, but emissions are likely to decrease in the years to come. As noted above, the maximum allowed sulphur content in marine fuels allowed globally will be reduced to 0.5% in 2020, reducing emissions also in EU waters that are not yet designated as SECAs. Furthermore, the North Sea and the Baltic Sea have been designated by the IMO as NECAs (NO_x emission control areas), i.e with stronger regulation on NO_x emissions. The NECA regulations will come into effect in 2021. These stricter NECA regulations will only apply to new ships, or ships undergoing major upgrades, resulting in a rather gradual decrease in NO_x emissions. Emissions may also be affected by technology shifts, and the use of more environmental friendly fuels as LNG (liquefied Natural Gas), bio-fuels, various degrees of electrification (hybrids or pure electric) etc.

For EMEP modelling, access to accurate emission data is of crucial importance. However, the judgement on which emission data set in regard to shipping is best fit for purpose is not a straightforward task because measurements to constrain the estimates are sparse. Uncertainties remain in the estimates of total fuel use, the spatial distribution of emissions, and in the emission factors (exhaust per kg of burnt fuel). The fact that the FMI data are available for 2015 was the main reason for choosing these data this year (for reporting status of 2015). Also, the use of AIS data as a basis for the FMI data ensures a high level of spatial and temporal accuracy.

Due to the large changes in sulphur emissions within the SECAs, we opted for not using the TNO-MACC-III emission data valid for 2011 anymore. With relevance for future EMEP modelling activities, the Copernicus Atmosphere Monitoring Service (CAMS), where both FMI, TNO, CEIP and the Norwegian Meteorological Institute are partners, is going to provide

updated ship emissions for the years after 2015. It is hoped that these will become available in time for next year's EMEP status reporting (on the status of 2016).

References

Gauss, M. and Jonson, J.: Emissions from international shipping, in: Transboundary particulate matter, photo-oxidants, acidifying and eutrophying components. EMEP Status Report 1/2016, pp. 103–109, The Norwegian Meteorological Institute, Oslo, Norway, 2016.

Jalkanen, J.-P., Johansson, L., and Kukkonen, J.: A comprehensive inventory of ship traffic exhaust emissions in the European sea areas in 2011, Atmos. Chem. Physics, 16, 71–84, doi:10.5194/acp-16-71-2016, URL http://www.atmos-chem-phys.net/16/71/2016/acp-16-71-2016.pdf, 2016.

Johansson, L., Jalkanen, J.-P., and Kukkonen, J.: Global assessment of shipping emissions in 2015 on a high spatial and temporal resolution, Atmos. Environ., in review, 2017.

Jonson, J. E., Jalkanen, J. P., Johansson, L., Gauss, M., and Denier van der Gon, H. A. C.: Model calculations of the effects of present and future emissions of air pollutants from shipping in the Baltic Sea and the North Sea, Atmospheric Chemistry and Physics, 15, 783–798, doi:10.5194/acp-15-783-2015, URL http://www.atmos-chem-phys.net/15/783/2015/, 2015.

Moldanová, J., Fridell, E., Popovicheva, O., Demirdjian, B., Tishkova, V., Faccinetto, A., and Focsa, C.: Characterisation of particulate matter and gaseous emissions from a large ship diesel engine, Atmos. Environ., 43, 2632–2641, URL https://doi.org/10.1016/j.atmosenv.2009.02.008, 2009.

Part IV

Appendices

APPENDIX A

National emissions for 2015 in the EMEP domain

This appendix contains the national emission data for 2015 used throughout this report for main pollutants and primary particle emissions in the EMEP domain.

The land-based emissions for 2015 have been derived from the 2017 official data submissions to UNECE CLRTAP (Mareckova et al. 2017).

Emission data for international shipping for year 2015 have been provided by the Finnish Meteorological Institute (FMI). The shipping emissions are calculated using the STEAM model (Jalkanen et al. 2016) based on real ship movements obtained from data collected through the Automatic Identification System (AIS). NMVOC emissions are not included in the FMI shipping emission inventory, these are therefore based on emissions data developed within the EU Horizon2020 project MACC-III (MACC-III 2015) by TNO.

Note that emissions in this appendix are given in different units than used elsewhere in this report in order to keep consistency with the reported data. Emissions from international shipping for the North-East Atlantic Ocean are not included in the emission totals.

References

Jalkanen, J.-P., Johansson, L., and Kukkonen, J.: A comprehensive inventory of ship traffic exhaust emissions in the European sea areas in 2011, Atmos. Chem. Physics, 16, 71–84, doi:10.5194/acp-16-71-2016, URL http://www.atmos-chem-phys.net/16/71/2016/acp-16-71-2016.pdf, 2016.

MACC-III: Report on the update of global and European anthropogenic emissions., Tech. Rep. COPERNICUS Grant agreement 633080, MACC-III (Monitoring Atmospheric Composition and Climate, 2015.

Mareckova, K., Pinterits, M., Tista, M., Ullrich, B., and Wankmüller, R.: Inventory review 2017. Review of emission data reported under the LRTAP Convention and NEC Directive. Stage 1 and 2 review. Status of gridded and LPS data, EMEP/CEIP 1/2017, EEA/CEIP Vienna, 2017.

Table A:1: National total emissions for 2015 in the EMEP domain. Unit: Gg. (Emissions of SO_x and NO_x are given as Gg(SO_2) and Gg(NO_2), respectively.)

Area/Pollutant	SOx	NOx	NH3	NMVOC	CO	PM2.5	PMco	PM10
Albania	23	33	25	39	196	10	12	22
Armenia	32	25	27	42	116	4	2	6
Austria	15	149	67	113	567	17	15	31
Azerbaijan	14	86	74	102	174	6	10	16
Belarus	54	160	142	331	845	41	12	53
Belgium	43	197	66	120	398	27	10	38
Bosnia and Herzegovina	193	31	20	35	95	14	12	26
Bulgaria	142	132	34	93	288	29	21	50
Croatia	15	53	30	61	216	20	7	27
Cyprus	13	15	5	7	14	1	1	2
Czech Republic	123	165	70	139	503	24	13	36
Denmark	11	114	73	109	327	20	10	30
Estonia	32	31	12	23	128	9	5	14
Finland	42	140	32	88	325	22	10	32
France	153	835	679	623	2994	165	101	266
Georgia	5	37	45	42	167	18	4	22
Germany	352	1187	759	1020	2683	99	122	221
Greece	137	230	60	154	504	39	15	54
Hungary	24	123	76	139	458	54	17	70
Iceland	56	21	6	7	119	1	0	2
Ireland	18	80	108	101	109	14	10	24
Italy	123	763	393	842	2356	160	19	179
Kazakhstan	2092	689	243	277	1354	232	89	321
Kyrgyzstan	50	59	58	26	302	11	10	20
Latvia	4	37	19	41	131	18	6	23
Lithuania	18	55	29	59	127	18	7	25
Luxembourg	1	22	6	10	22	2	0	2
Malta	3	3	1	2	0	0	0	0
Montenegro	40	13	3	9	33	5	7	12
Netherlands	30	228	128	139	570	13	14	26
Norway	16	151	27	156	383	28	9	37
Poland	690	714	267	531	2401	125	97	221
Portugal	37	170	45	176	266	45	12	57
Republic of Moldova	9	27	23	48	78	11	5	16
Romania	152	214	163	313	751	112	39	151
Russian Federation	3944	3434	1300	2787	13333	1273	1032	2305
Serbia	416	144	64	132	277	53	19	72
Slovakia	71	86	30	89	231	30	7	37
Slovenia	5	35	19	32	110	12	1	13
Spain	261	841	474	571	1629	123	43	166
Sweden	19	130	60	164	461	19	19	38
Switzerland	7	64	61	77	186	7	10	18
Tajikistan	65	103	62	48	809	26	26	52
TFYR of Macedonia	76	28	11	29	82	19	9	28
Turkey	1939	883	907	1115	2351	382	447	829
Turkmenistan	389	159	107	83	896	109	133	241
Ukraine	854	452	18	223	1057	38	83	121
United Kingdom	236	918	293	835	1645	105	41	145
Uzbekistan	1610	472	169	166	2540	321	489	811
North Africa	590	137	336	137	480	86	126	212
Asian areas	1846	552	1150	865	5233	236	282	518
Baltic Sea	11	321	0	7	22	9	0	9
Black Sea	72	172	0	2	13	5	0	5
Mediterranean Sea	715	1353	0	45	94	37	0	37
North Sea	25	695	0	17	51	20	0	20
Natural marine emissions	2454	0	0	0	0	0	0	0
Volcanic emissions	2070	0	0	0	0	0	0	0
TOTAL	22437	17968	8876	13441	51501	4324	3490	7809

APPENDIX B

Model Evaluation

The EMEP MSC-W model is regularly evaluated against various kinds of measurements, including ground-based, airborne and satellite measurements. As the main application of the EMEP MSC-W model within the LRTAP Convention is to assess the status of air quality on regional scales and to quantify long-range transboundary air pollution, the focus of the evaluation performed for the EMEP status reports is on the EMEP measurement sites.

Only parts of this evaluation are included in the printed version of the EMEP status report (see Chapter 2). A comprehensive collection of maps, graphs and statistical analyses, including a more detailed discussion of model performance, are freely available as supplementary material from the MSC-W report page on the EMEP website `http://emep.int/mscw/mscw_publications.html`

This year, the evaluation report is found under the link 'Supplementary material to EMEP Status Report 1/2017'. It contains a comprehensive evaluation of the EMEP MSC-W model for air concentrations and depositions in 2015. The report is divided into three chapters, dealing with pollutants responsible for eutrophication and acidification (Gauss et al. 2017b), ground level ozone and nitrogen dioxide (Gauss et al. 2017a), and particulate matter (Tsyro et al. 2017), respectively.

The agreement between model and measurements in 2015 is visualized as:

- scatter plots for the EMEP domain
- time series for individual EMEP stations
- horizontal maps combining model results and EMEP measurement data

Tables summarize common statistical measures of model score, such as bias, root mean square error, temporal and spatial correlations and the index of agreement (see Chapter 1).

This type of model evaluation is performed on an annual basis and can be downloaded from the same web page also for previous years.

References

Gauss, M., Hjellbrekke, A.-G., Aas, W., and Solberg, S.: Ozone, Supplementary material to EMEP Status Report 1/2017, available online at www.emep.int, The Norwegian Meteorological Institute, Oslo, Norway, 2017a.

Gauss, M., Tsyro, S., Fagerli, H., Hjellbrekke, A.-G., and Aas, W.: Acidifying and eutrophying components, Supplementary material to EMEP Status Report 1/2017, available online at www.emep.int, The Norwegian Meteorological Institute, Oslo, Norway, 2017b.

Tsyro, S., Gauss, M., Hjellbrekke, A.-G., and Aas, W.: PM10, PM2.5 and individual aerosol components, Supplementary material to EMEP Status Report 1/2017, available online at www.emep.int, The Norwegian Meteorological Institute, Oslo, Norway, 2017.

emep

Meteorological Synthesizing Centre – West
Norwegian Meteorological Institute
P.O.Box 43 – Blindern, NO-0313 Oslo, Norway

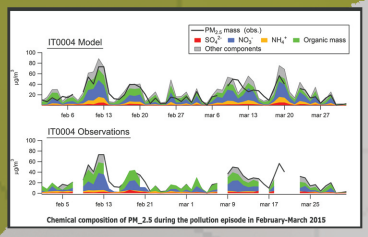

ccc
NILU
Norwegian Institute for Air Research
P.O. Box 100
NO-2027 Kjeller
Norway
Phone: +47 63 89 80 00
Fax: +47 63 89 80 50
E-mail: kjetil.torseth@nilu.no
Internet: www.nilu.no

ciam
International Institute for Applied Systems Analysis (IIASA)
Schlossplatz 1
A-2361 Laxenburg
Austria
Phone: +43 2236 807 0
Fax: +43 2236 71 313
E-mail: amann@iiasa.ac.at
Internet: www.iiasa.ac.at

ceip
Umweltbundesamt GmbH
Spittelauer Lände 5
1090 Vienna
Austria
Phone: +43-(0)1-313 04
Fax: +43-(0)1-313 04/5400
E-mail:
emep.emissions@umweltbundesamt.at
Internet:
http://www.umweltbundesamt.at/

msc-e
Meteorological Synthesizing Centre-East
2nd Roshchinsky proezd,
8/5, room 207
115419 Moscow
Russia
Phone +7 926 906 91 78
Fax: +7 495 956 19 44
E-mail: msce@msceast.org
Internet: www.msceast.org

msc-w
Norwegian Meteorological Institute (MET Norway)
P.O. Box 43 Blindern
NO-0313 OSLO
Norway
Phone: +47 22 96 30 00
Fax: +47 22 96 30 50
E-mail: emep.mscw@met.no
Internet: www.emep.int